Ricardo García

WILEY-VCH

Amplitude Modulation Atomic Force Microscopy

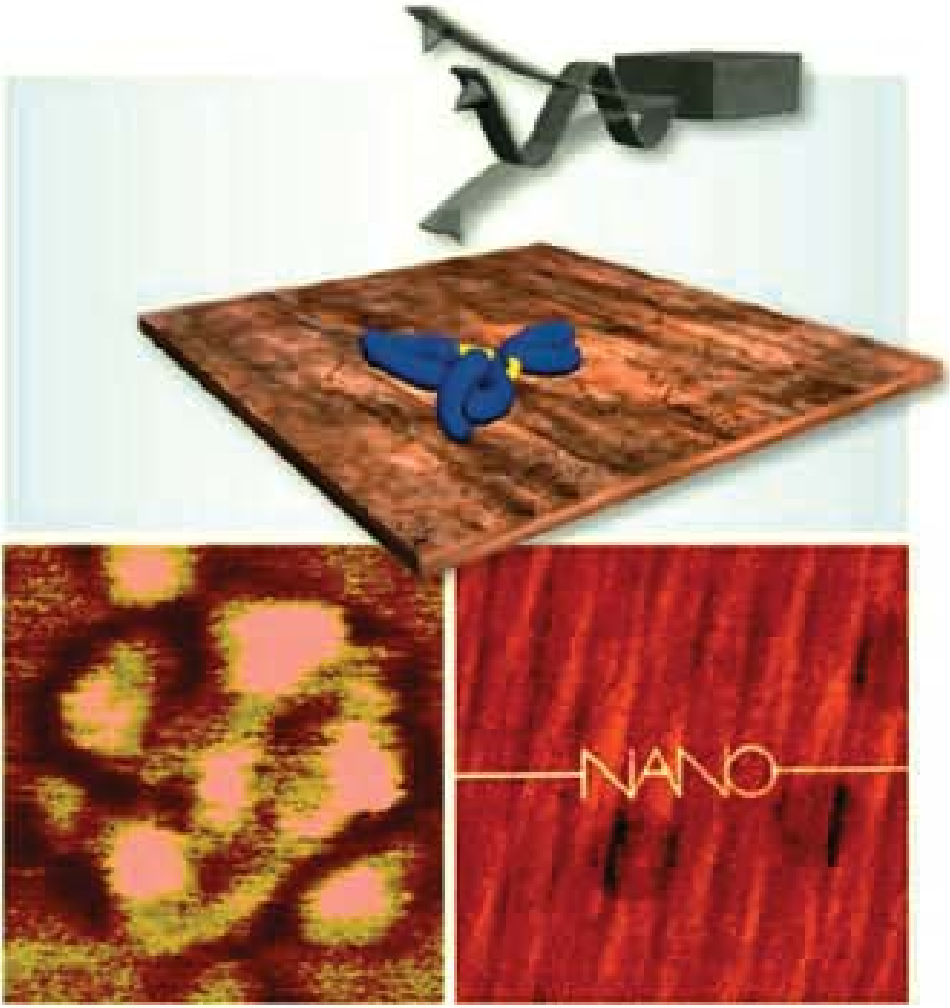

Ricardo García

Amplitude Modulation Atomic Force Microscopy

Related Titles

Sarid, D.

Exploring Scanning Probe Microscopy with MATHEMATICA

310 pages
2007
Hardcover
ISBN: 978-3-527-40617-3

Jena, B. P., Hoerber, J. K. H. (eds.)

Force Microscopy

Applications in Biology and Medicine

300 pages
2006
Hardcover
ISBN: 978-0-471-39628-4

Kumar, C. S. S. R. (ed.)

Nanosystem Characterization Tools in the Life Sciences

413 pages with 178 figures and 28 tables
2006
Hardcover
ISBN: 978-3-527-31383-9

Ricardo García

Amplitude Modulation Atomic Force Microscopy

WILEY-VCH Verlag GmbH & Co. KGaA

The Author

Prof. Dr. Ricardo García
Instituto de Microelectronica
de Madrid (CSIC)
Tres Cantos. Madrid, Spain
ricardo.garcia@imm.cnm.csic.es

Cover picture
Spiesz Design, Neu-Ulm

Library of Congress Card No.: applied for

British Library Cataloguing-in-Publication Data
A catalogue record for this book is available from the British Library.

Bibliographic information published by the Deutsche Nationalbibliothek
The Deutsche Nationalbibliothek lists this publication in the Deutsche Nationalbibliografie; detailed bibliographic data are available on the Internet at http://dnb.d-nb.de.

Cover Design Grafik-Design Schulz, Fußgönheim
Typesetting Thomson Digital, Noida, India
Printing and Binding Fabulous Printers Pte Ltd

Printed in the Federal Republic of Germany
Printed on acid-free paper

ISBN: 978-3-527-40834-4

The intellect of man is forced to choose
perfection of the life, or of the work,
And if it take the second must refuse
A heavenly mansion, raging in the dark.
When all that story's finished, what's the news?
In luck or out the toil has left its mark:
That old perplexity an empty purse,
Or the day's vanity, the night's remorse.

(William Butler Yeats, *The Choice*)

To my wife Begoña and children Leonardo and Adriano.
To my parents Graciana and Santiago.

Contents

Amplitude Modulation Atomic Force Microscopy. Ricardo García

ISBN: 978-3-527-40834-4

Preface

This book has two goals. First, it aims to describe how the physical forces acting between a vibrating probe and the sample atoms are transformed into amplitude and phase shift variations. Second, it aims to explain how from these variations it is possible to generate a high resolution image and to extract information on the properties of the sample surface.

My first experiment with an amplitude modulation atomic force microscope happened in the spring of 1993. Then, I was a postdoctoral fellow working with Carlos Bustamante. At that time, Bustamante's laboratory was at the forefront of AFM applications in biology. Tapping mode AFM was generating images of DNA and single proteins in liquid with an unprecedented resolution. The intellectual atmosphere of the laboratory was exuberant. Passionate discussions about image resolution were frequent. Sometimes, the emphasis was placed on the sample preparation, at others on the size and lifetime of the probe. We knew little about the cantilever dynamics. Mostly, we assumed that a microscope that provided impressive images had to have a well established theory behind it. After a few years of hard work, it emerged that further improvements in lateral resolution and material properties characterization would require a better understanding of the cantilever tip dynamics.

About 3 years ago, an editor from Wiley VCH invited me to write a book on amplitude modulation AFM. I had mixed feelings. Was this happening at the right time? Is it worth to devote time and energy to write a scientific book at the beginning of the twenty first century? The writing process has not been easy. On several occasions, I had to pause because I realized that my knowledge on dynamic AFM was uneven. It took me about 8 months to reach a steady writing rhythm. On other occasions, especially when I was under pressure of different submission deadlines, I went introspective. At the end, the aspirations harbored during the undergraduate and graduate years had more weight than other professional considerations.

The text is structured to satisfy the needs of beginners and experts alike. Every chapter starts with an introduction that summarizes the topics of the chapter. Most of the chapters can be read independently. Chapter 1 offers a historical perspective on the development of amplitude modulation force microscopy. Chapter 2 sum marizes the minimum knowledge that is required to properly operate the

Amplitude Modulation Atomic Force Microscopy. Ricardo García

ISBN: 978-3-527-40834-4

microscope. Chapter 3 introduces to the tip surface forces. Chapters 4 and 5 present several aspects of the cantilever dynamics in air. Chapter 6 extends the cantilever dynamics to liquid environments. Chapter 7 deals with the theory and applications of phase imaging AFM. Chapter 8 describes the factors that control lateral and vertical resolution of the instrument. Chapter 9 delves into the multifrequency AFM methods based on the use of several modes or harmonics. Finally, Chapter 10 presents some applications that go beyond topographic imaging such as nanolitho graphy, near field optics, or molecular recognition imaging.

The number of people who directly or indirectly have helped me understand atomic force microscopy is larger than I could cope to realize. However, I specifically want to acknowledge the graduate students that have trodden with me the manifold aspects of dynamic AFM. Javier Tamayo, Alvaro San Paulo, and Tomás R. Rodríguez belong to the first wave of graduate students involved in theoretical simulations of cantilever dynamics. They were genuine pioneers. Nicolás F. Martínez, José R. Lozano, Christian Dietz, and Elena T. Herruzo are contributing to expand amplitude modulation AFM into the multifrequency domain. I also want to acknowledge the graduate students and postdocs who carried some of its applications. Monserrat Calleja, Marta Tello, and Ramsés Martínez performed some key experiments to materialize the potential of AFM nanolithography. Javier Martínez, Carlos Gómez, Nuria S. Losilla, Jorge R. Ramos, and Marco Chiesa have participated in several projects where the AFM played a crucial role.

I have enjoyed the friendship and the intellectual rigor of many colleagues, in particular, Carlos Bustamante, Arvind Raman, Roger Proksch, Fabio Biscarini, José M. Soler, Rubén Pérez, Ozgur Sahin, Artuto Baró, Peter Hinterdorfer, Ali Passian, Julio Gómez, and Alexis Baratoff. Ron Reifenberger made a short visit to the laboratory in 1997. His genuine appraisal of the simulations we were conducting had a considerable effect on me to keep my interest on dynamic AFM.

The type of symbols to be used or the terms selected to describe a given concept posed some unexpected challenges. The books by Robert Gomer "Field Emission and Field Ionization" and Jacob Israelachvili "Intermolecular Forces and Surface Forces" provided some examples or served as models.

Tres Cantos, Spain *Ricardo Garcia*
February 25, 2010

Annotation List

A	amplitude
A_{sp}	set point amplitude
A_0	free amplitude
a	contact radius
a_0	intermolecular distance
B	frequency bandwidth
d	instantaneous tip–surface distance
E, E_{eff}	Young's modulus
E_{dis}	energy dissipated per cycle
F_{ad}	adhesion force
F_{DMT}	force as given by the DMT model
F_{ts}	tip–surface force
F_{vdW}	van der Waals force
F_0	external driving force
f	frequency
G	shear modulus
g	gain factor in Q control
H	Hamaker constant
h	cantilever thickness
I	area moment of inertia
k	force constant
k_B	Boltzmann constant
k_n	force constant nth eigenmode
L	cantilever length
l	lateral resolution
m_c	cantilever mass
m	effective mass
Q	quality factor
Q_n	quality factor nth eigenmode
R, R_t	tip's radius
T	period of the oscillation
t	time
V	external voltage

Amplitude Modulation Atomic Force Microscopy. Ricardo García

ISBN: 978-3-527-40834-4

W	cantilever width
$w(x,t)$	deflection of a continuous cantilever
z	instantaneous cantilever deflection
z_0	average cantilever deflection
z_c	average tip surface distance
γ	effective force damping factor, surface tension
δ	indentation
ε	dielectric constant, strain
$\varkappa_n$	eigenvalue of spatial argument
ϱ	cantilever density
ϕ	phase shift of the tip's oscillation
φ	phase shift in Q control
ω	excitation angular frequency
ω_0	fundamental angular frequency
ω_n	angular frequency of an eigenmode or higher harmonic

1
Introduction

1.1
Historical Perspective

The invention of scanning probe microscopy is considered one of the major advances in materials science since 1950 [1, 2]. Scanning probe microscopy includes a large family of microscopy methods that share two operational elements: the use of a sharp probe (tip) and the feedback mechanism. The feedback loop is characterized by keeping at a constant value the interaction parameter while the probe is scanned across the sample surface. Scanning probe microscopy started with the invention of the scanning tunneling microscope (STM) by Gerd Binnig and Heinrich Rohrer in 1982 [3, 4]. The STM works by detecting the current that flows between a metallic tip situated a few angstroms above a conductive surface when an external voltage is applied. The limitations of the STM to image poorly conducting materials such as biomolecules served as a motivation for Gerd Binnig, Calvin Quate, and Christoph Gerber to invent the atomic force microscope (AFM) in 1986 [5, 6]. The first AFM operated by measuring the static deflection of the probe. This method is called contact mode AFM. One year later Martin, Williams, and Wickramasinghe implemented the dynamic operation in force microscopy [7]. They wanted to use the AFM to measure long range forces over a distance range of 3 15 nm. They noticed that the amplitude of the tip's oscillation changed with the tip surface distance. These changes were related to the gradient of the tip surface force. At the same time, they proposed to use the amplitude in a feedback loop to get an image of the surface. Such an early start would have anticipated a sudden rise in the number of articles dealing with amplitude modulation AFM. However, it did not happen that way (Figure 1.1). In 1987, the technique was so new that only a handful of groups could master the instrumental and conceptual challenges to design and operate a dynamic AFM [7 11].

Amplitude Modulation Atomic Force Microscopy. Ricardo García

ISBN: 978-3-527-40834-4

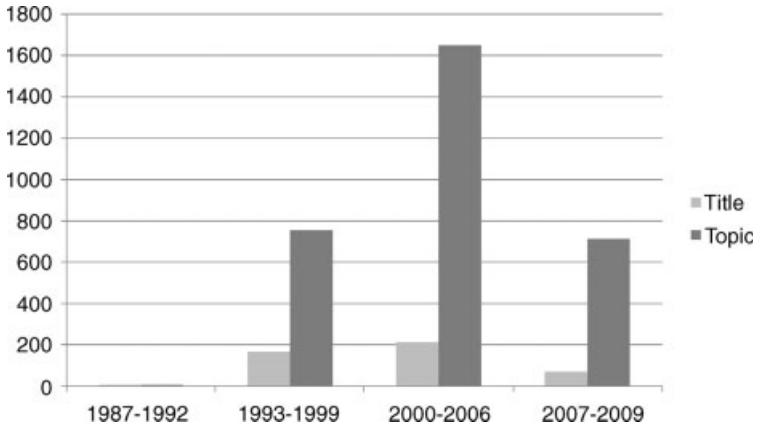

Figure 1.1 Histogram of the number of publications per period [104]. In dark gray are the publications that include in the abstract the keywords "tapping mode or tapping force or amplitude modulation force." In light gray are the publications that include the above key words in the title. The search for the first period was accomplished manually (12 publications). The above figures are merely indicative.

1.2 Evolution Periods and Milestones

The evolution of amplitude modulation AFM is interspersed with several periods where a few topics establish the frontiers of the technique. In some cases, a topic that contributes to shape the technique in a given period could have had its origin in an earlier period. The dates in brackets are indicative.

1.2.1 Early Times (1987 1992)

Martin and coworkers recorded the first AFM images obtained in a mode similar or identical to what today is known as amplitude modulation AFM. However, at that time, dynamic AFM was seen as an auxiliary microscopy its main advantage was its flexibility to be combined with other methods to map magnetic properties [9], electrostatic charges [10], or surface potential differences [11]. The few available dynamic force microscopes were rather complex instruments. For example, the deflection of the lever was measured by using optical inter ference and the levers were handmade, for example, by bending a tungsten wire.

Figure 1.2 shows the experimental setup of earliest dynamic AFM. The instrument is equipped with an interferometer to measure the lever deflection. The lever is a tungsten needle.

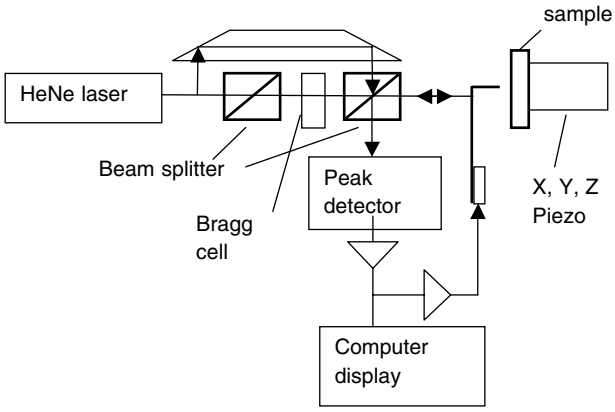

Figure 1.2 Schematic experimental setup of the first dynamic AFM. Notice the use of a bent tungsten wire as the integrated lever tip system. Adapted from Ref. [7].

1.2.2
Exploration and Expansion (1993 1999)

This period is marked by the rapid expansion and popularization of the technique for surface characterization with nanoscale resolution. The efforts were particularly significant and successful in imaging DNA, proteins and protein DNA com plexes [12 18], and polymer surfaces [19 24]. The progress was sustained by several factors. The implantation of the optical beam deflection method to detect the lever deflection [25, 26] and the fabrication of micromachined cantilevers [27, 28] con tributed to the availability of reliable commercial instruments [29]. The operation of tapping mode AFM in liquid [30, 31] made it possible to image dynamic processes, in particular those involving biomolecules with characteristic times in the range of several minutes [32]. The interpretation of the cantilever's resonance spectra in liquid was simplified by driving the cantilever oscillation with a magnetic force [33]. A significant breakthrough was to implement phase shift measurements simulta neously with topography [34]. This instrumental advance enabled to map compo sitional variations and changes in material properties in heterogeneous surfaces [35, 36]. In addition, amplitude modulation AFM found new applications by showing its potential for nanopatterning and nanolithography [37, 38].

The collaboration between Paul Hansma and Virgil Elings led to several instru mental and conceptual breakthroughs in probe microscopy. The fabrication of the first wave of short cantilevers is one of them [39]. These cantilevers were initially meant to reduce the thermal noise, but they would have a pivotal role in the development of fast AFM imaging [40].

This period witnessed the earliest attempts to simulate the cantilever tip dynamics in the presence of an external force [36, 41 44]. Numerical simulations explained the sudden changes, sometimes observed in the amplitude curves in terms of transitions

between attractive and repulsive tip surface interaction regimes [44 46]. Simulations also established that the phase contrast was directly related to energy dissipation processes [47]. This led to the deduction of the first analytical expressions that linked the sine of the phase shift to the energy dissipated by the tip on the sample [48, 49]. Another milestone was the publication of the first comprehensive attempt to describe the dynamics and performance of the microscope in liquid [50].

1.2.3 Cantilever Tip Dynamics (2000 2006)

Amplitude modulation AFM became so firmly established for nanoscale characterization of surfaces that theoretical contributions devoted to explain its dynamics were initially rejected in the most prestigious physics journals. In fact, during the first two periods, the experimental achievements preceded a comprehensive theoretical understanding of them. Fundamental questions such as the origin of the amplitude reduction, the reconstruction of the force from the observables, or the generation of higher harmonics remained unsatisfactorily addressed. It became evident that the lack of a theory was limiting the evolution of the technique. A significant number of publications were devoted to explain the nonlinear character of the cantilever dynamics [51 54], the generation [55, 56] and the use of higher harmonics, or modes to map material properties [57 59]. A remarkable result was the method developed by Stark and coworkers to obtain the time resolved force by integrating the higher harmonics of the oscillation [58]. The spatial reconstruction of the force from the amplitude and phase shift curves was also accomplished [60, 61].

Two experimental results highlighted the molecular resolution capabilities of the instrument. Muller and coworkers provided images of a purple membrane surface with a lateral resolution of 1.1 nm [62], a value almost identical to the one reported by the same authors with contact AFM. Later, Klinov and Magonov dispelled the myth that molecular resolution was incompatible with operation in air by imaging a polymer crystal with a resolution of about 0.4 nm [63].

Three instrumental developments underlined the vitality of the technique. First, the promise to observe dynamic processes in real time was eventually fulfilled by designing a microscope with a frame rate of $12.5\ s^{-1}$ [64]. Second, the observation that the oscillation is asymmetric in liquid led to combine topography and molecular recognition imaging, in a single pass, [65, 66]. Third, the simultaneous excitation of the first two cantilever modes provided a way to separate topography from compositional contrast and to enhance spatial resolution while minimizing tip surface forces [67, 68].

1.2.4 Multifrequency AFM (2007 to Present)

Several experimental schemes are being proposed to increase the capacities of the instruments to measure material properties while aiming molecular spatial resolution. These methods are based on the simultaneous detection of several harmonics

and/or modes of the tip oscillation. In some cases, such as in bimodal AFM, two modes of the cantilever are externally excited [69], while in other cases, for example, it happens in liquid, the higher modes or harmonics are activated by the tip surface interaction [70, 71]. In other cases, the use of a special cantilever where the tip is offset at one edge of the cantilever enables to measure time varying forces [72, 73]. Other approaches are exploring the cantilever response when the excitation involves a discrete series [74] or a band of frequencies [75].

The theoretical efforts are focused on two different directions. First, several aspects of the cantilever dynamics in liquid such as the origin of the asymmetry observed in the oscillation, the generation of higher harmonics, the interplay between damping and added mass effects, or the influence of the excitation mode on the dynamics are being addressed [76 81]. Second, the operation of the microscope in various multifrequency regimes is under investigation [80, 82].

1.3
Tapping Mode or Amplitude Modulation Force Microscopy?

Amplitude modulation AFM suffers from a problem of terminology. This is a common issue with scanning probe techniques where standardization is coming rather slowly. Different terms are being used to describe the same method or technique. This anomaly can be partially explained by the vitality of the technique that every now and then surprises with new developments. The first publication describing tapping mode AFM operation [19] makes a point in distinguishing tapping mode from the noncontact method proposed by Martin *et al.* [7]. Elings and coworkers emphasized that tapping mode AFM operated with amplitudes ranging between 20 and 100 nm, while amplitudes of 5 nm or less were required for noncontact operation. It was claimed that large amplitude values were needed to overcome the adhesion forces and reach stable imaging conditions. However, an analysis based on the equation of motion and the feedback mechanism shows that there are no grounds to support that distinction [83, 84]. The value of the free amplitude is certainly one of the factors that contributes to establishing the operation regime, attractive (usually noncontact) versus repulsive (intermittent contact). But there are other relevant factors such as the radius, the cantilever's force constant, or the surface energy. Furthermore, the attractive and the repulsive regimes are the solutions of the same equation of motion [46]. Nonlinear dynamics studies have shown that these solutions do coexist under the same operational parameters [52, 83]. The alternation between stable and unstable imaging while the set point amplitude is reduced represents a direct experimental evidence of the coexistence of solutions [52]. Furthermore, the coexistence of solutions is observed for amplitude values ranging from 5 to 25 nm. In fact, the technique is characterized by the use of the amplitude as the feedback parameter not by the values of the amplitude.

In this sense, amplitude modulation AFM seems a more appropriate name for the technique. Furthermore, this term helps us to rationalize the separation of dynamic AFM methods into two modes or techniques, frequency and amplitude modulation,

according to the parameter used to establish the feedback mechanism [84, 85]. Acceptable variations are amplitude modulated or amplitude mode AFM. Nonethe less, on a few occasions I will also use the tapping mode AFM term. The latter is both a tribute to its widespread use and a means to emphasize that we are dealing with the same experimental technique.

1.4 Other Dynamic AFM Methods

Nanoscience sets the scenario for an intense competition among the different microscopy techniques. In the field of force microscopy, there are two major dynamic modes that, on a few occasions, might be seen as competitors. The other technique uses the frequency as the feedback parameter and it is rightly called frequency modulation AFM.

1.4.1 Frequency Modulation AFM

In frequency modulation AFM, the feedback parameter is a frequency shift between the resonant frequency far from the sample surface and the resonant frequency closer to the surface [84, 86, 87]. The resonant frequency depends on the forces acting between the tip and the sample surface. The spatial dependence of the frequency shift, the difference between the actual resonant frequency and that of the free lever, is the source of contrast. An image is formed by profiling the surface topography with a constant frequency shift. FM AFM has been primarily used to obtain atomic resolution images of semiconductor, metals, insulators, or adsorbates in ultrahigh vacuum [88 94]. The ability to measure the tip surface force with great accuracy has led to several approaches to identify atoms [95, 96]. Initially, FM AFM operation was restricted to ultrahigh vacuum conditions; however, recent results show that mo lecular resolution imaging can also be achieved in liquid [97 100].

1.4.2 Amplitude Modulation versus Frequency Modulation AFM

Amplitude and frequency modulation AFM are both sophisticated instruments with atomic and molecular resolution capabilities. Mostly, they are seen as complementary dynamic AFM methods because they operate in different environments. However, FM AFM has also shown its capability to operate under air or liquid environments. This makes it pertinent to comment on the advantages of one method with respect to the other. Let us start by stating that there are no quantitative studies showing that one method has an intrinsic higher signal to noise ratio than the other. Some direct comparisons at nanoscale resolution have been attempted by imaging the same sample with the same instrument [101, 102]. However, the results seem to reflect more the skill of the microscopist with a given technique than an intrinsic difference

between them. More meaningful information could be extracted by comparing molecular resolution images obtained on the same surface. The cytoplasmic side of purple membrane has been imaged by both techniques [100, 103]. In this case, both methods produce images of similar spatial resolution. However, the versatility of amplitude modulation AFM in achieving molecular resolution while having the possibility of scanning μm^2 regions and coping with the presence of sudden height changes is still no mach for frequency modulation AFM instruments.

2
Instrumental and Conceptual Aspects

2.1
Introduction

This chapter introduces the main concepts and elements needed to operate an amplitude modulation AFM (AM AFM). Expressions for the cantilever force con stants and resonant frequencies as a function of geometry and material properties are described. The mathematical deductions are taken up in Chapters 4 and 5. Quan titative measurements require the calibration of several elements of the microscope, namely, the optical sensitivity and the force constant. The user should be aware that each cantilever resonance has its own optical sensitivity and force constant that might require an independent calibration experiment. The chapter also provides a defini tion of the different tip surface distances that exist in AM AFM.

2.2
Amplitude Modulation AFM

In amplitude modulation AFM, a sharp probe, often called the tip, is oscillated above but very close to the sample surface. The probe is at the end of a microcantilever that is mechanically excited at a fixed frequency, usually close to or at the first flexural resonant frequency. The tip surface interaction forces lead to a reduction in the amplitude of the oscillation from its free value. In amplitude modulation AFM, the experimental observables are the amplitude of the oscillation and the phase shift lag that exists between the external excitation and the tip motion. The amplitude is used as a feedback parameter to map the topography of the surface. The net value of the force exerted by the tip on the sample surface, either positive (repulsive) or negative (attractive), defines two different imaging regimes, repulsive or attractive, respec tively. For a fixed chemical composition for the tip surface interface, the force exerted by the tip on the sample surface depends on several factors such as the free amplitude, the tip radius, the value of the amplitude chosen to run the feedback, or the imaging regime.

Amplitude Modulation Atomic Force Microscopy. Ricardo García

ISBN: 978-3-527-40834-4

2.3
Elements of an Amplitude Modulation AFM

An atomic force microscope in general and an amplitude modulation AFM in particular has five major elements, the detection unit, the cantilever tip system, the tip sample motion unit, the feedback controller, and the image processing and display system (Figure 2.1). The first three elements are usually integrated into a single module that is called the microscope base (Figure 2.2). A detailed description of the technical features of the above elements has been reported by Ando *et al*. [1].

2.3.1
Feedback Controller

The cantilever tip system is excited at a single frequency. A lock in detector returns a signal related to the detection amplitude and phase of the input at the excitation frequency or its harmonics. The feedback loop maintains at constant the amplitude while the tip is either scanned across the sample surface or kept still above a given surface region. The root mean square value of the oscillation signal measured in the photodiode detector is kept constant in a process that involves the comparison between the instantaneous values of the amplitude A_i with respect to a

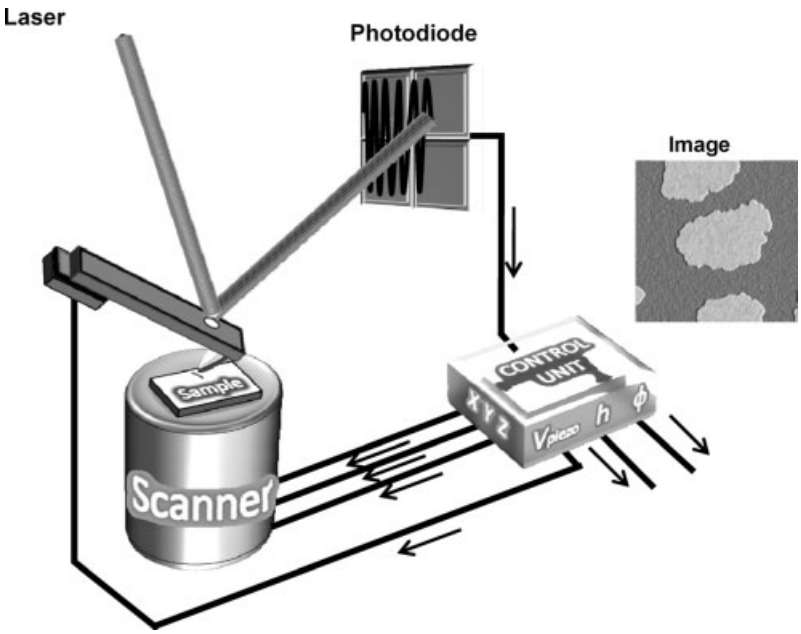

Figure 2.1 Scheme of the main elements of an amplitude modulation AFM.

Figure 2.2 *Top*: microscope setup in 2006. *Bottom*: images of two commercial microscope bases. The microscope base integrates the detection, the cantilever tip, and the tip sample units.

reference value (A_{sp}), called the set point amplitude. The practical goal of the feedback loop is to keep the error signal A_{sp} A_i as small as possible. The error signal is treated in the proportional integral differential system. Its output sends a voltage signal to the piezo z scanner to either approach or withdraw the tip in such a way as to minimize the difference between A_{sp} and A_i. The feedback loop sets the upper limit for the maximum scanning speed of the microscope. Current acquisition rates range from 60 to 500 kHz. Figure 2.3 shows the schematics of the feedback system.

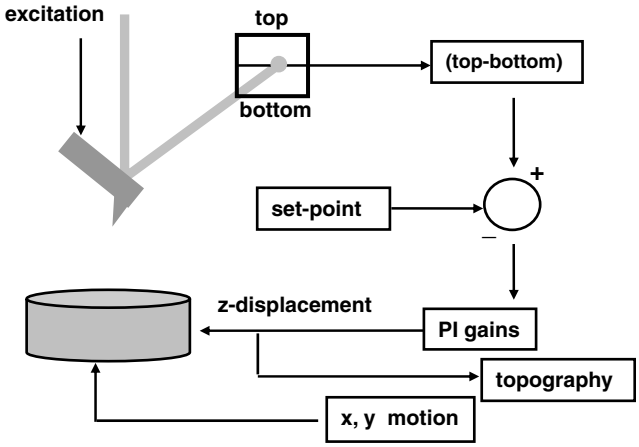

Figure 2.3 Simplified scheme of the feedback loop circuitry in amplitude modulation AFM.

2.3.2
Optical Beam Deflection

Methods of detecting the bending of the cantilever tip system produced by the tip surface forces are at the heart of force microscopy. The sensitivity and simplicity of the optical beam deflection method [2, 3] is one of the factors that have contributed to the rapid success of the AFM. A light beam coming from a solid state diode is reflected at the back of the cantilever and the deflection is monitored by a position sensitive photodetector consisting of several photodiodes (Figure 2.1). The photo currents are fed into a differential amplifier that generates an output signal in volts. The use of four segmented photodiodes enables the detection of both normal and lateral forces.

The ultimate detection sensitivity of the optical beam deflection method is limited by the thermal noise. A properly tuned beam deflection system enables detection of cantilever deflections below 0.01 nm. The beam deflection method has a caveat for it does not directly measure the deflection of the cantilever z (vertical displacement) but its change in slope dz/dx. A force applied on the tip produces both a change in the cantilever deflection and a change in the slope. For a rectangular cantilever, the application of the Euler Bernoulli theory and some geometrical considerations allow us to deduce a relationship between changes in slope and changes in deflection [4 6] (Figure 2.4).

The deflection along the cantilever length L produced by a force F applied at the free end is

$$z(x) = \frac{F}{2k}\left[3\left(\frac{x}{L}\right)^2 \quad \left(\frac{x}{L}\right)^3\right], \tag{2.1}$$

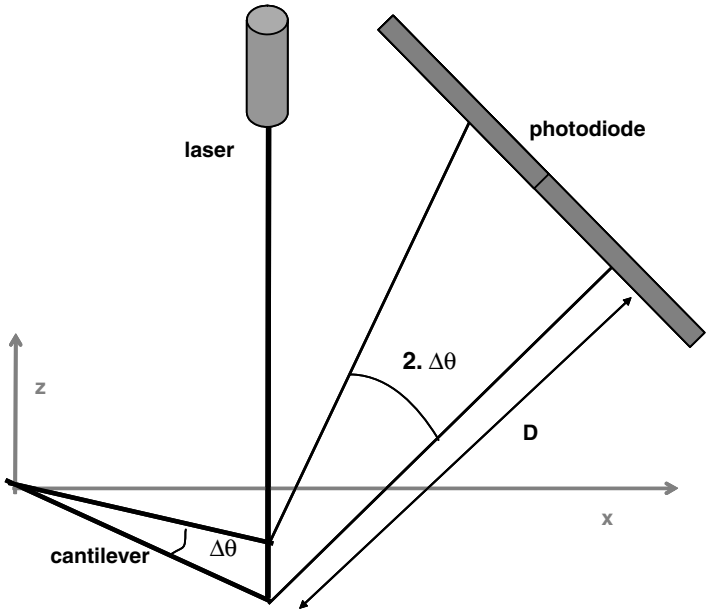

Figure 2.4 Standard geometry in an optical beam deflection system.

then

$$z(L) = \frac{2L}{3}\frac{\mathrm{d}z(L)}{\mathrm{d}x}. \tag{2.2}$$

The above equation is valid for a static force applied at the tip; nonetheless, it will also be used to describe AM AFM.

From Figure 2.4, it can also be deduced that the amplification of the deflection in the photodiode is proportional to the ratio between the cantilever photodiode distance D and the cantilever length,

$$\Delta A \approx 2\frac{D}{L}\Delta z. \tag{2.3}$$

2.3.3
Other Detection Methods

Several other methods have also been proposed and applied to detect the cantilever deflection [7 16]. Quate and coworkers introduced self sensing methods to detect the cantilever bending [10]. A piezoresistive layer deposited on top of the silicon cantilever changes its resistance with changes in the cantilever geometry. In this way, the cantilever deflection can be measured. Self sensing methods based on piezoelectric materials can be small size and compact; however, the signal to noise ratio is not as good as in optical beam deflection. Another type of self sensing method uses quartz tuning forks [12].

2.3.4
Tip Sample Motion System

Piezoelectric actuators provide positioning with high accuracy and subangstrom precision. Both the tip oscillation and the relative position of the tip to the sample surface are performed by means of piezoelectric actuators. Two different piezoelectric actuators are common in AM AFM. A dither piezo glued at the clamped end of the cantilever is used to excite the cantilever oscillation. The other piezo actuator is used to displace the tip with respect to the sample surface. This piezo scanner could be placed either underneath the sample surface or above it. Commonly, the piezo scanner is a hollow and segmented tube that enables motion in the x, y, and z directions. Tube scanners are preferred because they are compact, implying higher resonant frequencies. In addition, the same scanner could cover a wide range of scanning areas from nm^2 to μm^2. The downside is the existence of some coupling between the lateral and the vertical displacements.

Piezoelectric scanners do not have a linear relationship with the voltage that produces the mechanical deformation. They suffer from a series of problems such as hysteresis, creep, aging, or thermal drift. These factors might cause serious distortions in the imaging process. Hysteresis may be corrected by the use of algorithms implemented in the software that controls the tip displacement. Hysteresis and creep are more noticeable for large displacements while thermal drift is more visible for small tip displacements. The most effective way to minimize the difference between the real and the nominal tip displacements is by using the so called of close loop systems. In a close loop scanner, the actual displacement in x, y, or z direction is measured by a magnetic, capacitive, or optical system and is compared with its nominal value. An error signal is generated and a process to minimize this signal is implemented.

The sensitivity of piezoelectric scanners (volts/nm) might change with use and time. For this reason, it is advisable to recalibrate the scanners once per year by using calibration gratings for the x, y, and z axes.

A different tip motion system, called the force sensing integrated readout and active tip, has been proposed [14, 15]. This method integrates tip motion with force sensing by combining a micromachined electrostatic actuator to move the tip and an integrated optical interferometric displacement detector in a microscale volume.

2.3.5
Imaging Acquisition and Display

Imaging acquisition and display account for the processes performed on the signal coming out of the photodiodes to generate an image that conveys meaningful information on the topography and other properties of the surface. Many AFM manufacturers provide software for image processing and representation. An early introduction to the subject is provided by Guckenberger [17] and an example of AFM software can be found in Ref. [18].

A key factor to bear in mind is the limit that the frequency bandwidth imposes on the imaging acquisition time t_a. The imaging acquisition time can be conveniently expressed in terms of f_x, the scanning frequency in the fast moving direction, and the number of scan lines N in the tip's slow moving direction, $t_a = N/f_x$. The feedback bandwidth B should always be larger than $1/t_m$, where t_m is the time taken by the tip to travel between the closest features resolved by the instrument λ. Then,

$$B \geq 1/t_m = \frac{v_x}{\lambda} = \frac{2\Delta x f_x}{\lambda} = \frac{2\Delta x N}{\lambda t_a}, \tag{2.4}$$

where v_x is the tip speed in the fast moving direction and Δx lateral image size. The feedback bandwidth is determined by several factors such as the mechanical resonances of the cantilever and tip sample motion system, the quality factor, and the time response of the feedback controller [1, 19, 20].

2.4 Cantilever Tip System

The cantilever tip system has two elements, the cantilever and the tip. The cantilever is the transducer that converts the force sensed by the tip into a deflection that can be recorded and measured. The use of microelectronic processes has made possible the integration of the cantilever and the tip into a single device, the cantilever tip system (Figures 2.5 and 2.6). However, it seems convenient to describe the properties of the tip independent of those of the cantilever. On the one hand, the cantilever body outweighs the tip by several orders of magnitude meaning that inertial effects depend

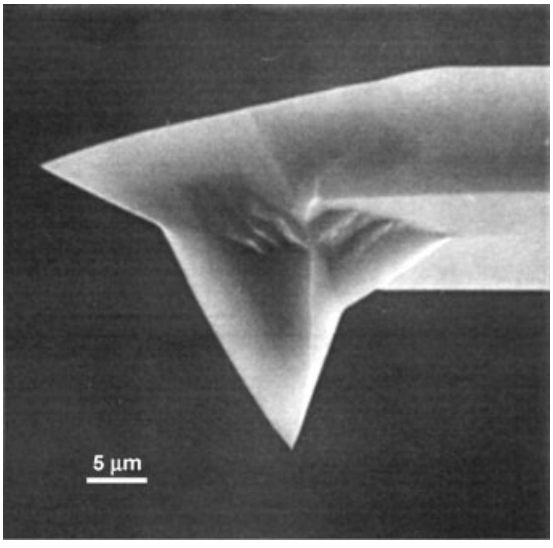

Figure 2.5 Scanning electron microscopy (SEM) image of a silicon cantilever tip system.

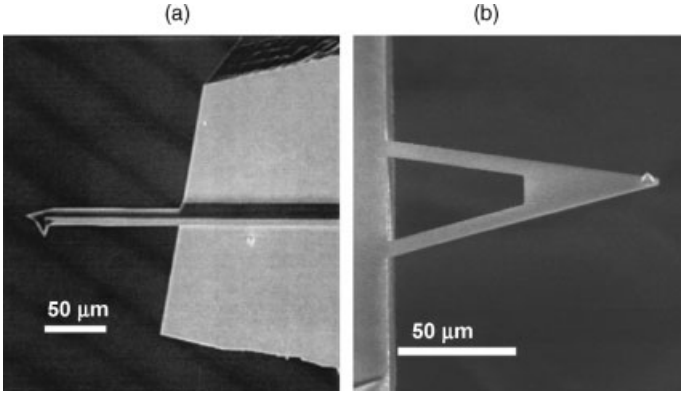

Figure 2.6 Scanning electron microscopy images of (a) rectangular and (b) triangular cantilevers.

mostly on the cantilever mass. On the other hand, the proximity of the tip to the surface makes it possible to confine the tip surface interaction to the size of the tip's apex.

2.4.1 Cantilevers

Cantilevers are fabricated in microelectronic facilities with some of the technologies used to fabricate integrated circuits such as photolithography and etching procedures [21, 22]. The majority of AFM cantilevers are made of either silicon or silicon nitride (Si_3N_4).

Most commercial cantilevers are either v shaped or rectangular beams. Rectan gular cantilevers have a trapezoidal shape. Nonetheless, some applications might require the development of special geometries to enhance the response of higher cantilever modes [23, 24]. Figure 2.6 shows the main cantilever geometries used in dynamic AFM. The dynamic quantities describing rectangular cantilevers are amenable of analytical treatments, so the rest of the section is devoted to them. For a theoretical description of triangular cantilevers, the reader may consult Refs [25, 26].

The cantilever properties of interest in AM AFM are the force constant, the resonant frequency, and the quality factor. The force constant enables to transform intermolecular and nanoscale forces into force measurements. The resonant fre quency is one of the factors that control the time response of the instrument and the quality factor is a measure of the hydrodynamic damping of the cantilever with the environment (liquid or gas). The quality factor Q also includes the cantilever internal energy losses, although these are usually negligible with respect to the hydrodynamic damping. The Q can be estimated by fitting the resonance curve to a Lorenztian function (Chapter 4).

The cantilever is a three dimensional continuous system with several resonances or eigenmodes. Each mode is characterized by its own force constant and quality factor. Furthermore, the cantilever has bending, torsion, and flexural modes. This

book is mostly focused on flexural vibrations, that is, those occurring in the plane perpendicular to the long cantilever axis. Whenever the cantilever is referred to by a single resonant frequency, quality factor or force constant is meant to be the values of the lowest flexural mode. The frequency of the lowest mode (first mode) is usually called the fundamental frequency. A more complete description of the flexural vibrations is provided in Chapters 5 and 9.

The static force constant of a rectangular beam can be expressed in terms of the Young's modulus of the material E and the size of the beam with L its length, W its width, and h its thickness [27, 28]:

$$k_s = k = \frac{EWh^3}{4L^3}. \tag{2.5}$$

The resonant frequency can be determined by

$$f_n = \frac{1}{2\pi}\frac{\varkappa_n^2}{\sqrt{12}}\sqrt{\frac{E}{\varrho}\frac{h}{L^2}}, \tag{2.6}$$

where ϱ is the mass density and $\varkappa_n$ are the solutions of the equation $\cos \varkappa_n \times \cos h\, \varkappa_n = -1$ with $\varkappa_1 \cong 1.875$ and $\varkappa_2 \cong 4.964$. The other coefficients are calculated by

$$\varkappa_n \cong \pi\left(n - \frac{1}{2}\right) \quad \text{for} \quad n \geq 3. \tag{2.7}$$

For convenience, in most of the equations the frequency is expressed in terms of the angular frequency $\omega_n = 2\pi f_n$. The frequency of the fundamental mode is commonly expressed as ω_0 ($\omega_0 = \omega_1$).

2.4.2 Tips

The size of the tip at its apex and the tip's aspect ratio has a defining role in determining the lateral resolution. Different microfabrication processes yield very sharp Si or Si_3N_4 tips with a radius down to 2 nm. However, the aspect ratio of microfabricated tips might compromise the lateral resolution when imaging surfaces with large features. Several alternative procedures have been developed to either reduce the tip's radius and/or to get better aspect ratios [29–32]. Both the formidable aspect ratio and the small diameter of single wall carbon nanotubes make them seemingly ideal candidates for AFM imaging (Figure 2.7) [29, 31]. However, the difficulties in attaching in a reliable and efficient manner carbon nanotubes to a Si cantilever have greatly limited its impact on AFM. Molecular resolution images in amplitude modulation AFM have been obtained either by using oxide sharpened silicon nitride tips [33] or by using sharp carbon whiskers grown by chemical vapor deposition on top of regular Si tips [30].

The tip's geometry might also be the source of several imaging artifacts. Etched Si tips are asymmetrical. The tip's angle depends on the scanning direction. This fact should be kept in mind to minimize tip convolution artifacts.

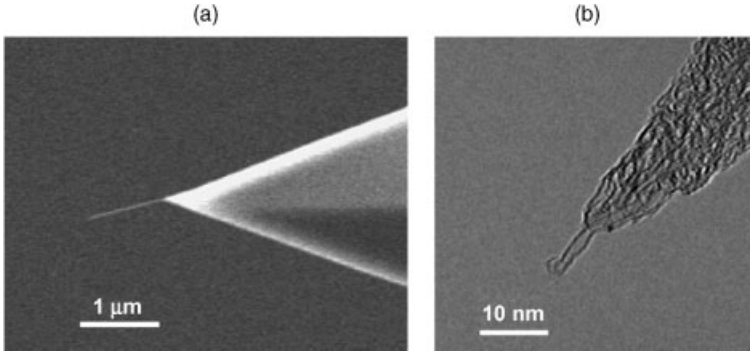

Figure 2.7 (a) SEM picture of multiwall carbon nanotube attached to a silicon nitride tip. (b) TEM image of a single wall carbon nanotube attached at the end of a silicon nitride tip. Adapted from Ref. [31].

2.4.3
Excitation of Cantilever Tip Oscillations

Three different excitation methods have been applied to vibrate the cantilever tip ensemble: acoustic, magnetic, and photothermal excitation (Figure 2.8). In the acoustic excitation mode, a piezoelectric actuator is attached below the substrate containing the cantilever tip ensemble [34]. The application of an oscillating voltage

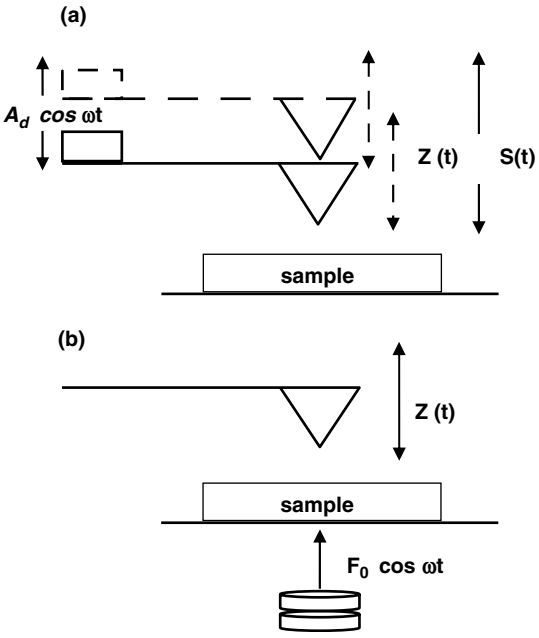

Figure 2.8 Schematics of (a) acoustic and (b) magnetic excitation methods.

to the actuator produces its vibration and this, in turn, produces the oscillation of the cantilever. This is by far the most common excitation mode in air and liquids, although in liquids it also excites the fluid (Chapter 6). The magnetic excitation mode uses magnetic forces to generate an oscillating magnetic field that causes the cantilever to vibrate [35 37]. This requires the magnetization of the cantilever or just the region close to the tip. Another method to excite the cantilever is provided by the photothermal excitation where a power modulated laser diode is focused on the backside of the cantilever [38, 39].

2.5 Calibration Protocols

AFM operation involves three main calibration procedures. Imaging applications requires the regular calibration of the *x*, *y*, and *z* scanners that form the tip sample motion system. Applications oriented to capture information on surface forces and/or material properties require the determination of the force constant of the cantilever and the optical sensitivity of the beam deflection method.

2.5.1 Optical Sensitivity

The output of the photodiode detector is a photocurrent that is eventually trans formed into an output voltage. To measure deflections and amplitudes in units of length, we require to determine the conversion factor between volts and nanometers. A commonly used sensitivity calibration method starts with the determination of sensitivity in the static case and then using the theoretical expressions that relate the sensitivities of the different cantilever eigenmodes to static sensitivity. The static sensitivity is determined by first plotting the dependence of the deflection as a function on the sample separation. This requires the use of a stiff tip sample interface, so the surface deformation upon contact is negligible with respect to the cantilever deflection. A line fit in the contact section is used to calibrate the detector signal (ΔV) with a known cantilever deflection. It is assumed that the cantilever deflection is equal to the *z* piezoscanner displacement Δz,

$$\sigma_s = \frac{\Delta V}{\Delta z}. \tag{2.8}$$

The above value depends on the laser spot position along the cantilever axis; as a consequence, the sensitivity will depend on the cantilever length and the alignment procedure.

The shape of the cantilever depends on the excited eigenmode so does the sensitivity. However, the sensitivity of mode n (σ_n) can be determined from the value of the static sensitivity σ_s by realizing that the ratio between the sensitivities is proportional to the cantilever slopes [27, 40]. By following Schäffer's hypothesis, the equation that relates the optical sensitivity of a mode (eigenmode) to the static

sensitivity is

$$\frac{\sigma_n}{\sigma_s} = \frac{dX_n/dx}{dX_s/dx} = (\quad 1)^{n+1}\frac{2\varkappa_n}{3}\frac{\sin\varkappa_n \sinh\varkappa_n}{\sin\varkappa_n + \sinh\varkappa_n}, \tag{2.9}$$

where $X(q)$ with $q = x/L$ is the modal shape of the n mode [40]. Equation 2.7 has been expressed for $q = 1$. The sensitivity ratio for the two lowest modes is, respectively, $\sigma_1/\sigma_s = 1.0898$ and $\sigma_2/\sigma_s = 0.3138$.

The optical sensitivity in dynamic AFM could also be modified by the tip surface forces. This is usually a minor effect. It is less noticeable for higher modes [41].

2.5.2
Calibration of the Cantilever Force Constant

Measurement of the tip surface forces requires the determination of the cantilever's force constant k. A variety of methods have been proposed [6, 42 50]; among them, the thermal noise and the Sader methods stand out because they are relatively easy to implement and provide values of the force constant with a relative error below 10% [45, 48]. A good introduction to the different calibration methods, and in particular to those described below, is provided by Cook *et al.* [48].

2.5.2.1 **Thermal Noise Method**

This method was first proposed by Hutter and Bechhoefer [42] and later refined by Butt and Jaschke [6]. It is based on the equipartition theorem that states that in thermal equilibrium the average value of each quadratic term in the Hamiltonian is given by $k_B T/2$. For a free cantilever at equilibrium with the environment,

$$\frac{1}{2}k\langle z^2\rangle = \frac{1}{2}k_B T, \tag{2.10}$$

where $\langle z^2\rangle$ is the mean square deflection of the cantilever caused by thermal vibrations. The deflection includes contributions from all the eigenmodes. To exactly determine $\langle z^2\rangle$, it requires to measure the power spectral density over all frequen cies. This might become a time consuming measurement. Butt and Jaschke simp lified the process by deducing a relationship between the total power and the power of the lowest eigenmode. First, the deflection power density of the lowest resonance P_d is measured. Then, its dependence on the frequency is fitted to the shape of single harmonic oscillator R (a Lorentzian function) with an added background term,

$$P_d = P_b + R(f), \tag{2.11}$$

$$\int_0^\infty R(f)df = \frac{\pi f_1 Q_1 A_1}{2} = \langle z_1^2\rangle = \frac{k_B T}{k_1}, \tag{2.12}$$

then

$$k_1 = \frac{4k_B T}{\omega_1 Q_1 A_1}. \tag{2.13}$$

A relationship between the cantilever static and the first mode force constants is derived by using the vibrational decomposition of the cantilever oscillations [6, 27],

$$k = \frac{k_B T}{\langle z^2 \rangle} = \frac{12 k_B T}{1.875^4 \langle z_1^2 \rangle} = 0.9707 k_1. \tag{2.14}$$

2.5.2.2 Sader Method

Sader *et al*. have studied the effect of fluid dissipation on the cantilever dynamics [44, 49, 50]. On the basis of these studies, they have developed a method to determine the force constant of a rectangular cantilever [49]. The method requires it to measure the quality factor, the resonant frequency of the fundamental mode, and the planview size of the cantilever,

$$k = 7.524 \varrho_f W^2 L Q_1 \Gamma_i(f_1) {f_1}^2, \tag{2.15}$$

where f_1 is the first resonance as measured in the fluid (air, vacuum, or liquids); $\Gamma_i(\omega)$ is the imaginary part of the hydrodynamic function (Chapter 6). The values of the hydrodynamic function are tabulated in Ref. [49].

2.6 Common Experimental Curves

The main observables in amplitude modulation AFM are the oscillation amplitude and the phase shift. To characterize the dependence of the amplitude and, to a lesser extent, the phase shift with respect to the excitation frequency is a necessary step to understand its dynamics.

2.6.1 Resonance Curves in Air and Liquids

Many aspects of the dynamics of an oscillator, and in particular of the cantilever tip system, are contained in its resonance curves [51 53]. The dependence of the amplitude upon the excitation frequency is usually called the resonance curve by the AFM community. More generally, the resonance curve involves the representa tion of A^2 versus the frequency. A resonance occurs when the interaction between the excitation force and the mechanical system is maximized, which happens when the excitation frequency matches the frequency of one of the eigenmodes of the system. Resonance curves serve several purposes. They are used to identify the different eigenmodes, to determine the quality factor, or to estimate the anharmonicity of the cantilever.

Figure 2.9 shows the resonance curves for the lowest eigenmode of a rectangular cantilever ($k = 0.75$ N/m) in air and water. The medium does considerably alter the resonance curves. In liquid, the resonance curve is wider ($Q_{water} = 3$ versus $Q_{air} = 60$ in this example). At the same time, the resonant frequency is shifted to lower values.

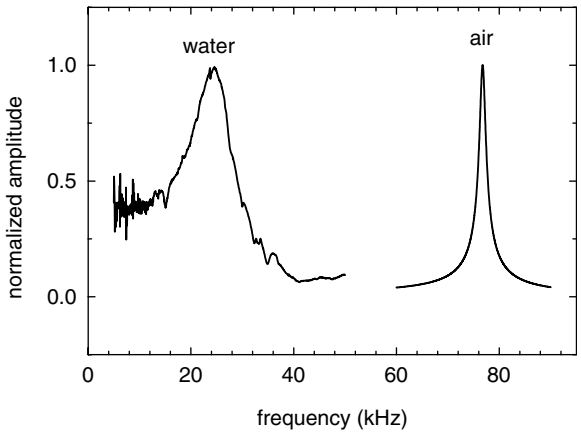

Figure 2.9 Experimental resonance curves in water and air. Notice the shift of the resonant frequency and the broadening of the resonance when the measurement is done in water. Adapted from Ref. [59].

The above curves were taken very far from the sample surface, so the tip surface forces did not affect the curve. However, in AM AFM the tip surface forces could substantially modify the shape of the resonance curve. Figure 2.10 shows three resonance curves taken in air at different separations from a mica surface (12, 6, and 5 nm). For separations larger than the free amplitude (7 nm), the curve has a

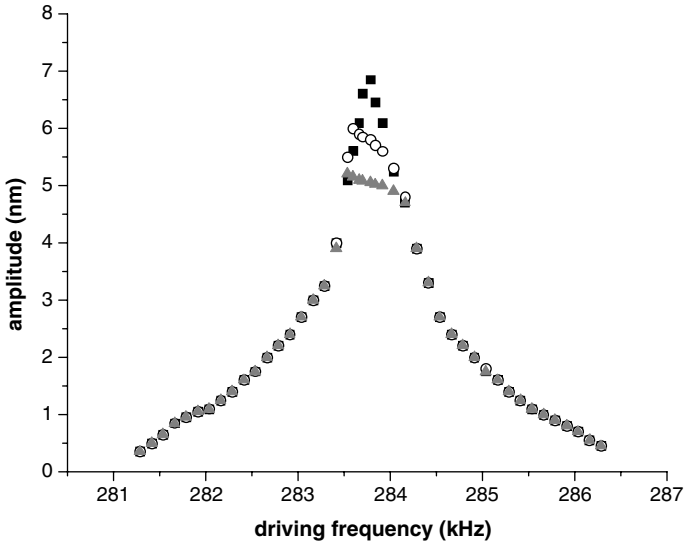

Figure 2.10 Resonance curves as a function of the tip surface distance (z_c 12, 6, 5 nm). At z_c 12 nm, a tip surface separation larger than the free amplitude (A_0 7 nm), the resonance curve shows a Lorentzian shape. At closer separations, the attractive tip surface forces truncate the top of the resonance curve. The experiment was performed in air with a Si cantilever on a mica sample.

Lorentzian shape. However, for separations smaller than the free amplitude, the tip surface forces truncate and distort the resonance curves. More details about resonance curves are provided in Chapters 5 and 6.

2.6.2
Amplitude and Phase Shift Distance Curves

The representation of the amplitude with respect to the average tip surface distance is called an amplitude distance curve. A similar curve where the phase shift is the observable is called a phase distance curve. When there is no ambiguity, they will be called, respectively, amplitude and phase curves. These curves have many applications; for example, they are essential to measure and identify the nature of the forces, either conservative or nonconservative [54]. They are also crucial to extract information about material properties. Amplitude or phase distance curves can also be used to identify the interaction regime either attractive or repulsive. The slope of the amplitude curve participates in the determination of the vertical noise of the instrument.

Amplitude curves may have different shapes [55–58]. The shape of an amplitude curve represents an interplay between the different instrumental parameters and the sample properties. Among the parameters that influence the shape of an amplitude curve are the free amplitude, the excitation frequency, and the tip radius. The sample properties that have more influence on the curve are the Young's modulus, Hamaker constant, and the surface energy. As a guiding rule, the amplitude decreases by approaching the tip toward the sample surface. The slope of the curve depends on the material. Stiff samples have a slope close to 1 while more compliant materials show smaller slopes. The monotonical decrease in amplitude with respect to tip surface distance could be altered by the presence of sharp discontinuities. These discontinuities reflect the transition from the attractive to the repulsive regime or vice versa.

Figure 2.11 shows some amplitude and phase distance curves obtained with a silicon tip on a silicon surface. The jump observed when the distance is decreased reveals a transition from the attractive to the repulsive regime. At the transition point, the amplitude shows an increase of about 1.5 nm, while the phase shift shows a jump from 110° to 65°.

2.7
Displacements and Distances

The analyst of amplitude modulation AFM experiments requires to be familiar with at least five different distances and/or displacements. In some cases, the conceptual differences among them are subtle; however, they have remarkable experimental implications. Figure 2.12 illustrates the definition of the tip deflection $z(t)$ and the tip displacement with respect to the sample surface $S(t)$. The optical beam deflection method directly measures the cantilever slope, which can relate to the tip deflection. The origin of the tip deflection is the rest position of the cantilever tip system. When

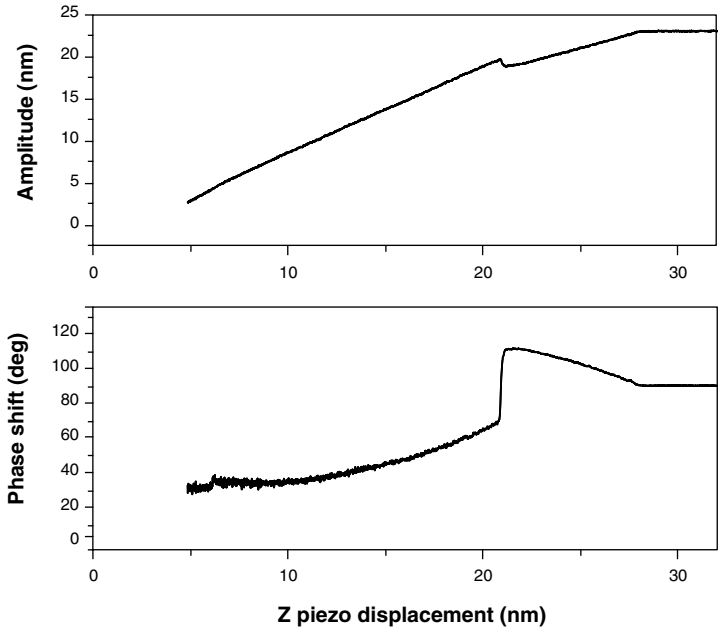

Figure 2.11 Amplitude and phase distance curves obtained in air with a silicon tip on a mica surface.

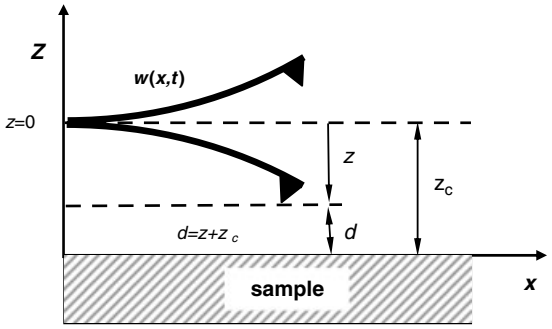

Figure 2.12 Scheme of the relevant distances in amplitude modulation AFM; d is the instantaneous tip surface separation, z is the instantaneous tip deflection, z_c is the average tip surface separation, x is the spatial coordinate along the longitudinal axis of the cantilever, and $w(x,t)$ is the cantilever bending.

the cantilever is excited by a mechanical force, the amplitude of the displacement of the cantilever base is A_d. For high Q values (>10), A_d is much smaller than z or S, then $z \approx S$. The definitions of the other distances are also shown in Figure 2.12: the instantaneous tip surface d and the average tip surface separations z_c; the spatial coordinate along the longitudinal axis of the cantilever is x and $w(x, t)$ is the cantilever bending.

3
Tip–Surface Interaction Forces

3.1
Introduction

The forces of interest in force microscopy are of electromagnetic origin. However, different intermolecular, surface, and macroscopic effects give rise to interactions with distinctive distance and geometry dependencies. In the absence of external fields, the dominant forces in air are van der Waals interactions, short range repulsive interac tions, and adhesion and capillary forces. In liquid, the solid liquid interfaces together with the presence of ions and electrolytes give rise to the presence of additional forces such as the electric double layer and the solvation forces. Some of the above forces are attractive while others are repulsive. In some cases, interaction forces could show oscillations. The repulsive or attractive character of electrostatic interactions could be changed in liquid by modifying the ionic strength. The variety of tip surface forces, their different character, and the difficulty in isolating a single interaction are some of the factors that contribute to making the technique hard to master.

A force curve acquired on a purple membrane surface is depicted in Figure 3.1. The force curve could be divided into the short range and long range regions. The short range region involves forces within 1 nm from the tip and sample uppermost atoms, while the long range region extends several nanometers above the sample surface. A practical description of the common forces to be encountered in a typical amplitude modulation AFM experiment in either air or liquid follows in the next section.

3.2
Van der Waals Forces

The universal character of long range interactions of van der Waals type between objects arises from the existing electromagnetic field fluctuations. These fluctuations arise from thermal and/or zero point quantum fluctuations. Several theoretical treat ments of varying complexity have been developed to introduce van der Waals forces [1 3]. Specifically, Israelachvili [1] and Butt *et al.* [2] give a detailed and comprehensive description of the van der Waals interactions adapted for an AFM like interface.

Amplitude Modulation Atomic Force Microscopy. Ricardo García

ISBN: 978-3-527-40834-4

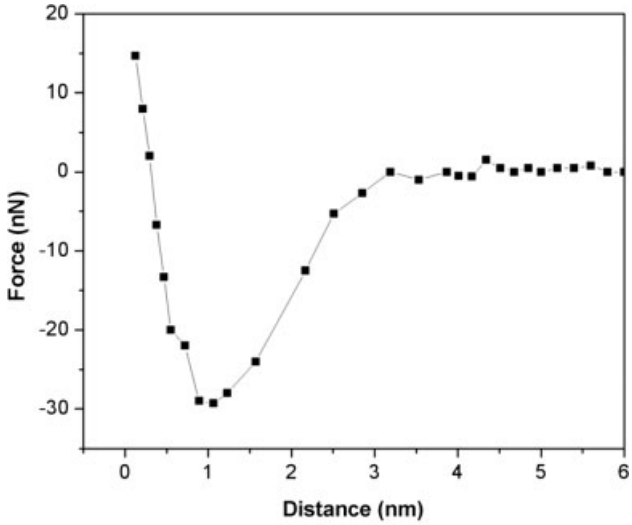

Figure 3.1 Force versus distance curve acquired on a purple membrane surface. Experiment performed in air.

The van der Waals forces between atoms and/or molecules have their origin in electric dipole interactions. The dipoles could be permanent or either induced by another permanent dipole or by thermal fluctuations. The three possible dipole interaction potentials, dipole dipole, dipole induced dipole, or induced dipole induced dipole, scale as $1/r^6$, where r is the distance between atoms or molecules. Force microscopy experiments usually deal with ensembles of atoms or molecules. The net van der Waals force is the result of adding all the individual dipole interactions between tip and surface atoms [1, 2]. The two most common approx imations to describe an AFM interface are the sphere flat and the conical tip sphere flat geometries (Figure 3.2). For a sphere flat geometry, the van der Waals force is given by

$$F_{\mathrm{vdW}} = \frac{HR}{6d^2}, \tag{3.1}$$

where H is the Hamaker constant, R the tip radius, and d is the instantaneous tip surface distance. The above equation diverges for $d \to 0$. To avoid the divergence for separations d smaller than the intermolecular distance a_0, the resulting van der Waals force is identified with the adhesion force derived from contact mechanics models. A reference value for the intermolecular distance is $a_0 = 0.165$ nm [1]. The Hamaker constant depends on the materials and the intervening medium, typical values are in the 10^{-20} J range [1, 2].

For a conical mesoscopic tip that ends in a half sphere [4, 5], the force is given by

$$F_{\mathrm{vdW}} = \frac{H}{6}\left(\frac{R}{d^2} + \frac{\tan^2\beta}{d + R_\beta} \quad \frac{R_\beta}{d(d + R_\beta)}\right), \tag{3.2}$$

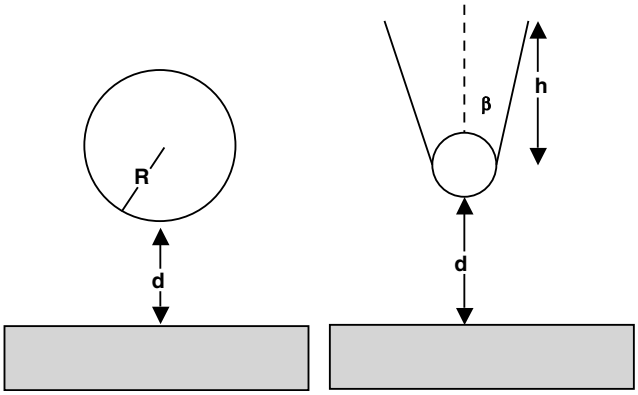

Figure 3.2 Models of the tip surface geometry: sphere flat and conical shaft capped with a half sphere flat.

where β is the half angle of the cone and $R_\beta = R(1 \quad \sin\beta)$. Notice that for $d < R$, the van der Waals force is dominated by the half sphere cap, then Equation 3.2 is well approximated by Equation 3.1. When the roughness of the sample surface is approximated by a succession of half spheres, the sphere sphere approximation could be applied to estimate the van der Waals force,

$$F_{\mathrm{vdW}} = \quad \frac{H}{6d^2}\frac{R_\mathrm{t}R_\mathrm{s}}{R_\mathrm{t}+R_\mathrm{s}}, \tag{3.3}$$

where R_t is the tip's radius and R_s is the effective radius of the surface under the tip.

The van der Waals force between two surfaces is usually attractive. Nonetheless, it is worth to summarize three relevant situations. The van der Waals force between two identical materials in a medium is always attractive. The van der Waals force between two different materials in air or in vacuum is also attractive. The van der Waals force between two different materials in liquids could be either attractive or repulsive depending on the values of the dielectric constants and the refractive indexes of the interface [1, 2]. In a heterogeneous interface, that is, an interface consisting of layers of different materials such as a rigid metallic substrate and a thin monolayer on top, the van der Waals force at larger distances could still bear the influence of the underlying substrate [2, 6, 7].

3.3
Contact Mechanics Forces

Repulsive forces between atoms or molecules arise from Pauli and ionic repulsion. However, if the contact area between two objects involves hundreds or thousands of atoms, the description of the effective repulsive force is provided by contact mechanics models [8, 13 18]. The surfaces of two bodies are deformed when they are brought into mechanical contact. The deformation depends on the applied force

(load) and the properties of the material. Continuum elasticity theories describe the contact and adhesion between finite bodies under an external load. The first model was proposed by Hertz in 1881, describing the deformation of two elastic spheres without adhesion forces [8]. Johnson, Kendall, and Roberts (JKR) [9] and Derjaguin, Muller, and Toporov (DMT) [10] models provide analytical relationships between the deformation and the applied load (force) in the presence of adhesion forces. More sophisticated and self consistent descriptions of the deformation, the stress, and the interaction forces between surfaces have been developed by Maugis [11] and Muller *et al.* [12].

Continuum mechanics models have provided good descriptions of some exper imental results [19 21]. Furthermore, atomistic simulations show that some of the parameters relevant to dynamic AFM such as the indentation or the contact area are well described by some contact mechanics models [22]. However, the use of continuum mechanics models to describe nanoscale mechanical properties has some limitations [14, 22 24].

To determine the deformation of two elastic objects in contact, here tip and sample, requires to establish and solve the relationship between the stress Γ and the strain ε tensors. This functional relationship is called the constitutive equation. For an isotropic material, it is deduced

$$\Gamma_{ij} = \lambda\varepsilon_{ll}\delta_{ij} + G\varepsilon_{ij}, \tag{3.4}$$

where λ is the Lamé coefficient and G is the shear modulus. The shear and the Young' modulus are related by

$$G = \frac{E}{2(1+\nu)}, \tag{3.5}$$

where ν is the Poisson ratio. In equilibrium, the form of the solutions of Equation 3.4 can be parameterized by the elasticity parameter λ_e

$$\lambda_e = \Gamma_0\left(\frac{9R}{2\pi W_{ad}E_{eff}}\right)^{1/3}, \tag{3.6}$$

$$\frac{1}{E_{eff}} = \left(\frac{1\ \nu_t^2}{E_t} + \frac{1\ \nu_s^2}{E_s}\right), \tag{3.7}$$

where W_{ad} is the work per unit of area required to fully separate the surfaces and Γ_0 is the stress at the equilibrium spacing; E_{eff} is the effective Young's modulus of the tip sample interface. The subscripts t and s stand for tip and sample, respectively.

The parameter λ_e compares the relative magnitude of the elastic deformation at pull off forces and the effective range of the surface force. It can be demonstrated that the general solutions of Equation 3.4 reduce to Hertz for $\lambda_e = 0$, DMT for $\lambda_e < 0.1$, and JKR for large λ_e ($\lambda_e > 5$). Figure 3.3 shows the adhesion map of Johnson and Greenwood [25] that describes the range of application of different contact mechanics models.

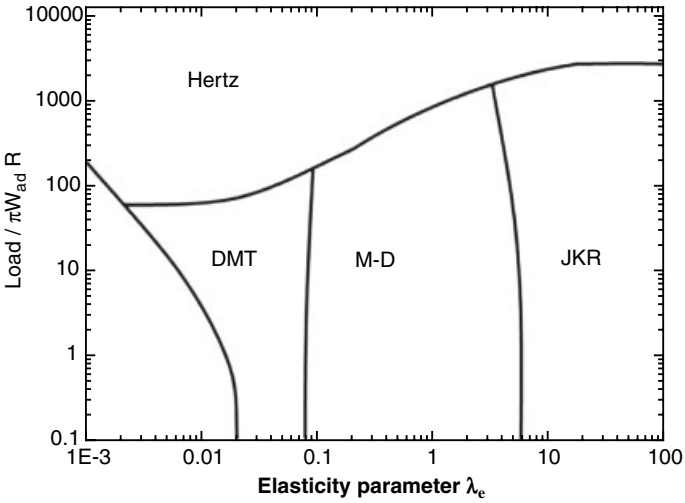

Figure 3.3 Adhesion map for the contact of elastic bodies. It shows the range of application of the different contact mechanics models. Adapted from Ref. [25].

DMT and JKR models are extensively applied in force microscopy because they provide analytical expressions to determine the force exerted on the sample surface as a function of the indentation. Both models share several assumptions, namely, (1) the deformations are elastic and follow a linear behavior; (2) the size of the contact is small with respect to the radius of the tip; and (3) the contact geometry is axisym metric with the absence of shear forces.

3.3.1
Derjaguin Muller Toporov Model

The Derjaguin Muller Toporov [10] model is valid for describing stiff contacts with low adhesion forces and small tip radii (Figure 3.3). The DMT model considers the existence of adhesion forces acting outside the contact area. The adhesion force is calculated by

$$F_{ad} = \quad 4\pi R\gamma. \tag{3.8}$$

In addition to the adhesion force, during the contact there is a repulsive force that at the atomic and molecular level comes from Pauli and ionic repulsion,

$$F_r = \frac{4}{3} E_{eff} \sqrt{R(a_0 \quad z \quad z_c)^{3/2}} \quad \text{for} \quad z_c + z \leq a_0, \tag{3.9}$$

where γ is the surface energy with $W_{ad} = 2\gamma$. The radius of the contact area is given by

$$a^3 = \frac{3R}{4E_{eff}} (F + F_{ad}), \tag{3.10}$$

where F is the applied load.

Figure 2.12 provides a definition of the coordinates and distances needed to operate with the above equations. These definitions are used throughout the book unless otherwise stated. Positive values of the sum $z_c + z$ define the instantaneous tip surface distance d, while negative values give the indentation δ. The DMT model also provides an expression for the indentation as a function of the load,

$$\delta = \frac{a^2}{R} = \frac{(F + F_{ad})^{2/3} F + F_{ad}}{\sqrt[3]{\frac{16}{9} R E_{eff}^2}}. \tag{3.11}$$

3.3.2
Johnson Kendall Roberts Model

The Johnson Kendall Roberts model considers that the adhesion force acts inside the contact area. This model should be the choice for studying contacts characterized by relatively low stiffness, high adhesion forces, and large tip radii [8, 9, 11]. The adhesion force is calculated by

$$F_{ad} = 3\pi R\gamma. \tag{3.12}$$

The JKR model enables us to express the indentation as a function of the applied force as

$$\overline{\delta} = 3\left(\overline{F_{JKR}} + 2 + 2\sqrt{1 + \overline{F_{JKR}}}\right)^{2/3} \quad 4\left(2 + \overline{F_{JKR}} + 2\sqrt{1 + \overline{F_{JKR}}}\right)^{1/6}, \tag{3.13}$$

where $\overline{\delta} = \delta/\delta_a$ and $\overline{F_{JKR}} = F_{JKR}/F_{ad}$ are, respectively, the normalized indentation and force. The parameter δ_a is the pull off separation given by

$$\delta_a = \left(\frac{\pi^2 R\gamma^2}{3E_{eff}^2}\right)^{1/3} \tag{3.14}$$

and the contact radius is obtained from

$$a^3 = \frac{3R}{4E_{eff}}\left(F + 2F_{ad} + 2\sqrt{F_{ad}F + F_{ad}^2}\right) \tag{3.15}$$

3.4
Capillary Force

Under ambient conditions, water spontaneously condenses from vapor into the cracks or pores of hydrophilic surfaces. Capillary condensation is a thermodynamic process that links the vapor pressure of a liquid to its curvature in the condensed form [26 28]. It is described by the Kelvin equation,

$$R_g T \log\frac{P}{P_0} = \frac{\gamma_L V_m}{r_k}. \tag{3.16}$$

The Kelvin radius r_k gives information on the size of the meniscus,

$$\frac{1}{r_k} = \frac{1}{r_1} + \frac{1}{r_2}, \tag{3.17}$$

where R_g is the gas constant, γ_L is the surface tension of liquid, P is the actual vapor pressure, P_0 is the vapor pressure at saturation, V_m is the molar volume of the liquid, and r_1 and r_2 are the principal radii of curvature of the meniscus. In the case of water condensation, P/P_0 is the relative humidity.

The Kelvin equation states that in equilibrium the size of the capillary where condensation occurs is determined by the vapor pressure. This property leads to capillary condensation and capillary adhesion forces in the presence of asperities. As a consequence, condensation occurs at a relative humidity below 100% for curved surfaces. For example, for a spherical concave water meniscus, Equation 3.16 gives $r_k \approx 0.78\,\text{nm}$ at $P/P_0 = 0.5$ and $T = 293\,\text{K}$ (50% relative humidity and $\gamma_L V_m / R^* T = 0.54\,\text{nm}$).

In AFM, a water meniscus could be formed whenever the tip and the sample gap distance is comparable to the Kelvin radius (Figure 3.4). Inside the meniscus, the pressure is larger than outside. The Young Laplace equation gives the pressure difference across the meniscus interface

$$\Delta P = \gamma_L \left(\frac{1}{r_1} + \frac{1}{r_2} \right). \tag{3.18}$$

The above equation enables us to calculate the adhesion force associated with the meniscus formation. The capillary force depends on the interface geometry. It requires to determine the contact angles between the surfaces and the liquid. In general, for a tip of arbitrary shape and a flat sample, it can be determined only by the numerical solution of the above equation. Nonetheless, several analytical or semi analytical expressions to determine the force between a sphere and a flat surface have been proposed [1, 2, 28 32]. Following Israelachvili, the capillary force between a

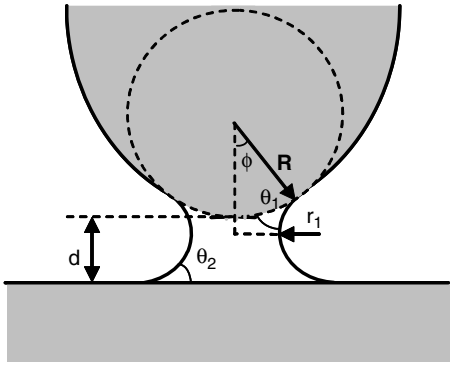

Figure 3.4 Definition of angles and distances needed to calculate the capillary force in AFM.

sphere and a flat surface [1] could be estimated by

$$F_{\text{cap}} = \frac{4\pi R\gamma_{\text{L}}\cos\theta}{1 + d/d_0}. \tag{3.19}$$

The maximum attraction force occurs when the spherical tip is in contact with the flat surface $d = 0$,

$$F_{\text{cap}} = 4\pi R\gamma_{\text{L}}\cos\theta. \tag{3.20}$$

Direct measurements of capillary forces performed with a surface force apparatus showed that the Equation 3.20 is valid for systems down to menisci of radius of 2 4 nm [1, 32]. The above equations give the force once the meniscus has been formed. However, it should be kept in mind that capillary condensation is an activated process that depends, among other things, on the relative humidity. The formation of a water meniscus is often observed in AFM experiments performed at ambient conditions. It has been observed in both contact and dynamic AFM experiments [33 36]. In fact, the control and manipulation of water menisci has given rise to a powerful AFM based nanolithography [37]. However, from an imaging point of view, the formation of a water meniscus should always be avoided. Capillary forces could disrupt the observed objects. Equation 3.19 shows that capillary force values in an AFM interface could be in the 1 100 nN range, that is, they could dominate all other tip surface forces.

3.5 Forces in Liquid

Capillary forces disappear when the tip and the sample are both immersed in a liquid; however, the interaction of the liquid with the solid surfaces gives rise to other forces such as solvation or electrostatic double layer forces.

3.5.1 Electrostatic Double-Layer Force

Solid surfaces are charged when they are in contact with polar liquids, in particular with water. A surface in a liquid could become charged by either the ionization and/or dissociation of surface atoms or by the adsorption of ions from solution onto the solid surface. With independence of the charging process, the surface charge must be compensated by the presence of an equal and opposite charge distributed within the liquid but in the vicinity of the surface. The extension of the electric double layer depends on the concentration and valence of the ions present in the liquid. It varies between $\sim$0.2 nm and tens or hundreds of nanometers. Two regions are distinguished: a very thin region of counterions transiently bound to the surface (Helmholtz layer) and a region of counterions in thermal motion extending farther from the surface (diffuse double layer). The electrical field created by the presence of ions of different signs attached to the surface and distributed in the liquid attracts

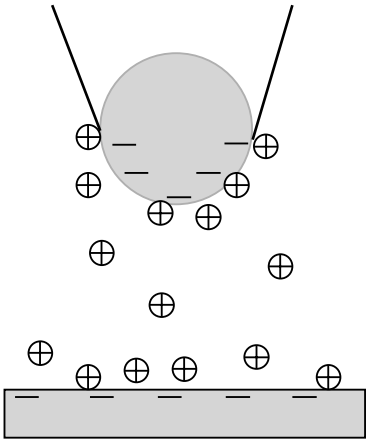

Figure 3.5 Schematic of the electric double layer in AFM.

back the dissolved ions to the surface; however, this force is balanced by the entropy that favors the distribution of ions away from the solid surface.

The double layer force appears when another solid surface is introduced. The second surface disturbs the double layer of the first and vice versa giving rise to the presence of the double layer force. The double layer force should always be considered when dynamic AFM experiments are performed in aqueous solutions (Figure 3.5). For two similarly charged surfaces, the double layer force is repulsive.

The relevance of electrostatic interactions in controlling the spatial resolution of the AFM should not be underestimated. Müller, Engel, and coworkers achieved molecular resolution images of protein membranes by screening the long range electrostatic between the tip and the membrane surface [38, 39]. The screening of long range electrostatic interactions is achieved by changing the ion concentration of the buffer solution [39, 40].

3.5.2
Derjaguin Landau Verwey Overbeek Forces

In liquid, the double layer force and the van der Waals force form the basis of the Derjaguin Landau Verwey Overbeek (DLVO) theory [41, 42]. A detailed account of DLVO theory is given by Israelachvili [1]. An account of the DLVO theory applied to AFM measurements is provided by Butt *et al.* [2].

For a spherical tip and a flat surface, the DLVO force can be approximated by

$$F_{\mathrm{DLVO}} = \frac{4\pi R}{\varepsilon\varepsilon_0}\sigma_t\sigma_s\lambda_D \exp(\quad d/\lambda_D) \quad \frac{HR}{6d^2}, \tag{3.21}$$

where λ_D, ε, and ε_0, are, respectively, the Debye length, the dielectric constant of the medium, and that of the free space; σ_t and σ_s are the surface charge densities of the tip and sample surface, respectively. Several assumptions have been applied to deduce

the above, in particular $d \gg \lambda_D$. To make a quantitative comparison with the experimental data it requires to determine the charging process occurring in surfaces.

The DVLO theory is able to explain a variety of phenomena in colloidal stability. Double layer and van der Waals forces have remarkable differences. First, for similar surfaces one is repulsive and the other attractive. Second, double layer forces depend on the electrolyte concentration, while the ion concentration does not affect van der Waals interactions. Third, the van der Waals attraction overcomes the double layer repulsion at very small separations ($1/d^2$ versus $\exp(-d/\lambda_D)$). These differences could give rise to a rich variety of tip–surface force curves in liquids.

3.5.3 Solvation Forces

Solvation forces include a variety of phenomena that can be explained only by the fact that liquids and surfaces are made of discrete entities such as atoms or molecules. A consequence of the intermolecular interactions is that the structure adopted by a very thin liquid films adsorbed onto a solid surface is generally different from the bulk structure [43, 44]. The most remarkable effect of the solvation forces is the structuring of organic liquid layers between two crystalline mica surfaces [44]. Geometric considerations imply that the liquid molecules must reorder themselves so as to accommodate between the two surfaces. If the liquid is squeezed between two surfaces, the solvation force could give rise to an oscillatory behavior.

Solvation forces introduce oscillations in the density of the liquid in the proximity of the solid surface with respect to the value of the bulk density. The oscillation region extends over a few molecular diameters. Its periodicity is the size of the molecule. Solvation forces have also been measured and observed with AFM. The oscillations are more easily observed when the experiments are performed with organic liquids formed by large molecules [45–47], but they have also been measured in water [48–50]. Yamada and coworkers have measured an oscillatory force while imaging a single crystal of polydiacetylene in water [49]. The period of the oscillation is 0.2 nm that matches the water molecule size. For example, Fukuma *et al*. [49] reported peak to peak force values of 0.1–0.2 nN distributed over ~0.25 nm in water.

Solvation forces between a sphere of radius R and a planar surface can be described by an exponentially decaying oscillating function [2, 51],

$$F_{sv} = F_0 \cos\left(\frac{2\pi d}{a_m} + \varphi\right) \exp(-d/\lambda_{sv}), \tag{3.22}$$

where a_m is the molecular diameter and $\tan\varphi = \lambda_{sv}/a_m$, then

$$F_0 = \frac{Rf_0}{[(2\pi\lambda_{sv})^{-2} + a_m^{-2}]^{1/2}}. \tag{3.23}$$

3.5.4
Other Forces in Aqueous Solutions

There are other types of forces that could be present in aqueous solutions such as the hydration forces. The proximity between the tip and the sample surfaces could disrupt the hydrogen bonding network of water leading to the appearance of oscillatory forces. Furthermore, surface solvent interactions can induce positional or orientation order in the adjacent liquid and give rise to a monotonic hydration force [52 54]. Hydration forces are separated into repulsive hydrophilic forces and attractive hydrophobic forces. In general, hydration forces are smaller in value than the previous forces. They are usually ignored.

3.6
Electrostatic Forces

Electrostatic forces, other than double layer forces, could arise from a variety of situations. Equilibrium conditions applied to an interface made of two different metallic surfaces (tip and sample) involve a transient flow of electrons. The associated electric field originates from a voltage difference across the interface called contact potential V_c. The contact potential is determined by the difference between the work functions of the metals $\Delta\psi$, $V_c = \Delta\psi/e$.

In some experiments, an external voltage is applied between the tip and the sample surface. That voltage generates an electrical field that in turn produces an attractive force. If the interface involves dielectric materials, long range electrostatic interac tion forces could appear due to the trapping of charges, ions or electrons, within the dielectric.

Electrostatic forces usually depend on a long range distance. This could imply that the force acting on the sample surface not only is due to the atoms or molecules at the tip's apex but also bears the influence of the atoms in the shank of the tip or even in the body of the cantilever. The electrostatic force between two surfaces can be calculated by knowing the electrostatic energy. This is given by $U = C(V \quad V_c)^2/2$, where C is the capacitance of the system and V the external applied voltage. Then, the electrostatic force is given by

$$F_e = \quad \frac{1}{2}\frac{dC}{dz}(V \quad V_c)^2. \tag{3.24}$$

The problem of calculating the electrostatic force is to determine the capacitance of the system for a realistic situation. This is a hard problem that involves a number of approximations that depend on the geometry of the interface [55 60]. A general expression for a conical tip of a half angle β capped with a half sphere of radius R is given by

$$F_e = \quad \pi\varepsilon_0(V \quad V_c)^2 g(d), \tag{3.25}$$

where ε_0 is the dielectric constant of the vacuum and $g(d)$ is a geometrical factor that contains contributions from the tip's apex, tip shank, and cantilever body [55, 57]. The contribution from the cantilever body introduces a constant offset to the electrostatic force that is at least one order of magnitude smaller than the other terms. It can be neglected in force microscopy experiments whenever the tip surface distance is $d <$ 100 nm. Then, for small cone angles [55],

$$F_e = \pi\varepsilon_0 (V - V_c)^2 \left[\frac{R^2}{d(d+R)} + p^2 \left(\log \frac{d+R}{h} - 1 + \frac{R}{\sin\beta (d+R)} \right) \right], \quad (3.26)$$

where h is the length of the cone and

$$p = \frac{1}{\log \tan(\beta/2)}. \quad (3.27)$$

In the above expression, the contribution from the spherical cap is

$$F_{apex} = \pi\varepsilon_0 \frac{R^2 (V - V_c)^2}{d(d+R)}. \quad (3.28)$$

Whenever the radius is far larger than the tip surface distance $R \gg d$, Equation 3.28 simplifies to

$$F_{apex} = \pi\varepsilon_0 \frac{R (V - V_c)^2}{d}, \quad (3.29)$$

which is the most common expression used to estimate electrostatic forces in AFM. Numerical simulations and experiments have shown that the electrostatic force follows the V^2/d dependence given by Equation 3.29 [57, 60].

3.7 Nonconservative Forces

The forces discussed in the previous sections are conservative; however, in many experiments it is rather common to find both conservative and nonconservative forces. Dissipation arises from a variety of processes that depend on both the material properties and the environment. For example, dissipation is involved in force induced atomic or molecular reorientations, interdigitation, and formation and rupture of liquid menisci, or whenever there is an exchange of atoms and molecules between the tip and the sample [61–65].

Dissipation at the nanoscale could be classified into two major mechanisms, surface adhesion hysteresis [66, 67] and velocity dependent processes such as viscoelasticity [68, 69]. Surface adhesion hysteresis might have two contributions: one coming from long range interactions and the other coming from short range atomic and molecular interactions. The key concept is that the work needed to separate two surfaces in the presence of surface adhesion hysteresis is always greater

than the originally gained by bringing the surfaces together. As a consequence, the surface energy of the system shows two different values, one during the approach half period γ_a and the other in the retraction half period γ_r. For example, surface adhesion hysteresis in the framework of the DMT could be described as

$$F_{sh} = \frac{4}{3} E_{eff} R^{1/2} \delta^{3/2} \quad 4\pi R \gamma_{a,r}, \tag{3.30}$$

where γ_a and γ_r are, respectively, used during the approach and retraction half periods.

Long range dissipative interfacial forces, that is, interactions that do not imply the mechanical contact between probe and surface (noncontact), could be calcu lated by using a time dependent power law interaction where the strength of the force α depends on whether the probe approaches α_a or retracts α_r away from the surface,

$$F_{lh} = \frac{\alpha(t)}{d^2}. \tag{3.31}$$

Figure 3.6 illustrates a tip surface force with both short and long adhesion range hysteresis.

A simplified expression for the viscous force is obtained by combining the relationship between the stress and the strain given by the Voigt model and the sample deformation obtained from the Hertz contact mechanics [68]. The above assumptions give a time dependent viscous force as

$$F_{vis} = \eta \sqrt{R\delta} \frac{d\delta}{dt}, \tag{3.32}$$

where η is the viscosity. Notice that the viscous force depends on both the defor mation and the deformation rate (Figure 3.7).

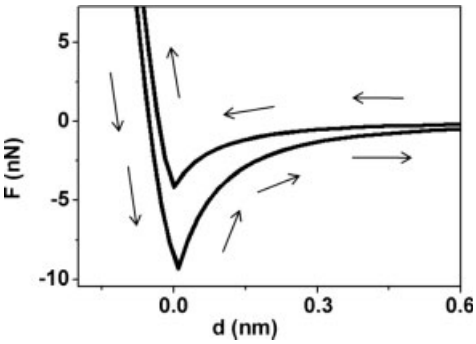

Figure 3.6 Example of a tip surface force that includes surface adhesion hysteresis. The arrows indicate the approach and retraction parts of the oscillation cycle.

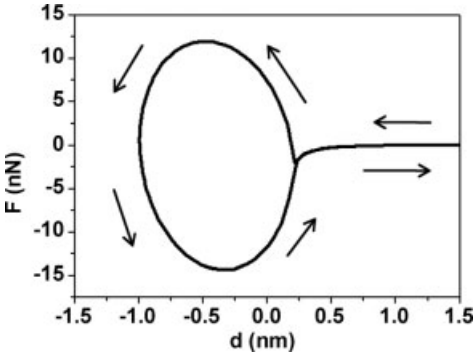

Figure 3.7 Tip surface force curve for a viscoelastic material. The arrows indicate the approach and retraction parts of the oscillation cycle.

3.8 Net Tip Surface Force

The first step to characterize and/or simulate an experiment is to establish which of the above forces participate in the net tip surface force. To illustrate the process to deduce the tip surface force from the specific interactions, it is instructive to examine two examples. The first case is characterized by an interface made of a spherical tip and a bulk elastic material. Nonconservative interactions are present through surface adhesion hysteresis. The second case involves a viscoelastic material. In both cases, we assume a sphere flat geometry.

3.8.1 Tip Surface Force for a Stiff Material with Surface Adhesion Hysteresis

First, we consider an interface with van der Waals forces, contact repulsion described by DMT, and surface adhesion hysteresis in the long range forces. At large tip surface distances $d > a_0$, the interaction is dominated by long range attractive forces,

$$F_{ts} = \frac{\alpha_{a,r}}{d^2}, \tag{3.33}$$

while for $d \leq a_0$

$$F_{ts} = \frac{4}{3} E_{eff} R^{1/2} \delta^{3/2} \quad 4\pi R \gamma_{a,r}, \tag{3.34}$$

where the subscripts indicate the presence of hysteresis in the adhesion forces. As a consequence, it must be distinguished between the approach and the retraction parts of the oscillation cycle. Figure 3.6 illustrates the tip surface forces during a period for a spherical tip and a bulk elastic material in the presence of surface adhesion hysteresis ($H = 6.7 \times 10^{-20}$ J, $R = 10$ nm, $E_{eff} = 150$ GPa, $\gamma_a = 33$ mJ/m^2, $\gamma_b = 66$ mJ/m^2, $\alpha_a = 1.11 \times 10^{-28}$ Nm^2, and $\alpha_b = 2.78 \times 10^{-28}$ Nm^2).

3.8.2
Tip Surface Force for a Viscoelastic Material

Now, we consider an interface characterized by the presence of long range van der Waals forces, contact repulsion, and a viscoelastic material. No surface adhesion hysteresis is present. Before tip surface contact, the force is dominated by van der Waals forces

$$F_{ts} = \frac{HR}{6d^2}. \tag{3.35}$$

Upon contact, three different forces are considered, the adhesion force, the contact repulsion, and the viscous force. The last force is given by Equation 3.32, while the other two are calculated by the equations given by the DMT model,

$$F_{ts} = \frac{4}{3} E_{eff} R^{1/2} \delta^{3/2} \quad 4\pi R\gamma \quad \eta\sqrt{R\delta}\frac{d\delta}{dt}. \tag{3.36}$$

To avoid the divergence of Equation 3.20, the van der Waals and adhesion forces are made equal at $d = a_0$,

$$4\pi R\gamma = \frac{HR}{6a_0^2}. \tag{3.37}$$

Figure 3.7 illustrates the force curve for a viscoelastic material ($H = 4.1 \times 10^{-20}$ J, $R = 10$ nm, $\eta = 800$ Pa s, and $E_{eff} = 500$ MPa).

4
Theory of Amplitude Modulation AFM

4.1
Introduction

It took 20 years to establish the fundamentals of amplitude modulation AFM (1998 2007). That is an unusually long period for one of the instruments that epitomizes the emergence of nanotechnology. There are two seemingly opposed reasons to explain this anomaly. First, the images provided by the microscope were so impressive and they came so soon after the invention of the technique that it conveyed the impression that the physical principles governing the operation of the instrument were already mastered. Second, it turned out that the dynamics of cantilever tip ensemble was rather complicated. By 2000, it became evident that the poor theoretical understanding of the tip dynamics was hampering the progress of the technique. This was the signal needed to develop a coherent theoretical framework.

The ultimate goal of any theory of dynamic AFM is to provide the mathematical link between the AFM observables, namely, the amplitude, the phase shift, and the resonant frequency, and the sample properties. The theory should also explain the dependence of the observables with respect to the tip surface separation. From these dependencies, it should be possible to establish the optimum imaging conditions and to determine the forces exerted on the sample surface.

At present, several theoretical formalisms compete to describe the various aspects of amplitude modulation AFM. In this chapter, I will present the main features of the point mass model approximation with an emphasis on the analytical or semianalytical approximations. The usefulness of numerical simulations is also underlined. The most complicated aspects of the point mass model such as the nonlinear dynamics properties and the self excitation modes (Q control) together with the introduction of the continuous beam equation (Euler Bernoulli) are discussed in Chapter 5. The theory for operation in liquid is presented in Chapter 6.

Amplitude Modulation Atomic Force Microscopy. Ricardo García

ISBN: 978-3-527-40834-4

4.2
Equation of Motion

Establishing the equation of motion of the vibrating cantilever tip system is the starting point of any theoretical description of the amplitude modulation AFM. The left panel of Figure 2.6 shows a scanning electron microscope image of a rectangular silicon cantilever. Solving its equation of motion under the influence of tip surface forces is a formidable task that involves the motion of a continuous three dimen sional object under the influence of short and long range interactions (Figure 4.1). A substantial simplification is attained by approximating the cantilever tip shape to a rectangular beam (Figure 4.2). The symmetry of the rectangular beam enables to

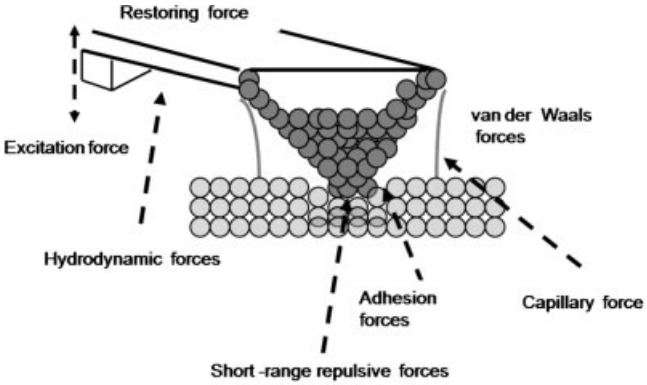

Figure 4.1 Scheme of the cantilever tip surface interface.

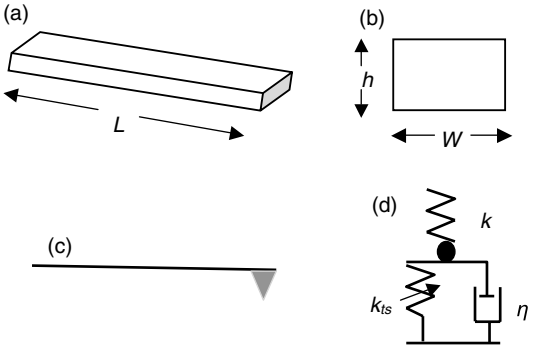

Figure 4.2 Geometries for the cantilever tip system. The geometry of the tip is not included in the modified Euler Bernoulli equation, but it appears for estimating the tip surface forces. (a) Rectangular beam. (b) Rectangular cross section of a rectangular beam. (c) One dimensional representation of a cantilever tip beam. (d) Point mass model representation of the cantilever tip surface interface. The arrow over k_{ts} indicates a "nonlinear" spring.

introduce a partial differential equation for the cantilever tip system. In fact, the equation is a modified Euler Bernoulli beam equation with the introduction of some dissipative elements and the tip surface force,

$$EI\frac{\partial^4}{\partial x^4}\left[w(x,t)+a_1\frac{\partial w}{\partial t}\right]+\varrho Wh\frac{\partial^2 w(x,t)}{\partial t^2}= \quad a_0\frac{\partial w}{\partial t}+\delta(x \quad L)[F_{\text{exc}}(x,t)+F_{\text{ts}}(d)]. \tag{4.1}$$

Here, $w(x,t)$ is the displacement of the cantilever beam perpendicular to its main axis; E, ϱ, and I are the Young modulus, mass density, and area moment of inertia, respectively; L, W, and h are the length, width, and thickness of the cantilever, respectively; a_0, a_1 are, respectively, the external and internal damping coefficients; $F_{\text{exc}}(x,t)$ is the excitation force; and F_{ts} represents all the tip surface interaction forces. The delta function indicates that the tip surface forces act only at the end of the tip. This approximation neglects the influence of the tip's shape in the motion of the system across the medium (air, liquid, or vacuum). In the above equation, the tip is a point object with its mass negligible with respect to the cantilever mass. However, the geometry of the tip is considered for determining the tip surface forces.

To find the solutions of Equation 4.1, it is required to introduce both the boundary conditions and the expression for the tip surface forces. The boundary conditions restrict the number of possible solutions. The mathematical process requires it to consider the multiple modes of the continuous system in the z direction. These modes are usually known as flexural modes (resonances). In the absence of internal damping, the number of cantilever resonances (eigenmodes) will be infinite. The process of deriving analytical or more properly semianalytical expressions of Equation 4.1 involves considerable mathematical tools and skills. The difficulties in tackling directly the above equation have prompted the development of several alternative theoretical and computational approaches [1 85]. In fact, analytical, semianalytical, or numerical solutions of a simpler equation of motion based on point mass models are widely used [1, 6, 13, 16, 21, 30, 35, 56, 85].

4.3 The Point-Mass Model: Elemental Aspects

A point mass model is the most straightforward approximation to model amplitude modulation AFM (or dynamic AFM). The cantilever tip system geometry is approximated by a point mass spring that is driven by an external force in the presence of the tip surface forces (Figure 4.2d). The relevant equation of motion is a nonlinear, second order differential equation,

$$m\ddot{z}= \quad kz \quad \frac{m\omega_0}{Q}\dot{z}+F_0\cos\omega t+F_{\text{ts}}(d), \tag{4.2}$$

where F_0 and ω are the amplitude and angular frequency of the driving force, respectively; m, Q, ω_0, and k are, respectively, the effective mass, quality factor,

angular natural frequency (undamped), and force constant of the free cantilever. It must be noted that the effective mass is related to the cantilever mass by $m \approx 0.25 m_c$, where m_c is the total cantilever mass (see Chapter 5). In amplitude modulation AFM, the excitation happens at the first natural resonance of the cantilever or at the frequency very close to it. The first resonance is sometimes called the fundamental resonance or mode. Unless otherwise stated Q, k, and ω_0 describe properties of the first mode.

The harmonic oscillator model provides a relationship between the force constant and the resonant frequency [87],

$$\omega_0 = \sqrt{k/m}. \tag{4.3}$$

To solve Equation 4.2, it is necessary to introduce an expression for the tip surface forces. However, the nonlinear character of the forces prevents the existence of analytical solutions. The above reason together with the similarities observed between the equation of motion of AM AFM and a forced damped harmonic oscillator has led to adoption of the harmonic oscillator model as a reference to understand dynamic AFM.

4.3.1
The Harmonic Oscillator

The tip motion of a vibrating tip in the proximity of a surface has many points in common with the motion of a driven harmonic oscillator with damping. In fact, in the absence of tip surface forces ($F_{ts} = 0$), Equation 4.2 becomes the equation of a forced harmonic oscillator with damping [87, 88],

$$m\ddot{z} = -kz - \frac{m\omega_0}{Q}\dot{z} + F_0 \cos \omega t. \tag{4.4}$$

The solutions of a driven damped harmonic oscillator provide many of the definitions and concepts needed to describe dynamic AFM. To be familiar with the properties of harmonic oscillators is a requirement to master any dynamic AFM experiment. Among the textbooks that introduce the dynamics of harmonic oscillators, I have followed the descriptions given by French [87] and Taylor [89].

Let us start with some qualitative considerations about the asymptotic limits of the oscillation amplitude as a function of the excitation frequency. At low driving frequencies with respect to the free resonant frequency, the response is controlled by the stiffness of the spring. The oscillator moves in step with the driving force with an amplitude close to F_0/k. At frequencies very large with respect to ω_0, the term kz is small compared to d^2z/dt^2 so the response is controlled by inertia. Then, a relatively small oscillation amplitude should be expected with a phase shift of 180° because the acceleration of a harmonic oscillator is 180° out of phase with the displacement.

The solution of a driven harmonic oscillator with damping has three different regimes [87, 89]. The relevant regime for most dynamic AFM experiments is the underdamped regime where $1/2Q < 1$. The solution in the underdamped regime has

a transient term and a steady motion,

$$z = B\exp\left(-\frac{\alpha}{2}t\right)\cos(\omega_r t - \beta) + A\cos(\omega t - \phi), \tag{4.5}$$

with $\alpha = \omega_0/Q$. Initially, both motions are prominent; however, after a time $2Q/\omega_0$, the transient term is reduced by a factor $1/e$. The steady motion is a sinusoidal function (harmonic) in a solution that oscillates with the excitation frequency ω and has a phase lag with respect to the excitation force. The transient term oscillates with a frequency ω_r that should be considered the new resonant frequency. The damping α modifies the resonant frequency of the harmonic oscillator. The new resonant frequency is related to the natural resonance frequency by

$$\omega_r = \omega_0\left(1 - \frac{1}{4Q^2}\right)^{1/2}. \tag{4.6}$$

For cantilevers with low quality factors, say $Q < 5$, Equation 4.6 shows that there are substantial differences between the actual and the natural resonant frequencies, otherwise, $\omega_r \approx \omega_0$. The dependence of the amplitude with the excitation frequency follows the Lorentzian expression,

$$A(\omega) = \frac{F_0/m}{\left[(\omega_0^2 - \omega^2)^2 + (\omega\omega_0/Q)^2\right]^{1/2}} \tag{4.7}$$

and the phase shift can be calculated by

$$\tan\phi = \frac{\omega\omega_0/Q}{\omega_0^2 - \omega^2}, \tag{4.8}$$

where ϕ is the angle by which the driving force leads the displacement.

Figure 4.3 shows, respectively, the amplitude and the phase shift as a function of the driving frequency for two different values of Q. In the presence of damping, the excitation frequencies at which the maxima of the amplitude and the energy absorbed by the harmonic oscillator occur do not coincide. The maximum in the amplitude happens at

$$\omega_m = \omega_0\left(1 - \frac{1}{2Q^2}\right)^{1/2} \tag{4.9}$$

and the amplitude takes a value of

$$A_m = \frac{QF_0}{k}\frac{1}{(1 - (1/4Q^2))^{1/2}}. \tag{4.10}$$

On the other hand, for the absorbed energy (or power) the maximum happens at ω_0. The phase shift is exactly 90° at $\omega = \omega_0$ with independence of the Q. These results emphasize the special significance of the natural frequency. Equation 4.7 is simplified by exciting the oscillator at its natural frequency ω_0,

$$A_0 = QF_0/k. \tag{4.11}$$

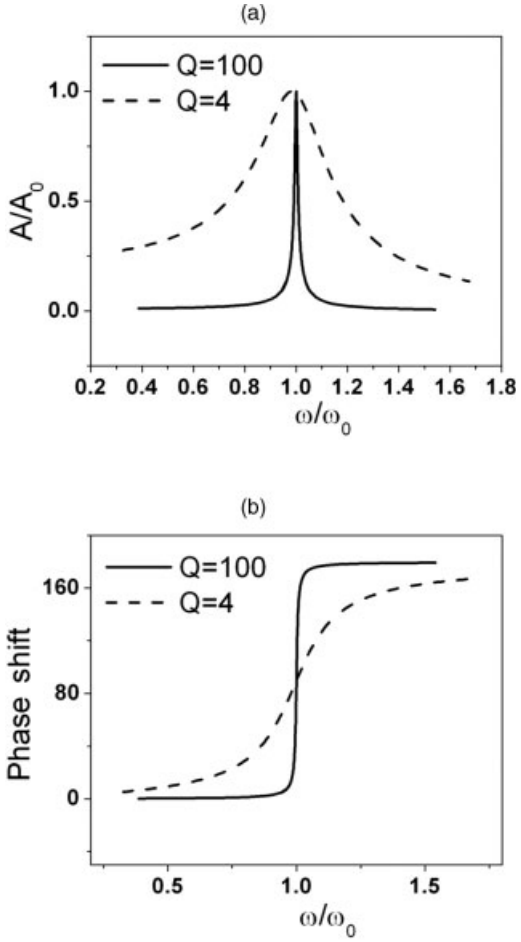

Figure 4.3 Dependence of the amplitude (a) and the phase shift (b) as a function of the excitation frequency for a forced harmonic oscillator with damping. The curves are plotted for two different Q values. The phase shift is in degrees.

4.3.2
Dynamics of a Weakly Perturbed Harmonic Oscillator

Let us assume that the point mass cantilever tip is oscillating under the influence of tip surface forces. The total force acting on the tip includes the elastic response $k(z \quad z_0)$, the hydrodynamic damping, and the interaction force F_{ts}. For small displacements with respect to the equilibrium position ($z = 0$), the tip surface force can be expressed by

$$F_{ts}(z) = F_{ts}(0) + (\mathrm{d}F_{ts}/\mathrm{d}z)_0 z. \tag{4.12}$$

In this approximation, the gradient of the force is the relevant factor that influences the tip motion. Then, the interaction can be characterized by an effective spring constant k_{ts},

$$k_{ts} = \quad (dF_{ts}/dz)_0. \tag{4.13}$$

By substituting the above equation into Equation 4.2, we recover the equation of a forced damped harmonic oscillator,

$$m\ddot{z} = \quad (k \quad k_{ts})z \quad \frac{m\omega}{Q}\dot{z} + F_0 \cos \omega t + F_{ts}(0) \tag{4.14}$$

with an effective spring constant k_{eff},

$$k_{eff} = k \quad (dF_{ts}/dz)_0. \tag{4.15}$$

Then, the new effective resonant frequency is calculated by

$$\omega_{eff} = (k_{eff}/m)^{1/2} \tag{4.16}$$

and the difference $\Delta\omega = \omega_{eff} \quad \omega_0$ can be approximated by

$$\Delta\omega \approx \quad (\omega_0 k_{ts}/2k). \tag{4.17}$$

The above equations show that whenever the interaction force can be approximated by its linear term, the amplitude modulation AFM behaves as a harmonic oscillator with a resonant frequency that depends on the gradient of the interaction.

The dependence of the amplitude on the excitation and effective resonant frequencies provides the first mechanism to explain the dependence of the oscillation amplitude with the strength of the interaction force, or in other words, with the tip surface separation [18]. Let us assume that the tip is excited at its natural frequency. Approaching the tip toward the surface will modify the resonant frequency that in turn implies a modification of the oscillation amplitude (Equation 4.7). The actual oscillation amplitude will be given by the value of the new resonance curve at the excitation frequency of the oscillator. As a consequence, the new oscillation amplitude would be smaller than the free amplitude (Figure 4.4). However, if the excitation frequency is just off resonance to the left, the oscillation amplitude could decrease or increase depending on the position of the new resonant frequency with respect to the natural frequency. This mechanism is called the detuning effect.

Approaches based on the harmonic oscillator model are useful to understand amplitude modulation AFM; however, in many cases, these approaches might fail to provide quantitative or even semiquantitative agreement with the experiments. They also might lead to misconceptions about AM AFM operation. The limitations of weakly perturbed harmonic models to describe dynamic AFM can be traced back to the implicit assumptions used to derive Equations 4.12 4.17. First, it was assumed that the tip surface force induces a frequency shift and not energy transfer. Second, the force gradient was assumed independent of the separation. Third, the force gradient was smaller than the cantilever force constant $k_{ts} \ll k$. However, many experiments imply oscillation amplitudes above 1 nm that violate one or more of the above

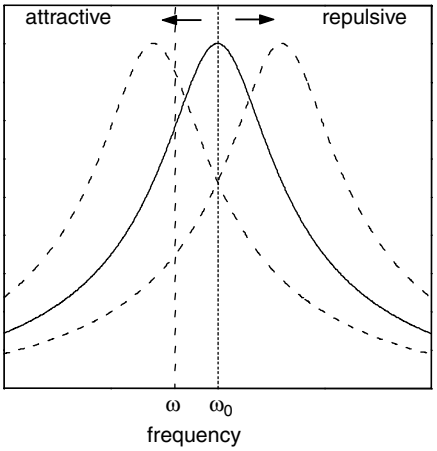

Figure 4.4 Detuning in a weakly perturbed harmonic oscillator. The gradient of the tip surface forces shifts the resonance curve to lower frequencies (attractive force) or to higher frequencies (repulsive force).

assumptions. A quantitative discussion on the limitations of the harmonic oscillator approach to interpreting dynamic AFM experiments is provided by Hölscher *et al.* [38].

4.4
The Point-Mass Model: Analytical Approximations

The goal of any theory of amplitude modulation AFM is to provide the relationships between the tip surface forces and the microscope observables. More specifically, it must explain the dependence of the amplitude and phase shift with both the tip surface distance and forces. Finally, these relationships will enable to extract quantitative information about the sample properties.

The nonlinear character of the tip surface forces prevents exact analytical solutions; however, several approximations do provide analytical or semianalytical solutions [15, 30, 35, 85]. Three theoretical frameworks have been used to describe dynamic AFM: harmonic approximations, nonlinear dynamics methods, and standard classical mechanics methods. However, the availability of numerical simulations has somehow weakened the need of analytical approaches. As a consequence, the AFM community has not yet reached a consensus on the most suitable analytical approximation to describe the operation of the instrument. Three analytical methods are described in the following sections. It should be said that in all cases, the motion is considered to be sinusoidal and in some cases the expressions resemble those of the single harmonic oscillator for the amplitude and phase shift as a function of the frequency. The analytical approaches neglect the average deflection of the cantilever and the higher harmonics components of the oscillation.

It is also worth mentioning the approach developed by Aimé and coworkers [30, 31]. They used a variational approach based on the principle of least action to obtain a relationship between the separation and the oscillation amplitude. In this model, the tip's dynamics is governed by the product of the quality factor and a reduced stiffness $\varkappa$, $Q\varkappa$. The reduced stiffness depends on the character of the interaction. However, the derived functional relationship between the amplitude and the distance is rather complex limiting the applications of this method.

4.4.1 Perturbed Harmonic Oscillator

Thurn Albrecht and coworkers [85] have revisited the description of the AM AFM as a perturbed harmonic oscillator. In this model, the starting hypothesis is to consider that the tip surface force can be expanded in a time dependent Fourier series [40, 45]

$$F_{ts} = b_0 + b_1 \cos \omega t + b_2 \cos 2\omega t + \cdots + c_1 \sin \omega t + c_2 \sin 2\omega t + \cdots \tag{4.18}$$

with

$$b_n = \frac{2}{T}\int_0^T F_{ts} \cos(n\omega t)\mathrm{d}t \tag{4.19}$$

and

$$c_n = \frac{2}{T}\int_0^T F_{ts} \sin(n\omega t)\mathrm{d}t. \tag{4.20}$$

This approach also considers an excitation force given by $F = F_0 \cos(\omega t\ \phi)$ and it assumes a sinusoidal solution given by $z = A\cos \omega t$. By reducing the force expansion to its first Fourier components ($n = 1$), Equation 4.2 shows that the effect of the interaction forces can be parameterized by introducing two parameters k_{eff} and α_{eff},

$$k_{eff} = k \quad (b_1/A) = k + k_{ts} \tag{4.21}$$

and

$$\alpha_{eff} = \alpha + (c_1/A\omega). \tag{4.22}$$

Then, the familiar dependences of a driven damped harmonic oscillator can be recovered by introducing new definitions for the resonant frequency and the quality factor,

$$A(\omega) = \frac{F_0/m}{\left[(\omega_{eff}^2 \quad \omega^2)^2 + (\omega\omega_{eff}/Q)^2\right]^{1/2}}, \tag{4.23}$$

$$\tan \phi = \frac{\omega\omega_{eff}/Q}{\omega_{eff}^2 \quad \omega^2}, \tag{4.24}$$

$$\omega_{eff} = \sqrt{k_{eff}/m}, \tag{4.25}$$

$$Q = (m\omega_{\text{eff}}/\alpha_{\text{eff}}). \tag{4.26}$$

The above expressions are formally identical to those of the harmonic model described in Section 4.3.1; however, there is a significant difference. The perturbed harmonic oscillator approach [85] establishes that the influence of the interaction force in the tip motion is averaged over the whole oscillation cycle, while in the harmonic oscillator model only the gradient of the force influences the tip motion.

4.4.2 Wang Model

By using methods from nonlinear dynamics models, Wang has deduced some semianalytical expressions [35, 36]. This approach assumes a steady state sinusoidal oscillation

$$z = A\cos(\omega t \quad \phi) = A\cos\theta \tag{4.27}$$

and by applying the Krylov Bogoliubov Mitroposky asymptotic approximation, the following relationships for the amplitude and phase shift are deduced:

$$A = \frac{F_0/k}{(1+\varpi)\sqrt{\alpha_{\text{eff}}^2 + (\varpi \quad \varpi_{\text{eff}})^2}}, \tag{4.28}$$

$$\tan\phi = \frac{\varpi_{\text{eff}} \quad \varpi}{\alpha_{\text{eff}}}, \tag{4.29}$$

where

$$\alpha_{\text{eff}} = \alpha_0 + \frac{2}{\pi}\int_0^{\theta_0} \alpha_s \sin^2\theta \, d\theta, \tag{4.30}$$

$$\varpi_{\text{eff}}^2 = 1 + \frac{1}{\pi k A}\int_0^{\theta_0} F_{\text{ts}}(z)\cos\theta \, d\theta, \tag{4.31}$$

where θ_0 is determined from the contact position

$$\cos\theta_0 = \frac{z_c + a_0}{A}, \tag{4.32}$$

where α_e is an effective damping factor that includes the hydrodynamic damping with the medium α_0 ($\alpha_0 = 1/2Q$) and the inelastic interactions in the sample α_s; ϖ and ϖ_{eff} are, respectively, the normalized driving frequency ω/ω_0 and effective (normalized) resonant frequency. Equation 4.28 resembles the Lorentzian expres sion for a forced harmonic oscillator with damping. It says that in the absence of tip surface inelastic interactions, the variations of the oscillation amplitude are related to changes in the effective resonant frequency of the system. The changes in resonance are induced by the tip surface interaction forces as it is shown by Equation 4.31. Thus, qualitatively this result coincides with the one derived by the perturbed harmonic oscillator model.

4.4.3 Virial Dissipation Method

Applying the virial theorem and the energy conservation principle over one period of the oscillation, Garcia, Lozano, and San Paulo deduced some analytical relationships [15, 21, 90]. These equations link the amplitudes and the phase shifts to two independent properties of the tip–surface interaction, the dissipated energy and the virial.

The instantaneous tip deflection can be approximated by

$$z(t) = A\cos(\omega_0 t - \phi). \tag{4.33}$$

The amount of energy dissipation and the virial are defined as

$$E_{ts} \equiv \int_0^{T_0} d\,t F_{ts}(d)\dot{z}(t) = \frac{\pi k A}{Q}(A_0 \sin\phi - A). \tag{4.34}$$

$$V_{ts} \equiv \frac{1}{T}\int_0^{T_0} d\,t F_{ts}(d) z(t) = -\frac{kA_0}{2Q} A\cos\phi, \tag{4.35}$$

with $A_0 = F_0 Q/k$ the free amplitude value.

Equation 4.34 represents the convolution of the interaction with the velocity, while Equation 4.35 is the convolution of the interaction with the position. We remark that both expressions are mathematically independent. Then, the following can be deduced [90]:

$$A = A_0\sqrt{(2\nu)^2 + \left(\frac{1 \pm \sqrt{1 - (4\nu)^2 - 4\beta/\pi}}{2}\right)^2}, \tag{4.36}$$

$$\phi = -\arctan\left(\frac{1 \pm \sqrt{1 - (4\nu)^2 - 4\beta/\pi}}{4\nu}\right), \tag{4.37}$$

where ν and β contain the effect of conservative and nonconservative forces, respectively, as given by

$$\beta = (QE_{ts}/kA_0), \tag{4.38}$$

$$\nu = (QV_{ts}/kA_0^2). \tag{4.39}$$

The amplitude now appears as a function of the values of the energy dissipated and the virial of the force. These values are averaged over a period. The amplitude is no longer explicitly expressed as a change of the resonant frequency (see Section 4.6). The virial dissipation method can be applied to describe conservative, nonconservative, or both tip–surface interactions.

4.5
Peak and Average Forces

In contact or static AFM, the force exerted by the tip on the sample surface is easily determined by measuring the cantilever deflection z. Once the deflection is mea sured, the application of the Hooke's law ($F = kz$) gives the force. In dynamic AFM, the deflection changes with time for two reasons. First, the proper cantilever tip vibration implies the changes in the deflection. Second, the tip surface force modifies the deflection. Because the tip surface distance changes with time so does the force and hence the deflection. It is not straightforward to separate these contributions, which in turn, makes it hard to measure the force (see also Section 5.8).

In general, two different force measurements are relevant, the force dependence on time and the force dependence on the tip surface distance. Figure 4.5 shows a

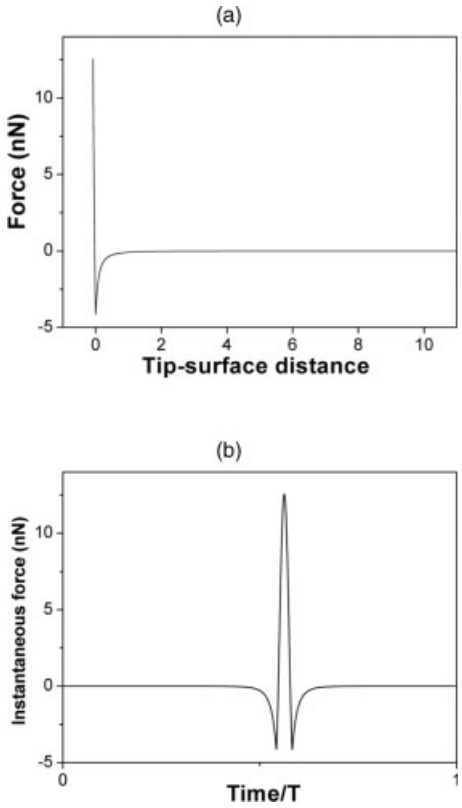

Figure 4.5 Numerical simulations of the time and distance dependencies of the tip surface force in AM AFM (E_{eff} 150 GPa, H 6.7×10^{-20} J, A_0 15 nm, R 10 nm, k 2 N/m, Q 150, f_0 59 kHz, z_c 6 nm).

force curve (a) simulated by using the DMT model ($E_{\text{eff}} = 150$ GPa, $H = 6.7 \times 10^{-20}$ J, $R = 10$ nm, $k = 2$ N/m, $Q = 150$, $f_0 = 59$ kHz). Figure 4.5b shows the time depen dence of the force during one oscillation ($A_0 = 15$ nm and $z_c = 6$ nm). Only during a fraction of the oscillation period, here about $1/6T$, are the tip surface forces noticeable. The methods to extract the dependence of the force on time and distance from the experimental data are mathematically demanding. They will be discussed in the next chapter. From an experimental point of view, it is convenient to distinguish two other types of force measurements, the peak force and the average force. The values of these forces are critical to estimate the nondestructive character of the measurements.

4.5.1
Peak Forces

The maximum force exerted by the tip on the sample surface is a parameter of special relevance to estimate the nondestructive character of the imaging process. By using the nonlinear asymptotic theory, Hu and Raman parameterized the peak forces in attractive and repulsive regimes [61]. For attractive forces of the van der Waals type described by Equation 3.1, the peak force is determined by

$$F_{\text{vdW}}^{\text{p}} = \frac{2\sqrt[3]{3}A_0^2}{(HR)^{1/3}(Q/k)^{4/3}}\left[\frac{A}{A_0} \quad \frac{A^3}{A_0^3}\right]^{2/3}, \tag{4.40}$$

while for repulsive forces described by the DMT model,

$$F_{\text{DMT}}^{\text{p}} = 2^{1/8}\left(\frac{\pi^3}{3}\right)^{1/4}\left(\frac{E_{\text{eff}}R^{1/2}k^3}{Q}\right)^{1/4}(A_0^8 A \quad A_0^6 A^3)^{1/8}. \tag{4.41}$$

The values provided by the above equations are in good agreement with numerical simulations of the peak forces under ambient or vacuum conditions.

4.5.2
Average Forces

The average force experienced by the tip during a cycle can be calculated by measuring the average tip deflection z_0, thus $\langle F_{\text{ts}}\rangle = kz_0$, or can be more easily calculated from the value of the amplitude according to the expression deduced from the virial dissipation method,

$$\langle F_{\text{ts}}\rangle \approx \frac{F_0}{2}\left[1 \quad \left(\frac{A}{A_0}\right)^2\right]^{1/2} = \frac{kA_0}{2Q}\left[1 \quad \left(\frac{A}{A_0}\right)^2\right]^{1/2}. \tag{4.42}$$

For small oscillations, say below 5 nm, the above expression provides a lower limit for the peak forces.

4.6
The Point-Mass Model: Numerical Solutions

Numerical simulations offer an alternative way to understand and explain amplitude modulation AFM experiments. Depending on the experimental conditions, numer ical simulations might provide quantitative, semiquantitative, or qualitative descrip tions of the experimental data. Simulations have been critical to understanding some nonlinear dynamics behavior such as the bistable tip motion. They have also paved the way for the development of multifrequency AFM approaches. A more practical outcome of numerical simulations has been that for a wide range of experimental conditions the tip deflection can be approximated by [17]

$$z(t) = z_0 + A\cos(\omega_0 t \quad \phi), \tag{4.43}$$

where z_0 is the mean value of the cantilever deflection. In many experimental situations, $|z_0| \ll |z_c + A\cos(\omega t \quad \phi)|$, and z_0 is neglected.

Figure 4.6 shows the amplitude, contact time, and the average force dependence on the average tip surface separation as obtained by numerical integration of the

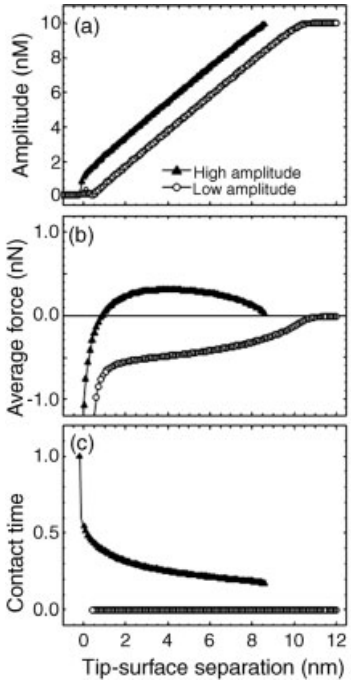

Figure 4.6 (a) Amplitude, (b) average force, and (c) contact time as a function of the average tip surface separation. Observe that in the attractive (low amplitude) solution the contact time per cycle is zero (E_{eff} 1.51 GPa, H 6.4×10^{-20} J, A_0 10 nm, R 20 nm, k 40 N/m, Q 400, f_0 350 kHz, z_c 6 nm).

point mass equation of motion ($E_{\text{eff}} = 1.51\,\text{GPa}$, $H = 6.4 \times 10^{-20}\,\text{J}$, $R = 20\,\text{nm}$, $k = 40$ N/m, $Q = 400$, $f_0 = 350\,\text{kHz}$).

4.6.1 Attractive and Repulsive Interaction Regimes

Anczykowski *et al.* noticed that the discontinuities observed in the amplitude curves could be related to transition points from different interaction regimes [6, 7]. The transition reflects the coexistence of two steady state solutions in the cantilever tip system [13, 14]. These solutions define two tip surface interaction regimes that may be classified, for many relevant experimental cases, according to the average value of the force

$$\langle F_{\text{ts}} \rangle = \frac{1}{T} \oint F_{\text{ts}} \mathrm{d}t. \tag{4.44}$$

Oscillations where the average value force is positive belong to the repulsive regime, while those where the average value of the force is negative belong to the attractive regime. As it is shown in Figure 4.6, the regimes coexist, that is, for the same external parameters the equation of motion has two stable solutions (high and low amplitude). The coexistence of two or more solutions is also reflected in the peculiar shape of the resonance curves (Figure 4.7). The explanation of this effect was one of the first successful applications of numerical simulations. Notice that for very small average tip surface separations (<1 nm), the low amplitude solution vanishes and the high amplitude solution changes from repulsive to attractive. In Chapter 5, the nonlinear dynamics properties of the microscope are discussed in detail.

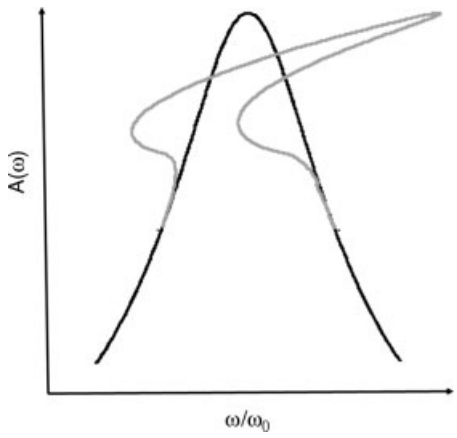

Figure 4.7 Resonance curves for a free vibrating tip (black) and for a tip that interacts with a surface via attractive and repulsive conservative forces (gray). The forces deform the resonance curve in the proximity of the natural frequency. The amplitude is multivaluated for certain frequencies.

4.6.2
Driving the Cantilever Below Resonance

Figure 4.7 shows that there is an interval of frequencies below resonance where the tip shows a single solution (repulsive). These frequencies could provide more stable oscillations with several advantages such as the ability to employ higher feedback gains [91]. However, numerical simulations show that, for the same amplitude ratios, the further the cantilever is driven below the resonance, the larger are the forces exerted on the sample surface. The predictions given by numerical simulations have also been confirmed by experiments [92].

4.7
The Effective Model

The above results allow us to propose an effective model to describe amplitude modulation AFM. The key elements of the model are the equation of motion, the tip surface interaction, and the expression for the deflection. The equation of motion of the point mass system (Equation 4.2) represents a good compromise between rigor and computational effort. The expression of the tip surface force depends on the properties of the interface. For experiments performed in air where the DMT is applicable (stiff materials and low adhesion forces), the force is calculated by

$$F_{\text{ts}} = \quad \frac{HR}{6d^2} \quad d > a_0, \tag{4.45}$$

$$F_{\text{ts}} = \frac{4}{3} E_{\text{eff}} \sqrt{R(a_0 \quad z \quad z_c)^{3/2}} + F_{\text{ad}} \quad d \leq a_0. \tag{4.46}$$

Under the above conditions, the approximate steady state solution has a sinusoidal form given by

$$z(t) = z_0 + A\cos(\omega_0 t \quad \phi). \tag{4.47}$$

The effective model is the starting point to describe an amplitude modulation AFM experiment. This book describes some experimental conditions under which the effective model is applicable and also describes other conditions that require the use of more sophisticated models.

Appendix A
The Runge Kutta Algorithm

The numerical solution of the point mass model is determined by using a fourth order Runge Kutta algorithm [93]. For a first order differential equation given by

$$\mathrm{d}z/\mathrm{d}t = f(t, z), \tag{A1}$$

which has a known value $z_i = z(t_0)$ for an initial value of the independent variable $t_i = t_0$. Then, the successive values of $z_n = z(t_n)$ with

$$t_{n+1} = t_n + \Delta t \tag{A2}$$

are generated by using the following algorithm:

$$z_{n+1} = z_n + \frac{\Delta t}{6}(\lambda_1 + 2\lambda_2 + 2\lambda_3 + \lambda_4), \tag{A3}$$

with

$$\lambda_1 = f(t_n, z_n), \tag{A4}$$

$$\lambda_2 = f\left(t_n + \frac{\Delta t}{2}, z_n + \frac{\Delta t}{2}\lambda_1\right), \tag{A5}$$

$$\lambda_3 = f\left(t_n + \frac{\Delta t}{2}, z_n + \frac{\Delta t}{2}\lambda_2\right). \tag{A6}$$

The Runge Kutta algorithm can be applied to solve a second order differential equation by transforming the second order differential equation into two first order differential equations,

$$\frac{\mathrm{d}y}{\mathrm{d}t} = \frac{\mathrm{d}^2 z}{\mathrm{d}t^2} = f(t, y), \tag{A7}$$

$$y = \frac{\mathrm{d}z}{\mathrm{d}t} = y(t, z). \tag{A8}$$

Then, Equations A7 and A8 are solved simultaneously by using Equation A3 and the initial conditions at $t_i = t_0$, $z_i = z(t_0)$, and $y_i = y(t_0)$.

5
Advanced Theory of Amplitude Modulation AFM

5.1
Introduction

This chapter deals with some aspects of the amplitude modulation AFM theory that might require familiarity with advanced mathematical methods. The chapter alternates models based on point mass approximations and continuous systems. Point mass models are used to develop the theory of self excitation modes, more commonly known as Q control theory. These models are also helpful in describing the nonlinear dynamics behavior of the microscope. An alternative description based on the systems theory is also presented. The section devoted to continuous models starts with a description of the method to solve the motion of a continuous cantilever beam. This is followed by a section devoted to discuss the equivalence between point mass parameters and continuous model concepts. The last section of the chapter introduces some of the current approaches to reconstruct the spatial and the temporal dependencies of the tip–surface force.

5.2
Q-Control

In the absence of inelastic tip–surface interactions, damping is controlled by the dissipation processes occurring inside the cantilever and those associated with the interaction between the cantilever and the surrounding medium. These are physical processes, thus, they cannot be altered by the electronics. However, how the energy is imparted or removed from the cantilever could be externally modified.

The first implementation of an active feedback in amplitude modulation AFM went almost unnoticed [1]. However, Q control has elicited considerable attention in both experiments [2–12] and theory [13–18] since it was claimed to be compatible with operation under very small forces [5]. Anczykowski *et al.* proposed the increase in the effective Q to favor the oscillation in the attractive regime [2]. Tamayo *et al.* pioneered its application in liquids to reduce the applied force while imaging [5, 6]. Other authors have implemented Q control to reduce the effective Q and, in this way, to

Amplitude Modulation Atomic Force Microscopy. Ricardo García

ISBN: 978-3-527-40834-4

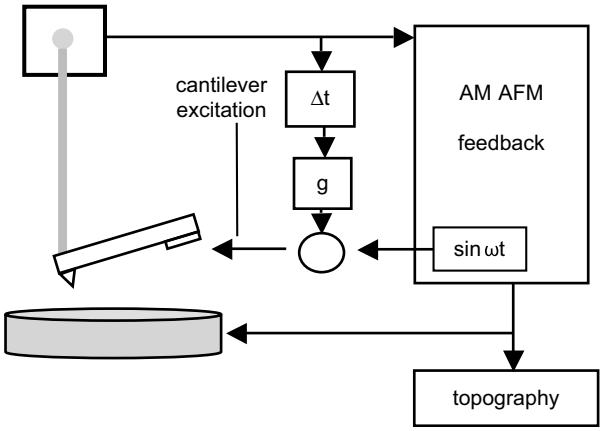

Figure 5.1 Schematic view of the Q control feedback. The new elements are the block to calculate the time delay, the gain, and the block that combines the sinusoidal excitation with a time delayed deflection.

increase the scanning speed of the microscope [8]. Numerical simulations tend to support the above applications, although they also limit their impact. High gains may cause instabilities in the feedback system [13]. Kokavecz *et al.* pointed out that the advantages of increasing the effective Q appear only while imaging soft materials [14].

The experimental effectiveness of Q control to provide higher resolution images of soft systems in liquid remains controversial. In fact, the highest resolution images of biomolecules are obtained by using the standard feedback circuitry. Ashby has proposed an explanation of what might be called the Q control paradox [17]. By including thermal noise into the simulations, he showed that Q control gives little advantage in terms of signal to noise ratio.

The theory of Q control has been thoroughly addressed [13 18]. The effective quality factor of a cantilever Q_{eff} can be modified by adding a self excitation force proportional to the cantilever deflection of an earlier time $z(t \quad \Delta t)$, then equation of motion is written as

$$m\ddot{z} + kz + \frac{m\omega_0}{Q}\dot{z} = F_0 \cos \omega t + kgz\left(t \quad \frac{\varphi}{\omega}\right), \tag{5.1}$$

where the time delay has been expressed in terms of a phase shift $\Delta t = \varphi/\omega$. The feedback circuitry for the Q control operation requires the addition of a time (phase) shifter (Figure 5.1). It is not possible to solve the above equation for arbitrary values of the gain g. However, for small gains, $g \in [0,\ 1/Q)$ the steady state solution can be approximated by

$$z(t) = A(\omega, g, \varphi)\cos[\omega t \quad \phi(\omega, g, \varphi]. \tag{5.2}$$

Then, the amplitude can be expressed analytically as

$$A = \frac{F_0/m}{\left[\left(\omega_0^2 \quad \omega^2 + (kg\cos\varphi/m)\right)^2 + ((\omega\omega_0/Q) \quad (kg\sin\varphi/m))^2\right]^{1/2}}. \tag{5.3}$$

Equation 5.3 shows that the amplitude depends on g and φ. By comparing the above equation with the Lorentzian expression of a forced harmonic oscillator with damping, it can be shown that the self excitation modifies both the resonant frequency and the term that carries the Q contribution. In particular, the Q_{eff} as measured from the width of the power resonance curve at half maximum ($\sim\omega_0/Q_{\text{eff}}$) is increased by choosing a φ in the 0 π range, while φ values in the interval (π, 2π) decrease it.

An approximate analytical expression of Q_{eff} can be deduced for $\varphi = \pi/2$,

$$\frac{1}{Q_{\text{eff}}} = \frac{1}{Q} \quad \frac{kg}{m\omega\omega_0}. \tag{5.4}$$

The effect of g on amplitude curves for a phase shift of $\varphi = 90^\circ$ and a driving force of $F_0 = 2$ nN is shown in Figure 5.2. The curve for the initial nonself excited system, its maximum is about 10 nm, appears as a straight line at the scale of the figure. An increase in g produces an increase in the amplitude, the shift of the resonant frequency to higher values, and also narrows the amplitude curves. The amplitude at resonance can be increased by two orders of magni tude with respect to the initial system, while the resonant frequency changes by a small factor (0.3%). In the example shown in Figure 5.2, an increase of g from 0 to 0.198 produces a two orders of magnitude increase in Q_{eff} (from 5 to 403).

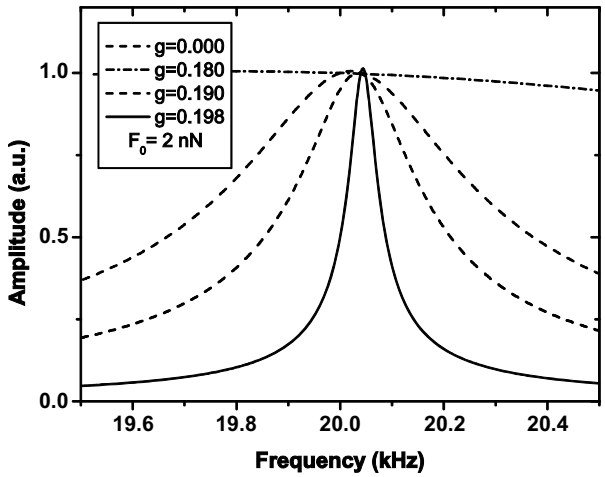

Figure 5.2 Normalized amplitude versus frequency for different values of the self excitation gain. The curves have been obtained for a system characterized by F_0 2 nN, k 1 N/m, $\omega_0/2\pi$ 20 kHz, and Q 5. In the frequency range shown in the figure, the resonance curve of the nonself excited system (g 0.0) hardly shows any change, while the one for g 0.198 shows a sharp peak ($Q_{\text{eff}} \approx 500$). Adapted from Ref. [13].

5.3 Nonlinear Dynamics

The tip surface forces relevant to AM AFM have a nonlinear dependence on distance. On the other hand, the amplitudes of interest range from 1 to 30 nm, that is, they are larger than the decay lengths associated with short range and van der Waals forces. Thus, the forces acting on the tip are nonlinear and, in most cases, they cannot be linearized. As a result, the tip motion might show some striking nonlinear dynamics features. A common observation is the hysteresis loop observed when a resonance curve is first measured by driving the cantilever from low to high frequencies and then from high to low frequencies [19 21]. Hysteresis loops can also be observed in the amplitude distance and the phase distance curves (Figure 5.3) [20, 22 24]. The step like discontinuities observed in the amplitude and the phase curves [22 26] and, in some cases, the noise in an image have their origin in nonlinear dynamics effects [27].

The above observations and their implications in the performance of the micro scope have generated a considerable amount of attention [27 58]. In particular, the potential of the microscope in studying different chaotic regimes such as homoclinic chaos or grazing bifurcations has attracted interest on its own [29, 30, 35, 36, 42 51].

In the conditions required for high resolution imaging, the hysteresis loops, the step like discontinuities, and the nonlinear dynamics noise are related to the coexistence of two stable oscillation states (low and high amplitude) [27, 40, 41]. These states are compatible with the same set of external parameters. For example, a step like discontinuity represents a single transition between the low and the high amplitude states (or vice versa), while a hysteresis loop happens when there are two transitions, one when the tip approaches and the other when it retracts from the sample surface. It is very unlikely that the transitions happen at the same tip surface distance, in the presence of a hysteresis loop. The presence of multiple transitions while imaging is a source of noise.

The resonance curve plotted in Figure 4.7 shows that for some frequencies, in particular for ω_0, there are three possible amplitudes. Each of these amplitudes represents a different oscillation state or solution. The top and the bottom states are stable and accessible while the middle represents a metastable state. These oscillation states have different properties [56]. In the top or high amplitude state, the tip touches the surface at the lower end of the oscillation (Figure 4.6). The average force for the most part of the dynamical range takes positive values. For the above reasons, the high amplitude state is usually called the repulsive or intermittent regime. None theless, it must be noticed that for very small average tip surface distances the force might be attractive (Figure 4.6b). The low amplitude state involves attractive forces and the absence of tip surface mechanical contact. The low amplitude solution is usually called the attractive or noncontact regime. In stiff samples, stable images can be obtained with either state. However, the state selected for imaging isolated biomolecules or soft materials does influence the spatial resolution and the sample deformation [40, 56 58].

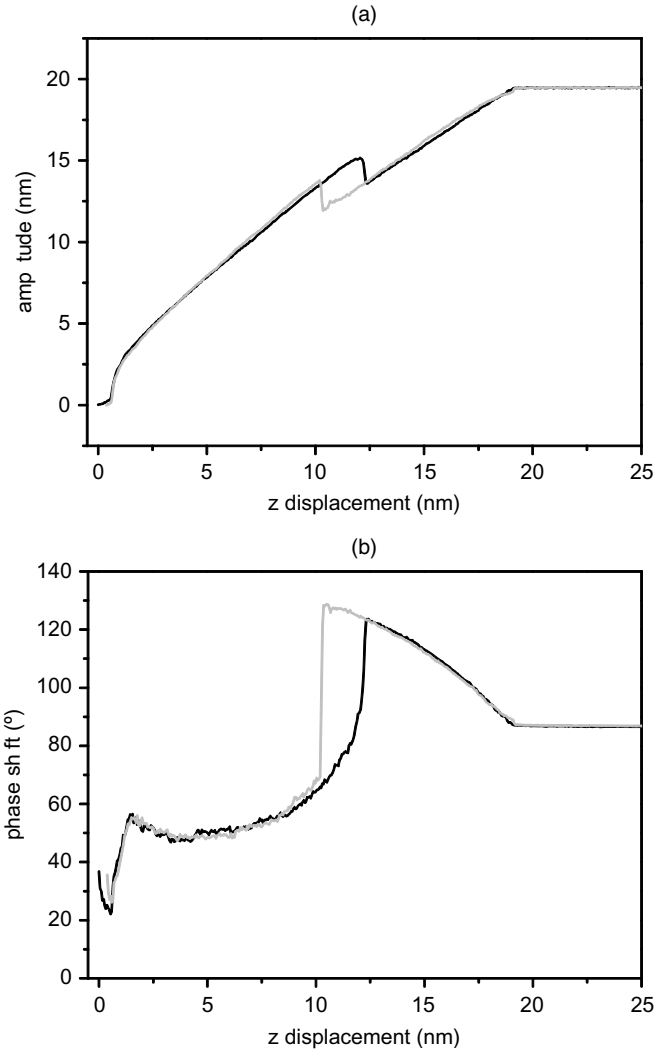

Figure 5.3 Experimental hysteresis loops in (a) amplitude distance and (b) phase distance curves. The experiments were performed on a mica surface in air. In grey and black are plotted, respectively, the approach and retraction curves.

The coexistence of two stable states depends on the experimental parameters (amplitudes and frequencies), tip's radius, and sample properties. Each state has its own basin of attraction that is formed by the points in the phase space that have the same attractor. In general, the basins of attraction have different sizes, and as a consequence one state might be dominant with respect to the other [27]. There are also cases where the system shows only one solution. As a rule, the attractive solution dominates for low A_0 values and set point amplitudes (A_{sp}) very close to the free

amplitude. In contrast, the repulsive solution dominates for high free amplitudes and medium to small set point amplitudes.

5.4 Continuous Cantilever Beam Model

Point mass models cannot describe the existence of multiple resonances or eigen modes; as a consequence, these models do not predict the influence of higher modes on the tip motion. The continuous character of the cantilever is captured either by solving a modified Euler Bernoulli equation [59 80] or by performing finite element simulations [81 83]. However, analytical or semianalytical solutions of the Euler Bernoulli equation provide a deeper understanding of the AFM dynamics than the results provided by finite element simulations. In what follows, a method to find the solutions of the AFM cantilever based on the discretization of the modified Euler Bernoulli equation is introduced [67].

The Euler Bernoulli equation describes the bending of a rectangular and homo geneous cantilever along its longitudinal axis without damping [70, 84]. Equation 4.1 is the modified Euler Bernoulli equation for a continuous and uniform cantilever beam under the action of external forces applied at its free end. This equation also includes external and internal damping. Because Equation 4.1 is crucial for the rest of this chapter, it is reproduced below

$$EI\frac{\partial}{\partial x^4}\left[w(x,t)+a_1\frac{\partial w(x,t)}{\partial t}\right]+\varrho Wh\frac{\partial^2 w(x,t)}{\partial t^2} = a_0\frac{\partial w(x,t)}{\partial t}+\delta(x \quad L)[F_{\text{exc}}(t)+F_{\text{ts}}(d)], \tag{5.5}$$

where $d = z_0 + z_c + w(L,t)$ is the instantaneous tip surface separation (Figure 2.12). The symbol definition is provided in Section 4.2.

5.4.1 One-Dimensional Model

To find the solutions of the modified Euler Bernoulli equation, we require to separate the general solution into spatial and temporal components $w(x,t) = X(x)Y(t)$, and the application of the boundary conditions. There are four main boundary conditions: (1) the vertical displacement at the clamped end of the cantilever is zero ($X(0) = 0$); (2) the slope is also zero at the clamped end ($X'(0) = 0$); (3) the internal torque in the perpendicular direction at the free end is zero ($X''(L) = 0$); and (4) the vertical internal force at $x = L$ is also zero ($X'''(L) = 0$). The boundary conditions introduce a discrete number of solutions called eigenmodes or resonances. On some occasions, if there is no ambiguity the term mode might also be used. Then, the general solution describing the vertical (flexural) displacement) can be expressed as a superposition of the response

of each eigenmode:

$$w(x,t) = \sum_{n\ 1}^{\infty} X_n(x)\,Y_n(t), \tag{5.6}$$

where $X_n(x)$ is defined as

$$X_n(x) = \cos\left(\varkappa_n \frac{x}{L}\right)\quad \cosh\left(\varkappa_n \frac{x}{L}\right)\quad \frac{\cos(\varkappa_n)+\cosh(\varkappa_n)}{\sin(\varkappa_n)+\sinh(\varkappa_n)}\left[\sin\left(\varkappa_n \frac{x}{L}\right)\quad \sinh\left(\varkappa_n \frac{x}{L}\right)\right] \tag{5.7}$$

with $\varkappa_n$ the nth positive real root of

$$1+\cos\varkappa_n \cosh\varkappa_n = 0 \tag{5.8}$$

with $\varkappa_1 = 1.8751$, $\varkappa_2 = 4.694$, $\varkappa_3 = 7.8548$, and $\varkappa_4 = 10.996$. Equation 2.7 allows one to derive the rest of the coefficients. On the other hand,

$$\int_o^L \mathrm{d}x X_n(x) X_m(x) = L\delta_{n,m} \tag{5.9}$$

with $X_n(0) = 0$ and $X_n(L) = 2(\quad 1)^n$.

The time dependent function for each eigenmode $Y_n(t)$ follows the set of anhar monic differential equations,

$$\ddot{Y}_n(t) + \frac{\omega_n}{Q_n}\dot{Y}_n(t) + \omega_n^2 Y_n(t) = \frac{F_n(t)}{m_n}, \tag{5.10}$$

where the eigenmode frequency, effective mass, quality factor, and external force are defined by

$$\omega_n^2 = \left(\frac{\varkappa_n}{L}\right)^4 \frac{EI}{\varrho Wh}, \tag{5.11}$$

$$m_n = \varrho Wh \int_0^L \mathrm{d}x\,[X_n(x)]^2 = \varrho WhL \equiv m_c, \tag{5.12}$$

$$Q_n = \frac{\omega_n}{(a_0/\varrho Wh) + a_1\omega_n^2}, \tag{5.13}$$

$$\begin{aligned} F_n(t) &= \int_0^L \mathrm{d}x f_{\mathrm{ext}}(x,t) X_n(x) = \int_0^L \mathrm{d}x \delta(x \quad L)\,[F_{\mathrm{ts}}(d) + F_{\mathrm{exc}}(t)] X_n(x) \\ &= 2(\quad 1)^n [F_{\mathrm{ts}}(d) + F_{\mathrm{exc}}(t)]. \end{aligned} \tag{5.14}$$

In the above equations, the total mass of the cantilever is expressed as m_c, while $f_{\mathrm{ext}}(x, t)$ represents the density of external forces per unit of length. Then, the actual tip motion can be calculated as

$$w(L,t) = \sum_{n\ 1}^{\infty} X_n(L)\,Y_n(t) = \sum_{n\ 1}^{\infty} 2(\quad 1)^n Y_n(t) \equiv \sum_{n\ 1}^{\infty} z_n(t), \tag{5.15}$$

Table 5.1 Relative frequencies, force constants, and quality factors of the first four eigenmodes of a rectangular and uniform cantilever.

Eigenmode	Frequency		Force constant		Quality factor (no internal damping)	
n	ω_n	$(\varkappa_n/\varkappa_1)^2\omega_1$	k_n	$(\omega_n/\omega_1)^2 k_1$	Q_n	$(\omega_n/\omega_1)Q_1$
1 (Fundamental)	ω_1	ω_0	k_1			
2	$6.27\omega_0$		$39.31k_1$		$6.27Q_1$	
3	$17.55\omega_0$		$308k_1$		$17.55Q_1$	
4	$34.39\omega_0$		$1183k_1$		$34.39Q_1$	

where the $z_n(t)$ is the mode projection at the tip end. By combining Equations 5.10 5.15, the following differential equations are deduced:

$$\ddot{z}_n(t) + \frac{\omega_n}{Q_n}\dot{z}_n(t) + \omega_n^2 z_n(t) = \frac{F_{\text{exc}}(t) + F_{\text{ts}}(d)}{m} \quad n = 1, 2, \ldots \tag{5.16}$$

and

$$m = 0.25 m_{\text{c}}. \tag{5.17}$$

The above equation shows that for a homogeneous and rectangular cantilever, the modal mass m is one fourth of the total mass of the cantilever. Please notice the subtle differences that exist between $z_n(t)$ and $Y_n(t)$. Each mode is characterized by three parameters: the eigenfrequency (ω_n), the force constant ($k_n = m\omega_n^2$), and the quality factor (Q_n). Table 5.1 summarizes the force constants, quality factors, and frequencies of the first four eigenmodes of a rectangular and uniform cantilever.

Figure 5.4 shows the shapes of the first four eigenmodes of a rectangular cantilever. The corresponding transfer function in the absence of tip surface forces is shown in Figure 5.5.

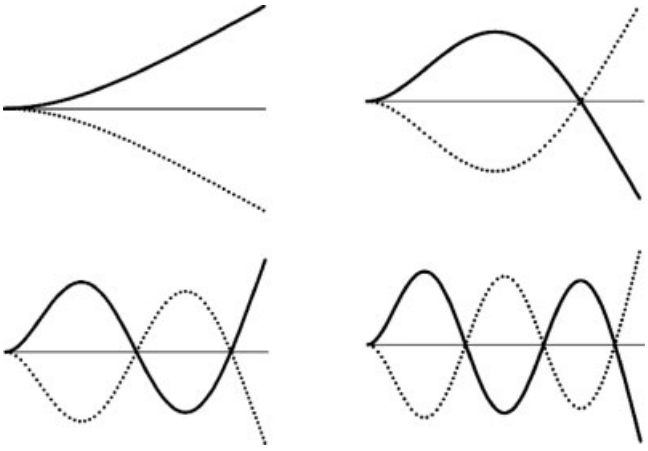

Figure 5.4 Shapes of the first four vibration modes of a rectangular and uniform cantilever beam.

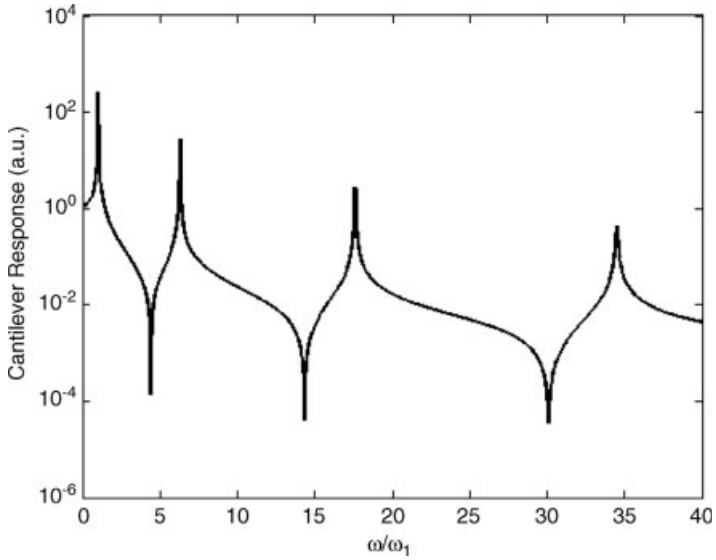

Figure 5.5 Amplitude response (transfer function) as a function of the excitation frequency for a one dimensional cantilever. The frequency is normalized with respect to the first eigenmode frequency.

5.5
Equivalence between Point-Mass and Continuous Models

The discretization of the modified Euler Bernoulli equation enables to relate the effective parameters of the point mass model such as the effective mass or the force constant to those of a continuous cantilever beam [67]. The first step in the equivalence process is to determine whether or not a single mode i dominates the dynamics of the cantilever beam. In the positive case, it can be assumed that the tip deflection carries information exclusively on this mode, then $w(L,t) = z_i(t)$, where $x = L$.

The description of a cantilever beam might require the introduction of several force constants. The force constants can be divided into three groups: the force constant associated with each mode k_i, the static force constant k_s, and the force constant of the equivalent point mass model k. The static cantilever force constant k_s is defined as the ratio between a static force F_0 applied at the free end of the cantilever and the deflection $w(L)$ caused by that force. The static deflection contains contribu tions from all the modes, thus

$$w(L) = \sum_{n\ 1}^{\infty} z_n = F_0 \sum_{n\ 1}^{\infty} \frac{1}{k_n} \equiv \frac{F_0}{k_s}, \tag{5.18}$$

where the nth mode deflection z_n is defined as

$$z_n = F_0/k_n. \tag{5.19}$$

Now, the static force constant can be expressed in terms of the individual mode force constants by

$$k_s = \left(\sum_{n\ 1}^{\infty} \frac{1}{k_n} \right)^{-1}. \tag{5.20}$$

It should also be kept in mind that Equation 5.16 implies

$$k_i = m\omega_i^2. \tag{5.21}$$

From Equations 5.11 and 5.21, we deduce

$$k_n = \frac{\varkappa_n^4}{4} \frac{EI}{L^3}. \tag{5.22}$$

The above equations give an analytical expression to the static force constant

$$k_s = 3EI/L^3, \tag{5.23}$$

where it has been considered that

$$\sum_{n\ 1} \frac{1}{\varkappa_n^4} = \frac{1}{12}. \tag{5.24}$$

In particular, it is deduced that the first mode force constant and the static force constant are almost identical

$$\frac{k_1}{k_s} = \frac{\varkappa_1^4}{12} = 1.030. \tag{5.25}$$

This justifies the implicit assumption of the point mass model derived in Chapter 4 where the force constant of the model was identified with the force constant of the cantilever $k_1 \approx k_s \approx k$.

Similarly, different masses can be associated with the cantilever. There is the cantilever mass, that is, the mass obtained from its geometry and density, m_c. Then, there is the effective mass (m) that appears in Equation 5.16. In many situations, the cantilever motion can be described with the sole contribution from the fundamental mode ($\omega_0 = \omega_1$); then another mass, the static mass, can be defined as the ratio between k_s and ω_1^2, which for a rectangular beam gives

$$m_s \equiv \frac{k_s}{\omega_1^2} = \frac{k_1/1.030}{\omega_1^2} = \frac{0.25}{1.030} m_c = 0.2425 m_c. \tag{5.26}$$

Other approaches have been applied to derive the equations that relate the effective parameters of the point mass model to those of the continuous cantilever [85, 86]. In particular, Melcher *et al.* have developed a method based on the assumption that a proper point mass model must possess the same elastic strain, kinetic, and tip sample interaction energies as the continuous cantilever for a given eigenmode [85]. For a rectangular and homogeneous cantilever with a point force applied at the free end, the expressions obtained with the energy balance method are identical to the

ones deduced in this section. However, Raman's approach [85] shows some advantages when the force acting on the cantilever is distributed along its length.

5.6 Systems Theory Description

An alternative description of dynamic AFM has been developed by using methods from the theory of complex systems [87–92]. In this approach, the cantilever–tip is described as a linear time invariant system that is actuated by a nonlinear feedback caused by the tip–surface forces. The cantilever–tip–sample interface is separated in two blocks. One block contains the cantilever system and the other the tip–surface interface system (see Figure 5.6). The first block is modeled as a linear time invariant system G while the tip–surface is modeled as a nonlinear system h. The linear operator G takes as input the sum of the excitation force $F_{\text{exc}}(t)$ and the tip–surface force $F_{\text{ts}}(t)$ (feedback block) and relates the cantilever position $P(t)$ to the total force $(F_{\text{exc}} + F_{\text{ts}})$ by

$$P(t) = G(F_{\text{exc}} + F_{\text{ts}}). \tag{5.27}$$

To simplify the notation, in the following discussion we replace $F_{\text{exc}}(t)$ by $g(t)$ and $F_{\text{ts}}(t)$ by $h(t)$. Because the excitation force $g(t)$ is periodic, the cantilever–tip oscillation has also a periodic solution with the same period T. Then, the time invariance of the interaction force implies that $h(t) = F(z(t))$ is also periodic. Thus, g, z, and h admit expansions in the form $g = \sum_{n=-\infty}^{\infty} g_n \exp(in\omega t)$. Then, it follows that

$$G(n\omega)(g_n + h_n) = p_n, n = 0, \pm 1, \pm 2, \ldots \tag{5.28}$$

The above relationship generates a series of equations that are called the harmonic balance equations [88]. If the transfer function of the cantilever G is determined [90], Equation 5.28 could be used to determine the Fourier coefficients of the tip–sample force because the coefficient of the excitation force g_n are known and those of p_n could be measured experimentally,

$$h_n = G^{-1}(n\omega)p_n \quad g_n. \tag{5.29}$$

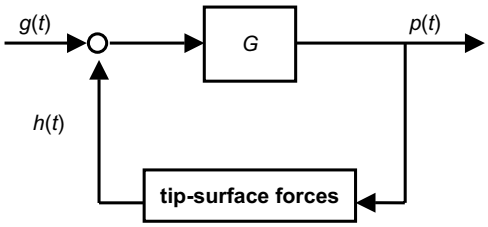

Figure 5.6 Block diagram of the amplitude modulation AFM. G is a linear and time invariant model of the cantilever–tip system.

This approach has also been extended to describe the continuous cantilever beam [91].

The shape of the transfer function for a driven and damped harmonic oscillator is easily determined,

$$G(\omega) = \frac{\omega_0^2}{k}\left[\left(\omega_0^2 \quad \omega^2\right)^2 + \left(\omega\omega_0/Q\right)^2\right]^{-1/2}. \tag{5.30}$$

The systems and control approach is less intuitive than the approaches based on the Newton equation. However, the system and control approach could be helpful to numerically describe the properties of the higher modes and harmonics. In partic ular, it gives all its potential to reconstruct the time resolved force interaction.

5.7
Force Reconstruction Methods: Force versus Distance

The tip surface forces that appear on the right hand side of Equation 4.2 as F_{ts} are usually not known. To reconstruct the force from the tip's trajectories, we require to invert Equation 4.2, consequently the process is called force inversion. Force inversion is technically demanding because the experimental quantities reflect the interaction averaged over a number of oscillations [93 99].

Frequency modulation AFM, the other major dynamic AFM method, faces similar challenges to reconstruct the force, so the reader interested in force inversion techniques could also check the contributions from Durig [100], Giessibl [101], and Sader *et al.* [102, 103].

5.7.1
Lee Jhe Method

Lee and Jhe force inversion method [93, 94] assumes a steady state sinusoidal solution given by $z \approx z_0 + A\cos(\omega t \quad \phi)$ (Equation 4.47). Then, it separates the interaction force into conservative and nonconservative components:

$$F_{ts}(s) = F_c + F_{nc} = F_c(s) \quad \Gamma(s)\dot{z}, \tag{5.31}$$

where s is a tip surface distance. Two independent equations are generated by the following method. First, the above force decomposition and the tip deflection are substituted into the general point mass model equation (Equation 4.2). Then both sides of the resulting equation are multiplied by sin $(\omega t \quad \phi)$ and integrated over a period. The other equation is obtained by repeating the above process but this time by multiplying Equation 4.2 by cos $(\omega t \quad \phi)$,

$$\int_0^{\pi} F_c(d)\cos\tau\frac{d\tau}{\pi} = \quad \frac{F_0}{2}\cos\phi(s) + \frac{A(s)}{2}(k \quad m\omega^2), \tag{5.32}$$

$$\int_0^{\pi} \Gamma(d) \sin^2 \tau \frac{d\tau}{\pi} = \frac{1}{2}\left(\frac{F_0}{A(s)\omega} \sin\phi(s) \quad \frac{m\omega_0}{Q}\right), \tag{5.33}$$

where the instantaneous tip surface distance is $d \approx z_c + A\cos(\omega t \quad \phi)$. The above equations connect the experimental observables $A(s)$ and $\phi(s)$ to the interaction forces. In practical terms, s can be identified with the average position of the cantilever z_c ($z_0 \approx 0$). By using the Laplace transform and some Bessel functions, the integral equations can be transformed into differential equations that are easier to compute,

$$\sum_{j\ 0}^{\infty} \frac{(\lambda A)^{2j+1}}{2^{2j+1} j!(j+1)!} \frac{d^{2j+1}}{dz^{2j+1}} F_c(s) = \quad \frac{F_0}{2}\cos\phi + \frac{A}{2}(k \quad m\omega^2), \tag{5.34}$$

$$\sum_{j\ 0}^{\infty} \frac{A^{2j}}{2^{2j+1} j!(j+1)!} \frac{d^{2j}}{ds^{2j}} \Gamma(s) = \frac{1}{2}\left(\frac{F_0}{A\omega}\sin\phi \quad \frac{m\omega_0}{Q}\right) \tag{5.35}$$

with the boundary conditions

$$\frac{d^j}{ds^j} F_c(s) = \frac{d^j}{ds^j}\Gamma(s) = 0 \quad \text{for} \quad s \to \infty. \tag{5.36}$$

The accuracy in the determination of F_{ts} will depend on the number of terms used in the above equations (Figure 5.7). For small amplitudes with respect to the charac teristic lengths of the interaction force, say below 1 nm, the first term ($j = 0$) could be enough to reconstruct the force,

$$F_c(s) = \int_s^{\infty} \left[\frac{F_0}{A(s)}\cos\phi(s) \quad (k \quad m\omega^2)\right] ds \tag{5.37}$$

and

$$\Gamma(s) = \frac{F_0}{A(s)\omega}\sin\phi(s) \quad \frac{m\omega_0}{Q}. \tag{5.38}$$

5.7.2 Hölscher Method

This method assumes a sinusoidal solution with $z_0 \approx 0$ (Equation 4.47). The tip surface forces are formally expanded into a Fourier series (see Equation 4.18), but only the terms oscillating with ωt are retained [95, 96]. The expansion also neglects the constant term that reflects the average force over a period ($b_0 = 0$). The substi tution of the force expansion into Equation 4.2 generates two coupled equations,

$$\frac{\omega_0^2 \quad \omega^2}{\omega_0^2} = I_+(s) + \frac{(F_0/k)}{A(s)}\cos\phi(s), \tag{5.39}$$

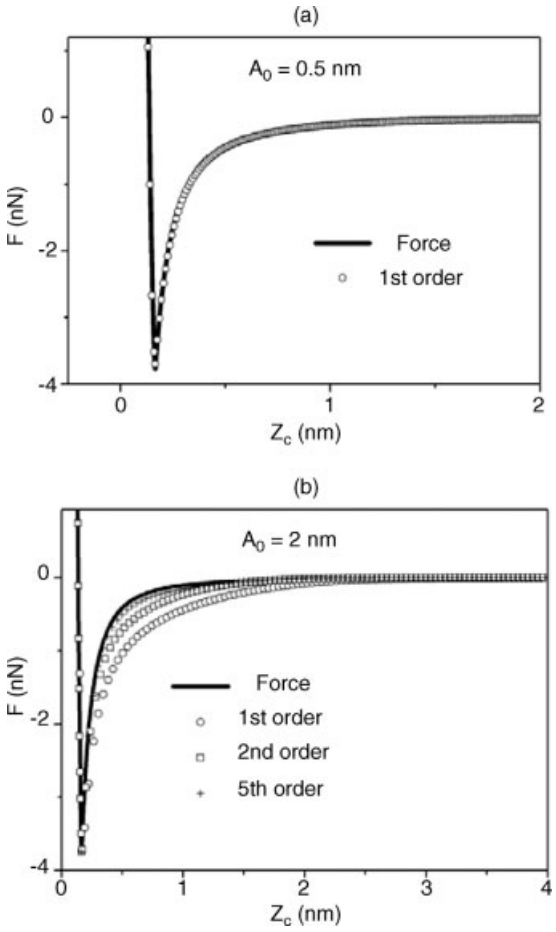

Figure 5.7 Force reconstruction with the Lee Jhe method. For small A_0 values (a) the first term is enough to reconstruct the force; however, for large A_0 the method requires the use of several terms. The input force has been obtained by using the DMT model with R 10 nm, Q 150, k 40 N/m, E_{eff} 150 GPa, and γ 30 mJ/m^2.

$$\frac{\omega}{Q\omega_0} = I_-(s) \quad \frac{(F_0/k)}{A(s)} \sin\phi(s), \tag{5.40}$$

where the integrals I_- and I_+ are defined as

$$\begin{aligned} I_+(s) &= \frac{2\omega}{kA}\int_0^T F_{\text{ts}}[S(t)]\cos(\omega t+\phi)\mathrm{d}t \\ &= \frac{1}{\pi kA^2}\int_{s-A}^{s+A}[F_{\text{ts}}(\downarrow)+F_{\text{ts}}(\uparrow)]\frac{S \quad s}{\sqrt{A^2 \quad (S \quad s)^2}}\mathrm{d}S, \end{aligned} \tag{5.41}$$

$$I_{-}(s) = \frac{2\omega}{kA}\int_0^T F_{ts}[S(t)]\sin(\omega t + \phi)dt = \frac{1}{\pi k A^2}\int_{s-A}^{s+A}[F_{ts}(\downarrow) \quad F_{ts}(\uparrow)]dS = \quad \frac{E_{ts}}{\pi k A^2}. \tag{5.42}$$

In the above equations, the symbol $S(t)$ with $S(t) = z_c + A\cos(\omega t \quad \phi)$ is used to define the instantaneous tip surface distance. In this way, any confusion with the symbol used for differential of a variable d is avoided. The integral I_+ is a weighted average of the sum of the tip surface forces during approach ($F_{\downarrow}$) and retraction ($F_{\uparrow}$). The integral I_- is connected to the energy dissipated by the tip surface forces. For a given z_c, F_0, and ω, the closest tip surface separation is defined as d_0. Then, by neglecting the contribution of the tip surface forces in the $d_0 + A$ and $d_0 + 2A$ range, we deduce

$$I_{+}(s) \approx \quad \frac{\sqrt{2}}{\pi k A^{3/2}}\int_{d_0}^{d_0+2A}\frac{F_{ts}(S)}{\sqrt{S \quad d_0}}dS, \tag{5.43}$$

which when substituted into Equation 5.39 gives an expression for the force as a function of the dependencies of the amplitude and the phase shift with the distance.

$$F_{ts}(s) \approx \quad \frac{\partial}{\partial d_0}\int_{d_0}^{d_0+2A}\frac{\varkappa(x)}{\sqrt{x \quad d_0}}dx, \tag{5.44}$$

$$\varkappa(x) = \frac{kA(x)^{3/2}}{\sqrt{2}}\left[\frac{(F_0/k)\cos\phi(x)}{A(x)} \quad \frac{\omega_0^2 \quad \omega^2}{\omega_0^2}\right], \tag{5.45}$$

where x is the distance included in the $[d_0, d_0 + 2A]$ interval. The method requires the experimental determination of $\varkappa(x) = \varkappa(s) \approx \varkappa(z_c)$. The approximations used to derive Equation 5.44, in particular, to neglect the tip surface force in the interval $[d_0 + A, d_0 + 2A]$, imply that Hölscher method should be applied for large amplitude values.

5.8 Time-Resolved Force

The time dependence of the force can be obtained by either indirect methods or direct experimental measurements. Indirect methods combine experimental measure ments of the amplitude distance and the phase distance curves and the use of a theoretical model to reconstruct the force. Direct methods require it to determine the instantaneous tip deflection with respect to a reference surface and the calibration of the force constant. Then, by applying the Hooke's law the force is deduced. Unfortunately, direct methods require special cantilever probes that incorporate optical diffraction gratings so they cannot be easily implemented in standard AM AFM instruments.

5.8.1
Acceleration

Kowalewski and coworkers proposed a method to obtain the instantaneous tip sur face forces based on the measurement of the tip's acceleration [104]. By rewriting Equation 4.2, the cantilever acceleration can be expressed as

$$\ddot{z} = \frac{1}{m}[F_{\text{ts}} \quad b\dot{z} \quad kz + \ldots]. \tag{5.46}$$

Thus, in a period the contribution to the acceleration due to the fast changing tip surface force may be distinguished from the other and slowly varying terms in the second derivative of the cantilever deflection signal. Although this approach is conceptually simple, it is rather challenging to implement it experimentally because any noise in the deflection signal is amplified in the second derivative.

5.8.2
Higher Harmonics Method

Stark *et al.* have proposed an elegant method to obtain the time resolved forces [105]. Their key insight came from the observation that a nonlinear tip surface force generates higher harmonics of the fundamental excitation. Thus, the tip surface force is encoded in the frequency spectra of the tip motion. To decode the information about the time varying force, they had to apply systems and control theory methods. The method can be divided into two steps. The first step requires it to express the cantilever trajectory in the frequency domain. The second step implies to perform the inverse Fourier of the cantilever trajectory divided by its transfer function. The method proposed by Stark *et al.* was improved in terms of signal to noise ratio by using the torsional harmonic cantilevers developed by Sahin *et al.* [106].

In Sahin's version of the higher harmonics method [106, 107], the linear operator representing the cantilever G relates the three dimensional cantilever displacement $\Psi(x, y, t)$ to the total force $F_{\text{exc}} + F_{\text{ts}}$ by

$$\Psi(x, y, t) = G(F_{\text{exc}} + F_{\text{ts}}). \tag{5.47}$$

The signal detected in the photodiode $\boldsymbol{s}$ can be considered a vector with vertical and lateral components s_z and s_y. These components are related to the cantilever displacement by $s_z = C_z\Psi(x, t)$ and $S_y = C_y\Psi(x, y, t)$. The photodetector signal is proportional to the slope of the cantilever, and $C_x = \partial/\partial x$ and $C_y = \partial/\partial y$ are evaluated at the location of the spot. Then, the relationship between the detector signals and the forces on the cantilever can be written as

$$s = CG(F_{\text{exc}} + F_{\text{ts}}). \tag{5.48}$$

The matrices G and C can be separated into flexural and torsional components,

$$\boldsymbol{s}_x = C_x G_x(F_{\text{exc}} + F_{\text{ts}}), \tag{5.49}$$

$$\boldsymbol{s}_y = C_y G_y F_{\text{ts}}, \tag{5.50}$$

$$F_{ts}(m) = \frac{1}{N}\sum_{j\ 1}^{N} H_y^{-1}(\omega_j) S_y(\omega_j) e^{i\omega_j(m-1)} \tag{5.51}$$

with

$$H_y(\omega) = c_{opt}\frac{\omega_{tor}^2/k_l}{\omega_{tor}^2 \quad \omega^2 + i\omega\omega_{tor}/Q_{tor}}, \tag{5.52}$$

where the subscript tor refers to the torsional resonance parameters, and c_{opt} is the scalar factor that relates the torsion of the cantilever to its bending angle.

Figure 5.8 shows the trace of the flexural and torsional signals (a) as a function of time. The flexural signal has a sinusoidal shape at the excitation frequency with the

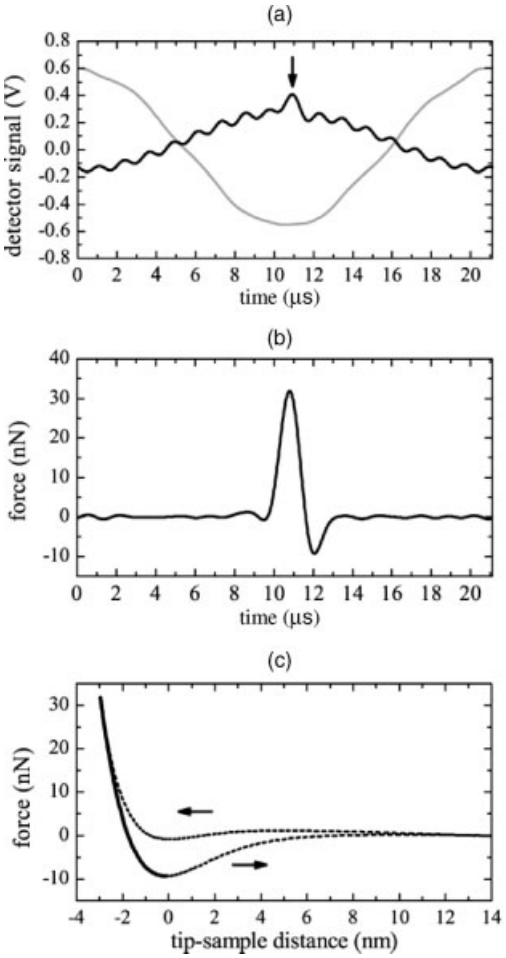

Figure 5.8 Reconstruction of the tip surface force. (a) shows the flexural (black) and torsional (gray) signals of a torsional harmonic cantilever on graphite; (b) shows the time resolved force; and (c) shows the force dependence on the tip surface distance. The arrows indicate the direction of motion. Adapted from Ref. [106].

presence of some minor distortions due to the higher harmonic contributions. On the other hand, the torsional signal shows a slowly decaying oscillation with a frequency close to the first torsional resonant frequency. Figure 5.8c shows the time resolved force obtained using the torsional signal in (a).

5.8.3 Direct Time-Resolved Force Measurements

Direct force measurements in amplitude modulation AFM are performed by measuring the tip deflection with respect to a reference surface that oscillates with the tip. That deflection is converted into a force by using the Hooke's law.

The first direct force measurement of the force exerted on the sample surface while operating an AM AFM gave average values. The average force was determined by measuring the deflection over a period. This was accomplished by replacing the sample with a piezoresistive cantilever with its own deflection detection system [108, 109].

The development of sophisticated sensors incorporating a diffraction based optical interferometer has enabled instantaneous measurement of the force. The actual procedure depends on the experimental setup [110 113], but the general principle is as follows. The micromachined sensor is made of two major elements, one with a high bandwidth response that also contains the tip and the other with lower bandwidth response. Both elements are driven by the same external force and move in unison. However, in the presence of a surface, the higher bandwidth element responds to the fast varying tip surface forces while the lower bandwidth element cannot follow these changes. Thus, the optical system can detect a difference in the relative position between these elements. This difference multiplied by the force constant gives the instantaneous value of the force.

6
Amplitude Modulation AFM in Liquid

6.1
Introduction

Operating an amplitude modulation AFM in liquid represents one of the most challenging and interesting applications of the instrument. The interest stems from its applications to study *in situ* nanoscale phenomena involving, for example, bimolecular interactions or phase transitions in nanostructured polymeric fluids. However, the technique is harder to master in liquid than in air. Instrumental details such as the design of the fluid cell or the excitation method are critical to properly tune the cantilever resonances. On the other hand, the tip surface forces are dominated by electrostatic and confinement interactions. This adds a level of conceptual difficulty that is rarely found in air applications.

6.2
Qualitative Aspects of the Cantilever Dynamics in Liquid

It is instructive to perform a comparison between the resonance curves of a cantilever in air and in liquid to become familiar with some of the remarkable features of dynamic AFM operation in liquid. The dynamics in liquid is influenced by two additional factors, the interaction of the cantilever with the liquid and a newly created interaction in the sample liquid tip interface. Thus, while describing dynamic AFM in liquid it is convenient to consider two situations, far and close to the sample surface.

6.2.1
Dynamics Far from the Surface

The cantilever dynamics shows a strong dependence on the medium be it a liquid, air, or vacuum. The strongest qualitative changes are observed when the same cantilever is vibrated in a relatively high quality factor environment such as air ($Q \sim 50$ 500) and, in a low quality factor environment, such as aqueous solutions ($Q \sim 1$ 5) [1, 2].

Amplitude Modulation Atomic Force Microscopy. Ricardo García

ISBN: 978-3-527-40834-4

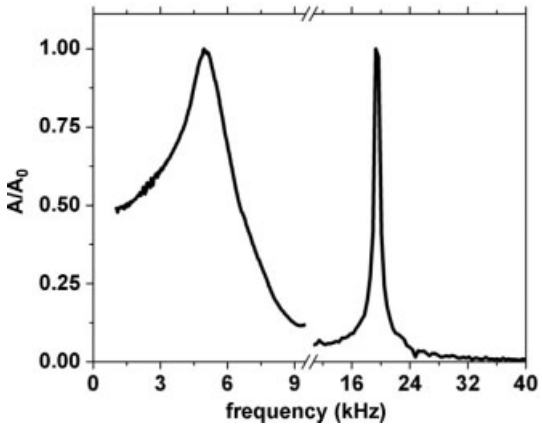

Figure 6.1 Resonance curves of rectangular cantilever in air and water (first mode). Immersion in water broadens the resonance curve (Q factor decreases) and reduces the resonant frequency.

A comparison between the resonance curves of the same cantilever taken in air and water shows two major changes (Figure 6.1). In water, the resonance curve is wider, that is, $Q_{water} < Q_{air}$, and at the same time the resonant frequency is shifted to lower frequencies. The frequency of the first resonance for a rectangular cantilever is reduced by a factor of 3 5 with respect to air (indicative rule).

The reduction in the resonant frequencies in liquid is due to the existence of a boundary layer of the fluid surrounding the cantilever. When the cantilever vibrates, it also has to displace this layer. This is an inertial effect that is commonly described in point mass models by introducing an effective mass for the cantilever. Because the density of a liquid is higher than that of the air, the effective mass is higher in liquid. In addition, the viscosity of the liquid gives rise to the hydrodynamic damping of the cantilever oscillation. The viscous components of the hydrodynamic loading are responsible for the reduction of the quality factor.

6.2.2
Dynamics Close to the Surface

When the tip of a vibrating cantilever is approached toward a solid surface in liquid, the resonance peaks of the different eigenmodes broaden and shift to lower frequency values. The rate of change of the quality factor and the resonant frequency with the gap distance varies with the eigenmode and with tilt angle of the cantilever with respect to the surface (Figures 6.2 and 6.3). This is a general behavior of cantilever beams. In the AFM context, the above behavior was first reported by Günther *et al.* [3]. More recently, Raman and coworkers have described it in detail by using finite element simulations [4].

Semianalytical models [5 9] and finite element simulations [4] have established that the dissipative effects in the fluid increase as the cantilever surface gap distance decreases. This can be explained by realizing that as the gap distance is decreased, the

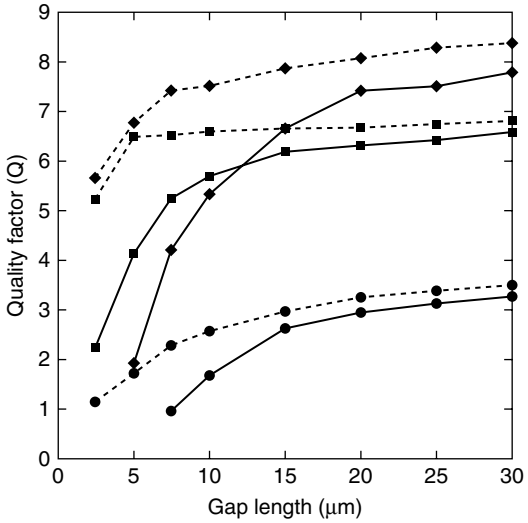

Figure 6.2 Dependence of the quality factor on the gap distance between a rectangular cantilever and a solid surface. Circles are for the first flexural mode, diamonds are for the second mode, and squares are for the first torsion mode. Solid lines indicate that the cantilever and the surface are parallel to each other. Dashed lines indicate that the cantilever is tilted 11° with respect to the sample surface. Adapted from Ref. [4].

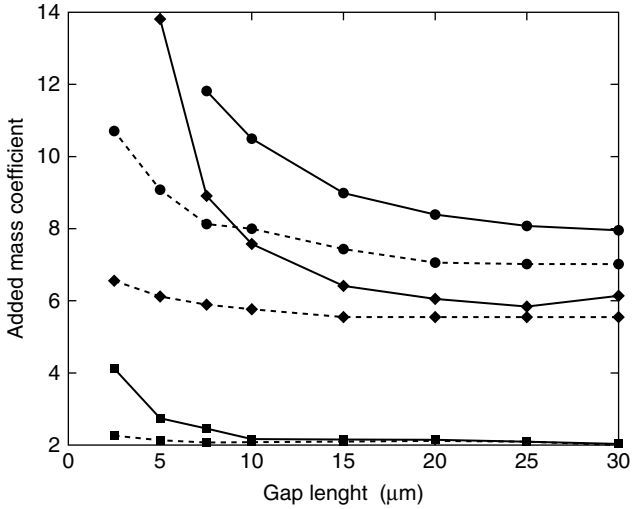

Figure 6.3 Dependence of the added mass coefficients on the gap distance between the cantilever and the sample surface in water. Circles are for the first flexural mode, diamonds are for the second mode, and squares are for the first torsion mode. Solid lines are for a cantilever surface parallel geometry. Dashed lines are for a cantilever tilted 11° with respect to the sample surface. Simulations are for a rectangular cantilever. Adapted from Ref. [4].

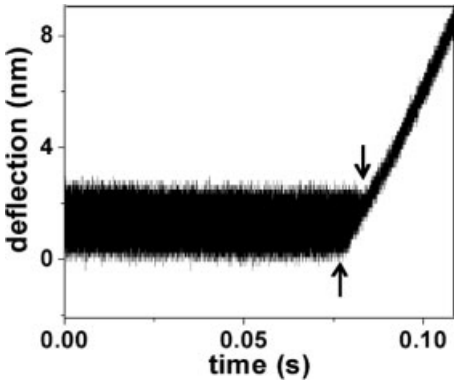

Figure 6.4 Dependence of the cantilever deflection on the tip sample distance in water. The reduction of the oscillation is asymmetric (region between arrows). The tip surface forces affect more strongly the bottom part of the oscillation than its top part. Experiment performed on a mica surface with a triangular cantilever.

boundary layers formed on both the cantilever and the sample surface occupy a greater fraction of the gap. This effect increases the fluid shear in the gap, which in turn, increases the damping. However, in a typical experiment it remains a good approximation to neglect Q and resonant frequency changes during the tip's oscillation. The typical amplitudes in experiments performed in liquid are in the sub 15 nm range. These values are considerably smaller than the distances where the hydrodynamic effect takes place (cantilever's body). The body of the cantilever is situated 5 20 μm above the sample surface. That distance is defined by the length of the tip, the length of the cantilever, and the tilt angle.

Amplitude modulation AFM operation in liquid introduces another relevant and surprising result. When the tip interacts with a solid surface, the cantilever's deflection is no longer symmetric (Figures 6.4 and 6.5). The distortion of the oscillation is more evident on the bottom than on the top side. This was one of the first experimental results brought by amplitude modulation AFM in liquid [10, 11]. It implies that the cantilever oscillation can no longer be approximated by a sinusoid wave form. This introduces another relevant difference with respect to operating in air or vacuum. In air or vacuum is a fairly good approximation to neglect the contribution of higher eigenmodes of the excitation frequency to the total motion. This approximation is no longer valid in liquid because the low Q enhances the contribution of higher harmonics and/or modes [12 14].

6.3
Interaction Forces in Liquid

The electrical double layer and the solvation interactions at the tip surface interface play a distinctive role in liquid. It is useful to remember that these forces have

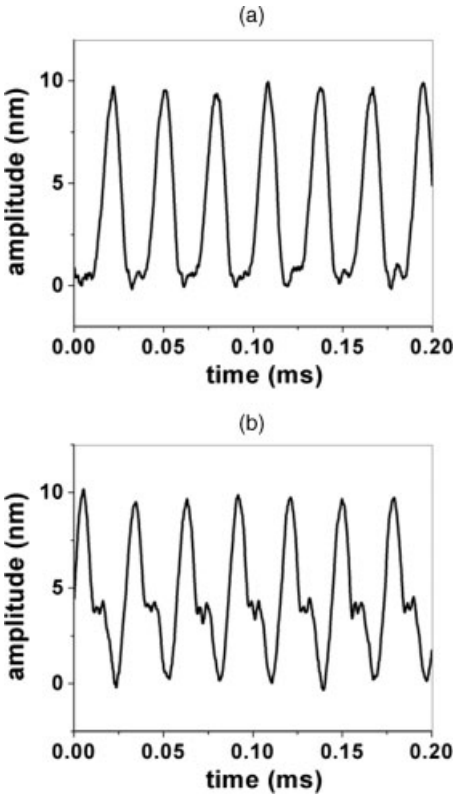

Figure 6.5 Steady state cantilever deflection in water for two values of the set point amplitude. The anharmonic component is more noticeable in the bottom part of the oscillation. By increasing the strength of the tip surface forces, the anharmonic components become more pronounced (b). Experiments performed on a mica surface with a rectangular cantilever ($k \approx 5$ N/m, A_{sp} $0.9A_0$ (a), A_{sp} $0.7A_0$ (b)).

different origins. Double layer forces have an electrostatic origin while solvation forces arise from confinement liquid film effects. On the other hand, immersion in liquid suppresses the formation of a meniscus, so capillary forces are not present. The reader may refer to Chapter 3 for a description of the relevant tip surface forces in liquid.

The relevance of controlling the electrostatic interactions to improve the spatial resolution and sensitivity of the instrument cannot be understated [15 20]. Müller, Engel, and coworkers achieved molecular resolution images of protein membranes by screening the long range electrostatic force between the tip and the membrane surface. This was achieved by changing the pH of the buffer solution [15 17].

Figure 6.6 shows a schematic representation of the tip surface forces in liquid. Thus, the force acting on the tip while imaging in fluids should be expressed as

$$F_{ts} = F_{DLVO} + F_{sv} + F_{DMT}. \tag{6.1}$$

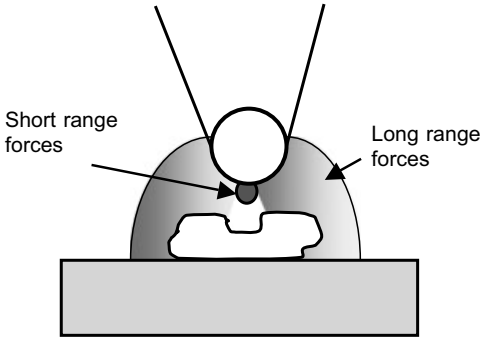

Figure 6.6 Illustration of the tip surface forces in liquid. High resolution imaging is achieved when the cantilever dynamics is dominated by the short range forces coming from a small region of the tip. This usually requires the screening of the long range repulsive forces by changing the pH of the buffer solution.

Whenever the solvation forces are negligible, the tip surface force can be calculated by

$$F_{ts} = F_{DLVO}(d) = \frac{4\pi R}{\varepsilon\varepsilon_0}\sigma_t\sigma_s\lambda_D \exp(-d/\lambda_D) - \frac{HR}{6d^2} \quad \text{for} \quad d > a_0, \tag{6.2}$$

$$F_{ts} = \frac{4}{3}E_{eff}\sqrt{R}(a_0 - d)^{3/2} + F_{DLVO}(a_0) \quad \text{for} \quad d \leq a_0. \tag{6.3}$$

6.4
Some Experimental and Conceptual Considerations

The fluid cell and the cantilever excitation method are some of the elements that shape the performance of a microscope in liquid. The two most common excitation methods, the mechanical (acoustic) and the magnetic, were introduced in Chapter 2. Figure 6.7 shows a scheme of the main elements of a fluid cell compatible with mechanical and magnetic excitation. In liquid, the frequency response of the cantilever depends on the excitation method at practical and conceptual levels [2, 21, 22]. A mechanically excited cantilever usually shows a complicated frequency response that contains many peaks (Figure 6.8) [23, 24]. The majority of these peaks do not reflect the mechanical resonances of the cantilever. They are associated with the resonances of the surrounding fluid and other parts of the fluid cell [23–28]. Some fluid cell designs such as the so called open cell might suppress some of the spurious resonances observed in the "closed" acoustic fluid cell [29]. On the other hand, a magnetically driven cantilever generates canonical resonance curves in liquids [30, 31], although this method requires the use of cantilevers coated with a thin magnetic film. The lifetime of magnetic coated cantilevers in liquid is usually shorter than that of the uncoated cantilevers.

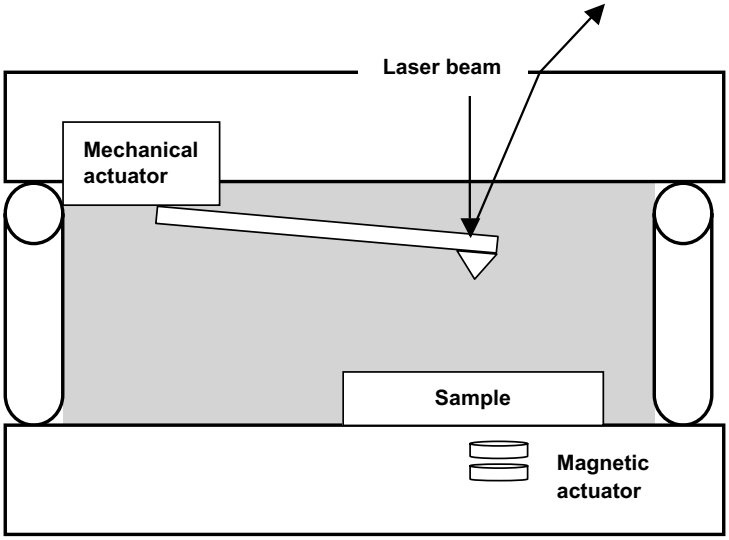

Figure 6.7 Scheme of a liquid cell. The scheme includes elements of magnetic and acoustic excitation methods.

Yet, at a fundamental level, the equation of motion also depends on the method chosen to excite the cantilever. In general, the tip displacement with respect to the sample surface does not coincide with the tip's deflection (relative tip motion to the base motion). In experiments performed in air, this difference is negligible; however,

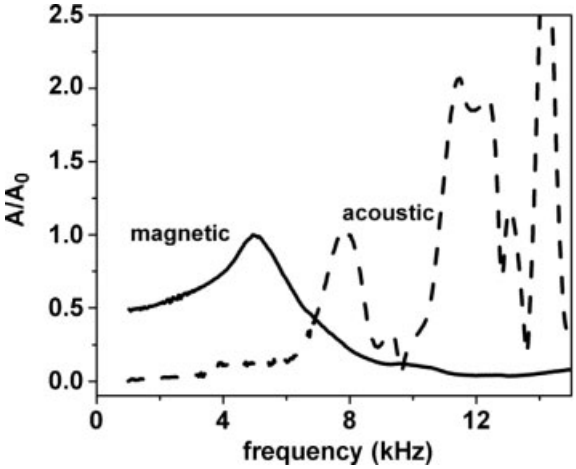

Figure 6.8 Influence of the excitation method on the shape of the resonance curve in liquid. Magnetic and acoustic resonance curves of a rectangular cantilever in water. The resonance curve obtained by using the magnetic excitation method avoids the presence of spurious fluid borne resonances.

this is no longer the case in liquid. As a consequence, the resonance curves depend on the way the cantilever is driven [2, 21, 27].

The low quality factor in liquid has been a point of concern for many experimentalists. This has led to several proposals to enhance the amplitude response of the cantilever in liquid (Section 5.2). However, molecular resolution images of different surfaces have been obtained without implementing any of the Q control methods. This somehow undermines the motivation to enhance the Q in liquid.

6.5 Theoretical Descriptions of Dynamic AFM in Liquid

Predicting the cantilever dynamics in liquid and in the proximity of a surface remains an open issue in amplitude modulation AFM. As a consequence, it is the focus of an emerging theoretical activity [32–41]. Four main theoretical approaches are being applied to describe amplitude modulation AFM in liquid: point mass models, semianalytical methods, finite element fluid–structure models, and one dimensional continuous models. A full understanding of this section requires some familiarity with the concepts and equations presented in Chapter 4.

6.5.1 Analytical Descriptions: Far from the Surface

Point mass models provide insight into the cantilever dynamics and, in some cases, do render numerical simulations and analytical approximations that are in good qualitative and even semiquantitative agreement with AFM experiments in liquid [2, 21, 26, 34–36]. Specifically, point mass models are suitable for analytically describing the dependence of the amplitude on the frequency when the tip is far from the sample surface, that is, in the absence of tip–surface simulations [2, 26, 33].

It has already been mentioned that in liquids the tip displacement does not coincide with the tip deflection (experimental observable); consequently, the equation of motion depends on the excitation method. The deflection of a cantilever–tip system driven by a force applied at the tip end in liquid (magnetically driven cantilever) and far from the sample surface can be described by [2]

$$\ddot{z}(t) + \frac{b}{m_{\text{eff}}}\dot{z}(t) + \frac{k}{m_{\text{eff}}}z(t) = \frac{F_0}{m_{\text{eff}}}\cos \omega t. \tag{6.4}$$

The above equation requires it to redefine the effective mass m_{eff} and the damping coefficient of the cantilever b. Here, the effective mass includes the cantilever mass in air m and the fluid mass in contact with the cantilever (added mass) [2, 42]. It can be calculated by

$$m_{\text{eff}} = 0.24m + 0.144\rho(WL)^{3/2} = \frac{k}{\omega_0^2}. \tag{6.5}$$

The density of the fluid is ϱ_f, and the coefficient b is calculated by using the string of spheres model [43],

$$b = \frac{L}{W}\left(\frac{3}{4}\pi W^2\sqrt{2\eta\varrho_f\omega} + 3\pi W\eta\right), \tag{6.6}$$

where L is the cantilever length, W is the cantilever width, m is the cantilever mass, and η is the fluid viscosity; ω_0 is the resonant angular frequency in the absence of any damping. Then, the effective quality factor is

$$Q = \frac{m_{\text{eff}}\omega_0}{b}. \tag{6.7}$$

The dependence of the amplitude on the excitation frequency has the well known Lorentzian expression,

$$A(\omega) = \frac{(F_0/k)\omega_0^2}{\sqrt{(\omega_0^2 \quad \omega^2)^2 + (\omega\omega_0/Q)^2}}. \tag{6.8}$$

For small excitation frequencies, A tends to be F_0/k, while for frequencies well above ω_0 the amplitude vanishes.

On the other hand, the motion of a cantilever tip system driven by a piezo actuator can be described by

$$\ddot{S}(t) + \frac{b}{m_{\text{eff}}}\dot{S}(t) + \omega_0^2 z(t) = 0, \tag{6.9}$$

where $z(t)$ and $S(t)$ are, respectively, the cantilever tip deflection and the cantile ver tip displacement as described in Figure 2.8. Because the optical beam deflection method directly measures the cantilever slope, the above equation has to be rewritten in terms of the observable,

$$z(t) = S(t) \quad A_d\cos\omega t = z_0 + A_z\cos\omega t, \tag{6.10}$$

where A_d is the amplitude of the base displacement, and then the amplitude is given by

$$A_z(\omega) = \frac{F_0/k\sqrt{\omega^4 + (\omega\omega_0/Q)^2}}{\sqrt{(\omega_0^2 \quad \omega^2)^2 + (\omega\omega_0/Q)^2}}. \tag{6.11}$$

Equation 6.11 shows that for $\omega \to 0$ the amplitude goes to zero ($A_z \to 0$). In the other limit, $\omega \to \infty$, the amplitude goes to $A_z = F_0/k$. The above behavior is in contrast to the result found previously (Equation 6.8 that gave $A = F_0/k$ ($\omega \to 0$) and $A = 0$ ($\omega \to \infty$). At resonance ($\omega = \omega_0$), Equation 6.11 gives

$$A_z = \frac{QF_0}{k}\left(1 + \frac{1}{Q^2}\right)^{1/2}, \tag{6.12}$$

while for the magnetic excitation (Equation 6.8), we obtain the well known result $A = \frac{QF_0}{k}$.

The resonance curves given by the above expressions are shown in Figure 6.9 ($Q = 2$). Notice that the influence of the driven method decreases for cantilevers with high force constants; in particular, the difference in the frequency response is very small for cantilevers with force constants above 10 N/m.

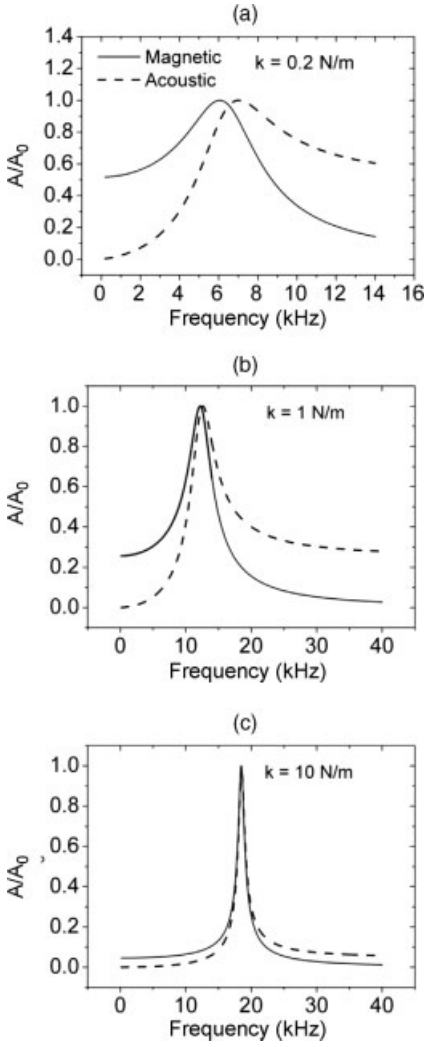

Figure 6.9 Acoustic and magnetic resonance curves (simulations) for different cantilevers in water (a) k 0.2 N/m, (b) k 1 N/m, and (c) k 10 N/m. The curves have been obtained for Q 2. Adapted from Ref. [2].

6.5.2
Analytical and Numerical Descriptions in the Presence of Tip Surface Forces

Point mass model simulations are also helpful in providing insight into the cantilever dynamics in the presence of tip surface forces. For instance, the asymmetric character of the tip oscillation observed in the experiments has been simulated by Legleiter and Kowalewski by introducing a tip surface force given by Equations 6.2 and 6.3 [35]. The asymmetry is due to the generation of higher harmonics (see Chapter 9).

De Beer and Mugele have proposed an analytical expression to describe the dependence of the amplitude on the tip surface effective parameters [36, 37]. By assuming that the tip surface force can be linearized as

$$F_{ts} = F_{ts}(z_c) \quad k_{ts}(z_c)(d \quad z_c) \quad \gamma_{ts}\dot{z}, \tag{6.13}$$

we deduce

$$A = \frac{A_d\sqrt{(m_{eff}\omega^2 \quad k_{ts})^2 + \omega^2((m_{eff}\omega_0/Q) + \gamma_{ts})^2}}{\sqrt{(k + k_{ts} \quad m_{eff}\omega^2)^2 + \omega^2((m_{eff}\omega_0/Q) + \gamma_{ts})^2}}. \tag{6.14}$$

The above expression could be used when the cantilever has very small amplitudes, say $A \leq 0.5$ nm. For a more general case, different experimental and theoretical results underline the influence of the cantilever higher modes in liquids [39, 40] and the existence of several tip surface impacts per cycle. These results place some limitations on the generality of results based on the use of a point mass model.

6.5.3
Semianalytical Models

Sader and Green have pioneered the development of analytical and/or semianalytical models to describe the dynamics of cantilever beams in viscous fluids [5 8]. Broadly speaking, these models aim to derive the resonant frequency and quality factor of the cantilever from the knowledge of the chemical composition and geometry of the beam and the viscosity and density of the fluid. Sader described the case of a cantilever vibrating very far from the sample surface (unbounded cantilever) [5]. In later contributions, Green and Sader described the case where the cantilever is in the proximity of a sample surface [6, 8]. The theory combines Navier Stokes and Euler Bernoulli equations. The Navier Stokes equation enables to determine the damping and inertial effects of the cantilever in the fluid, while the Euler Bernoulli equation provides the dynamics.

Let us consider a rectangular cantilever beam of a uniform cross section that vibrates in a viscous fluid. The theory has some relevant approximations. It assumes that the width W of the cantilever is uniform and much more smaller than its length L, $W \ll L$. It also considers the fluid as incompressible. Furthermore, internal damping in the cantilever is negligible with respect to the damping in the fluid. Finally, it

assumes that fluid flow around the cantilever beam can be replaced by the flow around a beam of infinite length. In mathematical terms, the velocity field in the fluid varies much faster over the width than it does over its length [6].

Following Sader, the Fourier transform of the Euler Bernoulli equation is

$$\frac{EI}{L^4}\frac{\mathrm{d}^4\hat{W}(\hat{x}|\omega)}{\mathrm{d}\hat{x}^4} \quad \varrho Wh\omega^2\hat{W}(\hat{x}|\omega) = \hat{F}_{\mathrm{hyd}}(\hat{x}|\omega) + \hat{F}_{\mathrm{exc}}(\hat{x}|\omega), \tag{6.15}$$

where

$$\hat{Y} = \int_{-\infty}^{\infty} y(t)\exp(\quad i\omega t)\mathrm{d}t \tag{6.16}$$

for any function of time $y(t)$ and $\bar{x} = x/L$.

The hydrodynamic load force is determined by solving the Navier Stokes equation for the fluid surrounding the cantilever,

$$\varrho_{\mathrm{f}}\frac{\partial\vec{u}}{\partial t} = \quad \nabla P(x) + \eta\nabla^2\vec{u}, \tag{6.17}$$

where $P(x)$ is the pressure exerted by the fluid on the cantilever; ϱ_{f} and η are the fluid density and viscosity, respectively; and $\vec{u}(x,t) = \vec{u}(x)\mathrm{e}^{i\omega t}$ is the fluid velocity. Then, the Fourier transform of the hydrodynamic load force on the cantilever takes the form of

$$\hat{F}_{\mathrm{hyd}}(\hat{x}|\omega) = \frac{\pi}{4}\varrho_{\mathrm{f}}\omega^2W^2\Gamma(\omega)\hat{W}(\hat{x}|\omega), \tag{6.18}$$

where a dimensionless function known as the hydrodynamic function $\Gamma(\omega)$ has been introduced. The hydrodynamic function carries the dependence of the damping and inertial effects on the cantilever surface separation.

$$\Gamma(\omega) = \Gamma_{\mathrm{r}}(\omega) + i\Gamma_{\mathrm{i}}(\omega) \tag{6.19}$$

The asymptotic limits of the hydrodynamic function can be expressed as a function of the Reynolds number $Re = \varrho_{\mathrm{f}}\omega W^2/(4\eta)$:

$$\Gamma(\omega) = 1_{\mathrm{i}} \quad \text{for} \quad Re \to \infty, \tag{6.20}$$

$$\Gamma(\omega) = \frac{4i}{Re\ln(\quad i\sqrt{i\mathrm{Re}})} \quad \text{for} \quad \mathrm{Re} \to 0. \tag{6.21}$$

For small dissipative effects in the fluid, the above equations with convenient mathematical transformations enable to deduce the resonant frequency and quality factor of the different cantilever modes,

$$\omega_n = \omega_{0,n}\left[1 + \frac{\pi\varrho_{\mathrm{f}}W^2}{4\mu}\Gamma_{\mathrm{r}}(\omega_n)\right]^{-1/2} \tag{6.22}$$

and

$$Q_n = \frac{(4\varrho h/\pi\varrho_{\mathrm{f}}W) + \Gamma_{\mathrm{r}}(\omega_n)}{\Gamma_{\mathrm{i}}(\omega_n)}. \tag{6.23}$$

In particular, for the frequency dependence of an inviscid fluid is obtained the known expression of

$$\omega_n = \omega_{0,n}\left[1 + \frac{\pi \varrho_f W}{4\varrho h}\right]^{-1/2}. \tag{6.24}$$

Once the hydrodynamic function has been computed, it can be applied to deduce the dynamic response of the cantilever beam. The most significant result of the theory is that dissipative effect is enhanced by the proximity of the sample surface. This effect becomes noticeable for cantilever surface separations smaller than the cantilever width. Another relevant conclusion is that the shift in the peak frequency is driven by the increase in dissipative effects as the cantilever approaches the surface, and not by the variation in inertial loading. This result does not affect the fact that the frequency and Q changes observed when the cantilever changes the medium, that is, from air to liquid, have both dissipative and inertial effects.

6.5.4
Finite Element Simulations

Three dimensional finite element simulations of cantilever in fluids provide a way both to test the above models and to visualize the regions of the cantilever that dominate the damping. These simulations also are useful to design cantilever geometries for optimum performance in liquids [4, 12, 44, 45]. Raman and coworkers have found that in an infinite medium (cantilever far from the sample surface) the main dissipation mechanism arises from the localized fluid shear close to the edges of the cantilever [4]. When the cantilever gets closer to the sample surface, dissipation arises due to a combination of squeeze film effects and localized shear close to the edges.

In the above simulations, the fluid is modeled as an incompressible, viscous fluid (Navier Stokes elements) and the cantilever is modeled using the equations of three dimensional linear elasticity. The simulations require the use of special fluid structure interaction codes since the motion of the solid and fluid are tightly coupled. The velocity of the fluid is made to match that of the cantilever on the cantilever surface and that of the substrate (zero velocity) on the substrate. These are called no slip boundary conditions. A large, but finite, hemispherical boundary completely encloses within it the cantilever, the substrate, and the fluid. At this boundary, the velocity and the pressure fields of the Navier Stokes elements are matched with the far field Green's functions of an inviscid fluid ensuring that normal waves generated by cantilever motion do not reflect back but rather propagate across this boundary to infinity. Careful meshing and time stepping analysis needs to be performed to ensure converged results. Once such a model is set up, it can be used to compute the damping and the resonant frequencies of the different eigenmodes as a function of cantilever substrate gap as follows. A transient fluid structure calculation is per formed where the cantilever is given initial velocity conditions in the shape of an eigenmode, and then the cantilever rings down. From the ring down time series at

any point on the cantilever, it is easy to measure the natural frequency and damping of that specific eigenmode by fitting the decaying oscillatory response to that of a point mass model. By comparing the resonant frequency values in air and in liquid, the added mass factor of the liquid can be extracted. For example, in Figures 6.2 and 6.3, the Q factors and added mass factors of the fundamental, second bending, and first torsional modes are plotted as a function of distance from the substrate. Since this is a computational model, it is also possible to perform the calculation for a slightly tilted cantilever as it approaches the substrate. From Figures 6.2 and 6.3, it is clear that (a) eigenmodes are more damped and their resonant frequencies shift to lower values as the cantilever approaches the surface; (b) the tilt of the cantilever with respect to the substrate strongly influences the damping, the greater the tilt the less the damping effect of the substrate; and (c) the gap at which the substrate first influences the cantilever damping depends on the resonant frequency and mode shape. For example, the second and torsion eigenmode "feels" the presence of the substrate only when brought quite close to the substrate. This is in part due the shape of the eigenmode and the shape of the accompanying fluid fields, and also due to their higher resonant frequencies that leads to smaller boundary layer thickness.

7
Phase Imaging Atomic Force Microscopy

7.1
Introduction

Back in 1995, Virgil Elings gave an informal presentation at an international conference. He talked enthusiastically about a novel imaging method that provided images with a striking contrast. He explained that the images were obtained by plotting the phase shift variations of the cantilever oscillation while taking the tapping mode AFM image (topography). He mentioned that the process or processes responsible for the contrast were not known. Since then, phase imaging AFM has become a powerful and widely used tool to map compositional variations on heterogeneous surfaces. The physical basis of phase imaging in air is nowadays established. A similar understanding of phase imaging in liquids is yet to be reached.

7.2
Phase Imaging Atomic Force Microscopy

Phase imaging AFM is an addition to amplitude modulation AFM that provides maps of compositional and/or energy dissipation variations of heterogeneous materials with nanoscale spatial resolution. A phase contrast image is obtained by plotting the phase shift of the oscillation while tracking the surface topography at a fixed amplitude [1 4]. Phase images are simultaneously acquired with topography.

The phase shift ϕ is measured with respect to the mechanical excitation of the cantilever. Phase shifts are relative measurements; thus, they require a reference system. This is provided by the harmonic oscillator model (Chapter 4). Figure 7.1 shows the dependence of the amplitude and the phase shift of a forced harmonic oscillator with damping with respect to the excitation frequency. At $\omega = \omega_0$, the phase lag of a forced harmonic oscillator with respect to the driving force is 90°.

The amplitude of the cantilever oscillation depends on the topography and the composition of the sample surface [5 8]. On the other hand, the phase shift signal depends on the energy transferred from the tip to the sample surface and on the strength of conservative interactions.

Amplitude Modulation Atomic Force Microscopy. Ricardo García

ISBN: 978-3-527-40834-4

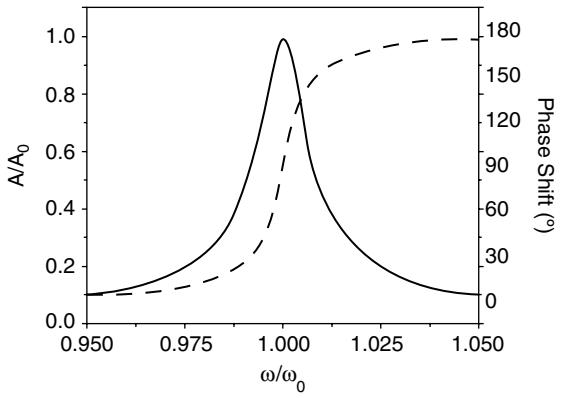

Figure 7.1 Amplitude (continuous line) and phase shift (dash line) dependencies of a forced harmonic oscillator with damping as a function of the excitation frequency (Q 100).

Figure 7.2 shows a scheme of phase imaging AFM operation. The surface is made of three different materials: a main flat substrate and two embedded regions B and Y. The dot B protrudes from the substrate baseline while the Y region is flat and shows changes only in material properties. The B region appears as a protrusion in the topography (height), while the Y region does not provide a height difference with

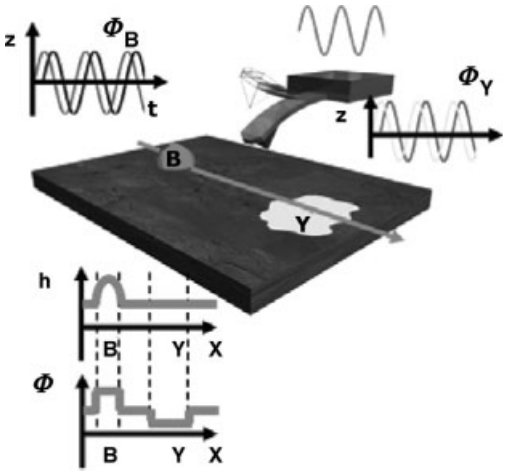

Figure 7.2 Scheme of phase imaging AFM operation. The cantilever oscillation depends on the topography and its composition. The image shows two different local regions on the flat substrate. The dot B is made of a different material and protrudes from the substrate baseline. The region Y is flat and shows only changes in material properties. The region B gives a signal in the topography, while the region Y does not give a height trace. However, both regions are distinguished from the substrate by recording and plotting the phase signal. Adapted from Ref. [1].

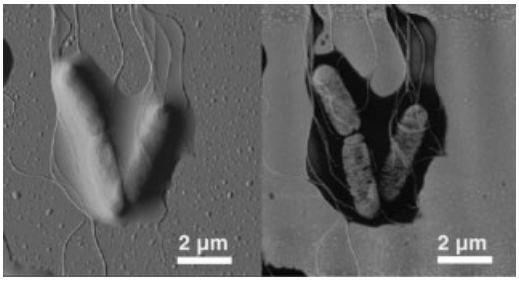

Figure 7.3 Topography (*left*) and phase image (*right*) of an aggregate of three *S. typhimurium* cells covered by an extracellular polymeric capsule. The phase image reveals both the inner structure of the cell and the continuity of the flagella. Adapted from Ref. [9].

respect to the substrate. However, both regions are clearly distinguished from the substrate by recording and plotting the phase signal.

The above considerations are experimentally illustrated by comparing the topog raphy and the phase shift contrast images of several materials. Figure 7.3 shows the topography of an aggregate of three *Salmonella typhimurium* cells covered by an extracellular polymeric capsule (left panel). The topography image does not provide any hint of the subsurface structure; however, the phase image (right panel) reveals both the inner structure of the cell and the continuity of the flagella [9]. Figure 7.4 shows the topography and phase image of a thin film of a hydrogenated diblock copolymer mesophase (poly ethyleneoxide (PEO) polybutadiene (PB)). The phase image (right panel) allows to resolve the individual spheres (12 nm in diameter). It also allows to distinguish between the crystalline (light) and the molten (dark) PEO micelles [10]. Figure 7.5 shows the topography (left panel) and phase image (right panel) of the extracellular surface purple membrane in liquid (Herruzo, E.T. and García, R. (unpublised results).). The purple membrane consists of 75% of proteins

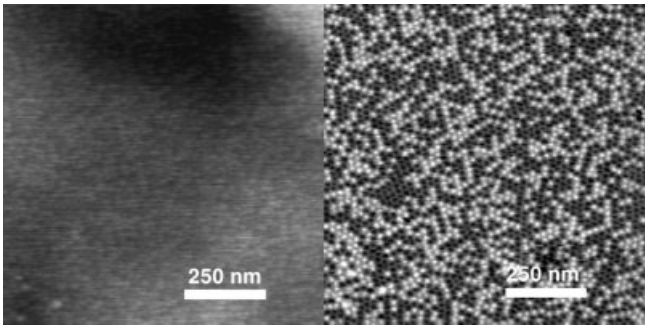

Figure 7.4 Topography (*left*) and phase image of a block copolymer mesophase. The phase image resolves the individual spheres (12 nm in diameter). It also distinguishes between the crystalline (light) and the molten (dark) poly ethyleneoxide micelles. Adapted from Ref. [10].

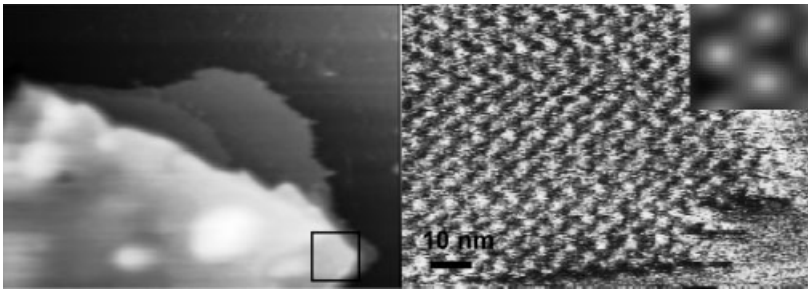

Figure 7.5 Topography (*left*) of several purple membranes. The image reveals the extracellular surface. The phase image (*right*) of the region marked in the topography shows the 2D peridiocity (raw data). The images have been obtained in buffer solution (10 mM Tris HCl, pH 8.1, 300 mM KCl). The inset shows the protein trimer unit after image processing. Adapted from Ref. (Herruzo, E.T. and García, R. (unpublised results).).

and 25% lipids. The bacteriorhodopsin ologomerizes into trimers that assemble into a bidimensional lattice (6.2 nm). The phase image of the trimer unit is shown in the inset.

Topography and phase images can be combined to produce a three dimensional characterization of the sample surface by providing simultaneous information on structure, composition, and height variations that enables us to describe the phase behavior of thin films in terms of surface reconstructions [11]. Figure 7.6 shows the complex phase structure of a triblock copolymer film made of polystyrene block

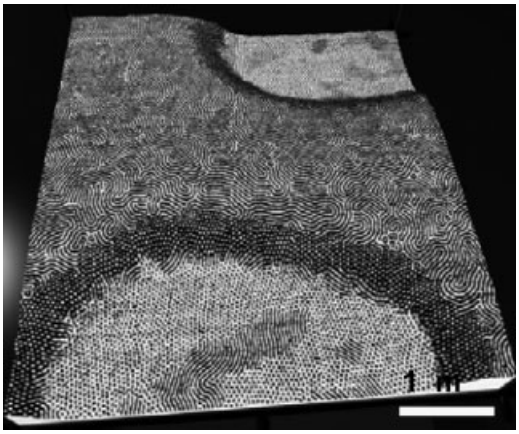

Figure 7.6 Three dimensional rendered AFM images using the height image as height field and the phase image as contrast. The images show the formation of terraces in a thin film of SBS block copolymer and the systematic change in microdomain structures along the changes in film thickness from 32 nm at the lower terrace to 57 nm at the higher terrace. Adapted from Ref. [11].

polybutadiene block polystyrene (SBS). The image shows how the microdomain structure depends on the film thickness. The upper terrace shows the polystyrene (PS) cylinders oriented parallel to the surface. In the thinner regions of the film (bottom terraces), two patterns are found. One is characterized by hexagonally ordered dark spots, indicative of a hexagonal PS lamella. In the other region, which is the thinnest, the polystyrene cylinders are oriented parallel to the surface as in the top terrace. The slope between terraces display a hexagonal pattern of bright dots, indicative of PS cylinders oriented perpendicular to the surface. In the above image, the contrast (bright versus dark regions) comes from the phase signal while the amplitude provides the height difference between terraces.

High compositional contrast together with the absence of major preparation protocols such as staining or fixation, and the ability, in a first approximation, to separate topography from composition information, explains the wide range of applications of phase imaging AFM. A large variety of materials with micrometer, submicrometer, nanoscale, or molecular features have been imaged by phase imaging AFM in different environments, and in their native state. The materials range from wood pulp fibers [12], polymeric materials [13 35], cells [9, 36, 37], proteins and protein membranes [38 43], DNA [44], liquid droplets and films [45 48], self assembled monolayers [49], molecular magnets [50] to sub 10 nm nanoscale patterns [51]. Phase measurements obtained during amplitude modulation AFM have been used to determine the energy involved in nanoscale processes [8, 52, 53]. The phase signal can also be used as a feedback parameter in an alternative imaging mode called phase modulation AFM [54 56], which is different from phase imaging AFM.

7.3
Theory of Phase Imaging AFM

The interpretation of phase images in terms of material properties and tip surface interactions is the focus of a strong scientific activity [57 87]. Several of its aspects are under debate. In what follows, the most accepted aspects of phase imaging AFM are described.

7.3.1
Phase Imaging Atomic AFM: High *Q*

Phase imaging contrast was initially explained in terms of local variations of the elastic properties of the material under examination [57, 58]. However, numerical simulations showed that the phase shift differences observed in heterogeneous surfaces could be explained only in terms of variations of the dissipated energy [2]. In fact, phase shifts depend on both conservative and nonconservative forces [66, 67].

Cleveland, Anczykowski, and collaborators [3, 61] and Tamayo and Garcia [62, 63] applied the point mass model introduced in Chapter 4 to deduce an analytical

expression that relates the observables to the energy transferred from the tip to the surface (dissipation). In Chapter 4, it was shown that the steady state oscillation of the AFM tip can be approximated by

$$z = z_0 + A\cos(\omega t \quad \phi). \tag{7.1}$$

To keep the cantilever oscillating in the presence of hydrodynamic damping and tip surface dissipative processes, the energy per cycle supplied by the external excitation $F_0 \cos \omega t$ (E_{exc}) must be equal to the energy per cycle dissipated by the tip surface forces (E_{dis}) and the hydrodynamic damping in the medium (E_{med}), that is,

$$E_{\text{exc}} = E_{\text{med}} + E_{\text{dis}}, \tag{7.2}$$

where the above quantities are defined as

$$E_{\text{exc}} = \oint F_0 \cos(\omega t) \frac{\mathrm{d}z}{\mathrm{d}t} \mathrm{d}t = \frac{\pi k A_0 A(\omega) \sin \phi}{Q}, \tag{7.3}$$

$$E_{\text{med}} = \oint \left(\frac{m\omega_0}{Q} \frac{\mathrm{d}z}{\mathrm{d}t} \right) \frac{\mathrm{d}z}{\mathrm{d}t} \mathrm{d}t = \frac{\pi k A^2}{Q} \frac{\omega}{\omega_0}, \tag{7.4}$$

$$E_{\text{dis}} = \oint (F_{\text{ts}}) \frac{\mathrm{d}z}{\mathrm{d}t} \mathrm{d}t. \tag{7.5}$$

By substituting the above equations into Equation 7.2, we deduce

$$\sin \phi = \frac{A\omega}{A_0 \omega_0} \left(1 + \frac{E_{\text{dis}}}{E_{\text{med}}} \right). \tag{7.6}$$

The sine of the phase shift lag ϕ is related to the set point amplitude A and to the energy per cycle dissipated in the sample by the nonconservative tip surface forces. Because the microscope operates under the condition of $A = A_{\text{sp}} = \text{constant}$, the prefactor in Equation 7.6 remains unchanged while imaging. Consequently, any of the recorded phase shift variations reflects local changes in the mechanical energy irreversibly transferred from the cantilever tip system to the surface. Numerical simulations and experiments performed on different surfaces such as polydimethyl siloxane samples of different cross link density [59], graphite, and purple mem branes [62] have confirmed the validity of Equation 7.6.

This remarkable and counterintuitive result is imposed by restriction the mapping of the surface to a constant amplitude. For example, let us suppose an ideal surface composed of two flat regions of vastly different stiffness. Let us also assume that tip surface forces are exclusively conservative. Phase imaging AFM would not reveal any contrast between these regions. The feedback system would compensate for the differences in the elastic properties by changing the mean tip surface distance z_c. Larger z_c values would be obtained in the stiffer regions, in this way, $\sin \phi = A/A_0$ remains constant.

Paulo and Garcia applied the virial theorem to derive a complementary expression to Equation 7.6 [65, 66],

$$\cos\phi = \frac{2Q}{kAA_0}\left[\frac{\langle F_{ts}\rangle^2}{k} \quad \langle F_{ts}z\rangle + \frac{1}{2}kA^2\left(1 \quad \frac{\omega^2}{\omega_0^2}\right)\right]. \tag{7.7}$$

Equation 7.7 can be simplified by driving the tip at resonance $\omega = \omega_0$ and by observing that, in many experimental situations, the mean deflection of the cantilever is negligible with respect to the oscillation amplitude ($z_0 \ll A$), thus

$$\cos\phi \approx \quad \frac{2Q\langle F_{ts}z\rangle}{kAA_0}. \tag{7.8}$$

The virial theorem applies to systems that perform periodic trajectories. It establishes a relationship between the average value of kinetic energy and the virial, is equal to $2\langle T\rangle = \quad \langle F_{ts}z\rangle$. It must be noted that the virial of a system that follows a sinusoidal trajectory in the presence of nonconservative forces that are proportional to $\dot{z}$ is zero. Thus, Equation 7.8 shows that phase shift variations in AM AFM could be associated with local changes in the virial of conservative forces. The fact that Equations 7.6 and 7.8 are complementary and must be satisfied simultaneously seems paradoxical because Equation 7.6 emphasizes dissipation while Equation 7.8 emphasizes elastic properties. The paradox is solved by observing that the virial depends on both forces and displacements. For the ideal case discussed above, local changes in the stiffness of the sample surface are compensated by changes in the average tip surface separation in such a way that the virial remains unchanged.

7.3.2
Phase Imaging AFM: Low *Q*

The conclusions presented in the above section remain valid as long as Equation 7.1 is a good description of the tip motion. For low Q values (<5), the Fourier transform of the oscillation shows a significant contribution from frequencies of the higher harmonics and modes. Then, Equation 7.1 is no longer a valid description of the tip motion. However, an analytical expression for the sine of phase shift can still be derived by neglecting the contribution from the higher modes of the cantilever. Then, the solution that takes into account the contribution from the higher harmonics of the excitation frequency is [1, 70]

$$z = z_0 + \sum_{n\ 1}^{\infty} A_n \cos(n\omega t \quad \phi_n). \tag{7.9}$$

By inserting the above solution into Equation 7.2, we deduce

$$\sin\phi_1 = \sum_{n\ 1}^{\infty} \frac{n^2A_n^2\omega}{A_0A_1\omega_0}\left(1 + \frac{E_{dis}}{E_{med}}\right). \tag{7.10}$$

Equation 7.10 establishes a relationship between the phase shift of the excitation frequency with the amplitude of the higher harmonics and the energy dissipated per cycle. It separates terms dominated by elastic contributions (A_n/A_1) from those dominated by dissipation. Consequently, phase shift variations will depend on both conservative and nonconservative interactions whenever the A_n components are not negligible with respect to A_1.

7.4 Energy Dissipation Measurements at the Nanoscale

The existence of micro and nanoelectromechanical devices where the separation between the relevant surfaces is in the nanometer range, scanning probe microscopes among them, emphasizes the importance of energy dissipation processes at the nanoscale [89–91]. Thus, the need for methods providing quantitative measurements of the energy transferred between moving objects. In this respect, phase shift measurements performed with an AM AFM can be a valuable source of information.

7.4.1 Energy Dissipation and Observables

Equation 7.6 can be easily transformed to determine either the power or the energy transferred (irreversibly) from the tip to the sample surface. Thus, we deduce

$$E_{\text{dis}} = \frac{\pi k A^2}{Q}\left(\frac{A_0}{A}\sin\phi \quad \frac{\omega}{\omega_0}\right), \tag{7.11}$$

or in terms of the average power transferred to the sample surface

$$\langle P_{\text{dis}}\rangle = \frac{kA^2\omega}{2Q}\left(\frac{A_0}{A}\sin\phi \quad \frac{\omega}{\omega_0}\right). \tag{7.12}$$

The above equations provide a direct and powerful method to measure dissipation at the nanoscale [3, 4, 8]. The value of the dissipated energy depends on both experimental parameters (free and set point amplitudes, cantilever force constant, or tip's radius) and tip–sample inelastic processes. Typical high resolution experiments involve energy dissipation values per cycle in the 0.5–50 eV range or in terms of power about 0.008–0.8 pW. For a spatial resolution of 2 nm, these values imply a dissipated energy per bond that ranges from 0.001 to 0.1 eV, that is, far less than the bonding energies of most materials. The above numbers underline that phase imaging experiments can be performed in a noninvasive manner. Furthermore, the method is very sensitive to spatially resolved regions with different properties [92]. Figure 7.7 shows an energy dissipation map of a sample made of several sexithiophene islands deposited on a silicon surface (Figure 7.7a). The energy dissipation histogram shows two peaks separated by 0.4 eV (Figure 7.7b).

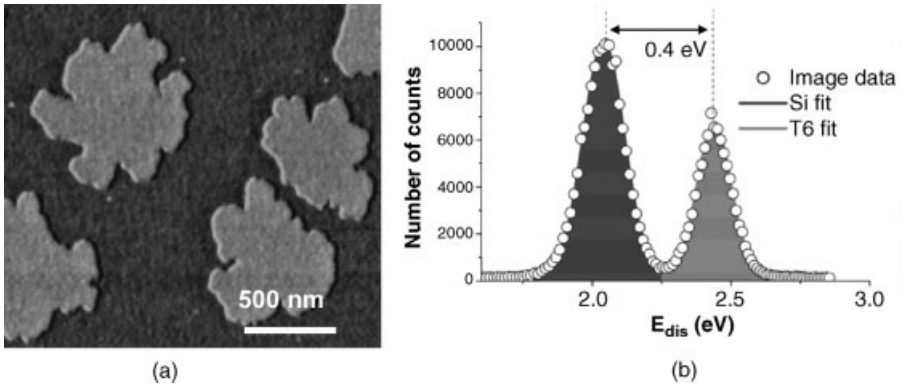

Figure 7.7 Phase imaging AFM map of several sexithiophene islands deposited on silicon (a) and energy dissipation histograms extracted from the phase image (b). Adapted from Ref. [92].

The analysis of AM AFM operation in air is completed by comparing the values of the mechanical energy of the tip, the energy dissipated in the environment, and the energy dissipated in the sample. These values depend on the experimental conditions, cantilever, and sample properties. However, as a guiding rule the mechanical energy of the tip is a factor of 10 higher than the energy dissipated in the air that, in turn, is at least a factor of 10 higher than the energy dissipated in the sample.

7.4.2 Identification of Energy Dissipation Processes

Equation 7.11 provides the basis to develop a method to identify energy dissipation processes at the nanoscale [4, 8, 92]. This requires us to determine the amount of energy dissipated by the tip on the sample surface for several values of the tip surface distance. This is accomplished by first measuring the dependencies of the amplitude and phase shift as a function of the amplitude while the tip approaches the surface. Then, Equation 7.11 enables to transform amplitudes and phase shifts into energy dissipation values. The representation of the dissipated energy and/or its derivative with respect to the amplitude is known as dynamic dissipation curve [4, 49]. Figure 7.8 illustrates the experimental steps to determine dynamic dissipation curves from the amplitude and phase shift dependencies on the tip surface distance.

Figure 7.9 provides an example of the use of dynamic dissipation curves to identify different dissipation processes [8]. The figure shows a comparison between the theory and the experiments performed on silicon and on a polystyrene region of a polymer blend. For all the cases studied, the experimental dynamic dissipation curves reproduce the behavior predicted by the theory. Energy dissipation curves for long range interactions and viscoelasticity may look similar (Figure 7.9a and c), but the derivative unambiguously singles out each dissipative process (Figure 7.9d f).

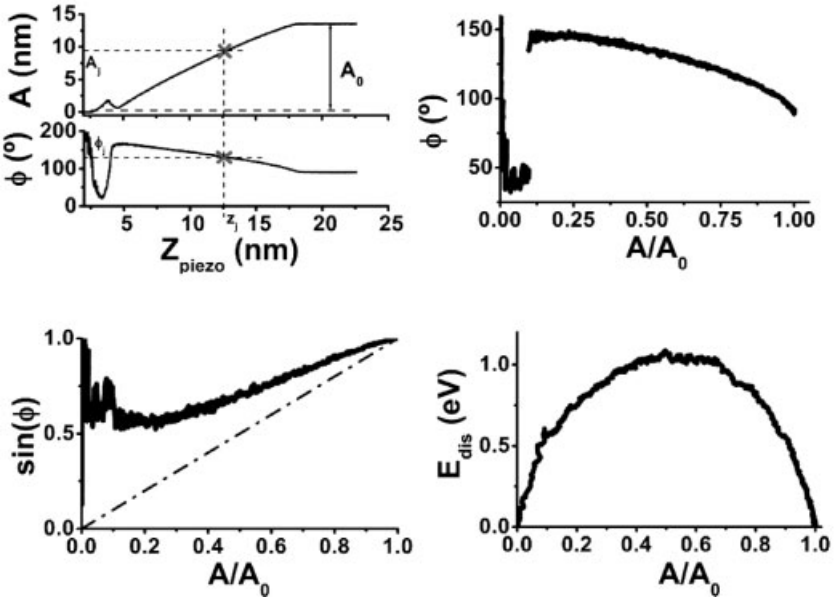

Figure 7.8 Method to obtain dynamic dissipation curves. Amplitude and phase shift curves are measured (top left panel). These curves make it possible to represent the phase shift and its sine as a function of the amplitude ratio (top right and bottom left panels, respectively). From these curves and Equation 7.11, the energy dissipated on the sample surface as a function of the amplitude ratio can be measured (bottom right panel). Experiments performed on a silicon surface with a silicon tip. Adapted from Ref. [4].

7.4.3
Atomic and Nanoscale Dissipation Processes

Dissipation in atomic force microscopy can be described at the molecular or nanoscale level. In the first case, the emphasis is placed on the specific atomic processes that enable the transformation of mechanical energy in atomic and molecular motions in the sample [93 95]. The atomistic and molecular mechanisms responsible of dissipation depend on material properties. They may involve force induced new stable atomic bonding configurations or molecular reorientations, interdigitation, exchange of atoms and molecules, or charge induced dissipation effects. At the nanoscale, the emphasis is placed on the quantitative relationship between dissipation processes such as surface adhesion hysteresis, viscoelasticity, friction, or long range dissipative interfacial interactions and macroscopic quantities such as surface adhesion energy, elastic modulus, stiffness, plasticity index, or viscous coefficient [8, 28, 77, 96].

A combined experimental and theoretical study on the energy transferred by a silicon dioxide tip into a region of sexithiophene molecules has enabled to link atomistic and nanoscale dissipation processes [92]. Phase imaging AFM was used to measure the energy transferred by a silicon dioxide tip into a region of sexithiophene

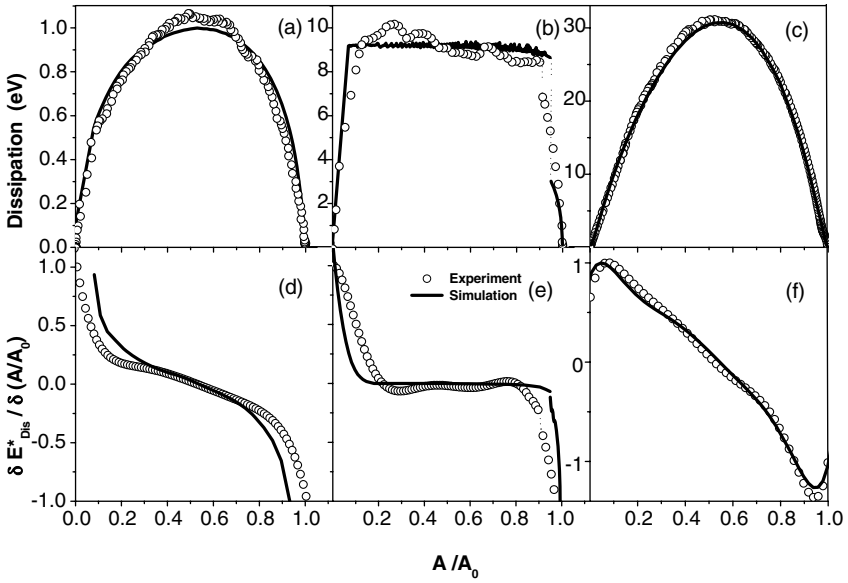

Figure 7.9 Measured and simulated dynamic dissipation curves on different surfaces. (a) On a Si surface when there is no mechanical contact between tip and surface; A_0 6.6 nm, k 2 N/m. (b) On silicon when there are surface energy hysteresis and long range interfacial interactions; A_0 32.5 nm, k 2 N/m. (c) On a polystyrene region (cross in the inset) of polystyrene/polybutadiene blend, A_0 15 nm. (d) (f) are the derivatives of the normalized energy dissipation curves shown in (a), (b), and (c), respectively. The step like discontinuities observed in Figure 7.9b mark the transition between attractive and repulsive interaction regimes. Adapted from Ref. [8].

molecules (1.4 eV per cycle). Contact mechanics modeling established an effective interaction diameter of 2 nm that implied a dissipation of 0.18 eV per molecular chain. This value is comparable to the average value (0.15 eV) determined from first principles calculations for an indentation of 0.20 nm. First principles calculations show that the adhesion hysteresis observed experimentally has its molecular origin in the rich configuration space of the system. During the approach (loading), the system is trapped, due to the presence of energy barriers, in several bonding configurations that differ from those sampled in the retraction stage of the tip (uploading). These configurations correspond to local energy minima.

8
Resolution, Noise, and Sensitivity

8.1
Introduction

Spatial resolution, noise, and sensitivity are concepts closely related in amplitude modulation AFM. The relationship that exists between noise and resolution is rather straightforward. The noise in the cantilever deflection establishes the upper reso lution limits of the microscope. Most AFM users have an intuitive definition of spatial resolution that might work well for flat surfaces. However, the imaging process is fundamentally nonlinear; as a consequence, it is hard to establish a more technical definition. In a heterogeneous surface, features of equal size but different properties might give rise to different values of the tip surface force. The sensitivity of the instrument to detect force variations might also control the achievable spatial resolution. This underlines the role of the sample's mechanical properties to reach a given spatial resolution.

8.2
Spatial Resolution

A topographic image is mathematically expressed as a function of the height variation $h(x, y)$ on the spatial coordinates x and y. Thus, AFM images require it to distinguish between vertical and lateral resolutions. Several factors contribute to determination of the resolution such as the electronic and mechanical noise, the tip's apex size, the decay length of the tip surface forces, and the sample compliance. The nonlinear character of the imaging process is another factor that controls the spatial resolution. By nonlinear imaging it is understood that the image of a surface is not the sum of the individual images of the features of the surface. This is also a difference from lens based microscopes where the imaging process is linear.

Amplitude Modulation Atomic Force Microscopy. Ricardo García

ISBN: 978-3-527-40834-4

8.2.1
Vertical Resolution and Noise

The vertical resolution is defined as the minimum step height variation measured on the surface. Thus, to detect atomic corrugations, the vertical noise should be below 0.1 nm. The vertical resolution is limited by the noise in the imaging signal δA (amplitude) (Figure 8.1). The vertical noise can be defined as the ratio between the noise in the amplitude signal and the slope of the amplitude with respect to the average tip surface distance,

$$\delta h_n = \frac{\delta A}{|\mathrm{d}A/\mathrm{d}z_c|}. \tag{8.1}$$

For stiff materials and measurements performed at the fundamental frequency, the slope of the imaging signal with respect to the tip surface distance is close to 1 [1, 2], then $\delta h_n \approx \delta A$. Under these conditions, the vertical noise coincides with the amplitude noise (or deflection noise δz). On the other hand, the slope of the amplitude distance curves for soft materials is in the 0.2 0.5 range, and δh_n lies between $2\delta A$ and $5\delta A$ [3]. The above definition of vertical noise is similar to the definition proposed for scanning tunneling microscopy and frequency modulation AFM [4].

The deflection noise has two major components, the thermal noise of the cantilever and the detector noise. These sources of noise are statistically independent,

$$\delta A \approx \delta z = \sqrt{\delta z_{\mathrm{th}}^2 + \delta z_{\mathrm{det}}^2}. \tag{8.2}$$

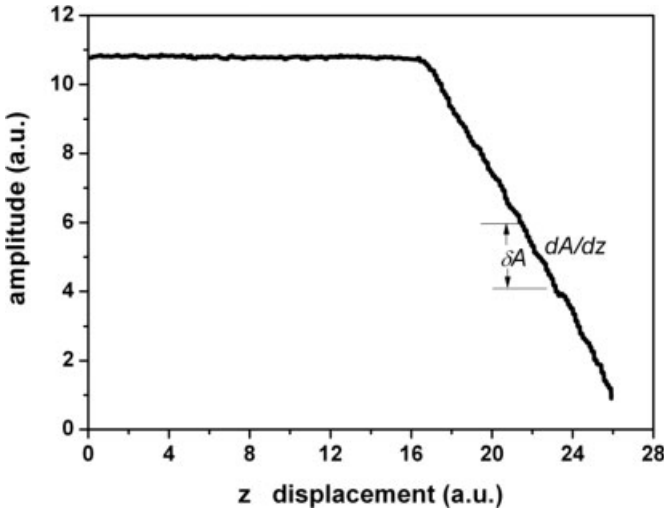

Figure 8.1 Amplitude distance curves. The vertical noise is given by the noise in the amplitude δA divided by slope of the amplitude curve $\mathrm{d}A/\mathrm{d}z_c$. In this case, a change in the z displacement is identified with a change in the average tip surface distance. This approximation remains valid as long as the mean deflection of the cantilever is negligible.

The detector noise is dominated by the optical detector noise. It is the major source of noise in an instrument that is properly shielded from acoustic and electromag netic noise. Its reduction is the focus of an intense scientific activity [4 9]. The thermal noise is usually much smaller than the detector noise. Consequently, it establishes the ultimate resolution limits of the instrument.

In dynamic AFM, the root mean square value of the amplitude spectral density induced by the thermal energy is calculated by [8, 10]

$$n_{zB} = \sqrt{\frac{2k_B T}{\pi f_0 k Q}} \frac{1}{\left[1 \quad (f/f_0)^2\right]^2 + \left[f/(f_0 Q)\right]^2}. \tag{8.3}$$

The spectral density is related to the deflection noise by

$$\delta z_{th}^2 = \int_0^\infty n_{zB}^2(f)\mathrm{d}f. \tag{8.4}$$

The components of the noise that influence the performance of the instrument are those included within the frequency bandwidth range, $f_0 \quad B$ to $f_0 + B$, where f_0 is the fundamental frequency. Then, the thermal noise of the deflection is calculated by [8]

$$\delta z_{th} = \sqrt{\frac{4k_B TQB}{\pi f_0 k}}. \tag{8.5}$$

The total noise induced by the thermal energy is obtained by integrating the spectral density over the whole frequency range or directly by applying the equipartition theorem,

$$\delta z_{th}(\text{total}) = \sqrt{\frac{k_B T}{k}}. \tag{8.6}$$

When the excitation frequency coincides with the fundamental frequency $f = f_0$, the spectral density and the deflection noise in the bandwidth range $f_0 \pm B$ are related by

$$n_{zB} = \frac{\delta z_{th}}{\sqrt{2B}}. \tag{8.7}$$

It is illustrative to compare the thermal noise of several common cantilevers (Table 8.1).

Table 8.1 Thermal noise for some common cantilevers.

k (N/m)	f_0 (Hz)	Q	δz_{th} (nm) (B 1 kHz)	n_{zB} (fm/Hz$^{1/2}$)
0.25	36 944	39	0.14 844	3319
0.25	8313	2	0.07 087	1585
0.74	68 143	108	0.10 572	2364
0.74	19 315	4	0.03 872	855
5.62	111 791	350	0.05 392	1206
28	318 000	400	0.01 531	342

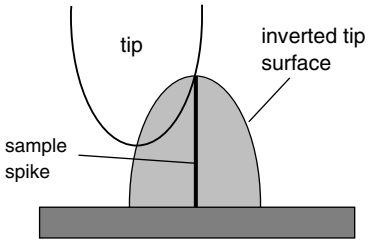

Figure 8.2 Schematic representation of the distortion introduced by the finite tip size while imaging a sharp feature. The apparent image is the inverted tip surface.

The thermal noise depends on the cantilever geometry and the environment. By using cantilevers with a high resonant frequency and a large force constant, the noise is decreased. Some cantilevers give a deflection noise below 0.05 nm that would enable subatomic resolution. To a certain extent, the frequency bandwidth can be changed by the operator. Thus, it seems more representative to present the noise in terms of spectral density values (Equation 8.7). For the above cantilevers, the spectral density noise ranges between 300 and 3400 $fm/Hz^{1/2}$.

8.2.2
Lateral Resolution

Bustamante and Keller [11] proposed a definition of lateral resolution that accounts for the tip finite size. This definition assumes that the tip and the surface are undeformable objects (Figure 8.2). The lateral resolution l is the minimum separation for which the dimple depth Δz arising from the intersection of the individual images of two sample features is larger than the noise (Fig ure 8.3). Mathematically, this definition states that the lateral separation l between two sharp features imaged by a parabolic tip with end radius R depends on the height difference Δh that exists between the adjacent features and the vertical

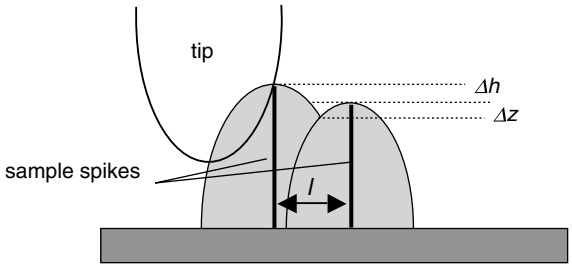

Figure 8.3 Scheme of the AFM imaging process performed by a parabolic tip of radius of curvature R over two sharp spikes. The minimum lateral separation between the spikes depends on the height difference that exists between the adjacent features. The height difference and the radius define the value of the dimple depth Δz. The dimple depth must be larger than the noise to be resolved. Adapted from Ref. [11].

resolution δh_r ($\delta h_r \approx \delta h_n$),

$$l = \sqrt{2R}\left(\sqrt{\delta h_r} + \sqrt{\delta h_r + \Delta h}\right). \tag{8.8}$$

The equation also reflects the nonlinear nature of the image formation in AFM because the lateral resolution is a function of the height difference between adjacent features. Consequently, it must be determined separately for each feature in the image. The above definition can be considered an analogue of the Rayleigh criterion for resolution in optical microscopy.

Figure 8.4 shows the lateral resolution (Equation 8.8) as a function of the radius for different relative height differences. As it could have been expected, atomic reso lution, say a lateral resolution below 0.5 nm, can be achieved only for very sharp tips, that is, those that have an apex with an effective radius of 1 nm or below. Atomic and molecular resolution imaging also requires the height difference between neigh boring features to be below 0.5 nm.

The lateral resolution could also be affected by the data recording process. A key factor to bear in mind is the relationship that exists between the number of pixels used to record the image and the scanning speed. Typical AFM software handles files with 256, 512, 1024, or even higher data points per scan line. For an image of a lateral size Δx, the spatial resolution cannot be better than $\Delta x/N_p$, with N_p denoting the number of pixels. The microscopist would be tempted to use the largest number of pixels provided by the software; however, this might significantly reduce the scanning speed. In addition, it will end up filling the memory of the computer. Recorded images with the highest number of pixels should be kept for the data deemed relevant. The ratio between the maximum voltage that could be applied to z scanner

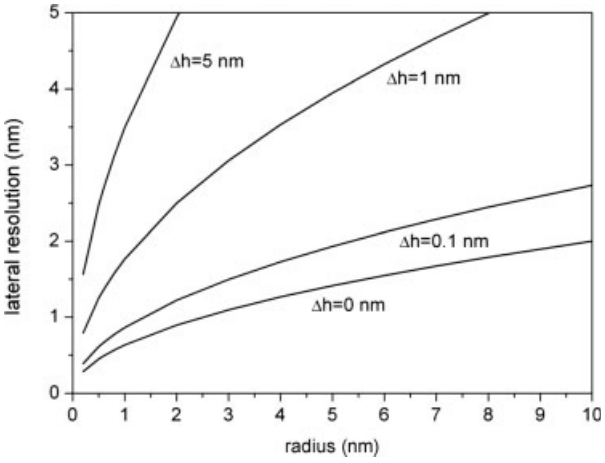

Figure 8.4 Lateral resolution as a function of the radius for two adjacent features (Equation 8.8). The height difference between the features is Δh 0, 0.5, 1, and 5 nm. A vertical resolution of 0.05 nm is assumed.

and the number of bits of the digital to analogical converter is another factor that could affect the vertical resolution of the image.

8.3
Image Distortion and Surface Reconstruction

Figures 8.2 and 8.3 illustrate some of the main concerns while imaging nonflat surfaces. AFM images are highly influenced by the finite size of the tip. Tip induced distortions are significant whenever the surface has features with aspect ratios comparable to or sharper than those of the tip apex [11 22]. This phenomenon is known as dilation. When confronted with this problem, most AFM users will either use a tip with an aspect ratio sharper than that of the features of the surface or provide width values in terms of the full width at half maximum (FWHM). Accurate image reconstruction methods have also been proposed [13, 14, 16 18]. Some of the proposed algorithms rely upon the principle that at the point of the closest distance, both the tip and the surface have the same tangent line. In particular, Keller proposed a method where the reconstructed image is synthesized from the original, distorted image as the envelope of a set of tip surface functions [13]. Villarrubia has proposed reconstruction algorithms based on mathematical morphology [17]. Once the tip's geometry has been determined, the above methods can be applied to reconstruct from the image the surface geometry.

Figure 8.5 illustrates the nature of the dilation process in AFM. The convolution process arises because there is a difference between the tip's apparent and true imaging points. An image is formed by the trace of the tip end. The imaging process assumes that the tip end is always the closest point to the surface. That assumption breaks down when the surface has features sharper than the tip's apex. In addition,

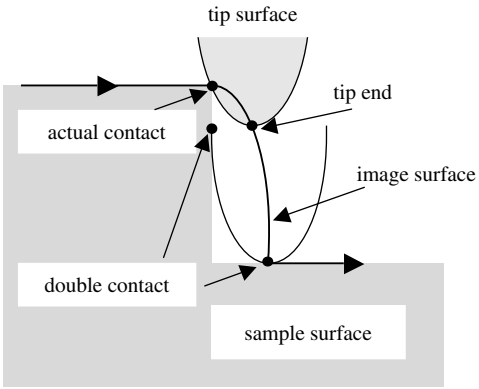

Figure 8.5 An image is formed by the trace of the tip end. In some cases, the actual point of contact may be different from the tip end. In other cases, there are two contact points. Adapted from Ref. [14].

when the curvature of a sample feature exceeds the curvature of the tip, there will be regions where the tip simultaneously touches the sample at two points. Keller has shown [13, 14] that the existence of double contact points implies the existence of unreconstructable regions (Figure 8.5). An ideal tip characteristically has the apex and the sidewalls sharper and steeper, respectively, than those of the sample surface.

8.4
Force-Induced Surface Deformations

A factor that has not been included in the above definition of lateral resolution is the deformation of the sample surface. The force exerted by the tip usually deforms the sample surface. As a guiding rule, the lateral resolution cannot be better than the *real* or effective tip surface contact area. The contact area reflects the interplay that exists among the tip surface forces and the mechanical compliance of both tip and surface.

Molecular dynamics simulations illustrate the deformation of a sexithiophene molecule under the force exerted by a silicon dioxide tip that penetrates 0.2 nm into the monolayer (Figure 8.6) [23]. Under these conditions, the maximum force is about 1 nN. That force produces the bending of the molecules. For small applied forces (loads), the deformation is mainly elastic and the molecules recover its shape once the

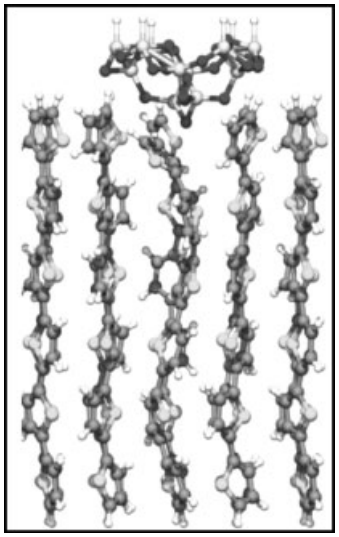

Figure 8.6 Deformation induced on a sexithiophene chain by the force exerted by a silica tip. The force produces the bending of the molecular groups and its transmission through the whole chain. Color code for atoms: oxygen (black), sulfur (dark gray), carbon (gray), hydrogen (white), and silicon (light gray). Adapted from ref. [23].

load is removed. In other cases, the applied force could lead to the irreversible modification of the molecules.

Contact mechanics simulations provide a complementary perspective on surface deformation and lateral resolution. The force exerted by the tip produces the deformation of the surface implying the existence of a finite contact area. Increasing the applied force increases both the contact area and the deformation (see Chapter 3). The lateral resolution can be calculated as a function of the applied force by identifying the contact diameter with the lateral resolution [24 26]. The Hertz model provides the lateral resolution as a function of the tip's radius, the applied force F, and the effective Young's modulus of the interface E_{eff},

$$l = 2\left(\frac{3RF}{4E_{\text{eff}}}\right)^{1/3}. \tag{8.9}$$

Equation 8.9 shows that subnanometer resolution requires the use of tips with small radius and the application of forces below 1 nN (Figure 8.7). It also explains why atomic and subnanometer resolutions are more easily achieved on stiffer materials than on the more compliant ones. Usually, the deformation of the tip is ignored. Tips are made of silicon or silicon nitride characterized by having high Young's modulus values (above 150 GPa). However, whenever the tip and the sample have comparable Young's moduli, the tip deformation should also be considered. A description that considers both the tip and the sample deformations has been performed by Heuberger *et al.* [24].

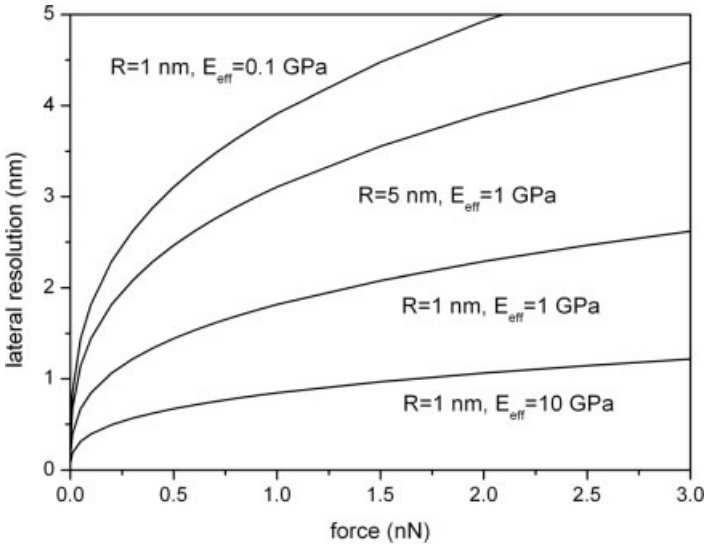

Figure 8.7 Lateral resolution (Hertz model) as a function of the applied force for different tip radii and material properties.

8.5
Atomic, Molecular, and Subnanometer Lateral Resolution

It is useful to provide a practical definition of atomic and subnanometer resolution. Following Gan [26], atomic resolution is defined as the capability to resolve single or multiple atomic scale features separated by an atomic scale distance. Atomic scale features include atoms, molecules, point defects, and grain boundaries. Similarly, subnanometer resolution is defined as the ability to resolve single or multiple subnanometer features. Subnanometer resolution images are of especial relevance to biology. To achieve a given lateral resolution, the contact diameter (or its equivalent in noncontact measurements) must be equal to or smaller than the size of the observed feature.

In spite of a large community of its users, amplitude modulation AFM has been slow in providing atomic and subnanometer resolution images. This paradoxical situation might be explained by two factors. On the one hand, so much information is provided by nanoscale resolution images that the need to improve the resolution is somehow diminished. On the other hand, atomic resolution images can be achieved only on atomically flat surfaces. Because AM AFM operates in either air or liquid, it is sometimes assumed that either the tip or the sample surface contamination could suppress atomic resolution.

Ohnesorge reported the first atomic resolution images obtained with an AM AFM [27]. Monoatomic steps and atomic defects were observed on a calcite surface in liquid. Also in liquid, Muller and coworkers showed images of a purple membrane with a lateral resolution of 1.1 nm (Figures 8.8 and 8.9) [28], a result that has been

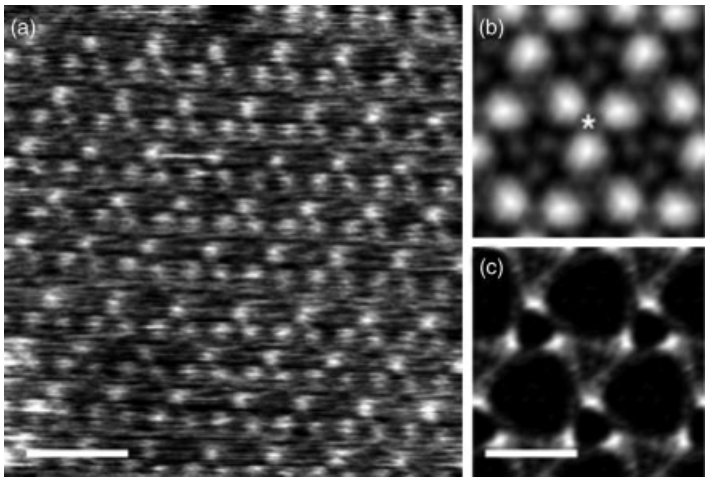

Figure 8.8 Image of the extracellular purple membrane surface in buffer solution. The trimeric structures protrude 0.4 nm from the lipid bilayer. The trimers are arranged in a trigonal lattice of 6.2 nm. (a) Raw data. Scale bar 10 nm. (b) Image after performing a threefold symmetrized correlation average from 35 unit cells. (c) Threefold symmetrized standard deviation map of (b). Scale bar 5 nm. Adapted from Ref. [28].

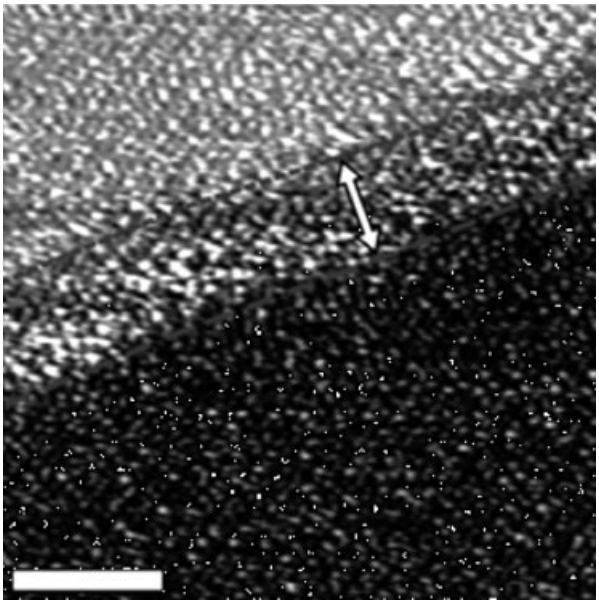

Figure 8.9 Atomic resolution image of a calcite ($CaCO_3$) surface in water. The image shows two terraces separated by biatomic step. Scale bar 5 nm. Adapted from Ref. [39].

either reproduced or improved by several groups [29 33]. These results prompted a quest to obtain molecular resolution images on other biological systems that form packed structures such as chaperonin (GroEL) patches [34, 35] or bacterial mem branes [36]. A further step in consolidating the technique for subnanometer resolution imaging was given by Magonov and coworkers [37, 38]. By using tips with an apex below 1 nm, images of subnanometer resolution (0.36 nm periodi cities) were reported on a polymer crystal (polydiacetylene) [38]. These experiments were performed in air. Another example of molecular resolution ($\sim$0.7 nm) is the observation of the different ligand species in mixed self assembled monolayers [27].

8.5.1 True Resolution

Back in the early days of force microscopy, Ohnesorge and Binnig coined the term true atomic resolution [40] to distinguish AFM images that showed the presence of atomic size defects from those that showed a perfect crystalline surface with no defects. Images that show a perfect crystalline surface are relatively common in contact AFM experiments. Then, it is convenient to distinguish between the ability to resolve atoms from the ability to resolve the lattice parameter. In the first case, the contact involves a few atoms while in the latter the contact might involve hundreds or

thousands of atoms. The above situation is not common in amplitude modulation AFM, but the reader should be aware of it. Examples of high resolution ghost images due to multiple tip and/or high loads are provided by Gan [26].

8.6
High-Resolution Imaging of Isolated Molecules

Atomic resolution images might be obtained on relatively stiff and crystalline materials that have atomically flat surfaces. Dealing with soft materials and surfaces that show height changes of 1 nm or above imposes some limits on the lateral resolution. The expected lateral resolution of a good image of isolated feature deposited on a flat surface such as a single protein on mica should be in the 1 2 nm range. For example, features on antibodies separated by 1.4 nm distances have been resolved in air [41 43] and liquid [31, 44]. Dunlap imaged packed DNA loops in liquid with a lateral resolution of 4 nm [45].

The imaging of DNA provides an interesting example of the confusion that sometimes might arise between lateral and vertical resolutions. Double stranded DNA has a mean diameter of 2 nm. In fact, DNA has been imaged a large number of times by AM AFM; however, in many images the apparent width of the DNA molecule is several times wider than its nominal value [46 53]. Even images with apparent widths within the 20 nm range are not uncommon. In these images, the observation of DNA molecules arises from the vertical resolution of the instrument and not from its lateral resolution.

8.7
Conditions for High-Resolution Imaging

High resolution imaging is a difficult experimental task that is simplified by following some guiding rules, namely,

1) The instrumental noise should be smaller than the aimed resolution.
2) The lateral resolution cannot be smaller than the size of the tip apex.
3) The decay length of the tip surface interaction should be smaller than the tip apex.
4) Imaging isolated three dimensional objects imposes limits on the lateral resolution.
5) The adhesion energy should be minimized. This is usually achieved by using sharp tips.
6) The applied force should be as small as possible.
7) Under identical conditions (tip radius and applied force), the stiffer the sample the better the lateral resolution.

These rules share several points with the conditions summarized by Gan [26], Weihs *et al.* [25], and Schwarz *et al.* [54].

8.8
Image Artifacts

Image artifacts could come from different sources. The dilation of image features produced by the tip's finite size is one of them. Belikov and Magonov have provided an example of how the subnanometer resolution on a polymer crystal changes with the tip radius [38]. In fact, the presence of several nanotips within the same probe could give rise to very subtle image artifacts at atomic (see Section 8.5.1) and nanometer scales (Figure 8.10). Another potential source of artifacts is the tip load. Hoogenboom *et al.* [55] observed the different components of the cytoplasmic surface of purple membrane by changing the load. At low forces, the most prominent feature is the bulk peptide connecting the transmembrane helices. At slightly higher loads, this loop bends and otherwise hidden shorter loops become visible. Of course, imaging soft materials under high forces can damage the object. Figure 8.11 illustrates the morphological changes observed in a single human serum albumina antibody by applying different forces [41]. The top image has been obtained by applying a maximum force of 0.4 nN, while the bottom image is achieved by applying a force of 3.5 nN. At low forces, the image shows the three fragments and the hinge regions of the antibody. The image taken at 3.5 nN shows a featureless globular

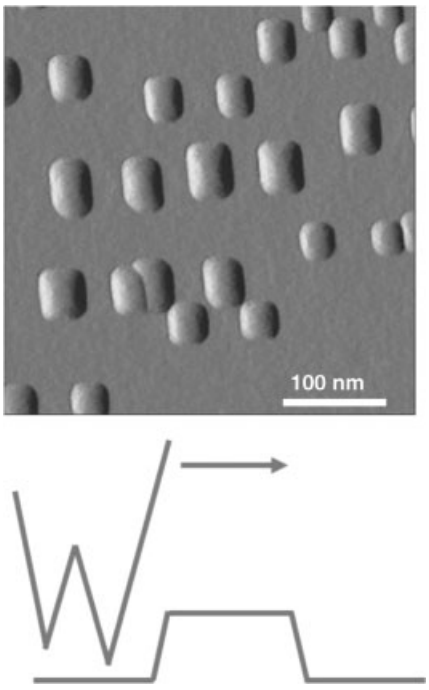

Figure 8.10 Phase image of a distribution of semiconductor dot structures formed on GaAs after the growth of two monolayers of InSb. The dots are duplicated. The bottom panel shows an interpretation of the image artifact.

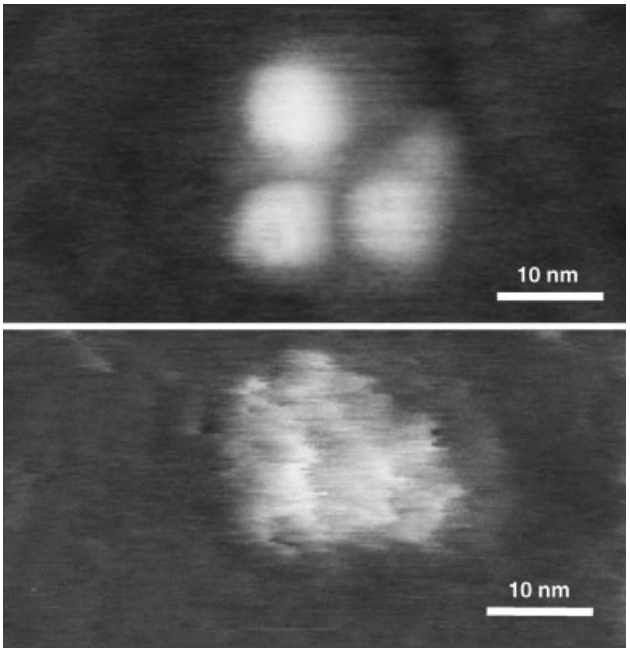

Figure 8.11 *Top*: High resolution image of a single human serum albumin antibody obtained by applying a peak force of 0.4 nN. The image resolves the three fragments and the hinge regions of the antibody. *Bottom*: The image of the same antibody obtained by applying a peak force of 4 nN. Adapted from Ref. [41].

structure with the same overall size. In fact, images obtained at high forces can induce the irreversible deformation of the molecule. In general, high resolution images of isolated biomolecules require the application of peak forces below 1 nN. In liquid, the salt concentration could also be a source of image artifacts. The salt concentration controls the strength of the electrostatic and these, in turn, control the apparent morphology of the biological membrane [56, 57].

9
Multifrequency Atomic Force Microscopy

9.1
Introduction

Improving spatial resolution, data acquisition times, and material properties imag ing are perennial goals in amplitude modulation AFM. At present, the most promising approaches to reach these goals involve the excitation and the detection of several frequencies of the tip's oscillation. These frequencies are usually associated with either the higher harmonics of the oscillation or the eigenmodes of the cantilever. The diversity of multifrequency approaches, the use of novel excitation or detection schemes, and the emphasis placed on mixing several frequencies configure a new subfield in force microscopy that is called multifrequency AFM.

9.2
Normal Modes and Harmonics

It is pertinent to remember the distinction between normal modes and harmonics (see Chapters 4 and 5). A normal mode is one of the discrete solutions of the beam model of the cantilever. Normal modes are also called eigenmodes or resonances. A harmonic is a component of the oscillation that vibrates with frequency equal to an integer multiple of the excitation frequency ($\omega_n = n\omega$). Figures 5.4 and 5.5 illustrate the geometry and transfer function of the first four flexural modes of a continuous rectangular cantilever. Figure 9.1 shows the harmonics of a cantilever that is excited at its fundamental frequency (lowest resonance). The amplitude of the harmonics is modulated by the resonances of the cantilever (arrows in the horizontal axis).

9.2.1
Generation of Higher Harmonics

It can be deduced that for a forced harmonic oscillator with damping, the presence of a tip surface force that has a linear dependence on the distance does not generate higher harmonics of the excitation frequency (Section 4.3.2). Thus, the generation of

Amplitude Modulation Atomic Force Microscopy. Ricardo García

ISBN: 978-3-527-40834-4

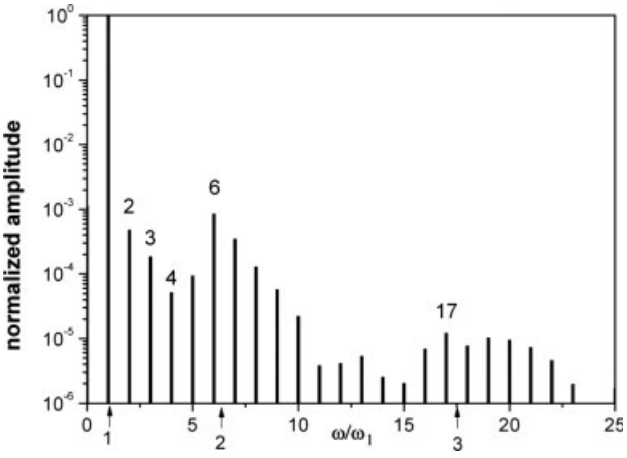

Figure 9.1 Frequency spectrum of a one dimensional cantilever tip system in AM AFM. The amplitude components of the higher harmonics are modulated by the normal modes or resonances (eigenmodes) of the cantilever. The arrows in the horizontal axis mark the positions of the first three flexural eigenmodes.

higher harmonics is related to the presence of a nonlinear force. Several experimental and theoretical studies describe the generation of higher harmonics in AM AFM [1 23] (Herruzo, E.T. and García, R., unpublished.). Some contributions illustrate the influence of the van der Waals forces or the contact stiffness on the harmonics components [1 13], while others explore the experimental use of higher harmonics to map surface properties or improve spatial resolution [14 22]. In several contri butions, the focus is on the coupling between harmonics and eigenmodes (Section 9.2.2). Although the presence of higher harmonic components is a common feature, its relevance in experiments performed in air is diminished by the obser vation that under gentle imaging conditions, the amplitude of the fundamental component ($n = 1$) is two to three orders of magnitude higher than any of the amplitudes of the other harmonics [4]. Higher harmonic components are enhanced by operating the microscope in liquid [21, 23] or by using cantilevers specifically designed to enhance a given harmonic [16].

The potential of higher harmonics for high resolution imaging is illustrated in Figure 9.2. A high spatial resolution image of a bacterial S membrane is generated by plotting the amplitude of the 2nd harmonic of the fundamental frequency. This image is obtained simultaneously with the topography (feedback on the amplitude component of the fundamental frequency) [21]. The frequency spectra taken on top of a protein (position 2) or in the hole within the unit cell (position 1) shows the differences in the harmonic components.

Several aspects of higher harmonics generation are well accounted for by some of the theoretical models described in Chapters 4 and 5. However, there are some issues, such as the interplay between conservative and dissipative forces or the influence of the environment (liquid or air) on the higher harmonics, that remain

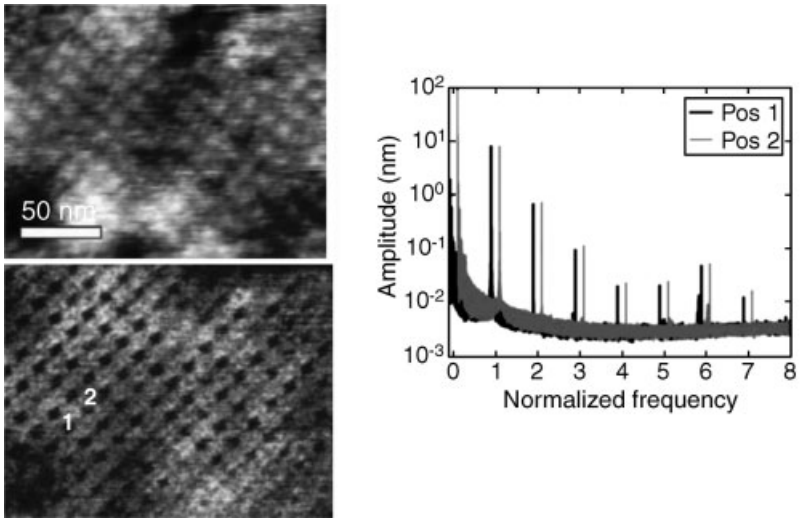

Figure 9.2 Image of a bacterial S layer: topography (top panel) and second harmonic image (bottom panel). Substructures within the unit cell can be observed in the second harmonic image (spatial resolution ~0.5 nm). The frequency spectra taken at two difference positions of the membrane show the spatial dependence of the higher harmonic components (lateral panel). The spectra are shifted with respect to the normalized frequency for better visibility. Adapted from Ref. [21].

poorly understood. An insight into the generation of higher harmonics is gained by using the point mass model to derive some analytical or semianalytical expressions. The first hypothesis is to assume that the tip motion in the presence of a force $F(d)$ is described by

$$z = z_0 + \sum_{n\ 1}^{\infty} A_n \cos(n\omega t \quad \phi_n). \tag{9.1}$$

In a three step process, an expression for A_n as a function of the physical parameters is obtained. First, the deflection z is replaced by the above expression and inserted into the equation of motion (Equation 4.2). Then, the resulting equation is multiplied by $\cos(n\omega t)$. Finally, by integrating over a period, it is found that

$$\omega_0^2 A_n \frac{\pi}{\omega} \quad n^2\omega^2 A_n \frac{\pi}{\omega} = \frac{\omega_0^2}{k}\int_0^T F_{\mathrm{ts}}(d)\cos(n\omega t \quad \phi_n). \tag{9.2}$$

Similarly, by repeating the process with $\sin(n\omega t)$ another independent equation is obtained,

$$\frac{\omega_0}{Q} n\omega A_n \frac{\pi}{\omega} = \frac{\omega_0^2}{k}\int_0^T F_{\mathrm{ts}}(d)\sin(n\omega t \quad \phi_n). \tag{9.3}$$

From Equations 9.2 and 9.3 is deduced

$$A_n = S\frac{\omega_0}{k}\sqrt{\left(\int_0^T F_{ts}(d)\cos(n\omega t)\mathrm{d}t\right)^2 + \left(\int_0^T F_{ts}(d)\sin(n\omega t)\mathrm{d}t\right)^2}, \tag{9.4}$$

where the term S is given by

$$S = \left(\sqrt{\frac{n^2}{Q^2} + \frac{\pi^2\omega_0^2}{\omega^2}\left(1 \quad \frac{n^2\omega^2}{\omega_0^2}\right)^2}\right)^{-1}. \tag{9.5}$$

The process used to deduce the above equations is equivalent to applying the virial dissipation method described in Chapter 4 (Herruzo, E.T. and García, R., unpublished.).

Equation 9.4 shows that the presence of a higher harmonic component depends on the spatial projection of its wave form on the interaction force. In a first approxi mation, the projection could be parameterized in terms of two parameters, the peak force and the contact time.

From Equation 9.5, it is also deduced that for Q values above 5 and $\omega \approx \omega_0$ the amplitude of a given harmonic decays with its order,

$$S \approx \frac{1}{\pi n^2} \quad \text{and} \quad n > 3. \tag{9.6}$$

9.2.2
Coupling Eigenmodes and Harmonics

The amplitude of the higher harmonics decreases with the increasing order. This result has been deduced within the framework of a point mass model. However, with some corrections, it also applies to cantilever beams. For example, whenever a harmonic frequency ($n\omega$) is close to a resonant frequency (ω_i), the amplitude of the harmonic is enhanced with respect to the neighboring harmonics. This is because of the resonant amplification in the vicinity of an eigenmode. This is the case for a rectangular and uniform cantilever where the frequency of the 2nd eigenmode $\omega_2 = 6.27\omega_0$ is very close to the sixth harmonic of the fundamental mode ($6\omega_0$) (Figure 9.1).

Tuning an eigenmode and a harmonic can be accomplished by modifying the mass distribution along the cantilever. A modification of the cantilever geometry changes its transfer function; however, it is possible to perform some modifications in such a way that the changes are confined to the transfer function of a given flexural mode. For example, by removing mass from a region where a given mode has a much higher curvature than the fundamental mode, the frequency of the higher eigenmode is greatly modified. However, the frequency of the fundamental mode remains practically unaffected. Following this approach, Sahin *et al.* [16] made a square hole 1/3 from the free end of a rectangular cantilever (Figure 9.3). The process enhanced the amplitude of the 16th harmonic and, at the same time,

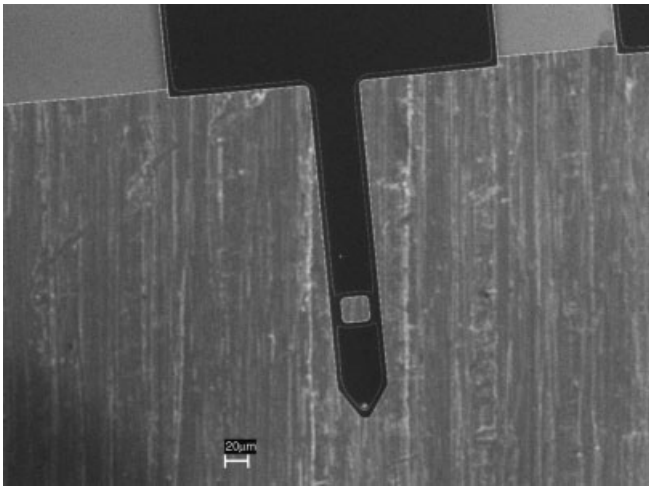

Figure 9.3 Scanning electron micrograph image of a harmonic cantilever. The hole in the cantilever is designed to match the frequency of the third order flexural mode and that of the 16th harmonic of the fundamental mode. Adapted from Ref. [16].

brought the frequency of the 16th harmonic very close to the 3rd eigenmode frequency.

9.2.3
Imaging Beyond the Fundamental Mode

By far, amplitude modulation AFM experiments are performed by exciting the cantilever at its fundamental resonance or at a frequency very close to it. At first glance, the fundamental mode offers several advantages with respect to the higher resonances. It requires less sophisticated electronics because the frequency range is smaller. In addition, the optical sensitivity of the fundamental resonance is close to the static value, so the calibration procedures are easier to perform. On the other hand, the use of a higher resonance for imaging might offer some attractive features. The effective force constant of a higher eigenmode is higher than the fundamental value, thus the capture of the tip by the attractive surface forces might be avoided. For the same reason, a higher force constant favors the use of smaller amplitudes that eventually may lead to a higher spatial resolution. In addition, the relaxation time for a cantilever that has internal damping decreases with the mode order implying an overall faster response ($Q_i T_i < Q_{i-1} T_{i-1}$).

In the 1990s, AFM controllers could not cope with the data acquisition processes associated with excitation frequencies in the MHz regime. However, this is no longer an issue, so imaging at the second, third, or higher resonances has been demonstrated [24 31]. Nonetheless, this approach has not been pursued in earnest. Arguably, the most significant result to date has been the operation of an AM AFM under ultrahigh vacuum. This was achieved by exciting the 2nd cantilever resonance and using the amplitude of that resonance to establish the feedback mechanism [26].

On the other hand, imaging at higher resonances has been more thoroughly explored in frequency modulation AFM [27 31]. Atomic and molecular resolution images of several surfaces have been obtained [29 31].

The optical sensitivity depends on the mode that is used for imaging. The calibration of the optical sensitivity is somehow more complicated for higher modes than for the fundamental mode. Calibration methods for higher modes are discussed in detail in Chapters 2 and 5.

9.3 Bimodal AFM

In bimodal AFM, the cantilever is simultaneously excited by two driving forces. The excitation frequencies of the driving forces are tuned to match two of the flexural eigenmodes of the cantilever, usually the first and the second eigenmodes [32 35]. The output signal of the amplitude of the first mode is used to image the topography of the surface, exactly in the same way as in amplitude modulation AFM. An output signal of the second mode, either the amplitude or the phase shift, is used to map changes in mechanical, magnetic, or electrical properties of the surface (Figure 9.4).

Bimodal AFM offers a straightforward approach to separate topography from other interactions influencing the tip motion. Thus, the different resonances act as signal channels that allow accessing and separating material properties [36 38]. One remarkable aspect of bimodal AFM is its ability to achieve topographic and compo sitional contrast by applying forces below 100 pN. Low forces enable high resolution and noninvasive imaging of single biomolecules that are weakly absorbed to a mica surface (Figure 9.5). The straightforward approach to reduce the force exerted on the sample is to pull back the tip. This in turn reduces the topography and/or dissipation contrast carried out by the parameters of the AM AFM. However, under these conditions, bimodal AFM is still able to resolve the structure of the observed object.

The above property is illustrated by imaging the same system under the same conditions by amplitude modulation and bimodal AFM and comparing the resulting images. Figure 9.6 shows three images of an immunoglobulin G (IgG) antibody. All the images have been obtained by applying a peak force of about 90 pN. The AM AFM topography (left) and phase (right) images do not provide information on the antibody structure; however, the bimodal AFM image (second mode phase) resolves the three subunits of the protein.

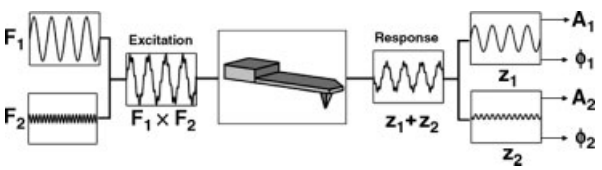

Figure 9.4 Scheme of the signal excitation and detection in bimodal AFM. The signals labeled as excitation and response correspond to experimental signals during bimodal AFM operation. Adapted from Ref. [34].

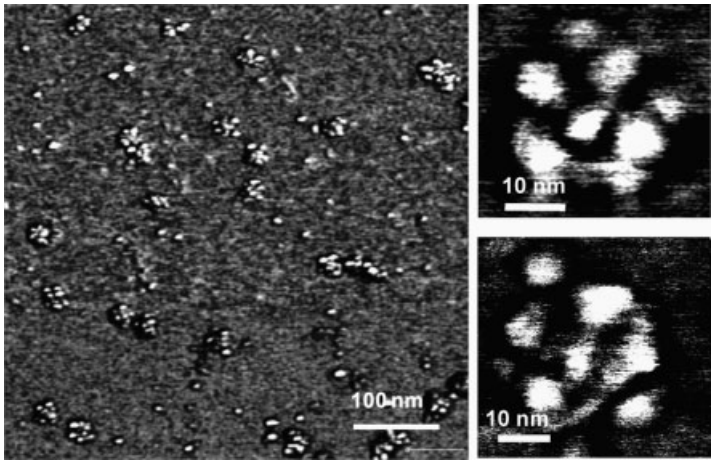

Figure 9.5 Bimodal AFM phase images of physisorbed immunoglobulin M (IgM) pentamers on a mica surface. The lateral panels show two individual pentamers extracted from the lower resolution panel. The high resolution images show the five subunits surrounding the central structure (J chain). Adapted from Ref. [35].

Bimodal AFM is compatible with air and liquid environments [33 36, 39]. It can be performed in the attractive [34 36] and repulsive [33, 40] interaction regimes, or can be used to control the transition between attractive and repulsive interaction regimes [41]. It is also compatible with the detection of different interactions such as mechanical, electrostatic [42 44], or magnetic [45]. Bimodal excitation has also been applied in frequency modulation AFM experiments in ultrahigh vacuum. An enhancement in atomic resolution images has been reported while imaging an ionic crystal surface KBr(001) [46].

Some cantilevers have been designed to enhance the response of a higher order resonance [36, 47]; however, bimodal AFM operation does not require the use of special cantilevers. In fact, the majority of the experiments have been performed with conventional cantilevers. Thus, the versatility and the sensitivity of bimodal excitation and detection have led to other applications such as the detection and imaging of the

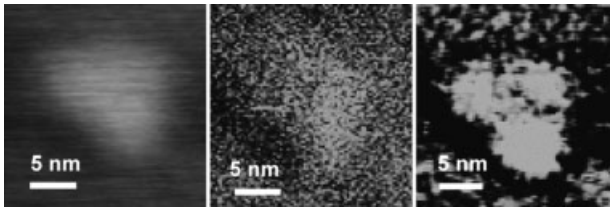

Figure 9.6 Comparison between amplitude modulation and bimodal AFM. From left to right, topography (first mode), phase image (first mode), and bimodal AFM (second mode phase) of a physisorbed IgG antibody. The images have been obtained with the same tip and the same peak force (~90 pN). In the tree images, the vertical scale has been optimized to achieve the best contrast. Adapted from Ref. [35].

eigenmodes of high frequency nanoelectromechanical systems. Specifically, it has been applied to image the waveforms of the resonances of suspended carbon nanotubes and graphene sheets [48, 49].

Multifrequency excitation and detection has also been used to supply the effective resonant frequency and the quality factor of the cantilever while an image is acquired [50]. In this case, the cantilever is excited at its free resonant frequency and two other frequencies close to the fundamental resonance. The output signal at the free resonant frequency is used to establish the feedback, while the signals associated with the other frequencies are combined to determine the quality factor and actual resonant frequency of the cantilever.

9.3.1
Intermodulation Frequencies

The concept of bimodal excitation has been extended to nonresonant frequencies, for example, two frequencies that are in the vicinity of a resonance [51, 52]. Under these conditions, when the tip is approached toward the surface, the nonlinear tip surface forces generate a new set of frequencies that bear the influence of the excitation frequencies. The new frequencies are called intermodulation products. These products form a series of peaks close to the fundamental resonance with spacing ($n(f_2 \quad f_1)$) from the two excitation frequencies (Figure 9.7). The intermodulation products depend on the tip surface distance; thus, they carry information on the local properties of the sample. Nonetheless, a significant theoretical effort remains to be made in order to relate the new set of frequencies to a change in a given property of the sample surface.

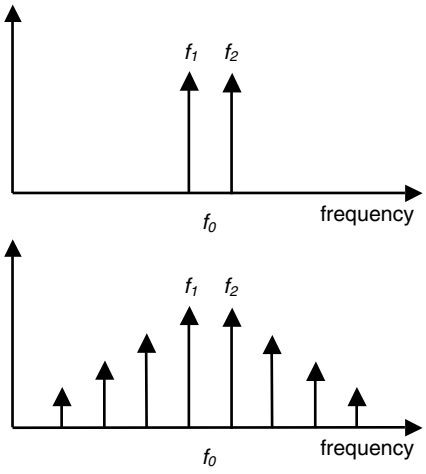

Figure 9.7 Intermodulation products. A cantilever that is driven with two frequencies f_1 and f_2 responds with an oscillation that is characterized by the excitation frequencies. The top panel shows the linear response of the cantilever away from the surface. The bottom panel illustrates the response in the presence of a nonlinear tip surface force. Adapted from Ref. [51].

9.4
Mode-Synthesizing Atomic Force Microscopy

Mode synthesizing AFM combines elements derived from ultrasonic [53 60] and dynamic [48, 61, 62] force microscopies to generate images of structures that lie below the surface of biological or synthetic materials. The method used by Passian and coworkers [63] is based on the simultaneous excitation of the sample and the probe (tip). The mechanical excitation of the sample generates waves that propagate through the sample. The mechanical waves are scattered by the internal features or structures of the material. As a consequence, the amplitude and the phase shift of the waves are modified by the interaction with the inner structures of the material. The modification depends on the local mechanical properties of the features. Eventually, the scattered waves emerge on the surface where they can influence the tip surface coupling.

In this method, the probe has a dual role. First, it collects the mechanical waves coming from beneath the surface to generate an image of the subsurface. Second, it mixes them with its own frequency components to generate a new set of frequencies. From these modes, the tip sample interaction synthesizes new modes, which can be seen in the plot of signal S versus frequency (Figure 9.8). The signal is Fourier transformed to obtain the frequency spectrum. The newly created frequency com ponents reflect the nanomechanical coupling between the probe and the sample. At

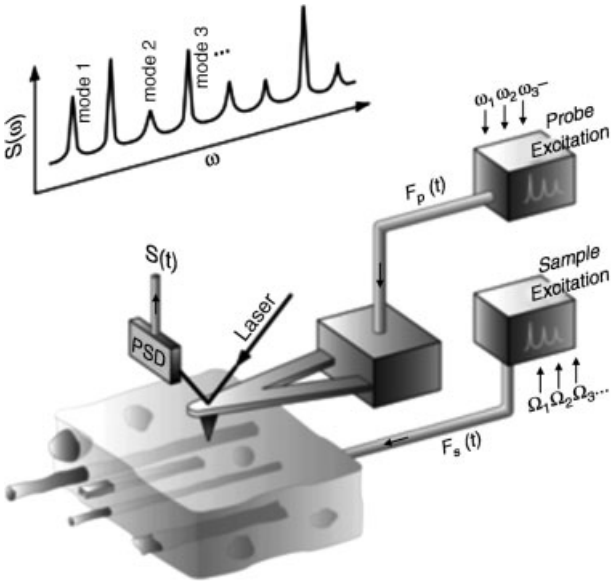

Figure 9.8 Scheme of mode synthesized AFM. The probe and the sample are mechanically excited by signals that contain a number of known frequency components. From these frequency components, the tip sample interaction synthesizes new modes (signal S) that carry information on the subsurface structures. Adapted from Ref. [62, 63].

the core of this coupling is the nonlinear character of the tip surface interaction force. The frequency of a given synthesized mode is a linear combination of the frequencies used to excite the tip and the sample. An image can be acquired from the phase or amplitude of the signal S by using a lock in amplifier that is referenced to one of the synthesized modes. Thus, several images of the subsurface structure can be generated, one for mode. Each image will reveal a different texture of the embedded and/or surface features of the sample.

The use of delocalized mechanical waves to generate images of the subsurface structure leaves several interpretation challenges. For example, it is not straightfor ward to transform frequency or phase shifts into specific information about the inner structure of the material.

9.5 Torsional Harmonic AFM

Torsional harmonic AFM enables one to generate a topographic image of the sample surface at the same time as the time varying forces are recorded [64 67]. The topographic image is a conventional amplitude modulation AFM image, that is, the cantilever is excited at its fundamental (flexural) resonance and the feedback acts on the amplitude of this mode. At the same time, the tip surface force is obtained by integrating the higher harmonics of the torsional signal (Section 5.8.2). Torsional harmonic AFM requires the use of specially designed cantilevers in order to excite the torsional oscillation and their higher harmonics [64]. Sahin has called them torsional harmonic cantilevers. In these cantilevers, the tip is offset from the cantilever axis. This design favors the existence of a torque around the axis of the cantilever. As a consequence, the nonlinear forces excite harmonics in both the flexural and the torsional signal. The presence of a rich harmonic spectrum in the torsional signal enables a quick calculation of the time varying force (Chapter 5). An appealing feature of this method is its ability to map the topography simultaneously with the measurement of a mechanical property, such as the Young's modulus. Figure 9.9 illustrates this property by showing the topography of a purple membrane at the same time as the effective Young's modulus (flexibility) is measured. Remarkably, Sahin *et al.* have measured the flexibility of the proteins within the membrane with sub 5 nm spatial resolution (Figure 9.10).

The ability of torsional harmonic AFM to spatially resolve mechanical properties, in particular, the effective Young's modulus of the interface, has been applied to detect and count hybridized DNA molecules. In this case, the technique measures the differences in the stiffness between unbounded single stranded DNA and those bounded with complementary target DNA molecules. In this way, torsional harmonic AFM can become an effective sensing approach to measure genetic material. The method has claimed sensitivity in the attomolar range, which is several orders of magnitude better than existing methods [68].

Torsional harmonic AFM should not be confused with torsional resonance AFM. In torsional resonance AFM, the cantilever is oscillated about its long axis and the

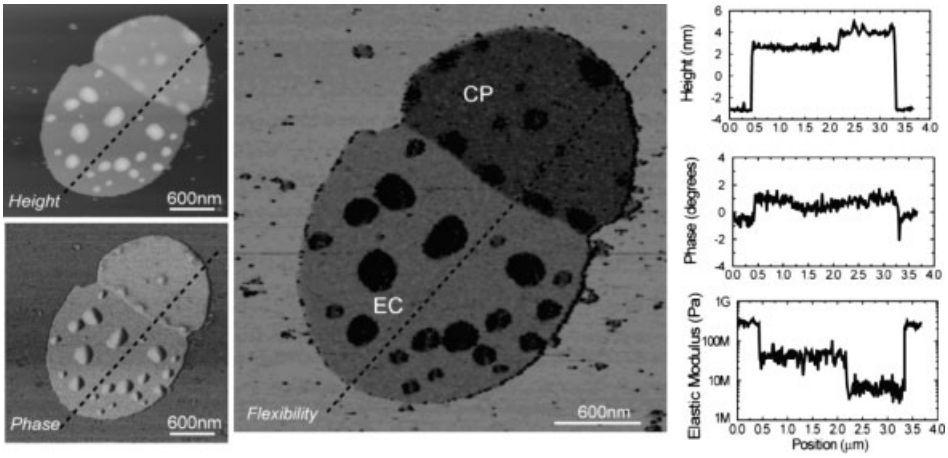

Figure 9.9 High resolution mapping of protein flexibility in purple membrane by torsional harmonic AFM. Height (top left), phase image (bottom left), and effective Young's modulus map of the cytoplasmic side (middle panel). The far right panel shows the numerical values of height, phase, and flexibility obtained, respectively, from the dashed lines shown in the image panels. Adapted from Ref. [67].

feedback is established on the amplitude of the driven torsional signal [69 75]. In fact, torsional resonance AFM is an AM AFM method where the excited and detected signals correspond to those of a torsional motion.

9.6 Band Excitation

The band excitation approach is a multifrequency excitation and detection method aimed at improving the ability to acquire different dynamic curves while the topography of the surface is recorded. The band excitation approach provides an alternative to standard lock in detection or phase locked loop detection methods and frequency sweeps by simultaneously exciting and detecting the response at all

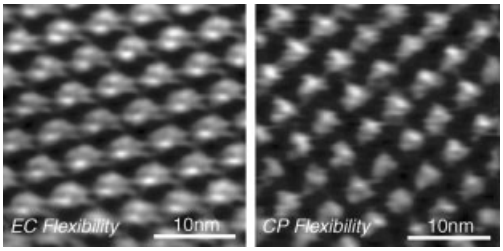

Figure 9.10 High resolution map of the flexibility of the proteins in the purple membrane. The image of the extracellular side is shown on the left and the image of the cytoplasmic side is shown on the right panel. Adapted from Ref. [67].

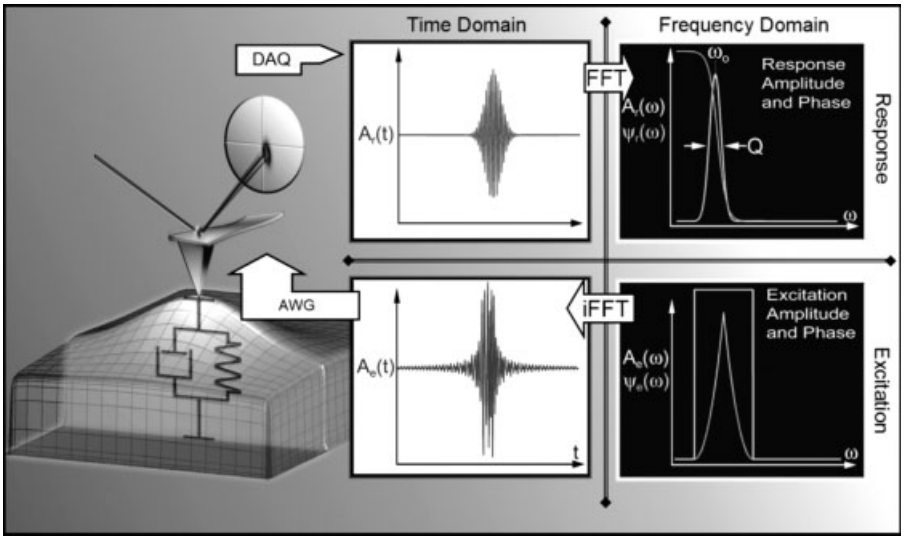

Figure 9.11 Scheme of band excitation AFM. The excitation signal is digitally synthesized to have a predefined amplitude and phase in a given frequency window. The cantilever response is detected and Fourier transformed at each pixel in an image. The ratio of the fast Fourier transforms of response and excitation signals yields the transfer function. The amplitude, the resonant frequency, and the *Q* factor can be determined at each point of the surface by fitting the response to the simple harmonic oscillator model. Adapted from Ref. [76].

frequencies within a band. Band excitation introduces a synthesized digital signal that spans a continuous band of frequencies, and monitors the response within the same or even larger frequency band [76 79]. The cantilever response is detected using high speed data acquisition methods and then Fourier transformed. The resulting amplitude frequency and phase frequency curves are collected at each point of the surface and stored in three dimensional data arrays. This data is analyzed to extract some of the relevant parameters that characterize the cantilever behavior (Figure 9.11). For example, in the single harmonic oscillator approximation, the resonant frequencies, the amplitude, and the *Q* factor are deconvoluted and stored as images and, in the case of adaptive control, can be used as a feedback signal in microscope operation.

Band excitation can be used in combination with other AFM techniques such as magnetic force microscopy or Kelvin probe AFM. It has been applied to the piezo response force microscopy and spectroscopy, in particular to probe the electromech nical coupling in soft biological systems in liquids by distinguishing among damping, Young's modulus, and electromechanical contributions [80, 81].

10
Beyond Topographic Imaging

10.1
Introduction

Any major microscopy aspires to be a technique that supplies more than topo graphic images. Phase imaging and some multifrequency AFM approaches are examples of the capability of amplitude modulation AFM to convey material properties that go beyond topography. In this chapter, scattering near field optical microscopy, topography and recognition imaging, and AFM oxidation nanolitho graphy illustrate the versatility and some future applications of amplitude modu lation AFM.

10.2
Scattering Near-Field Optical Microscopy

The invention of the STM stimulated a strong research activity toward developing an optical microscope that could break the Abbe's diffraction based resolution limit of about $\lambda/2$ [1 7]. From this activity emerged the scanning near field optical micro scope (SNOM). Near field optical microscopy can be performed with a metallic aperture that confines and transmits the near field emitted light [4, 5] or with an apertureless probe where the probe acts as a scatter center [6 8]. For a number of years, progress on near field microscopy was slow because of a combination of practical and fundamental factors. It was hard to fabricate reliable probes and the signal to noise ratio was far from optimum. The use of amplitude modulation AFM in scattering SNOM (s SNOM) has been a key factor in improving the signal to noise ratio, the spatial resolution, and the sensitivity [9 12]. Figure 10.1 shows the main elements of an s SNOM.

In scattering near field optical microscopy, the probe (tip) is polarized by an incoming electric field E_i perpendicular to the surface. The polarization of the tip induces an image dipole on the sample, which in turn induces an electrical field on

Amplitude Modulation Atomic Force Microscopy. Ricardo García

ISBN: 978-3-527-40834-4

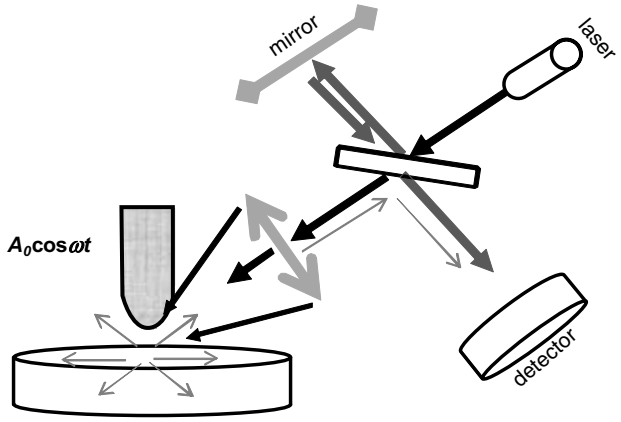

Figure 10.1 Scheme of s SNOM. A focused light beam illuminates the tip surface interface of an amplitude modulation AFM. By recording the scattered light in the backward direction, an optical image is generated. The tip oscillates at a frequency ω. As a consequence, the near field optical signal becomes modulated at the harmonics of tip's excitation frequency. Adapted from Ref. [9].

the tip (Figure 10.2). Keilman and Hillenbrand have found that the effective result is the presence of a scattered field given by [10]

$$E_s = \alpha_{eff} E_i \tag{10.1}$$

with the effective polarizability defined as

$$\alpha_{eff} = \frac{\alpha_t(1+\beta)}{1 - \frac{\alpha_t \beta}{16\pi(d+R)^3}} \tag{10.2}$$

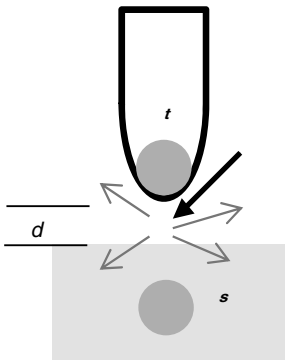

Figure 10.2 Scheme of the electromagnetic interaction in scattering near field optical microscopy. The tip is replaced by a point dipole that induces an image dipole on the sample.

and

$$\alpha_t = 4\pi R^3 \frac{\varepsilon_t \quad 1}{\varepsilon_t + 2}, \tag{10.3}$$

$$\beta = \frac{\varepsilon_s \quad 1}{\varepsilon_s + 2}. \tag{10.4}$$

The scattering light depends on the tip and surface dielectric constants at the wavelength of the incident light, the tip's radius, and the tip sample distance *d*. The dielectric properties of the tip and its geometry remain unchanged during the experiment. Thus, the scattered light reflects changes in the dielectric properties of the surface and the tip surface distance. The probing region is the gap between the tip apex and the sample. A critical issue in scattering near field optical microscopy is the presence of a strong background scattering. The intensity of the background scattered light is significantly larger than the scattered light coming from the regions of the tip closer to the sample surface because the laser spot is much larger than the probing region. As a consequence, the scattering light that carries information on the sample properties is buried in the background scattering.

The use of amplitude modulation AFM as a probe for SNOM has provided a solution to the above problem. Amplitude modulation AFM generates a sinusoidal variation of the gap distance with time; this in turn produces a strong modulation of the near field scattering. This is in contrast with the scattered light that emanates from the shaft of the tip that is barely modulated and therefore can be electronically eliminated from the detector signal. By taking the Fourier transform, the demodu lated components of the harmonic components $n\omega$ can be obtained.

The capability for material recognition and conductivity mapping of scattering SNOM is exemplified by imaging the cross section of a metal oxide semiconductor contact [11]. The infrared s SNOM images show a rich and distinctive contrast among all the components of the device. On the other hand, the AFM topographic image shows no hint of the device structure (Figure 10.3). The s SNOM image reveals the W contact, the interface between Si and SiO_2, and the presence of a very thin layer of Si_3N_4 ($\sim$10 nm). From its FWHM ($\sim$30 nm), a spatial resolution of $\lambda/333$ with $\lambda = 10.8\,\mu$m can be estimated. It is interesting to note that the near field amplitude

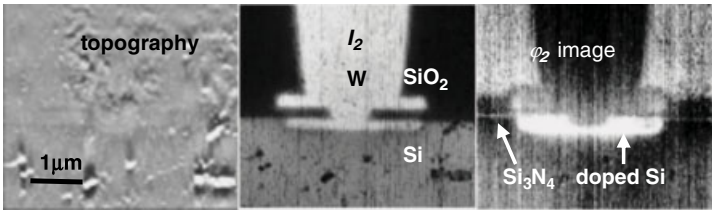

Figure 10.3 Topography and infrared s SNOM image of a cross section of a metal oxide semiconductor contact. The topographic image of the polished cross section shows no hint of the device structure (*left*). The infrared amplitude (*middle*) and phase (*right*) images show both distinct material and doping contrasts. Adapted from Refs [11,12].

and phase shift images carry complementary information. The highest infrared amplitudes occur at the metallic parts (W), while the phase contrast is more sensitive to changes in the doping concentration of the semiconductor.

10.3
Topography and Recognition Imaging

The force sensitivity together with the straightforward approach to capture force distance curves has been exploited to develop a method to measure inter and intramolecular interactions [13 21]. The method requires it to attach on the tip's surface a molecule (ligand) that has specific interactions with some molecules deposited on or belonging to the sample surface (receptor molecules). Molecule force spectroscopy is performed with a force microscope operated in the contact mode. Usually, single molecule force spectroscopy experiments are not accompanied by high spatial resolution images.

The use of functionalized tips in amplitude modulation AFM has led to the development of an imaging method that combines the sensitivity of force spectros copy to detect specific interactions with the high resolution imaging of AM AFM in liquid. The method developed by Hinterdorfer and coworkers is known as topog raphy and recognition imaging (TREC) [22 25]. This method requires it to split the oscillation into its top and the bottom parts. The bottom part is used to run feedback that generates the topography, while the top part is used to detect the presence of molecular recognition events (Figure 10.4).

Figure 10.5 shows an image of the specific binding events between the antibiotin antibodies and a biotin molecule attached via a distensible linker to a magnetically coated silicon nitride tip [26]. The topographic image (Figure 10.5a) reveals several antibodies deposited on top of pentacene islands. In the recognition image (Figure 10.5b), the binding events appear as black dots. The cross section along the white lines marked in the topography and recognition images shows that the recognition event is associated with a sudden decrease in the upper part of the oscillation. A comparison between the topography and the recognition cross sections indicates that some changes in the topography are not associated with binding events.

TREC relies on a subtle property of the cantilever dynamics in liquid. The tip's oscillation is asymmetric in the absence of specific interactions (Chapter 6). The

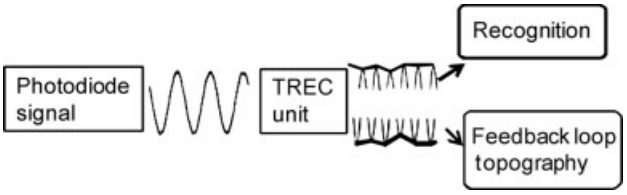

Figure 10.4 Scheme of the signal processing in topography and recognition imaging. The oscillation signal is split in its top and bottom parts. The top is used for recognition, while the bottom enters the feedback loop to generate the topography. Adapted from Ref. [23].

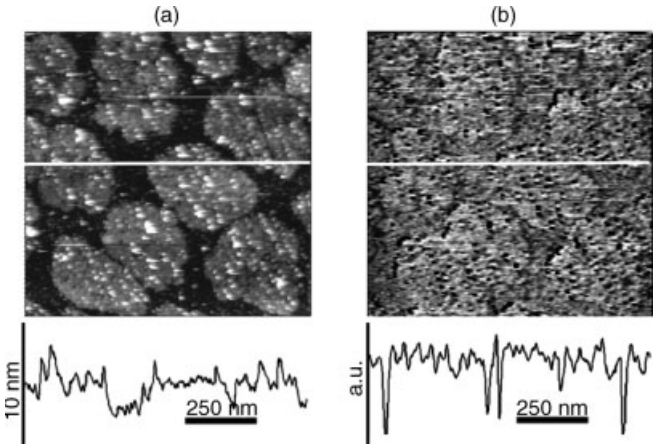

Figure 10.5 Topography (a) and recognition (b) images of antibiotin antibodies deposited on pentacene monolayer islands. The respective cross sections are taken along the white lines marked in the top images. A recognition event produces a sharp depression in the top part of the tip's oscillation. Adapted from Ref. [26].

repulsive tip surface forces modify more strongly the shape of the lower part of the oscillation than its top part. In contrast, when a tip tethered ligand binds to a molecule on the sample surface, the molecules and the tether are stretched during the upward movement of the tip. The stretching involves the transfer of mechanical energy from the cantilever to the molecule. This loss in the mechanical energy of the cantilever produces a decrease in the top peaks of the oscillation. A successful TREC experiment requires using a peak to peak amplitude value smaller than the combined length of the molecules and the linker.

10.3.1
Tip Functionalization

The biological ligands are not directly attached to the tip. They are tethered to a linker that is, in turn, attached to the tip [27]. The use of a linker is advantageous because it reduces the occurrence of multiple binding events. It is also useful in exploring several orientations of the ligand with respect to the receptor to enhance the probability of a binding event. The main steps of the tip's functionalization process are shown in Figure 10.6. First, the tip's apex is amine functionalized with amino propyltriethoxysilane (APTES) molecules by a vapor phase deposition method. In the second step, a linker is attached to the tip. Polyethylene glycol is a common linker in force spectroscopy. The linker is functionalized at both ends in order to be attached to the tip and to attach a ligand to it. An *N* hydroxysuccinimide ester on one end provides a way to form a stable bond with the amine terminated tip. The other functional group depends on the ligand. For example, an aldehyde group is suitable to form an amide bond with the amino groups present in many proteins.

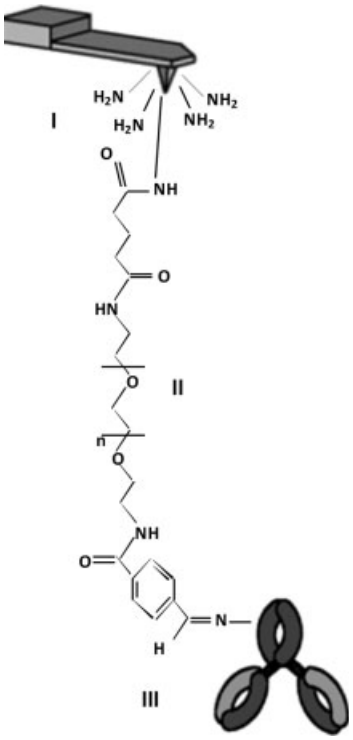

Figure 10.6 Scheme of tip's functionalization for a topography and recognition experiment. The first step involves the preparation of an amine terminated tip. In the second step, a linker is attached at the end of the tip. In the last step, a ligand is attached to the linker. Adapted from Ref. [27].

10.4
Nanofabrication by AFM

There is an astounding variety of tip based nanofabrication methods to pattern surfaces [28 42] or to make nanoscale devices [43 51]. In many of them such as nanomaching, thermomechanical writing, or dip pen nanolithography, the AFM is used in the contact mode. However, AM AFM makes a difference in AFM oxidation nanolithography by improving the reproducibility of the patterning process and reducing the minimum feature size [52, 53].

10.4.1
AFM Oxidation Nanolithography

Versatility and reproducibility are some of the features that characterize AFM oxidation. These features, together with an astonishing variety of materials ame

nable to anodic oxidation, explain the prominence of this method. Local oxidation patterns can be fabricated with either an STM or an AFM; however, it has been in combination with amplitude modulation AFM where oxidation nanolithography has reached its resolution and patterning limits. AFM oxidation nanolithography has several names. Sometimes, it is called AFM nanooxidation or AFM anodic oxidation. In some cases, more generic names such as local oxidation or scanning probe oxidation are used.

In AFM oxidation, the tip is used as a cathode and the water meniscus formed between the tip and the surface provides the electrolyte. The condensation of a water meniscus in the tip surface interface is usually driven by the application of an electrical field [53, 54]. The result is the formation of a nanometer size electro chemical cell (Figure 10.7). In AM AFM, it is possible to control the meniscus

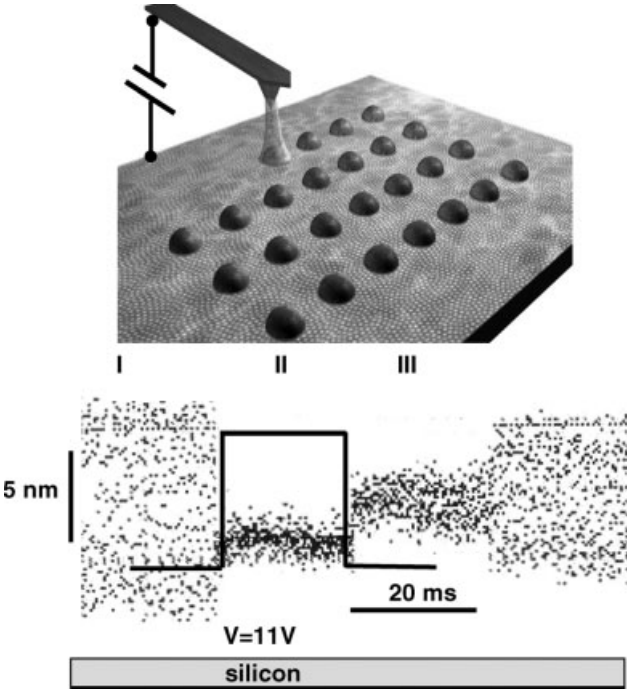

Figure 10.7 Scheme of AFM oxidation nanolithography (top panel). The bottom panel shows the tip's oscillation during AFM oxidation. Each point indicates the instantaneous value of the deflection. The oscillation appears as a forest of points because the period of the oscillation is shorter than the pulse duration. (I) Before the application of the voltage pulse. (II) The application of the pulse deflects the tip toward the sample and the amplitude is reduced. (III) The amplitude remains damped once the pulse is off. This is indicative of the formation of a water meniscus. The voltage pulse is plotted in thick black. Adapted from Ref. [55].

diameter down to 10–20 nm by changing the tip–surface gap distance [55]. This has led to the reproducible fabrication of sub 10 nm structures in Si and even smaller structures in titanium films. In contact AFM oxidation, the water meniscus size is defined by the tip's radius, the relative humidity, the temperature, and the surface energies.

A large number of materials have been oxidized with the force microscope, including silicon, compound III–V semiconductors, and silicon carbide; several metals such as titanium, tantalum, aluminum, molybdenum, nickel, and niobium; perovskite manganite thin films; dielectrics such as silicon nitride films; and organosilane self-assembled monolayers, dendritic objects, and carbonaceous films.

The kinetics of the oxidation process is dominated by the electrical field and the diffusion of the oxyanions [56, 57]. Very high fields of 1–5 V/nm are present during the oxidation process. As a consequence, the local oxide retains some trapped charges. The dot size depends linearly on the voltage strength, but the dot height shows a power law dependence of the type

$$h \sim (t/t_0)^{\gamma}, \tag{10.5}$$

where γ is in the 0.1–0.3 range. Voltage pulses usually change from experiment to experiment, but they are in 10–30 V and 0.005–1 s range, respectively. The local oxidation process is accompanied by an extremely small current. The value depends on the final dot size. Common values are in the subpicoampere regime [56].

The use of the noncontact regime in AFM oxidation has resulted in enhancing the tip's lifetime, which in turn has improved the repeatability of the process (Figure 10.7). AFM nanolithography requires switching between imaging and patterning modes.

The dynamics of the tip oscillation can be followed in real time (bottom panel in Figure 10.7). Stage (I) shows the tip's oscillation in the imaging mode. The application of a voltage pulse has two effects (II). It modifies the average value of the deflection by approaching the tip toward the sample. It also reduces the value of the amplitude. It is interesting to observe that once the pulse is off, the capillary force prevents the amplitude to reach its imaging value (III). It is only when microscope returns to the imaging mode that the meniscus is broken and the amplitude recovers its initial value.

10.4.2
Patterning and Devices

AFM oxidation enables the direct fabrication of three elements, dielectric barriers, masks for selective etching, and templates. A combination of these elements allows the fabrication of a wide range of patterns, molecular architectures, and devices. In some cases, the AFM is used in combination with other techniques such as

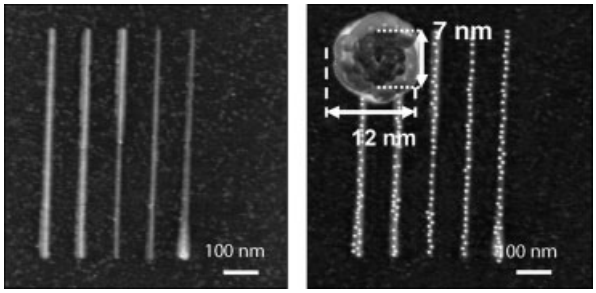

Figure 10.8 Nanoscale organization of ferritin molecules. AFM image of a parallel array of silicon oxide lines fabricated by AFM oxidation (*left*). Image of the distribution of the proteins on the nanopattern. The AFM image shows the ferritin aligned along the oxide lines. The width of the line matches the size of a single ferritin molecule (~12 nm). Adapted from Ref. [58].

photolithography, electron beam lithography, or plasma etching. The smallest features of the device are fabricated by AFM oxidation.

A remarkable application of AFM oxidation nanolithography is the fabrication of templates for the growth of molecular architectures [30, 34, 58]. Template growth is achieved by controlling and directing electrostatic interactions. Figure 10.8 shows the formation of an array of parallel strings of ferritin molecules [58]. The nanoscale organization of ferritin molecules involves four steps. First, the silicon surface is functionalized with an octadecyltrichlorosilane (OTS) monolayer. This replaces the OH groups that dominate the native silicon surfaces in air with a methyl terminated (CH_3) surface. Second, a region of the functionalized surface is locally oxidized. This process removes the OTS monolayer. Third, the sample is immersed in an APTES solution. Thus, we have generated a heterogeneous region that, at neutral pH, has positively charged stripes (APTES) and neutral regions (OTS). The last step involves the deposition of the proteins. The comparison between the nanopattern before and after the deposition of the proteins illustrates both the preferentiality and the selectivity of the deposition process. The attractive interaction between the positively charged stripes and the negatively charged proteins gives the preferentiality in the deposition process.

The fabrication of silicon nanowire field effect transistors illustrates the ability of AFM oxidation nanolithography to fabricate nanoelectronic devices. Local oxidation defines a narrow silicon dioxide mask on top of a silicon on insulator substrate. The mask, a long and narrow stripe of silicon dioxide, is fabricated by applying a sequence of voltage pulses between the AFM tip and the silicon surface. The next step involves the etching of the unmasked silicon by plasma etching. After etching, the nanowire is contacted to micrometer size platinum source and drain contacts.

Figure 10.9 shows a nanowire that in its narrowest section is about 14 nm in width and 36 nm in height [52]. In this figure, the Si nanowire has a section with the shape of

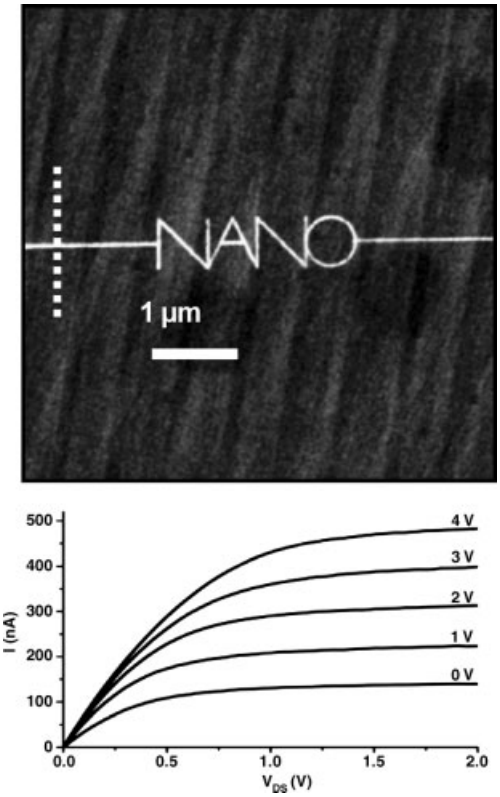

Figure 10.9 Image of a Si nanowire transistor fabricated by AFM oxidation nanolithography. The nanowire combines linear and circular regions (top panel). The output characteristics of the Si nanowire field effect transistor are shown in the bottom panel. Adapted from Ref. [52].

the term "NANO," that is, it includes linear and circular elements. The presence of a gate electrode transforms the nanowire into a nanoscale field effect transistor. The output characteristics of the transistor are shown in the bottom panel. At low voltages, the nanowire shows an ohmic response.

References

1 Wood, J. (2008) The top ten advances in materials science. *Mater. Today*, **11**, 40.
2 Ball, P. (2008) Material witness: greatest hits. *Nat. Mater.*, **7**, 102.
3 Binnig, G., Rohrer, H., and Gerber, C. (1982) Surface studies by scanning tunneling microscopy. *Phys. Rev. Lett.*, **49**, 57.
4 Binnig, G. and Rohrer, H. (1983) Scanning tunneling microscopy. *Surf. Sci.*, **126**, 236.
5 Binnig, G., Quate, C.F., and Gerber, C. (1986) Atomic force microscope. *Phys. Rev. Lett.*, **56**, 930.
6 Rugar, D. and Hansma, P. (1990) Atomic force microscopy. *Phys. Today*, **43**, 23.
7 Martin, Y., Williams, C.C., and Wickramasinghe, H.K. (1987) Atomic force microscope: force mapping and profiling on a sub 100 angstrom scale. *J. Appl. Phys.*, **61**, 4723.
8 McClelland, G.M., Erlandsson, R., and Chiang, S. (1987) *Review of Progress in Nondestructive Evaluation*, vol. **6B** (eds D.O. Thompson and D.E. Chimenti), Plenum Press, New York.
9 Martin, Y. and Wickramasinghe, H.K. (1987) Magnetic imaging by force microscopy with 1000 Å resolution. *Appl. Phys. Lett.*, **50**, 1455.
10 Terris, B.D., Stern, J.E., Rugar, D., and Mamin, H.J. (1989) Contact electrification using force microscopy. *Phys. Rev. Lett.*, **63**, 2669.
11 Nonnenmacher, M., O'Boyle, M.P., and Wickramasinghe, H.K. (1991) Kelvin probe force microscopy, *Appl. Phys. Lett.*, **58**, 2921.
12 Radmacher, M., Fritz, M., Hansma, H.G., and Hansma, P.K. (1994) Direct observation of enzyme activity with the atomic force microscope. *Science*, **265**, 1577.
13 Fritz, M., Radmacher, M., Cleveland, J.P., Allersma, M.W., Stewart, R.J., Gieselmann, R., Janmey, P., Schmidt, C.F., and Hansma, P.K. (1995) Imaging globular and filamentous proteins in physiological buffer solutions with tapping mode atomic force microscopy. *Langmuir*, **11**, 3529.
14 Leuba, S.H., Yang, G.L., Robert, C., Samorí, B., Vanholde, K., Zlatanova, J., and Bustamante, C. (1994) 3 dimensional structure of extended chromatin fibers as revealed by tapping mode scanning force microscopy. *Proc. Natl. Acad. Sci. USA*, **91**, 11621.
15 Bustamante, C. and Keller, D. (1995) Scanning force microscopy in biology. *Phys. Today*, **12**, 32.
16 Rivetti, C., Guthold, M., and Bustamante, C. (1996) Scanning force microscopy of DNA deposited onto mica: equilibration versus kinetic trapping studied by statistical polymer chain analysis. *J. Mol. Biol.*, **264**, 919.
17 Lyubchenko, Y.L. and Shlyakhtenko, L.S. (1997) Visualization of supercoiled DNA with atomic force microscopy *in situ*. *Proc. Natl. Acad. Sci. USA*, **94**, 496.
18 Anselmetti, D., Luthi, R., Meyer, E., Richmond, T., Dreier, M., Frommer, J.E., and Gundherodt, H.J. (1994) Attractive mode imaging of biological materials with dynamic force microscopy. *Nanotechnology*, **5**, 87.

Amplitude Modulation Atomic Force Microscopy. Ricardo García

ISBN: 978-3-527-40834-4

19 Zhong, Q., Inniss, D., Kjoller, K., and Elings, V.B. (1993) Fractured polymer/silica fiber surface studied by tapping mode atomic force microscopy. *Surf. Sci. Lett.*, **290**, L688.

20 Spatz, J.P., Sheiko, S., and Moller, M. (1996) Ion stabilized copolymer micelles: film formation and intermicellar interaction. *Macromolecules*, **29**, 3220.

21 Leclere, P., Lazzaroni, R., and Bredas, J.L. (1996) Microdomain morphology analysis of block copolymers by atomic force microscopy with phase detection imaging. *Langmuir*, **12**, 4317.

22 Magonov, S.N. and Reneker, D.H. (1997) Characterization of polymer surfaces with atomic force microscopy. *Annu. Rev. Mater. Sci.*, **27**, 175.

23 Bar, G., Thomann, Y., Brandsch, R., Cantow, H.J., and Whangbo, M.H. (1997) Factors affecting the height and phase images in tapping mode atomic force microscopy. Study of phase separated polymer blends of poly(ethene *co* styrene) and poly(2,6 dimethyl 1,4 phenylene oxide). *Langmuir*, **13**, 3807.

24 Scott McLean, R. and Sauer, B.B. (1997) Tapping mode AFM studies using phase detection for resolution of nanophases in segmented polyurethanes and other block copolymers. *Macromolecules*, **30**, 8314.

25 Meyer, G. and Amer, N.M. (1988) Novel optical approach to atomic force microscopy. *Appl. Phys. Lett.*, **53**, 1045.

26 Alexander, S., Hellemans, L., Marti, O., Schneir, J., Elings, V., and Hansma, P.K. (1989) An atomic resolution atomic force microscope implemented using an optical lever. *J. Appl. Phys.*, **65**, 164.

27 Albrecht, T.R., Akamine, S., Carver, T.E., and Quate, C.F. (1990) Microfabrication of cantilever styli for the atomic force microscope. *J. Vac. Sci. Technol. A*, **8**, 3386.

28 Walter, O., Bayer, T., and Greshner, J. (1991) Micromachined silicon sensors for scanning probe microscopy. *J. Vac. Sci. Technol. B*, **9**, 1353.

29 MultiMode, Digital Instruments, Santa Barbara (1993).

30 Hansma, P.K., Cleveland, J.P., Radmacher, M., Walters, D.A., Hillner, P.E., Benazilla, M., Fritz, M., Hansma, H.G., Prater, C.B., Massie, J., Fukunaga, L., Gurley, J., and Elings, V. (1994) Tapping mode AFM in liquids. *Appl. Phys. Lett.*, **64**, 1738.

31 Putman, C.A.J., Van der Werf, K.O., De Grooth, B.G., Van Hulst, N.F., and Greve, J. (1994) Tapping mode atomic force microscopy in liquid. *Appl. Phys. Lett.*, **64**, 2454.

32 Kasas, S., Thomson, N.H., Smith, B.L., Hansma, H.G., Zhu, X.S., Guthold, M., Bustamante, C., Kool, E.T., Kashlev, M., and Hansma, P.K. (1997) *Escherichia coli* RNA polymerase activity observed using atomic force microscopy. *Biochemistry*, **36**, 461.

33 Han, W., Lindsay, S.M., and Jing, T. (1996) A magnetically driven oscillating probe microscope for operation in liquids. *Appl. Phys. Lett.*, **69**, 4111.

34 Babcok, K.L. and Prater, C.B. (1995) Phase imaging: beyond topography, Digital Instruments, Santa Barbara; technical application note available at www.veeco.com.

35 Chernoff, D.A. (1995) High resolution chemical mapping using tapping mode AFM with phase contrast. *Proc. Microsc. Microanal.*, 888.

36 Tamayo, J. and Garcia, R. (1996) Deformation, contact time and phase contrast in tapping mode scanning force microscopy. *Langmuir*, **12**, 4430.

37 Perezmurano, F., Abadal, G., Barniol, N., Aymerich, X., Servat, J., Gorostiza, P., and Sanz, F. (1995) Nanometre scale oxidation of Si(100) surfaces by tapping mode atomic force microscopy. *J. Appl. Phys.*, **78**, 6797.

38 Garcia, R., Calleja, M., and Rohrer, H. (1999) Patterning of silicon surfaces with noncontact atomic force microscopy: field induced formation of nanometer size water bridges. *J. Appl. Phys.*, **86**, 1898.

39 Walters, D.A., Cleveland, J.P., Thomson, N.H., Hansma, P.K., Wendman, M.A., Gurley, G., and Elings, V. (1996) Short cantilevers for atomic force microscopy. *Rev. Sci. Instrum.*, **67**, 3583.

40 Viani, M.B., Schaffer, T.E., and Paloczi, G.T. *et al.* (1999) Fast imaging and fast force spectroscopy of single biopolymers

with a new atomic force microscope designed for small cantilevers. *Rev. Sci. Instrum.*, **70**, 4300.

41 Chen, J., Workman, R.K., Sarid, D., and Hoper, R. (1994) Numerical simulations of a scanning force microscope with a large amplitude vibrating cantilever. *Nanotechnology*, **5**, 199.

42 Winkler, R.G., Spatz, J.P., Sheiko, S., Moller, M., Reineker, P., and Marti, O. (1996) Imaging material properties by resonant tapping force microscopy: a model investigation. *Phys. Rev. B*, **54**, 8908.

43 Burnham, N.A., Behrend, O.P., Oulevey, F., Gremaud, G., Gallo, P.J., Gourdon, D., Dupas, E., Kulik, A.J., Pollock, H.M., and Briggs, G.A.D. (1997) How does a tip tap? *Nanotechnology*, **8**, 67.

44 Anczykowski, B., Kruger, D., and Fuchs, H. (1996) Cantilever dynamics in quasinoncontact force microscopy: spectroscopic aspects. *Phys. Rev. B*, **53**, 15485.

45 Khule, A., Sorensen, A.H., and Bohr, J. (1997) Role of attractive forces in tapping tip force microscopy. *J. Appl. Phys.*, **81**, 6562.

46 Garcia, R. and San Paulo, A. (1999) Attractive and repulsive tip sample interaction regimes in tapping mode atomic force microscopy. *Phys. Rev. B*, **60**, 4961.

47 Tamayo, J. and Garcia, R. (1997) Effects of elastic and inelastic interactions on phase contrast images in tapping mode scanning force microscopy. *Appl. Phys. Lett.*, **71**, 2394.

48 Cleveland, J.P., Anczykowski, B., Schmid, A.E., and Elings, V.B. (1998) Energy dissipation in tapping mode atomic force microscopy. *Appl. Phys. Lett.*, **72**, 2613.

49 Tamayo, J. and Garcia, R. (1998) Relationship between phase shift and energy dissipation in tapping mode scanning force microscopy. *Appl. Phys. Lett.*, **73**, 2926.

50 Lantz, M., Liu, Y.Z., Cui, X.D., Tokumoto, H., and Lindsay, S.M. (1999) Dynamic force microscopy in fluid. *Surf. Interface Anal.*, **27**, 354.

51 Nony, L., Boisgard, R., and Aime, J.P. (1999) Nonlinear dynamical properties of an oscillating tip cantilever system in tapping mode. *J. Chem. Phys.*, **111**, 1615.

52 Garcia, R. and Paulo, A.S. (2000) Dynamics of a vibrating tip near or in intermittent contact with a surface. *Phys. Rev. B*, **61**, R13381.

53 Sebastian, A., Salapaka, M.V., Chen, D.J., and Cleveland, J.P. (2001) Harmonic and power balance tools for tapping mode atomic force microscope. *J. Appl. Phys.*, **89**, 6473.

54 Lee, S.I., Howell, S.W., Raman, A., and Reifenberger, R. (2002) Nonlinear dynamics of microcantilevers in tapping mode atomic force microscopy: a comparison between theory and experiment. *Phys. Rev. B*, **66**, 115409.

55 Stark, R.W. and Heckel, W.M. (2000) Fourier transformed atomic force microscopy: tapping mode atomic force microscopy beyond the Hookian approximation. *Surf. Sci.*, **457**, 219.

56 Rodriguez, T.R. and Garcia, R. (2002) Tip motion in amplitude modulation (tapping mode) atomic force microscopy: comparison between continuous and point mass models. *Appl. Phys. Lett.*, **80**, 1646.

57 Sahin, O., Quate, C.F., Sogaard, O., and Atalar, A. (2004) Resonant harmonic response in tapping mode atomic force microscopy. *Phys. Rev. B*, **69**, 165416.

58 Stark, M., Stark, R.W., Heckl, W.H., and Guckenberger, R. (2002) Inverting dynamic force microscopy: from signals to time resolved interaction forces. *Proc. Natl. Acad. Sci. USA*, **99**, 8473.

59 Rodriguez, T.R. and Garcia, R. (2004) Compositional mapping of surfaces in atomic force microscopy by excitation of the second normal mode of the cantilever. *Appl. Phys. Lett.*, **84**, 449.

60 Lee, M.H. and Jhe, W. (2006) General theory of amplitude modulation atomic force microscopy. *Phys. Rev. Lett.*, **97**, 036104.

61 Holscher, H. (2006) Quantitative measurement of tip sample interactions in amplitude modulation AFM. *Appl. Phys. Lett.*, **89**, 123109.

62 Moller, C., Allen, M., Elings, V., Engel, A., and Muller, D.J. (1999) Tapping mode atomic force microscopy produces

faithful high resolution images of protein surfaces. *Biophys. J.*, **77**, 1150.

63 Klinov, D. and Magonov, S. (2004) True molecular resolution in tapping mode atomic force microscopy with high resolution probes. *Appl. Phys. Lett.*, **84**, 2697.

64 Ando, T., Kodera, N., Takai, E., Maruyama, D., Saito, K., and Toda, A. (2001) A high speed atomic force microscope for studying biological macromolecules. *Proc. Natl. Acad. Sci. USA*, **98**, 12468.

65 Stroh, C., Wang, H., Bash, R., Ashcroft, B., Nelson, J., Gruber, H., Lohr, D., Lindsay, S.M., and Hinterdorfer, P. (2004) Single molecule recognition imaging microscopy. *Proc. Natl. Acad. Sci. USA*, **101**, 12503.

66 Stroh, C.M., Ebner, A., Geretschlager, M., Freudenthaler, G., Kienberger, F., Kamruzzahan, A.S.M., Smith Gil, S.J., Gruber, H.J., and Hinterdorfer, P. (2004) Simultaneous topography and recognition imaging using force microscopy. *Biophys. J.*, **87**, 1981.

67 Martinez, N.F., Patil, S., Lozano, J.R., and Garcia, R. (2006) Enhanced compositional sensitivity in atomic force microscopy by the excitation of the first two flexural modes. *Appl. Phys. Lett.*, **89**, 153115.

68 Proksch, R. (2006) Multifrequency, repulsive mode amplitude modulated atomic force microscopy. *Appl. Phys. Lett.*, **89**, 113121.

69 Martinez, N.F., Lozano, J.R., Herruzo, E.T., Garcia, F., Ritchter, C., Sulzbach, T., and Garcia, R. (2008) Bimodal atomic force microscopy imaging of isolated antibodies in air and liquids. *Nanotechnology*, **19**, 384011.

70 Preiner, J., Tang, J., Pastushenko, V., and Hinterdorfer, P. (2007) Higher harmonic atomic force microscopy: imaging of biological membranes in liquid. *Phys. Rev. Lett.*, **99**, 046102.

71 Melcher, J., Xu, X., Raman, A., Carrasco Pulido, C., Gomez Herrero, J., de Pablo, P.J., and Carrascosa, J.L. (2009) Origins of phase contrast in the atomic force microscope in liquids. *Proc. Natl. Acad. Sci. USA*, **106**, 13655.

72 Sahin, O., Quate, C.F., Solgaard, O., and Atalar, A. (2007) An atomic force microscope tip designed to measure time varying nanomechanical forces. *Nat. Nanotechnol.*, **2**, 507.

73 Dong, M., Husale, S., and Sahin, O. (2009) Determination of protein structural flexibility by microsecond force spectroscopy. *Nat. Nanotechnol.*, **4**, 514.

74 Platz, D., Tholén, E.A., and Haviland, D.B. (2008) Intermodulation atomic force microscopy. *Appl. Phys. Lett.*, **92**, 153106.

75 Jesse, S., Kalinin, S.V., Proksch, R., Baddorf, A.P., and Rodriguez, B.J. (2007) The band excitation method in scanning probe microscopy for rapid mapping of energy dissipation on the nanoscale. *Nanotechnology*, **18**, 435503.

76 Basak, S. and Raman, A. (2007) Dynamics of tapping mode atomic force microscopy in liquids: theory and experiments. *Appl. Phys. Lett.*, **91**, 064107.

77 Xu, X. and Raman, A. (2007) Comparative dynamics of magnetically, acoustically, and Brownian motion driven microcantielvers in liquids. *J. Appl. Phys.*, **102**, 034303.

78 Herruzo, E.T. and Garcia, R. (2007) Frequency response of an atomic force microscope in liquids and air: magnetic versus acoustic excitation. *Appl. Phys. Lett.*, **91**, 143113.

79 De Beer, S., van den Ende, D., and Mugele, F. (2008) Atomic force microscopy dynamics in liquid in the presence of tip sample interaction. *Appl. Phys. Lett.*, **93**, 253106.

80 Lozano, J.R. and Garcia, R. (2008) Theory of multifrequency AFM. *Phys. Rev. Lett.*, **100**, 076102.

81 Li, H., Chen, Y., and Dai, L. (2008) Concentrated mass cantilever enhances multiple harmonics in tapping mode atomic force microscopy. *Appl. Phys. Lett.*, **92**, 151903.

82 Stark, R. (2009) Dynamics of repulsive dual frequency atomic force microscopy. *Appl. Phys. Lett.*, **94**, 063109.

83 Marth, M., Maier, D., Honerkamp, J., Brandsch, R., and Bar, G. (1999) A unifying view on some experimental effects in tapping mode atomic force microscopy. *J. Appl. Phys.*, **85**, 7030.

84 Garcia, R. and Perez, R. (2002) Dynamic atomic force microscopy methods. *Surf. Sci. Rep.*, **47**, 197.

85 Gotsmann, B., Seidel, C., Anczykowski, B., and Fuchs, H. (1999) Conservative and dissipative tip sample forces probed with dynamic AFM. *Phys. Rev.*, **60**, 11051.

86 Albrecht, T.R., Grutter, P., Horne, D., and Rugar, D. (1991) Frequency modulation detection using high *Q* cantilevers for enhanced force microscope sensitivity. *J. Appl. Phys.*, **69**, 668.

87 Giessibl, F.J. (2003) Advances in atomic force microscopy. *Rev. Mod. Phys.*, **75**, 949.

88 Giessibl, F.J. (1995) Atomic resolution of the silicon (111) (7 × 7) surface by atomic force microscopy. *Science*, **267**, 68.

89 Kitamura, S. and Itwasuki, M. (1995) Observation of 7 × 7 reconstructed structure on the silicon (111) surface using ultra high vacuum non contact atomic force microscopy. *Jpn. J. Appl. Phys.*, **34**, L145.

90 Bennewitz, R., Foster, A.S., Kantorovich, L.N., Bammerlin, M., Loppacher, C., Schar, S., Guggisberg, M., Meyer, E., and Shluger, A.L. (2000) Atomically resolved edges and kinks of NaCl islands on Cu(111): experiment and theory. *Phys. Rev. B*, **62**, 2074.

91 Barth, C. and Reichling, M. (2001) Imaging the atomic arrangements on the high temperature reconstructed α Al_2O_3 surface. *Nature*, **414**, 54.

92 Kawai, S. and Kawakatsu, H. (2006) Atomically resolved dynamic force microscopy operating at 4.7 MHz. *Appl. Phys. Lett.*, **88**, 133103.

93 Gross, L., Mohn, F., Moll, N., Liljeroth, P., and Meyer, G. (2009) The chemical structure of a molecule resolved by atomic force microscopy. *Science*, **325**, 1110.

94 Ternes, M., Lutz, C.P., Hirjibehedin, C.F., Giessibl, F.J., and Heinrich, A.J. (2008) The force needed to move an atom on a surface. *Science*, **319**, 1066.

95 Sugimoto, Y., Pou, P., Abe, M., Jelinek, P., Perez, R., Morita, S., and Custance, O. (2007) Chemical identification of individual surface atoms by atomic force microscopy. *Nature*, **446**, 64.

96 Albers, B.J., Schwendemann, T.C., Baykara, M.Z., Pilet, N., Liebmann, M., Altman, E.I., and Schwarz, U.D. (2009) Three dimensional imaging of short range chemical forces with picometre resolution. *Nat. Nanotechnol.*, **307**, 4.

97 Fukuma, T., Chi, T., Kobayashi, K., Yamada, H., and Matsushige, K. (2005) True molecular resolution imaging by frequency modulation atomic force microscopy in various environments. *Appl. Phys. Lett.*, **86**, 034103.

98 Yamada, H., Kobayashi, K., Fukuma, T., Hirata, Y., Kajita, T., and Matsushige, K. (2009) Molecular resolution imaging of protein molecules in liquid using frequency modulation atomic force microscopy. *Appl. Phys. Lett.*, **2**, 095007.

99 Higgins, M.J., Sader, J.E., and Jarvis, S.P. (2006) Frequency modulation atomic force microscopy reveals individual intermediates with each unfolded I27 titin domain. *Biophys. J.*, **90**, 640.

100 Hoogenboom, B.W., Hug, H. J., Pellmont, Y., Martin, S., Frederix, P.L.T.M., Fotiadis, D., and Engel, A. (2006) Quantitative dynamic mode scanning force microscopy in liquid. *Appl. Phys. Lett.*, **88**, 193109.

101 Yang, C.W., Hwang, I.S., Chen, Y.F., Chang, C.S., and Tsai, D.P. (2007) Imaging of soft matter with tapping mode atomic force microscopy and non contact mode atomic force microscopy. *Nanotechnology*, **18**, 084009.

102 Palacios Lidón, E., Pérez García, B., and Colchero, J. (2009) Enhancing dynamic scanning force microscopy in air: as close as possible. *Nanotechnology*, **20**, 085707.

103 Kienberger, F., Mueller, H., Pastushenko, V., and Hinterdorfer, P. (2004) Following single antibody binding to purple membranes in real time. *EMBO Rep.*, **5**, 579.

104 ISI Web of Knowledge (2009).

Chapter 2

1 Ando, T., Uchihashi, T., and Fukuma, T. (2008) High speed atomic force microscopy for nano visualization of dynamic biomolecular processes. *Prog. Surf. Sci.*, **83**, 337.

2 Meyer, G. and Amer, N.M. (1988) Novel optical approach to atomic force microscopy. *Appl. Phys. Lett.*, **53**, 1045 1047.

3 Alexander, S., Hellemans, L., Marti, O., Schneir, J., Elings, V., and Hansma, P.K. (1989) An atomic resolution atomic force microscope implemented using an optical lever. *J. Appl. Phys.*, **65**, 164.

4 Gould, S.A.C., Drake, B., Prater, C.B., Weisenhorm, A.L., Manne, S., Kelrderman, G.L., Butt, H. J., Hansma, H., Hansma, P.K., Magonov, S., and Cantow, H.J. (1990) The atomic force microscope: a tool for science and industry. *Ultramicroscopy*, **33**, 93.

5 Sarid, D. (1994) *Scanning Force Microscopy*, Oxford University Press, New York.

6 Butt, H.J. and Jascke, M. (1995) Calculation of thermal noise in atomic force microscopy. *Nanotechnology*, **6**, 1.

7 Martin, Y., Williams, C.C., and Wickramasinghe, H.K. (1987) Atomic force microscope force mapping and profiling on a sub 100 angstrom scale. *J. Appl. Phys.*, **61**, 4723.

8 Rugar, D., Mamin, H.J., and Guthner, P. (1989) Improved fiber optic interferometer for atomic force microscopy. *Appl. Phys. Lett.*, **55**, 2588.

9 Hoogenboom, B.W., Frederix, P.L.T.M., Fotiadis, D., Hug, H.J., and Engel, A. (2008) Potential of interferometric cantilever detection and its application for AFM in liquids. *Nanotechnology*, **19**, 384019.

10 Barret, R.C., Tortonese, M., and Quate, C.F. (1993) Atomic resolution with an atomic force microscope using piezoresistive detection. *Appl. Phys. Lett.*, **62**, 834.

11 Adams, J.D., Manning, L., Rogers, B., Jones, M., and Minne, S.C. (2005) Piezoelectric self sensing of adsorption induced microcantilever bending. *Sens. Actuators A*, **121**, 262.

12 Giessibl, F.J. (2000) Atomic resolution on Si(111) (7×7) by noncontact atomic force microscopy with a force sensor based on a quartz tuning fork. *Appl. Phys. Lett.*, **76**, 1470.

13 Sarioglu, A.F. and Solgaard, O. (2008) Cantilevers with integrated sensor for time resolved force measurement in tapping mode atomic force microscopy. *Appl. Phys. Lett.*, **93**, 23114.

14 Onaran, A.G., Balantekin, M., and Lee, W. *et al.* (2006) A new atomic force microscope probe with force sensing integrated readout and active tip. *Rev. Sci. Instrum.*, **77**, 023501.

15 Torum, H., Sutanto, J., Sarangapani, K.K., Joseph, P., Degertekin, F.L., and Zhun, C. (2007) A micromachined membrane based active probe for biomolecular mechanics measurement. *Nanotechnology*, **18**, 165303.

16 Meyer, E., Hug, H.J., and Bennewitz, R. (2004) *Scanning Probe Microscopy*, Springer, Berlin.

17 Guckenberger, R. (1998) *Image Processing, Evaluation and Presentation in Procedures in Scanning Probe Microscopies*, John Wiley & Sons, Ltd., Chichester.

18 Horcas, I., Fernandez, R., Gomez Rodriguez, J.M., Colchero, J., Gomez Herrero, J., and Baro, A.M. (2007) WSXM: a software for scanning probe microscopy and a tool for nanotechnology. *Rev. Sci. Instrum.*, **78**, 013705.

19 Sulchek, T., Yaralioglu, G.C., Quate, C.F., and Minne, S.C. (2002) Characterization and optimization of scan speed for tapping mode atomic force microscopy. *Rev. Sci. Instrum.*, **73**, 2928.

20 Kokavecz, J., Marti, O., Heszler, P., and Mechler, A. (2006) Imaging bandwidth of the tapping mode atomic force microscope probe. *Phys. Rev. B*, **77**, 083704.

21 Albrecht, T.R., Akamine, S., Carver, T.E., and Quate, C.F. (1990) Microfabrication of cantilever styli for the atomic force microscope. *J. Vac. Sci. Technol. A*, **8**, 3386.

22 Walter, O., Bayer, T., and Greshner, J. (1991) Micromachined silicon sensors for scanning probe microscopy. *J. Vac. Sci. Technol. B*, **9**, 1353.

23 Sahin, O., Yaralioglu, G., Grow, R., Zappe, S.F., Atalar, A., Quate, C., and Solgaard, O. (2004) High resolution imaging of elastic properties using harmonic cantilevers. *Sens. Actuators A*, **114**, 183.

24 Martinez, N.F., Lozano, J.R., Herruzo, E.T., Garcia, F., Ritchter, C., Sulzbach, T., and Garcia, R. (2008) Bimodal atomic

force microscopy imaging of isolated antibodies in air and liquids. *Nanotechnology*, **19**, 384011.
25 Stark, R.W., Drobek, T., and Heckl, W.M. (2001) Thermomechanical noise of a free V shaped cantilever for atomic force microscopy. *Ultramicroscopy*, **86**, 207 215.
26 Sader, J.E. (1995) Parallel beam approximation for V shaped atomic force microscope cantilevers. *Rev. Sci. Instrum.*, **66**, 4583 4587.
27 Schaffer, T.E. (2005) Calculation of thermal noise in an atomic force microscope with a finite optical spot. *Nanotechnology*, **16**, 664 670.
28 Cleland, A.N. (2003) *Foundations of Nanomechanics*, Springer, Berlin.
29 Cheung, C.L., Hafner, J.H., and Lieber, C.M. (2000) Carbon nanotube atomic force microscopy tips: direct growth by chemical vapor deposition and application to high resolution imaging. *Proc. Natl. Acad. Sci. USA*, **97**, 3809.
30 Klinov, D. and Magonov, S. (2004) True molecular resolution in tapping mode atomic force microscopy with high resolution probes. *Appl. Phys. Lett.*, **84**, 2697.
31 Martinez, J., Yuzvinsky, T.D., Fennimore, A.M., Zettl, A., Garcia, R., and Bustamante, C. (2005) Length control and sharpening of atomic force microscope carbon nanotube tips assisted by an electron beam. *Nanotechnology*, **16**, 2493.
32 Snow, E.S., Campbell, P.M., and Novak, J.P. (2002) Single wall carbon nanotube atomic force microscope probes. *Appl. Phys. Lett.*, **80**, 2002.
33 Moller, C., Alen, M., Elings, V., Engel, A., and Muller, D.J. (1999) Tapping mode atomic force microscopy produces faithful high resolution images of protein surfaces. *Biophys. J.*, **77**, 1150.
34 Anselmetti, D., Luthi, R., Meyer, E., Richmond, T., Dreier, M., Frommer, J.E., and Guntherodt, H. J. (1994) Attractive mode imaging of biological materials with dynamic force microscopy. *Nanotechnology*, **5**, 87.
35 Florin, E.L., Radmacher, M., Fleck, B., and Gaub, H.E. (1994) Atomic force microscope with magnetic force modulation. *Rev. Sci. Instrum.*, **65**, 639.
36 O'Shea, S.J., Welland, M.E., and Pethica, J.B. (1994) Atomic force microscopy of local compliance at solid liquid interfaces. *Chem. Phys. Lett.*, **223**, 336.
37 Han, W., Lindsay, S.M., and Jing, T. (1996) A magnetically driven oscillating probe microscope for operation in liquids. *Appl. Phys. Lett.*, **69**, 4111.
38 Umeda, N., Ishizaki, S., and Uwai, H. (1991) scanning attractive force microscope using photothermal vibration. *J. Vac. Sci. Technol. B*, **9**, 1381.
39 Ramos, D., Tamayo, J., Mertens, J., and Calleja, M. (2006) Photothermal excitation of microcantilevers in liquids. *J. Appl. Phys.*, **99**, 1911.
40 Schaffer, T.E. and Fuchs, H. (2005) Optimized detection of normal vibration modes of atomic force microscope cantilevers with the optical beam deflection method. *J. Appl. Phys.*, **97**, 083524.
41 Liu, Y., Guo, Q., Nie, H.Y., Lau, W.M., and Yang, J. (2009) Optimization and calibration of atomic force microscopy sensitivity in terms of tip sample interactions in high order dynamic atomic force microscopy. *J. Appl. Phys.*, **106**, 124507.
42 Hutter, J.L. and Bechhoefer, J. (1993) Calibration of atomic force microscope tips. *Rev. Sci. Instrum.*, **64**, 1868.
43 Cleveland, J.P., Manne, S., Bocek, D., and Hansma, P.K. (1993) A non destructive method for determining the spring constant of cantilevers for scanning force microscopy. *Rev. Sci. Instrum.*, **64**, 403.
44 Sader, J.E., Larson, I., Mulvaney, P., and White, L.R. (1995) Method for the calibration of atomic force microscope cantilevers. *Rev. Sci. Instrum.*, **66**, 3789.
45 Burnham, N.A., Chen, X., Hodges, C.S., Matei, G.A., Thoreson, E.J., Roberts, C.J., Davies, M.C., and Tendler, S.J.B. (2003) Comparison of calibration methods for atomic force microscopy cantilevers. *Nanotechnology*, **14**, 1 6.
46 Levy, R. and Maaloum, M. (2002) Measuring the spring constant of atomic force microscope cantilevers: thermal fluctuations and other methods. *Nanotechnology*, **13**, 33.

47 Clifford, C.A. and Sheah, M.P. (2005) The determination of atomic force microscope cantilever spring constants via dimensional methods for nanomechanical analysis. *Nanotechnology*, **16**, 1666.
48 Cook, S.M., Schaffer, T.E., Chynoweth, K.M., Wigton, M., Simmonds, R.W., and Lang, K.M. (2006) Practical implementation of dynamic methods for measuring atomic force microscope cantilever spring constants. *Nanotechnology*, **17**, 2135 2145.
49 Sader, J.E., Chon, J.W.M., and Mulvaney, P. (1999) Calibration of rectangular atomic force microscope cantilevers. *Rev. Sci. Instrum.*, **70**, 3967.
50 Sader, J.E., Pacifico, J., Green, C.P., and Mulvaney, P. (2005) General scaling law for stiffness measurement of small bodies with applications to the atomic force microscope. *J. Appl. Phys.*, **97**, 124903.
51 French, A.P. (1971) *Vibrations and Waves*, W.W. Norton & Company, New York.
52 Paulo, A.S. and Garcia, R. (2002) Unifying theory of tapping mode AFM. *Phys. Rev. B*, **66**, 041406.
53 Revenko, I. and Proksch, R. (2000) Magnetic and acoustic tapping mode microscopy of liquid phase phospholipids bilayers and DNA molecules. *J. Appl. Phys.*, **87**, 526.
54 Martinez, N.F. and Garcia, R. (2006) Measuring phase shifts and energy dissipation with amplitude modulation atomic force microscopy. *Nanotechnology*, **17**, S167 S172.
55 Garcia, R. and San Paulo, A. (1999) Attractive and repulsive interaction regimes in tapping mode atomic force microscopy. *Phys. Rev. B*, **60**, 4961.
56 San Paulo, A. and Garcia, R. (2001) Amplitude, deformation and phase shift in amplitude modulation atomic force microscopy: a numerical study for compliant materials. *Surf. Sci.*, **471**, 71 79.
57 Anczykowski, B., Kruger, D., and Fuchs, H. (1996) Cantilever dynamics in quasinoncontact force microscopy: spectroscopic aspects. *Phys. Rev. B*, **53**, 15485.
58 Haugstad, G. and Jones, R.R. (2000) Mechanisms of dynamic force microscopy on polyvinyl alcohol: region specific non contact and intermittent contact regimes. *Ultramicroscopy*, **11**, 192.
59 Garcia, R. and Perez, R. (2002) Dynamic atomic force microscopy methods. *Surf. Sci. Rep.*, **47**, 197.

Chapter 3

1 Israelachvili, J. (1994) *Intermolecular and Surface Forces*, Academic Press, London.
2 Butt, H.J., Capella, B., and Kappl, M. (2005) Force measurements with the atomic force microscope: technique, interpretation and applications. *Surf. Sci. Rep.*, **59**, 1 152.
3 Hartmann, U. (1993) *Theory of STM and Related Scanning Probe Methods*, Springer, Berlin.
4 Argento, C. and French, R.H. (1996) Parametric tip model and force distance relation for Hamaker constant determination from atomic force microscopy. *J. Appl. Phys.*, **80**, 6081.
5 Garcia, R. and Perez, R. (2002) Dynamic atomic force microscopy methods. *Surf. Sci. Rep.*, **47**, 197.
6 Ashby, P.D., Chen, L., and Lieber, C.M. (2000) Probing intermolecular forces and potentials with magnetic feedback chemical force microscopy. *J. Am. Chem. Soc.*, **122**, 9467.
7 Ederth, T. (2001) Computation of Lifshitz van der Waals forces between alkylthiol monolayers on gold films. *Langmuir*, **17**, 3329.
8 Johnson, K.L. (1985) *Contact Mechanics*, Cambridge University Press, Cambridge.
9 Jonhson, K.L., Kendall, K., and Roberts, A.D. (1971) Surface energy and contact of elastic solids. *Proc. R. Soc. A*, **324**, 301.
10 Derjaguin, B.V., Muller, V.M., and Toporov, Yu.P. (1975) Effect of contact deformations on adhesion of particles. *J. Colloid Interface Sci.*, **53**, 314.
11 Maugis, D. (1992) Adhesion of spheres. The JKR DMT transition using a Dugdale model. *J. Colloid Interface Sci.*, **150**, 243.
12 Muller, V.M., Yushchenko, V.S., and Derjaguin, B.V. (1983) General theoretical consideration on the influence of surface forces on contact deformations and the

reciprocal adhesion of elastic spherical particles. *J. Colloid Interface Sci.*, **92**, 92.
13 Barthel, E. (1998) On the description of the adhesive contact of spheres with arbitrary interaction potentials. *J. Colloid Interface Sci.*, **200**, 7.
14 Unertl, W.N. (1999) Implications of contact mechanics models for mechanical properties measurements using scanning force microscopy. *J. Vac. Sci. Technol. A*, **17**, 1779 1785.
15 Schwarz, U.D. (2003) A generalized analytical model for the elastic deformation of an adhesive contact between a sphere and a flat surface. *J. Colloid Interface Sci.*, **261**, 99.
16 Landau, L.D. and Lifshitz, E.M. (1986) *Theory of Elasticity*, Pergammon Press, Oxford.
17 Taylor, J.R. (2005) *Classical Mechanics*, University Science Books, Sausalito, CA.
18 Capella, B. and Dietler, G. (1999) Force distance curves by atomic force microscopy. *Surf. Sci. Rep.*, **34**, 1.
19 Lantz, M.A., O'Shea, S.J., Welland, M.E., and Johnson, K.L. (1997) Atomic force microscope study of contact area and friction on $NbSe_2$. *Phys. Rev. B*, **55**, 10776.
20 Meyer, E., Hug, H.J., and Bennewitz, R. (2004) *Scanning Probe Microscopy*, Springer, Berlin.
21 Carpick, R.W. and Salmeron, M. (1997) Scratching the surface: fundamental investigations of tribology with atomic force microscopy. *Chem. Rev.*, **97**, 1163.
22 Luan, B. and Robbins, M.O. (2006) Contact of single asperities with varying adhesion: comparing continuum mechanics to atomistic simulations. *Phys. Rev. E*, **74**, 02611.
23 Luan, B. and Robbins, M.O. (2005) The breakdown of continuum models for mechanical contacts. *Nature*, **435**, 929.
24 Attard, P. (2007) Measurement and interpretation of elastic and viscoelastic properties with the atomic force microscope. *J. Phys.: Condens. Matter*, **19**, 473201.
25 Johnson, K.L. and Greenwood, J.A. (1997) An adhesion map for the contact of elastic spheres. *J. Colloid Interface Sci.*, **192**, 326.
26 Adamson, A.W. (1990) *Physical Chemistry of Surfaces*, John Wiley & Sons, Inc., New York.
27 de Gennes, P.G., Brochard Wyart, F., and Queré, D. (2004) *Capillarity and Wetting Phenomena: Drops, Bubbles, Pearls, Waves*, Springer Science, New York.
28 Atkins, P.W. (1990) *Physical Chemistry*, 4th edn, W.H. Freeman and Co., New York.
29 Orr, F.M., Scriven, L.E., and Rivas, A.P. (1975) Pendular rings between solids. Meniscus properties and capillary force. *J. Fluid Mech.*, **67**, 723.
30 Bayramli, E., Abou Obeid, A., and Vam de Ven, T.G.M. (1987) *J. Colloid Interface Sci.*, **116**, 490.
31 Garcia, R., Calleja, M., and Rohrer, H. (1999) Patterning of silicon surfaces with noncontact atomic force microscopy: field induced formation of nanometer size water bridges. *J. Appl. Phys.*, **86**, 1898.
32 Fisher, L.R. and Israelachvili, J.N. (1981) Experimental studies on the applicability of the Kelvin equation to highly curved concave menisci. *Colloids Surf.*, **3**, 303.
33 Colchero, J., Gil, A., and Baro, A.M. (2001) Resolution enhancement and improved data interpretation in electrostatic force microscopy. *Phys. Rev. B*, **64**, 245403.
34 Zitzler, L., Herminghaus, S., and Mugele, F. (2002) Capillary forces in tapping mode atomic force microscopy. *Phys. Rev. B*, **66**, 155436.
35 Stiffer, T., Marti, O., and Bhushan, B. (2000) Theoretical investigation of the distance dependence of capillary and van der Waals forces in scanning force microscopy. *Phys. Rev. B*, **62**, 13667.
36 Sirghi, L., Szoszkiewicz, R., and Riedo, E. (2006) Volume of a nanoscale water bridge. *Langmuir*, **22**, 1093.
37 Garcia, R., Martinez, R.V., and Martinez, J. (2006) Nano chemistry and scanning probe nanolithographies. *Chem. Soc. Rev.*, **35**, 29.
38 Muller, D.J., Fotiadis, D., Scheuring, S., Muller, S.A., and Engel, A. (1999) Electrostatically balanced subnanometer imaging of biological specimens by atomic force microscope. *Biophys. J.*, **76**, 1101.
39 Muller, D.J. and Engel, A. (2007) Atomic force microscopy and spectroscopy of

native membrane proteins. *Nat. Protoc.*, **2**, 2191.

40 Sotres, J. and Baró, A.M. (2010) AFM imaging and analysis of electrostatic double layer forces on single DNA molecules. *Biophys. J.*

41 Derjaguin, B.V. and Landau, L. (1941) A theory of the stability of strongly charged lyophobic sols. *Acta Physicochim. URSS*, **14**, 633.

42 Verwey, E.J.W. and Overbeek, J.T.G. (1948) *Theory of the Stability of Lyophobic Colloids*, Elsevier Publishing Inc., New York.

43 Verdaguer, A., Sacha, G.M., Bluhm, H., and Salemeron, M. (2006) Molecular structure of water at interfaces: wetting at the nanometer scale. *Chem. Rev.*, **106**, 1478 1510.

44 Israelachvili, J.N. and McGuiggan, P.M. (1990) Adhesion and short range forces between surfaces. 1. New apparatus for surface force measurements. *J. Mater. Res.*, **5**, 2232 2243.

45 O'Shea, S.J. and Welland, M.E. (1998) Atomic force microscopy at solid liquid interfaces. *Langmuir*, **14**, 4186 4197.

46 Han, W. and Lindsay, S.M. (1998) Probing molecular ordering at a liquid solid interface with a magnetically oscillated atomic force microscope. *Appl. Phys. Lett.*, **72**, 1656.

47 Franz, V. and Butt, H.J. (2002) Confined liquids: solvation forces in liquid alcohols between solid surfaces. *J. Phys. Chem. B*, **106**, 1703.

48 Antognozzi, M., Humphris, A.D.L., and Miles, M.J. (2001) Observation of molecular layering in a confined water film and study of the layers viscoelastic properties. *Appl. Phys. Lett.*, **78**, 300.

49 Fukuma, T., Kobayashi, K., Matsushige, K., and Yamada, H. (2005) True molecular resolution in liquid by frequency modulation atomic force microscopy. *Appl. Phys. Lett.*, **86**, 193108.

50 Uchiasi, T., Higgins, M., Nakayama, Y., Sader, J., and Jarvis, S.P. (2005) Quantitative measurement of solvation shells using frequency modulated atomic force microscopy. *Nanotechnology*, **16**, S49.

51 Kocevar, K., Blinc, R., and Musevic, I. (2000) Atomic force microscope evidence for the existence of smecticlike surface layers in the isotropic phase of a nematic liquid crystal. *Phys. Rev. E*, **62**, R3055.

52 Israelachvili, J.N. and Pashley, R.M. (1983) Molecular layering of water at surfaces and origin of repulsive hydration forces. *Nature*, **306**, 249.

53 Christenson, H.K. and Claesson, P.M. (1988) Cavitation and the interaction between macroscopic hydrophobic surfaces. *Science*, **239**, 390.

54 Katan, A.J. and Oosterkamp, T.H. (2008) Measuring hydrophobic interactions with three dimensional nanometer resolution. *J. Phys. Chem. C*, **112**, 9769 9776.

55 Hudlet, S., Saint Jean, M., Guthmann, C., and Berger, J. (1998) Evaluation of the capacitive force between an atomic force microscopy tip and a metallic surface. *Eur. Phys. J. B*, **2**, 5.

56 Colchero, J., Gil, A., and Baro, A.M. (2001) Resolution enhancement and improved data interpretation in electrostatic force microscopy. *Phys. Rev. B*, **64**, 245403.

57 Law, B.M. and Rieutord, F. (2002) Electrostatic forces in atomic force microscopy. *Phys. Rev. B*, **66**, 035402.

58 Léveque, G., Cadet, P., and Arinero, R. (2005) Sensitivity and resolution in noncontact electrostatic force microscopy in the case of a constant potential. *Phys. Rev. B*, **71**, 205419.

59 Sacha, G.M., Sahagun, E., and Saenz, J.J. (2007) A method for calculating capacitances and electrostatic forces in atomic force microscopy. *J. Appl. Phys.*, **101**, 024310.

60 Sacha, G.M., Verdaguer, A., Martinez, J., Saenz, J.J., and Salmeron, M. (2005) Effective tip radius in electrostatic force microscopy. *Appl. Phys. Lett.*, **86**, 123101.

61 Loppacher, C., Bennewitz, R., Pfeiffer, O., Guggisberg, M., Bammerlin, M., Schar, S., Barwich, V., Baratoff, A., and Meyer, E. (2000) Dynamic force microscopy of copper surfaces: atomic resolution and distance dependence of tip sample interaction and tunneling current. *Phys. Rev. B*, **62**, 13674.

62 Hugh, H.J. and Baratoff, A. (2002) in *Noncontact Atomic Force Microscopy* (eds S. Morita, R. Wiesendanger, and E. Meyer), Springer, Berlin, p. 395.

63 Oyabu, N., Pou, P., Sugimoto, Y., Jelinek, P., Abe, M., Morita, S., Perez, R., and Custance, O. (2006) Single atomic contact adhesion and dissipation in dynamic force microscopy. *Phys. Rev. Lett.*, **96**, 106101.
64 Kantorovich, L.N. and Trevethan, T. (2004) General theory of microscopic dynamical response in surface probe microscopy: from imaging to dissipation. *Phys. Rev. Lett.*, **93**, 236102.
65 Sahagun, E., Garcia Mochales, P., Sacha, G.M., and Saenz, J.J. (2007) Energy dissipation due to capillary interactions: hydrophobicity maps in force microscopy. *Phys. Rev. Lett.*, **98**, 176106.
66 Yoshizawa, H., Chen, Y.L., and Israelachvili, J. (1993) Fundamental mechanisms of interfacial friction. 1. Relation between adhesion and friction. *J. Phys. Chem.*, **97**, 4128.
67 Garcia, R., Tamayo, J., and San Paulo, A. (1999) Phase contrast and surface energy hysteresis in tapping mode scanning force microscopy. *Surf. Interface Anal.*, **27**, 312.
68 Paulo, A.S. and Garcia, R. (2001) Amplitude, deformation and phase shift in amplitude modulation atomic force microscopy: a numerical study for compliant materials. *Surf. Sci.*, **471**, 71.
69 Schirmeisen, A. and Holscher, H. (2005) Velocity dependence of energy dissipation in dynamic force microscopy: hysteresis versus viscous damping. *Phys. Rev. B*, **72**, 5431.

Chapter 4

1 Chen, J., Workman, R.K., Sarid, D., and Hoper, R. (1994) Numerical simulations of a scanning force microscope with a large amplitude vibrating cantilever. *Nanotechnology*, **5**, 199.
2 Sarid, D., Ruskell, T.G., Workman, R.K., and Chen, D. (1996) Driven nonlinear atomic force microscopy cantilevers: from noncontact to tapping modes of operation. *J. Vac. Sci. Technol. B*, **14**, 864.
3 Chen, G.Y., Warmack, R.J., Huang, A., and Thundat, T. (1995) Harmonic response of near contact force microscopy. *J. Appl. Phys.*, **78**, 1465.
4 Spatz, J.P., Sheiko, S., Moller, M., Winkler, R.G., Reineker, P., and Marti, O. (1995) Forces affecting the substrate in resonant tapping force microscopy. *Nanotechnology*, **6**, 40.
5 Winkler, R.G., Spatz, J.P., Sheiko, S., Moller, M., Reineker, P., and Marti, O. (1996) Imaging material properties by resonant tapping force microscopy: a model investigation. *Phys. Rev. B*, **54**, 8908.
6 Anczykowski, B., Kruger, D., and Fuchs, H. (1996) Cantilever dynamics in quasinoncontact force microscopy: spectroscopic aspects. *Phys. Rev. B*, **53**, 15485.
7 Anczykowski, B., Kruger, D., Babcok, K.L., and Fuchs, H. (1996) Basic properties of dynamic force spectroscopy with the scanning force microscope in experiment and simulation. *Ultramicroscopy*, **66**, 251.
8 Cleveland, J.P., Anczykowski, B., Schmid, A.E., and Elings, V.B. (1998) Energy dissipation in tapping mode atomic force microscopy. *Appl. Phys. Lett.*, **72**, 2613.
9 Gotsmann, B., Seidel, C., Anczykowski, B., and Fuchs, H. (1999) Conservative and dissipative tip sample interaction forces probed with dynamic AFM. *Phys. Rev. B*, **60**, 11051.
10 Tamayo, J. and Garcia, R. (1996) Deformation, contact time and phase contrast in tapping mode scanning force microscopy. *Langmuir*, **12**, 4430.
11 Tamayo, J. and Garcia, R. (1997) Effects of elastic and inelastic interactions on phase contrast images in tapping mode scanning force microscopy. *Appl. Phys. Lett.*, **71**, 2394.
12 Tamayo, J. and Garcia, R. (1998) Relationship between phase shift and energy dissipation in tapping mode scanning force microscopy. *Appl. Phys. Lett.*, **73**, 2926.
13 Garcia, R. and San Paulo, A. (1999) Attractive and repulsive tip sample interaction regimes in tapping mode atomic force microscopy. *Phys. Rev. B*, **60**, 4961.
14 Garcia, R. and Paulo, A.S. (2000) Dynamics of a vibrating tip near or in intermittent contact with a surface. *Phys. Rev. B*, **61**, R13381.
15 San Paulo, A. and Garcia, R. (2001) Tip surface forces, amplitude, and energy

dissipation in amplitude modulation (tapping mode) force microscopy. *Phys. Rev. B*, **64**, 193411.
16 Paulo, A.S. and Garcia, R. (2002) Unifying theory of tapping mode atomic force microscopy. *Phys. Rev. B*, **66**, 041406(R).
17 Rodriguez, T.R. and Garcia, R. (2002) Tip motion in amplitude modulation (tapping mode) atomic force microscopy: comparison between continuous and point mass models. *Appl. Phys. Lett.*, **80**, 1646.
18 Garcia, R. and Perez, R. (2002) Dynamic atomic force microscopy methods. *Surf. Sci. Rep.*, **47**, 197.
19 Rodriguez, T.R. and Garcia, R. (2004) Compositional mapping of surfaces in atomic force microscopy by excitation of the second normal mode of the cantilever. *Appl. Phys. Lett.*, **84**, 449.
20 Herruzo, E.T. and Garcia, R. (2007) Frequency response of an atomic force microscope in liquids and air: magnetic versus acoustic excitation. *Appl. Phys. Lett.*, **91**, 143113.
21 Lozano, J.R. and Garcia, R. (2008) Theory of multifrequency atomic force microscopy. *Phys. Rev. Lett.*, **100**, 076102.
22 Khule, A., Sorensen, A.H., and Bohr, J. (1997) Role of attractive forces in tapping tip force microscopy. *J. Appl. Phys.*, **81**, 6562.
23 Burnham, N.A., Behrend, O.P., Oulevey, F., Gremaud, G., Gallo, P.J., Gourdon, D., Dupas, E., Kulik, A.J., Pollock, H.M., and Briggs, G.A.D. (1997) How does a tip tap? *Nanotechnology*, **8**, 67.
24 Berg, J. and Briggs, G.A.D. (1997) Nonlinear dynamics of intermittent contact mode atomic force microscopy. *Phys. Rev. B*, **55**, 14899.
25 Magonov, S.N., Elings, V., and Whangbo, M.H. (1997) Phase imaging and stiffness in tapping mode atomic force microscopy. *Surf. Sci.*, **375**, L385.
26 Whangbo, M.H., Bar, G., and Brandsch, R. (1998) Description of phase imaging in tapping mode atomic force microscopy by harmonic approximation. *Surf. Sci.*, **411**, L794.
27 Marth, M., Maier, D., Honerkamp, J., Brandsch, R., and Bar, G. (1999) A unifying view on some experimental effects in tapping mode atomic force microscopy. *J. Appl. Phys.*, **85**, 7030.
28 Delineau, L., Brandsch, R., Bar, G., and Whangbo, M.H. (2000) Harmonic responses of a cantilever interacting with elastomers in tapping mode atomic force microscopy. *Surf. Sci.*, **448**, L179.
29 Boisgard, R., Michel, D., and Aime, J.P. (1998) Hysteresis generated by attractive interaction: oscillating behaviour of a vibrating tip microlever system bear a surface. *Surf. Sci.*, **401**, 199.
30 Nony, L., Boisgard, R., and Aime, J.P. (1999) Nonlinear dynamical properties of an oscillating tip cantilever system in tapping mode. *J. Chem. Phys.*, **111**, 1615.
31 Aime, J.P., Boisgard, R., Nony, L., and Couturier, G. (1999) Nonlinear dynamic behaviour of an oscillating tip microlever system and contrast at the atomic scale. *Phys. Rev. Lett.*, **82**, 3388.
32 Knopp Marsaudon, S., Leclere, P., Dubourg, F., Lazzaroni, R., and Aime, J.P. (2000) Quantitative measurement of the mechanical contribution to tapping mode atomic force microscopy images of soft materials. *Langmuir*, **16**, 8432.
33 Martin, P., Marsaudon, S., Aime, J.P., and Benneteau, B. (2005) Experimental determination of conservative and dissipative parts in the tapping mode of a grafted layer: comparison with frequency modulation data. *Nanotechnology*, **16**, 901.
34 Boisgard, R., Aime, J.P., and Couturier, G. (2007) Dynamic operation modes of AFM: non linear behaviour and theoretical analysis of the stability of the AFM oscillator. *Int. J. Nonlinear Mech.*, **42**, 673.
35 Wang, L. (1998) Analytical descriptions of the tapping mode atomic force microscopy response. *Appl. Phys. Lett.*, **73**, 3781.
36 Wang, L. (1999) The role of damping in phase imaging in tapping mode atomic force microscopy. *Surf. Sci.*, **429**, 178.
37 Sasaki, N., Tsukada, M., Tamura, R., Abe, K., and Sato, N. (1998) Dynamics of the cantilever in noncontact atomic force microscopy. *Appl. Phys. A*, **66**, S287.
38 Holscher, H., Schwarz, U.D., and Weisendanger, R. (1999) Calculation of the frequency shift in dynamic force microscopy. *Appl. Surf. Sci.*, **140**, 344.

39 Holscher, H. (2002) *Q* controlled dynamic force spectroscopy. *Surf. Sci.*, **515**, 517.

40 Holscher, H. (2006) Quantitative measurement of tip sample interactions in amplitude modulation atomic force microscopy. *Appl. Phys. Lett.*, **89**, 123109.

41 Holscher, H. and Schwarz, U.D. (2006) *Q* controlled amplitude modulation atomic force microscopy in liquids: an analysis. *Appl. Phys. Lett.*, **89**, 073117.

42 Holscher, H. and Schwarz, U.D. (2007) Theory of amplitude modulation atomic force microscopy with and without *Q* control. *Int. J. Nonlinear Mech.*, **42**, 608.

43 Bielefeldt, H. and Giessibl, F.J. (1999) A simplified but intuitive analytical model for intermittent contact mode force microscopy based on Hertzian mechanics. *Surf. Sci. Lett.*, **440**, L863.

44 Lantz, M., Liu, Y.Z., Cui, X.D., Tokumoto, H., and Lindsay, S.M. (1999) Dynamic force microscopy in fluid. *Surf. Interface Anal.*, **27**, 354.

45 Stark, R.W. and Heckel, W.M. (2000) Fourier transformed atomic force microscopy: tapping mode atomic force microscopy beyond the Hookian approximation. *Surf. Sci.*, **457**, 219.

46 Stark, M., Stark, R.W., Heckl, W.H., and Guckenberger, R. (2002) Inverting dynamic force microscopy: from signals to time resolved interaction forces. *Proc. Natl. Acad. Sci. USA*, **99**, 8473.

47 Stark, R.W. (2004) Optical lever detection in dynamic atomic force microscopy. *Rev. Sci. Instrum.*, **75**, 5053.

48 Stark, R.W., Schitter, G., Stark, M., Guckenberger, R., and Stemmer, A. (2004) State space model of freely vibrating and surface coupled cantilever dynamics in atomic force microscopy. *Phys. Rev. B*, **69**, 085412.

49 Rubio Sierra, F.J. and Stark, R.W. (2006) Transfer function analysis of the micro cantilever used in atomic force microscopy. *IEEE Trans. Nanotechnol.*, **5**, 692.

50 Salapaka, M.V., Chen, D.J., and Cleveland, J.P. (2000) Linearity of amplitude and phase in tapping mode atomic force microscopy. *Phys. Rev. B*, **61**, 1106.

51 Sebastian, A., Salapaka, M.V., Chen, D.J., and Cleveland, J.P. (2001) Harmonic and power balance tools for tapping mode atomic force microscope. *J. Appl. Phys.*, **89**, 6473.

52 Sebastian, A., Gannepalli, A., and Salapaka, M.V. (2007) A review of the systems approach to the analysis of dynamic mode atomic force microscopy. *IEEE Trans. Control Syst. Technol.*, **15**, 952.

53 Durig, U. (2000) Interaction sensing in dynamic force microscopy. *New J. Phys.*, **2**, 51.

54 Sahin, O. and Atalar, A. (2001) Analysis of tip sample interaction in tapping mode atomic force microscope using an electrical circuit simulator. *Appl. Phys. Lett.*, **78**, 2973.

55 Balantekin, M. and Atalar, A. (2003) Power dissipation analysis in tapping mode atomic force microscopy. *Phys. Rev. B*, **67**, 193404.

56 Sahin, O., Quate, C.F., Solgaard, O., and Atalar, A. (2007) An atomic force microscope tip designed to measure time varying nanomechanical forces. *Nat. Nanotechnol.*, **2**, 507.

57 Sahin, O. (2008) Time varying tip sample force measurements and steady state dynamics in tapping mode atomic force microscopy. *Phys. Rev. B*, **77**, 11505.

58 Wolf, K. and Gottlieb, O. (2002) Nonlinear dynamics of a noncontacting atomic force microscope cantilever actuated by a piezoelectric layer. *J. Appl. Phys.*, **91**, 4701.

59 Lee, S.I., Howell, S.W., Raman, A., and Reifenberger, R. (2003) Nonlinear dynamic perspectives on dynamic force microscopy. *Ultramicroscopy*, **97**, 185.

60 Crittenden, S., Raman, A., and Reifenberger, R. (2005) Probing attractive forces at the nanoscale using higher harmonic dynamic force microscopy. *Phys. Rev. B*, **72**, 235422.

61 Hu, S. and Raman, A. (2007) Analytical formulas and scaling laws for peak interaction forces in dynamic atomic force microscopy. *Appl. Phys. Lett.*, **91**, 123106.

62 Basak, S. and Raman, A. (2007) Dynamics of tapping mode atomic force microscopy in liquids: theory and experiments. *Appl. Phys. Lett.*, **91**, 064107.

63 Melcher, J., Hu, S.Q., and Raman, A. (2007) Equivalent point mass models of

continuous atomic force microscope probes. *Appl. Phys. Lett.*, **91**, 053101.
64 Xu, X. and Raman, A. (2007) Comparative dynamics of magnetically, acoustically, and Brownian motion driven microcantilevers in liquid. *J. Appl. Phys.*, **102**, 034303.
65 Hu, S. and Raman, A. (2008) Inverting amplitude and phase to reconstruct tip sample interaction forces in tapping mode atomic force microscopy. *Nanotechnology*, **19**, 375704.
66 Shapiro, I.R., Solares, S.D., Espandiu, M.J., Wade, L.A., Goddard, W.A., and Collier, C.P. (2004) Influence of elastic deformation on single wall carbon nanotube atomic force microscopy probe resolution. *J. Phys. Chem. B*, **108**, 13613.
67 Kutana, A., Giapis, K.P., Chen, J.Y., and Collier, C.P. (2006) Amplitude response of single wall carbon nanotube probes during tapping mode atomic force microscopy: modeling and experiment. *Nano Lett.*, **6**, 1669.
68 Solares, S.D. and Crone, J.C. (2007) Real time simulations of isolated biomolecule characterization with frequency and force modulation atomic force microscopy. *J. Phys. Chem.*, **111**, 2125.
69 Yagasaki, K. (2004) Nonlinear dynamics of vibrating microcantilevers in tapping mode atomic force microscopy. *Phys. Rev. B*, **70**, 245419.
70 Yagasaki, K. (2007) Bifurcations and chaos in vibrating microcantilevers of tapping mode atomic force microscopy. *Int. J. Nonlinear Mech.*, **42**, 658.
71 Legleiter, J. and Kowalewski, T. (2005) Insights into fluid tapping mode atomic force microscopy provided by numerical simulations. *Appl. Phys. Lett.*, **87**, 163120.
72 Legleiter, J., Park, M., Cusick, B., and Kowalewski, T. (2006) Scanning probe acceleration microscopy in fluids: mapping mechanical properties of surfaces at the nanoscale. *Proc. Natl. Acad. Sci. USA*, **103**, 4813.
73 Dareing, D.W., Thundat, T., Jeon, S.M., and Nicholson, M. (2005) Modal analysis of microcantilevers with environmental damping. *J. Appl. Phys.*, **97**, 084902.
74 Lee, M.H. and Jhe, W. (2006) General theory of amplitude modulation atomic force microscopy. *Phys. Rev. Lett.*, **97**, 036104.
75 Seo, Y. and Jhe, W. (2008) Atomic force microscopy and spectroscopy. *Rep. Prog. Phys.*, **71**, 016101.
76 Ashby, P.D. (2007) Gentle imaging of soft materials in solution with amplitude modulation atomic force microscopy: *Q* control and thermal noise. *Appl. Phys. Lett.*, **91**, 254102.
77 Chen, L., Yu, X., and Wang, D. (2007) Cantilever dynamics and quality factor control in AC mode AFM height measurements. *Ultramicroscopy*, **207**, 275.
78 Jai, C., Cohen Bouhacina, T., and Maali, A. (2007) Analytical description of the motion of an acoustic driven atomic force microscope cantilever in liquid. *Appl. Phys. Lett.*, **90**, 113512.
79 Dankowicz, H., Zhao, X.P., and Misra, S. (2007) Near grazing dynamics in tapping mode atomic force microscopy. *Int. J. Nonlinear Mech.*, **42**, 697.
80 Hashemi, N., Dankowicz, H., and Paul, M.R. (2008) The nonlinear dynamics of tapping mode atomic force microscopy with capillary force interactions. *J. Appl. Phys.*, **103**, 093512.
81 Martin, M.J., Fathy, H.K., and Houston, B.H. (2008) Dynamic simulation of atomic force microscope cantilevers oscillating in liquid. *J. Appl. Phys.*, **104**, 044316.
82 Song, Y.X. and Bhushan, B. (2008) Atomic force microscopy dynamic modes: modeling and applications. *J. Phys.: Condens. Matter*, **20**, 225012.
83 Lin, S.M. (2006) Energy dissipation and frequency shift of a damped dynamic force microscopy. *Ultramicroscopy*, **106**, 516.
84 Lee, H.L. and Chang, W.J. (2008) Coupled lateral bending torsional vibration sensitivity of atomic force microscope cantilever. *Ultramicroscopy*, **108**, 707.
85 Schroter, K., Petzold, A., Henze, T., and Thurn Albrecht, T. (2009) Quantitative analysis of scanning force microscopy data using harmonic models. *Macromolecules*, **42**, 1114.
86 http://nanohub.org/.
87 French, A.P. (1971) *Vibrations and Waves*, W.W. Norton & Company, New York.
88 Martin, Y., Williams, C.C., and Wickramasinghe, H.K. (1987) Atomic

force microscope force mapping and profiling on a sub 100 angstrom scale. *J. Appl. Phys.*, **61**, 4723.
89 Taylor, J.R. (2005) *Classical Mechanics*, University Science Books, Sausalito.
90 Lozano, J.R. and Garcia, R. (2009) Theory of phase spectroscopy in bimodal atomic force microscopy. *Phys. Rev. B*, **79**, 014110.
91 Kowalewski, T. (2006) Imaging stability and average tip sample force in tapping mode atomic force microscopy. *J. Appl. Phys.*, **99**, 064903.
92 Legleiter, J. (2009) The effect of drive frequency and set point amplitude on tapping forces in atomic force microscopy: simulation and experiment. *Nanotechnology*, **20**, 245703.
93 Press, W.H., Teukolsky, S.A., Vetterling, W.T., and Flannery, B.P. (1992) *Numerical Recipes in Fortran 77*, 2nd edn, Cambridge University Press, Cambridge.

Chapter 5

1 Mertz, J., Marti, O., and Mlynek, J. (1993) Regulation of a microcantilever response by force feedback. *Appl. Phys. Lett.*, **62**, 2344.
2 Anczykowski, B., Cleveland, J.P., Kruger, D., Elings, V., and Fuchs, H. (1998) Analysis of the interaction mechanisms in dynamic mode SFM by means of experimental data and computer simulation. *Appl. Phys. A*, **66**, S885.
3 Holscher, H. (2002) *Q* controlled dynamic force spectroscopy. *Surf. Sci.*, **515**, 517.
4 Ebeling, D., Holscher, H., Fuchs, H., Anczykowski, B., and Schwarz, U.D. (2006) Imaging of biomaterials in liquids: a comparison between conventional and *Q* controlled amplitude modulation ('tapping mode') atomic force microscopy. *Nanotechnology*, **17**, S221.
5 Tamayo, J., Humpries, A.D.L., and Miles, M.J. (2000) Piconewton regime dynamic force microscopic in liquid. *Appl. Phys. Lett.*, **77**, 582.
6 Tamayo, J., Humpries, A.D.L., Owen, R.J., and Miles, M.J. (2001) High *Q* dynamic force microscopy in liquid and its application to living cells. *Biophys. J.*, **81**, 526.
7 Tamayo, J. and Lechuga, L.M. (2003) Decrease of the resonance bandwidth of micromechanical oscillators by phase control of the driving force. *Appl. Phys. Lett.*, **82**, 2919.
8 Sulchek, T., Hsieh, R., Adams, J.D., Yarilioglu, G.G., Minne, S.C., Quate, C.F., Cleveland, J.P., Atalar, A., and Adderton, D.M. (2000) High speed tapping mode imaging with active *Q* control for atomic force microscopy. *Appl. Phys. Lett.*, **76**, 1473.
9 Jaggi, R.D., Franco Obregón, A., Studerus, P., and Ensslin, K. (2001) Detailed analysis of forces influencing lateral resolution for *Q* control and tapping mode. *Appl. Phys. Lett.*, **79**, 135.
10 Jahng, J., Lee, M., Noh, H., Seo, Y., and Jhe, W. (2007) Active *Q* control in tuning fork based atomic force microscopy. *Appl. Phys. Lett.*, **91**, 023103.
11 Gunev, I., Varol, A., Karaman, S., and Basdogan, C. (2007) Adaptative *Q* control for tapping mode nanoscanning using a piezoactuated bimorph probe. *Rev. Sci. Instrum.*, **78**, 043707.
12 Varol, A., Gunev, I., Orun, B., and Basdogan, C. (2008) Numerical simulation of nano scanning in intermittent contact mode AFM under *Q* control. *Nanotechnology*, **19**, 075503.
13 Rodriguez, T.R. and Garcia, R. (2003) Theory of *Q* control in atomic force microscopy. *Appl. Phys. Lett.*, **82**, 4821.
14 Kokavecz, J., Horvath, Z.L., and Melcher, A. (2004) Dynamic properties of the *Q* controlled atomic force microscope. *Appl. Phys. Lett.*, **85**, 3232.
15 Holscher, H. and Schwarz, U.D. (2006) Q controlled amplitude modulation atomic force microscopy in liquids: an analysis. *Appl. Phys. Lett.*, **89**, 073117.
16 Holscher, H. and Schwarz, U.D. (2007) Theory of amplitude modulation atomic force microscopy with and without *Q* control. *Int. J. Nonlinear Mech.*, **42**, 608 625.
17 Ashby, P.D. (2007) Gentle imaging of soft materials in solution with amplitude modulation atomic force microscopy.

Q control and thermal noise. *Appl. Phys. Lett.*, **91**, 254102.
18 Kobayashi, N., Li, Y.J., Naitoh, Y., Kageshima, M., and Sugawara, Y. (2008) Theoretical investigation on force sensitivity in *Q* controlled phase modulation atomic force microscopy in constant amplitude mode. *J. Appl. Phys.*, **103**, 054305.
19 Gleyzes, P., Kuo, P.K., and Boccara, A.C. (1991) Bistable behaviour of a vibrating tip near a solid surface. *Appl. Phys. Lett.*, **58**, 2889.
20 Khule, A., Sorensen, A.H., and Bohr, J. (1997) Role of attractive forces in tapping tip force microscopy. *J. Appl. Phys.*, **81**, 6562.
21 Garcia, R. and San Paulo, A. (1999) Attractive and repulsive tip sample interaction regimes in tapping mode atomic force microscopy. *Phys. Rev. B*, **60**, 4961.
22 Anczykowski, B., Kruger, D., and Fuchs, H. (1996) Cantilever dynamics in quasinoncontact force microscopy: spectroscopic aspects. *Phys. Rev. B*, **53**, 15485.
23 Boisgard, R., Michel, D., and Aime, J.P. (1998) Hysteresis generated by attractive interaction: oscillating behaviour of a vibrating tip microlever system near a surface. *Surf. Sci.*, **401**, 199.
24 Garcia, R. and Perez, R. (2002) Dynamic atomic force microscopy methods. *Surf. Sci. Rep.*, **47**, 197.
25 Nony, L., Boisgard, R., and Aime, J.P. (1999) Nonlinear dynamical properties of an oscillating tip cantilever system in tapping mode. *J. Chem. Phys.*, **111**, 1615.
26 Haugstad, G. and Jones, R.R. (2000) Mechanisms of dynamic force microscopy on polyvinyl alcohol: region specific non contact and intermittent contact regimes. *Ultramicroscopy*, **11**, 192.
27 Garcia, R. and Paulo, A.S. (2000) Dynamics of a vibrating tip near or in intermittent contact with a surface. *Phys. Rev. B*, **61**, R13381.
28 Sarid, D., Ruskell, T.G., Workman, R.K., and Chen, D. (1996) Driven nonlinear atomic force microscopy cantilevers: from noncontact to tapping modes of operation. *J. Vac. Sci. Technol. B*, **14**, 864.
29 Hunt, J.P. and Sarid, D. (1998) Kinetics of lossy grazing impact oscillators. *Appl. Phys. Lett.*, **72**, 2969.
30 Berg, J. and Briggs, G.A.D. (1997) Nonlinear dynamics of intermittent contact mode atomic force microscopy. *Phys. Rev. B*, **55**, 14899.
31 Sasaki, N., Tsukada, M., Tamura, R., Abe, K., and Sato, N. (1998) Dynamics of the cantilever in noncontact atomic force microscopy. *Appl. Phys. A*, **66**, S287.
32 Wang, L. (1998) Analytical descriptions of the tapping mode atomic force microscopy response. *Appl. Phys. Lett.*, **73**, 3781.
33 Wang, L. (1999) The role of damping in phase imaging in tapping mode atomic force microscopy. *Surf. Sci.*, **429**, 178.
34 Aime, J.P., Boisgard, R., Nony, L., and Couturier, G. (1999) Nonlinear dynamic behaviour of an oscillating tip microlever system and contrast at the atomic scale. *Phys. Rev. Lett.*, **82**, 3388.
35 Ashhab, M., Salapaka, M.V., and Dahleh, M. *et al.* (1999) Dynamical analysis and control of microcantilevers. *Automatica*, **35**, 1663 1670.
36 Ashhab, M., Salapaka, M.V., Dahleh, M. *et al.* (1999) Melnikov based dynamical analysis of microcantilevers in scanning probe microscopy. *Nonlinear Dyn.*, **20**, 197.
37 Salapaka, M.V., Chen, D.J., and Cleveland, J.P. (2000) Linearity of amplitude and phase in tapping mode atomic force microscopy. *Phys. Rev. B*, **61**, 1106.
38 Basso, M., Materassi, D., and Salapaka, M. (2008) Hysteresis models of dynamic mode atomic force microscopes: analysis and identification via harmonic balance. *Nonlinear Dyn.*, **54**, 297.
39 Marth, M., Maier, D., Honerkamp, J., Brandsch, R., and Bar, G. (1999) A unifying view on some experimental effects in tapping mode atomic force microscopy. *J. Appl. Phys.*, **85**, 7030.
40 Tello, M., San Paulo, A., Rodriguez, T.R., Blanco, M.C., and Garcia, R. (2003) Imaging cobalt nanoparticles by amplitude modulation atomic force microscopy: comparison between low

and high amplitude solutions. *Ultramicroscopy*, **97**, 171.
41 Paulo, A.S. and Garcia, R. (2002) Unifying theory of tapping mode atomic force microscopy. *Phys. Rev. B*, **66**, 041406(R).
42 van de Water, W. and Molenaar, J. (2000) Dynamics of vibrating atomic force microscopy. *Nanotechnology*, **11**, 192.
43 Wolf, K. and Gottlieb, O. (2002) Nonlinear dynamics of a noncontacting atomic force microscope cantilever actuated by a piezoelectric layer. *J. Appl. Phys.*, **91**, 4701.
44 Lee, S.I., Howell, S.W., Raman, A., and Reifenberger, R. (2003) Nonlinear dynamic perspectives on dynamic force microscopy. *Ultramicroscopy*, **97**, 185.
45 Lee, S.I., Howell, S.W., Raman, A., Reifenberger, R., Nguyen, C.V., and Meyyappan, M. (2004) Nonlinear tapping dynamics of multi walled carbon nanotube tipped atomic force microcantilevers. *Nanotechnology*, **15**, 416.
46 Hu, S. and Raman, A. (2006) Chaos in force microscopy. *Phys. Rev. Lett.*, **96**, 036107.
47 Raman, A., Melcher, J., and Tung, R. (2008) Cantilever dynamics in atomic force microscopy. *Nano Today*, **3**, 20.
48 Materassi, D., Basso, M., and Genesio, R. (2003) A model for impact dynamics and its application to frequency analysis of tapping mode atomic force microscopes. Proceedings of the 42nd IEEE Conference on Decision and Control, Vol. 6, pp. 6218 6223.
49 Yagasaki, K. (2004) Nonlinear dynamics of vibrating microcantilevers in tapping mode atomic force microscopy. *Phys. Rev. B*, **70**, 245419.
50 Yagasaki, K. (2007) Bifurcations and chaos in vibrating microcantilevers of tapping mode atomic force microscopy. *Int. J. Nonlinear Mech.*, **42**, 658.
51 Jamitzky, F., Stark, M., Bunk, W., Heckl, W.M., and Stark, R.W. (2006) Chaos in dynamic atomic force microscopy. *Nanotechnology*, **17**, S213.
52 Dankowicz, H., Zhao, X.P., and Misra, S. (2007) Near grazing dynamics in tapping mode atomic force microscopy. *Int. J. Nonlinear Mech.*, **42**, 697.
53 Hashemi, N., Dankowicz, H., and Paul, M.R. (2008) The nonlinear dynamics of tapping mode atomic force microscopy with capillary force interactions. *J. Appl. Phys.*, **103**, 093512.
54 Dankowicz, H., Nonlinear dynamics as an essential tool for non destructive characterization of soft nanostructures using tapping mode atomic force microscopy. *Philos. Trans. R. Soc. Lond. A.*
55 Polesel Maris, J., Piednoir, A., Zambelli, T., Bouju, X., and Gauthier, S. (2003) Experimental investigation of resonance curves in dynamic force microscopy. *Nanotechnology*, **14**, 1036.
56 San Paulo, A. and Garcia, R. (2000) High resolution imaging of antibodies by tapping mode atomic force microscopy: attractive and repulsive tip sample interaction regimes. *Biophys. J.*, **78**, 1599.
57 Pignataro, B., Chi, L., Gao, S., Anczykowski, B., Niemeyer, C., Adler, M., and Fuchs, H. (2002) Dynamic scanning force microscopy study of self assembled DNA protein nanostructures. *Appl. Phys. A*, **74**, 447.
58 Round, A.N. and Miles, M.J. (2004) Exploring the consequences of attractive and repulsive interaction regimes in tapping mode atomic force microscopy of DNA. *Nanotechnology*, **15**, S176.
59 Sarid, D. (1994) *Scanning Force Microscopy*, Oxford University Press, New York.
60 Chen, G.Y., Warmack, R.J., Thundat, T., Allison, D.P., and Huang, A. (1994) Resonance response of scanning force microscopy cantilevers. *Rev. Sci. Instrum.*, **65**, 2532.
61 Butt, H.J., and Jascke, M. (1995) Calculation of thermal noise in atomic force microscopy. *Nanotechnology*, **6**, 1.
62 Rabe, U., Janser, K., and Arnold, W. (1996) Vibrations of free and surface coupled atomic force microscope cantilevers: theory and experiment. *Rev. Sci. Instrum.*, **67**, 3281.
63 Rabe, U., Turner, J., and Arnold, W. (1998) Analysis of the high frequency response of atomic force cantilevers. *Appl. Phys. A*, **66**, S277.
64 Stark, R.W. and Heckel, W.M. (2000) Fourier transformed atomic force

microscopy: tapping mode atomic force microscopy beyond the Hookian approximation. *Surf. Sci.*, **457**, 219.
65 Stark, R.W., Schitter, G., Stark, M., Guckenebrger, R., and Stemmer, A. (2004) State space model of freely vibrating and surface coupled cantilever dynamics in atomic force microscopy. *Phys. Rev. B*, **69**, 085412.
66 Rodriguez, T.R. and Garcia, R. (2002) Tip motion in amplitude modulation (tapping mode) atomic force microscopy: comparison between continuous and point mass models. *Appl. Phys. Lett.*, **80**, 1646.
67 Lozano, J.R. and Garcia, R. (2009) Theory of phase spectroscopy in bimodal atomic force microscopy. *Phys. Rev. B*, **79**, 014110.
68 Sahin, O., Quate, C.F., Sogaard, O., and Atalar, A. (2004) Resonant harmonic response in tapping mode atomic force microscopy. *Phys. Rev. B*, **69**, 165416.
69 Green, C.P. and Sader, J.E. (2005) Frequency response of cantilever beams immersed in viscous fluids near a solid surface with applications to the atomic force microscope. *J. Appl. Phys.*, **98**, 114913.
70 Cleland, A.N. (2003) *Foundations of Nanomechanics*, Springer, Berlin.
71 Schaffer, T.E. (2005) Calculation of thermal noise in an atomic force microscope with a finite optical spot. *Nanotechnology*, **16**, 664 670.
72 Dareing, D.W., Thundat, T., Jeon, S.M. and Nicholson, M. (2005) Modal analysis of microcantilevers with environmental damping. *J. Appl. Phys.*, **97**, 084902.
73 Wang, W.L. and Hu, S.J. (2005) Modal response and frequency shift of the cantilever in a noncontact atomic force microscope. *Appl. Phys. Lett.*, **87**, 183506.
74 Lin, S.M., Liauh, C.T., Wang, W.R., and Ho, S.H. (2006) Analytical solutions of the first three frequency shifts of AFM non uniform probe subjected to the Lennard Jones force. *Ultramicroscopy*, **106**, 508.
75 Lin, S.M., Lee, S.Y., and Lin, K.W. (2007) Exact solutions of AFM scanning probes subjected to tip sample forces. *J. Mech. Mater. Struct.*, **2**, 897.
76 Hsu, J.C., Lee, H.L., and Chang, W.J. (2007) Flexural vibration frequency of atomic force microscope cantilevers using Timoshenko beam theory. *Nanotechnology*, **18**, 285503.
77 Lee, H.L. and Chang, W.J. (2008) Coupled lateral bending torsional vibration sensitivity of atomic force microscope cantilever. *Ultramicroscopy*, **108**, 707.
78 Martin, M.J., Fathy, H.K., and Houston, B.H. (2008) Dynamic simulation of atomic force microscope cantilevers oscillating in liquid. *J. Appl. Phys.*, **104**, 044316.
79 Song, Y.X. and Bhushan, B. (2008) Atomic force microscopy dynamic modes: modeling and applications. *J. Phys.: Condens. Matter*, **20**, 225012.
80 Li, H., Chen, Y., and Dai, L. (2008) Concentrated mass cantilever enhances multiple harmonics in tapping mode atomic force microscopy. *Appl. Phys. Lett.*, **92**, 151903.
81 Basak, S., Raman, A., and Garimella, S.V. (2006) Hydrodynamic loading of microcantilevers vibrating in viscous fluids. *J. Appl. Phys.*, **99**, 114906.
82 Clark, M.T. and Paul, M.R. (2006) The stochastic dynamics of an array of atomic force microscopes in a viscous fluid. *Int. J. Nonlinear Mech.*, **42**, 690.
83 Song, Y.X. and Bhushan, B. (2006) Simulation of dynamic modes of atomic force microscopy using a 3D finite element model. *Ultramicroscopy*, **106**, 847.
84 Meirovitch, L. (1997) *Principles and Techniques of Vibrations*, Prentice Hall, New Jersey.
85 Melcher, J., Hu, S., and Raman, A. (2007) Equivalent point mass models of continuous atomic force microscope probes. *Appl. Phys. Lett.*, **91**, 053101.
86 Kokavecz, J. and Mechler, A. (2008) Spring constant of microcantielvers in fundamental and higher eigenmodes. *Phys. Rev. B*, **78**, 172101.
87 Sebastian, A., Salapaka, M.V., Chen, D.J., and Cleveland, J.P. (1999) Harmonic analysis based modelling of tapping mode AFM. Proceedings of the 1999 American Control Conference, pp. 232.
88 Salapaka, M.V., Chen, D.J., and Cleveland, J.P. (2000) Linearity of

amplitude and phase in tapping mode atomic force microscopy. *Phys. Rev. B*, **61**, 1106.

89 Sebastian, A., Salapaka, M.V., Chen, D.J., and Cleveland, J.P. (2001) Harmonic and power balance tools for tapping mode atomic force microscope. *J. Appl. Phys.*, **89**, 6473.

90 Sebastian, A., Gannepalli, A., and Salapaka, M.V. (2007) A review of the systems approach to the analysis of dynamic mode atomic force microscopy. *IEEE Trans. Control Syst. Technol.*, **15**, 952.

91 Stark, M., Guckenberger, R., Stemmer, A., and Stark, R.W. (2005) Estimating the transfer function of the cantilever in atomic force microscopy: a system identification approach. *J. Appl. Phys.*, **98**, 114904.

92 Rubio Sierra, F.J. and Stark, R.W. (2006) Transfer function analysis of the micro cantilever used in atomic force microscopy. *IEEE Trans. Nanotechnol.*, **5**, 692.

93 Lee, M.H. and Jhe, W.H. (2006) General theory of amplitude modulation AFM. *Phys. Rev. Lett.*, **97**, 036104.

94 Seo, Y. and Jhe, W. (2008) Atomic force microscopy and spectroscopy. *Rep. Prog. Phys.*, **71**, 016101.

95 Holscher, H. (2006) Quantitative measurement of tip sample interactions in amplitude modulation AFM. *Appl. Phys. Lett.*, **89**, 123109.

96 Holscher, H. and Schwarz, U.D. (2007) Theory of amplitude modulation atomic force microscopy with and without *Q* control. *Int. J. Nonlinear Mech.*, **42**, 608.

97 Hu, S. and Raman, A. (2008) Inverting amplitude and phase to reconstruct tip sample interaction forces in tapping mode AFM. *Nanotechnology*, **19**, 375704.

98 Katan, A.J. (2007) Measuring interactions in fluids with small cantilever AFM, PhD Thesis, Universiteit Leiden, The Netherlands.

99 Katan, A.J., van Es, M.H., and Oosterkamp, T.H. (2009) Quantitative force versus distance measurements in amplitude modulation AFM: a novel force inversion technique. *Nanotechnology*, **20**, 165703.

100 Durig, U. (2000) Extracting interaction forces and complementary observables in dynamic probe microscopy. *Appl. Phys. Lett.*, **76**, 1203.

101 Giessibl, F.J. (1997) Forces and frequency shifts in atomic resolution dynamic force microscopy. *Phys. Rev. B*, **56**, 16010.

102 Sader, J.E. and Jarvis, S.P. (2004) Accurate formulas for interaction force and energy in frequency modulation force spectroscopy. *Appl. Phys. Lett.*, **84**, 1801.

103 Sader, J.E., Uchihashi, T., Higgins, M.J., Farrell, A., Nakayama, Y., and Jarvis, S.P. (2005) Quantitative force measurements using frequency modulation atomic force microscopy: theoretical foundations. *Nanotechnology*, **16**, S94.

104 Legleiter, J., Park, M., Cusick, B., and Kowalewski, T. (2006) Scanning probe acceleration microscopy in fluids: mapping mechanical properties of surfaces at the nanoscale. *Proc. Natl. Acad. Sci. USA*, **103**, 4813.

105 Stark, M., Stark, R.W., Heckl, W.H., and Guckenberger, R. (2002) Inverting dynamic force microscopy: from signals to time resolved interaction forces. *Proc. Natl. Acad. Sci. USA*, **99**, 8473.

106 Sahin, O., Quate, C.F., Solgaard, O., and Atalar, A. (2007) An atomic force microscope tip designed to measure time varying nanomechanical forces. *Nat. Nanotechnol.*, **2**, 507.

107 Sahin, O. (2008) Time varying tip sample force measurements and steady state dynamics in tapping mode atomic force microscopy. *Phys. Rev. B*, **77**, 11505.

108 Fain, S.C., Barry, K.A., Bush, M.G., Pittenger, B., and Louie, R.N. (2000) *Appl. Phys. Lett.*, **76**, 930.

109 Su, C., Huang, L., and Kjoller, K. (2004) Direct measurement of tapping force with a cantilever deflection sensor. *Ultramicroscopy*, **100**, 233.

110 Degertekin, F.L., Onaran, A.G., Balentekin, M., Lee, W., Hall, N.A., and Quate, C.F. (2005) Sensor for direct measurement of interaction forces in probe microscopy. *Appl. Phys. Lett.*, **87**, 213109.

111 Torum, H., Sutanto, J., Sarangapani, K.K., Joseph, P., Degertekin, F.L., and Zhun, C.

(2007) A micromachined membrane based active probe for biomolecular mechanics measurement. *Nanotechnology*, **18**, 165303.

112 Park, Z., Hadizadeh, R., Balantekin, M., and Degertekin, F.L. (2009) Controlling tip sample interaction forces during a single tap for improved topography and mechanical property imaging of soft materials by AFM. *Ultramicroscopy*, **109**, 1121.

113 Sarioglu, A.F. and Solgaard, O. (2008) Cantilevers with integrated sensor for time resolved force measurements in tapping mode atomic force microscopy. *Appl. Phys. Lett.*, **93**, 023114.

Chapter 6

1 Butt, H. J., Siedle, P., Seifert, K., Fendler, K., Seeger, T., Bamberg, E., Weisenhorn, A.L., Goldie, K., and Engel, A. (1993) Scan speed limit in atomic force microscopy. *J. Microsc.*, **169**, 75.

2 Herruzo, E.T. and Garcia, R. (2007) Frequency response of an atomic force microscope in liquids and air: magnetic versus acoustic excitation. *Appl. Phys. Lett.*, **91**, 143113.

3 Gunther, P., Fisher, U.C., and Dransfeld, K. (1989) Scanning near field acoustic microscopy. *Appl. Phys. B*, **48**, 89.

4 Basak, S., Raman, A., and Garimella, S.V. (2006) Hydrodynamic loading of vibrating microcantilevers in viscous fluids. *J. Appl. Phys.*, **99**, 114906.

5 Sader, J.E. (1998) Frequency response of cantilever beams immersed in viscous fluids with applications to the atomic force microscope. *J. Appl. Phys.*, **84**, 64.

6 Green, C.P. and Sader, J.E. (2005) Frequency response of cantilever beams immersed in viscous fluids near a solid surface with applications to the atomic force microscope. *J. Appl. Phys.*, **98**, 114913.

7 Green, C.P. and Sader, J.E. (2005) Small amplitude oscillations of a thin beam immersed in a viscous fluid near a solid surface. *Phys. Fluids*, **17**, 73102.

8 Green, C.P. and Sader, J.E. (2002) Torsional frequency response of cantilever beams immersed in viscous fluids with applications to the atomic force microscope. *J. Appl. Phys.*, **87**, 6262.

9 Scherer, M.P., Frank, G., and Gummer, A.W. (2000) Experimental determination of the mechanical impedance of atomic force microscopy cantilevers in fluids up to 70 kHz. *J. Appl. Phys.*, **88**, 2912.

10 Putman, C.A.J., Van der Werf, K.O., De Grooth, B.G., Van Hulst, N.F., and Greve, J. (1994) Tapping mode atomic force microscopy in liquid. *Appl. Phys. Lett.*, **64**, 2454.

11 Lantz, M., Liu, Y.Z., Cui, X.D., Tokumoto, H., and Lindsay, S.M. (1999) Dynamic force microscopy in fluid. *Surf. Interface Anal.*, **27**, 354.

12 Raman, A., Melcher, J., and Tung, R. (2008) Cantilever dynamics in atomic force microscopy. *Nano Today*, **3**, 20.

13 Basak, S. and Raman, A. (2007) Dynamics of tapping mode atomic force microscopy in liquids: theory and experiments. *Appl. Phys. Lett.*, **91**, 064107.

14 Tamayo, J. (1999) Energy dissipation in tapping mode scanning force microscopy with low quality factors. *Appl. Phys. Lett.*, **75**, 3569.

15 Muller, D.J., Schabert, F.A., Buldt, G., and Engel, A. (1995) Imaging purple membranes in aqueous solutions at subnanometer resolution by atomic force microscopy. *Biophys. J.*, **68**, 1681.

16 Muller, D.J., Fotiadis, D., Scheuring, S., Muller, S.A., and Engel, A. (1999) Electrostatically balanced subnanometer imaging of biological specimens by atomic force microscope. *Biophys. J.*, **76**, 1101.

17 Muller, D.J. and Engel, A. (2007) Atomic force microscopy and spectroscopy of native membrane proteins. *Nat. Protoc.*, **2**, 2191.

18 Gan, Y. (2009) Atomic and subnanometer resolution in ambient conditions by atomic force microscopy. *Surf. Sci. Rep.*, **64**, 99.

19 Butt, H.J., Capella, B., and Kappl, M. (2005) Force measurements with the atomic force microscope: technique, interpretation and applications. *Surf. Sci. Rep.*, **59**, 1.

20 Wu, Y., Gupta, C., and Shannon, M.A. (2008) Effect of solution concentration, surface bias and protonation on the

dynamic response of amplitude modulated atomic force microscopy in water. *Langmuir*, **24**, 10817.

21 Legleiter, J., Park, M., Cusick, B., and Kowalewski, T. (2006) Scanning probe acceleration microscopy in fluids: mapping mechanical properties of surfaces at the nanoscale. *Proc. Natl. Acad. Sci. USA*, **103**, 4813.

22 Jai, C., Cohen Bouhacina, T., and Maali, A. (2007) Analytical description of the motion of an acoustic driven atomic force microscope cantilever in liquid. *Appl. Phys. Lett.*, **90**, 113512.

23 Schaffer, T.E., Cleveland, J.P., Ohnesorge, F., Walters, D.A., and Hansma, P.K. (1996) Studies of vibrating atomic force microscope cantilevers in liquid. *J. Appl. Phys.*, **80**, 3622.

24 Revenko, I. and Proksch, R. (2000) Magnetic and acoustic tapping mode microscopy of liquid phase phospholipid bilayers and DNA molecules. *J. Appl. Phys.*, **87**, 526.

25 Volkov, A.O., Burnell Gray, J.S., and Datta, P.K. (2004) Frequency response of atomic force microscope cantilever driven by fluid. *Appl. Phys. Lett.*, **85**, 5397.

26 Kokavecz, J. and Mechler, A. (2007) Investigation of fluid cell resonances in intermittent contact mode atomic force microscopy. *Appl. Phys. Lett.*, **91**, 023113.

27 Xu, X. and Raman, A. (2007) Comparative dynamics of magnetically, acoustically, and Brownian motion driven microcantilevers in liquids. *J. Appl. Phys.*, **102**, 034303.

28 Kueng, A., Kranz, C., Mizaikoff, B., Lugstein, A., and Bertagnolli, E. (2003) Combined electrochemical atomic force microscopy for tapping mode imaging. *Appl. Phys. Lett.*, **82**, 1592.

29 Maali, A., Hurth, C., Cohen Bouhacina, T., Couturier, G., and Aimé, J.P. (2006) Improved acoustic excitation of atomic force microscope cantilevers in liquids. *Appl. Phys. Lett.*, **88**, 163504.

30 Han, W., Lindsay, S.M., and Jing, T. (1996) A magnetically driven oscillating probe microscope for operation in liquids. *Appl. Phys. Lett.*, **69**, 4111.

31 O'Shea, S.J., Lantz, M.A., and Tokumoto, H. (1999) Damping near solid liquid interfaces measured with atomic force microscopy. *Langmuir*, **15**, 922.

32 Chen, G.Y., Warmack, R.J., Thundat, T., Allison, D.P., and Huang, A. (1994) Resonance response of scanning force microscopy cantilevers. *Rev. Sci. Instrum.*, **65**, 2532.

33 O'Shea, S.J. and Welland, M.E. (1998) Atomic force microscopy at solid liquid interfaces. *Langmuir*, **14**, 4186.

34 Lantz, M., Liu, Y.Z., Cui, X.D., Tokumoto, H., and Lindsay, S.M. (1999) Dynamic force microscopy in fluid. *Surf. Interface Anal.*, **27**, 354.

35 Legleiter, J. and Kowalewski, T. (2005) Insights into fluid tapping mode atomic force microscopy provided by numerical simulations. *Appl. Phys. Lett.*, **87**, 163120.

36 de Beer, S., van den Ende, D., and Mugele, F. (2008) Atomic force microscopy cantilever dynamics in liquid in the presence of tip simple interaction. *Appl. Phys. Lett.*, **93**, 253106.

37 de Beer, S. and Mugele, F. (2009) Small amplitude AFM spectroscopy of dissipation in confined liquid films. *Microsc. Anal.*, **23**, 11.

38 Martin, M.J., Fathy, H.K., and Houston, B.H. (2008) Dynamic simulation of atomic force microscope cantilevers oscillating in liquid. *J. Appl. Phys.*, **104**, 044316.

39 Melcher, J., Xu, X., and Raman, A. (2008) Multiple impact regimes in liquid environment dynamic force microscopy. *Appl. Phys. Lett.*, **93**, 093111.

40 Xu, X., Melcher, J., Basak, S., Reinferberger, R., and Raman, A. (2009) Compositional contrast of biological materials in liquids using the momentary excitation of higher eigenmodes in dynamic AFM. *Phys. Rev. Lett.*, **102**, 060801.

41 Paul, M.R., Clark, M.T., and Cross, M.C. (2006) The stochastic dynamics of micron and nanoscale elastic cantilevers in fluid: fluctuations from dissipation. *Nanotechnology*, **17**, 4502.

42 Greenspon, J.E. (1961) Vibrations of cross stiffened and sandwich plates with application to underwater sound radiators. *J. Acoust. Soc. Am.*, **33**, 1485.

43 Hosaka, H., Itao, K., and Kuroda, S. (1995) Damping characteristics of beam shaped micro oscillators. *Sens. Actuators A*, **49**, 87.
44 Maali, A., Hurth, C., Boisgard, R., Jai, C., Cohen Bouhacina, T., and Aimé, J.P. (2005) Hydrodynamics of oscillating cantilevers in viscous fluids. *J. Appl. Phys.*, **97**, 74907.
45 Maali, A., Cohen Bouhacina, T., Jai, C., Hurth, C., Boisgard, R., Aimé, J.P., Mariolle, D., and Bertin, F. (2006) Reduction of the cantilever hydrodynamic damping near a surface by ion milling. *J. Appl. Phys.*, **99**, 024908.

Chapter 7

1 Garcia, R., Magerle, R., and Perez, R. (2007) Nanoscale compositional mapping with gentle forces. *Nat. Mater.*, **6**, 405.
2 Tamayo, J. and Garcia, R. (1997) Effects of elastic and inelastic interactions on phase contrast images in tapping mode scanning force microscopy. *Appl. Phys. Lett.*, **71**, 2394.
3 Cleveland, J.P., Anczykowski, B., Schmid, A.E., and Elings, V.B. (1998) Energy dissipation in tapping mode atomic force microscopy. *Appl. Phys. Lett.*, **72**, 2613.
4 Martinez, N.F. and Garcia, R. (2006) Measuring phase shifts and energy dissipation with amplitude modulation atomic force microscopy. *Nanotechnology*, **17**, S167.
5 Garcia, R. and Perez, R. (2002) Dynamic atomic force microscopy methods. *Surf. Sci. Rep.*, **47**, 197.
6 Knoll, A., Magerle, R., and Krausch, G. (2001) Tapping mode atomic force microscopy on polymers: where is the true sample surface? *Macromolecules*, **34**, 4159.
7 Raman, A., Melcher, J., and Tung, R. (2008) Cantilever dynamics in atomic force microscopy. *Nano Today*, **3**, 20.
8 Garcia, R., Gomez, C.J., Martinez, N.F., Patil, S., Dietz, C., and Magerle, R. (2006) Identification of nanoscale dissipation processes by dynamic atomic force microscopy. *Phys. Rev. Lett.*, **97**, 016103.
9 Suo, Z., Yang, X., Avci, R., Kellerman, L., Pascual, D.W., Fries, M., and Steele, A. (2007) HEPES stabilized encapsulation of *Salmonella typhimurium*. *Langmuir*, **23**, 1365.
10 Reiter, G., Castelein, G., Sommer, J.U., Rottele, A., and Thurn Albrecht, T. (2001) Direct visualization of random crystallization and melting in arrays of nanometer size polymer crystals. *Phys. Rev. Lett.*, **87**, 226101.
11 Knoll, A., Magerle, R., and Krausch, G. (2004) Phase behavior in thin films of cylinder forming ABA block copolymers: experiments. *J. Chem. Phys.*, **120**, 1105.
12 Chernoff, D.A. (1995) High resolution chemical mapping using tapping mode AFM with phase contrast. *Proc. Microsc. Microanal.*, 888.
13 Leclere, P., Lazzaroni, R., and Bredas, J.L. (1996) Microdomain morphology analysis of block copolymers by atomic force microscopy with phase detection imaging. *Langmuir*, **12**, 4317.
14 Jeusette, M., Leclere, P., Lazzaroni, R., Simal, F., Vaneecke, J., Lardot, T., and Roose, P. (2007) New all acrylate block copolymers: synthesis and influence of the architecture on the morphology and the mechanical properties. *Macromolecules*, **40**, 1055.
15 Magonov, S.N., Elings, V., and Papkov, V.S. (1997) AFM study of thermotropic structural transitions in poly (diethylsiloxane). *Polymer*, **38**, 297.
16 Bar, G., Thomann, Y., and Whangbo, M.H. (1998) Characterization of the morphologies and nanostructures of blends of polystyrene *block* poly(ethane *co* but 1 ene) blocl polystyrene with isotactic and atactic polypropylenes by tapping mode AFM. *Langmuir*, **14**, 1219.
17 Brandsch, R., Bar, G., and Whangbo, M.H. (1997) On the factors affecting the contrast of height and phase images in tapping mode atomic force microscopy. *Langmuir*, **13**, 6349.
18 Krausch, G. and Magerle, R. (2002) Nanostructured thin films via self assembly of block copolymers. *Adv. Mater.*, **14**, 1579.
19 Knoll, A., Lyakhova, K.S., Horvat, A., Krausch, G., Sevink, G.J.A., Zvelindovsky, A.V., and Magerle, R. (2004) Direct imaging and mesoscale modelling of

phase transitions in a nanostructured fluid. *Nat. Mater.*, **3**, 886.
20 Tsarkova, L., Knoll, A., and Magerle, R. (2006) Rapid transitions between defect configurations in a block copolymer melt. *Nano Lett.*, **6**, 1574.
21 Dietz, C., Zerson, M., Riesch, C., Franke, M., and Magerle, R. (2008) Surface properties of elastomeric polypropylenes studied by AFM. *Macromolecules*, **41**, 9259.
22 Harrison, C., Adamson, D.H., Cheng, Z., Sebastian, J.M., Sethuraman, S., Huse, D.A., Register, R.A., and Chaikin, P.M. (2000) Mechanisms of ordering in striped patterns. *Science*, **290**, 1558.
23 Marcus, M.S., Carpick, R.W., Sasaki, D.Y., and Eriksson, M.A. (2002) Material anisotropy revealed by phase contrast in intermittent contact AFM. *Phys. Rev. Lett.*, **88**, 226103.
24 Scott, W.W. and Bhushan, B. (2003) Use of phase imaging in atomic force microscopy for measurement of viscoelastic contrast in polymer nanocomposites and molecularly thick lubricant films. *Ultramicroscopy*, **97**, 2003.
25 Kasai, T., Bhushan, B., Huang, L., and Su, C. (2005) Topography and phase imaging using torsional resonance mode. *Nanotechnology*, **15**, 731.
26 Xu, J., Guo, B.H., Zhang, Z.M., Zhou, J.J., Jiang, Y., Yan, S., Li, L., Wu, Q., Chen, G.Q., and Schultz, J.M. (2004) Direct AFM observation of crystal twisting and organization in banded spherulites of chiral poly(3 hydroxybutyrate *co* 3 hydroxyhexanoate). *Macromolecules*, **37**, 4118.
27 Wu, W., Matyjaszewski, K., and Kowalewski, T. (2005) Monitoring surface thermal transitions of ABA triblock copolymers with crystalline segments using phase contrast tapping mode atomic force microscopy. *Langmuir*, **21**, 1143.
28 Xu, W.S., Wood Adams, P.M., and Robertson, C.G. (2006) Measuring local viscoelastic properties of complex materials with tapping mode atomic force microscopy. *Polymer*, **47**, 4798.
29 Djurisic, A.B., Wang, H., Chan, W.K., and Xie, M.H. (2006) Characterization of block copolymers using scanning probe microscopy. *J. Scann. Probe Microsc.*, **1**, 21.
30 Uchihashi, T., Ando, T., and Yamashita, H. (2006) Fast phase imaging in liquids using a rapid scan atomic force microscope. *Appl. Phys. Lett.*, **89**, 213112.
31 Vasilev, C., Reiter, G., and Pispas, S. *et al.* (2006) Crystallization of block copolymers in restricted cylindrical geometries. *Polymer*, **47**, 330.
32 Boschetti de Fierro, A., Spindler, L., and Reiter, G. *et al.* (2007) Thin film morphology in triblock terpolymers with one and two crystallizable blocks. *Macromolecules*, **40**, 5487.
33 Aytun, T., Mutaf, O.F., el Atwani, O.J., and Ow Yang, C.W. (2008) Nanoscale composition of segregation in micelles with tapping mode atomic force microscopy. *Langmuir*, **24**, 14183.
34 Artyushkova, K., Farrar, J.O., and Fulghum, J.E. (2009) Data fusion of XPS and AFM images for chemical phase identification in polymer blends. *Surf. Interface Anal.*, **41**, 119.
35 Sirghi, L. *et al.* (2009) Atomic force microscopy characterization of the chemical contrast of nanoscale patterns fabricated by electron beam lithography on polyethylene glycol oxide thin films. *Ultramicroscopy*, **109**, 222.
36 Nagao, E. and Dvorak, J.A. (1999) Phase imaging by atomic force microscopy: analysis of living homoeothermic vertebrate cells. *Biophys. J.*, **76**, 3289.
37 Schweitzer, M.H., Suo, Z., Avci, R., Asara, J.M., Allen, M.A., Arce, F.T., and Horner, J.R. (2007) Analyses of soft tissue from *Tyrannosaurus rex* suggest the presence of protein. *Science*, **316**, 277.
38 Stark, M., Moller, C., Muller, D.J., and Guckenberger, R. (2001) From images to interactions: high resolution phase imaging in tapping mode AFM. *Biophys. J.*, **80**, 3009.
39 Lysetska, M. *et al.* (2002) UV light damaged DNA and its interaction with human replication protein A: an AFM study. *Nucleic Acids Res.*, **30**, 2686.
40 Casero, E., Vazquez, L., and Martin Benito, J. *et al.* (2002) Immobilization of metallothionein on gold/mica surfaces: relationship between surface morphology and protein substrate interaction. *Langmuir*, **18**, 5909.

41 Thomson, N.H. (2005) Imaging the substructure of antibodies with tapping mode AFM in air: the importance of a water layer on mica. *J. Microsc.*, **217**, 193.

42 Hernandez, J.C.R., Sanchez, M.S., and Soria, J.M. *et al.* (2007) Substrate chemistry dependent conformations of single laminin molecules on polymer surfaces are revealed by the phase signal of atomic force microscopy. *Biophys. J.*, **93**, 202.

43 Abou Saleh, R.H., Connell, S.D., and Harrand, R. *et al.* (2009) Nanoscale probing reveals that reduced stiffness of clots from fibrinogen lacking 42 N terminal Bβ chain residues is due to the formation of abnormal oligomers. *Biophys. J.*, **96**, 2415.

44 Klinov, D., Dwir, B., Kapon, E., Borovok, N., Molotsky, T., and Kolyar, A. (2007) High resolution atomic force microscopy of duplex and triplex DNA molecules. *Nanotechnology*, **18**, 225102.

45 Tamayo, J. and Garcia, R. (1996) Deformation, contact time and phase contrast in tapping mode scanning force microscopy. *Langmuir*, **12**, 4430.

46 Pompe, T., Fery, A., and Herminghaus, S. (1998) Imaging liquid structures on inhomogeneous surfaces by scanning force microscopy. *Langmuir*, **14**, 2585.

47 Checco, A., Cai, Y., Gang, O., and Ocko, B.M. (2006) High resolution non contact AFM imaging of liquids onto chemically nanopatterned surfaces. *Ultramicroscopy*, **106**, 703.

48 Mendez Vilas, A., Jodar Reyes, A.B., and Gonzalez Martin, M.L. (2009) Ultrasmall liquid droplets on solid surfaces: production, imaging, and relevance for current wetting research. *Small*, **5**, 1366.

49 Ashby, P.D. and Lieber, C.M. (2005) Ultra sensitive imaging and interfacial analysis of patterned hydrophilic SAM surfaces using energy dissipation chemical force microscopy. *J. Am. Chem. Soc.*, **127**, 6814.

50 Martinez, R.V., Garcia, F., Garcia, R., Coronado, E., Forment Aliaga, A., Romero, F.M., and Tatay, S. (2007) Nanoscale deposition of single molecule magnets onto SiO_2 patterns. *Adv. Mater.*, **19**, 291.

51 Martinez, R.V., Losilla, N.S., Martinez, J., and Garcia, R. (2007) Patterning polymeric structures with 2 nm resolution at 3 nm half pitch in ambient conditions. *Nano Lett.*, **7**, 1846.

52 Zitzler, L., Herminghaus, S., and Mugele, F. (2002) Capillary forces in tapping mode atomic force microscopy. *Phys. Rev. B*, **66**, 155436.

53 Mougin, K., Gnecco, E., and Rao, A. *et al.* (2008) Manipulation of gold nanoparticles: influence of surface chemistry, temperature, and environment (vacuum versus ambient atmosphere). *Langmuir*, **24**, 1577.

54 Kobayashi, N., Li, Y.J., Naitoh, Y., Kageshima, M., and Sugawara, Y. (2006) High sensitivity force detection by phase modulation atomic force microscopy. *Jpn. J. Appl. Phys.*, **45**, L793.

55 Fukuma, T., Kilpatrick, J.I., and Jarvis, S.P. (2006) Phase modulation atomic force microscope with true atomic resolution. *Rev. Sci. Instrum.*, **77**, 123703.

56 Holscher, H. (2008) Theory of phase modulation atomic force microscopy with constant oscillation amplitude. *J. Appl. Phys.*, **103**, 064317.

57 Magonov, S.N., Elings, V., and Whangbo, M.H. (1997) Phase imaging and stiffness in tapping mode atomic force microscopy. *Surf. Sci.*, **375**, L385.

58 Whangbo, M.H., Bar, G., and Brandsch, R. (1998) Description of phase imaging in tapping mode atomic force microscopy by harmonic approximation. *Surf. Sci.*, **411**, L794.

59 Bar, G., Delineau, L., Brandsch, R., Bruch, M., and Whangbo, M.H. (1999) Importance of the indentation depth in tapping mode AFM study of compliant materials. *Appl. Phys. Lett.*, **75**, 4198.

60 Bar, G., Brandsch, R., and Whanbo, M.H. (1999) Correlation between frequency sweep hysteresis and phase imaging instability in tapping mode AFM. *Surf. Sci.*, **436**, L715.

61 Anczykowski, B., Gotsman, B., Fuchs, H., Cleveland, J.P., and Elings, V.B. (1999) How to measure energy dissipation in dynamic mode atomic force microscopy. *Appl. Surf. Sci.*, **140**, 376.

62 Tamayo, J. and Garcia, R. (1998) Relationship between phase shift and energy dissipation in tapping mode scanning force microscopy. *Appl. Phys. Lett.*, **73**, 2926.

63 Garcia, R., Tamayo, J., Calleja, M., and Garcia, F. (1998) Phase contrast in tapping mode scanning force microscopy. *Appl. Phys. A*, **66**, S312.

64 Garcia, R., Tamayo, J., and San Paulo, A. (1999) Phase contrast and surface energy hysteresis in tapping mode scanning force microscopy. *Surf. Interface Anal.*, **27**, 312.

65 San Paulo, A. and Garcia, R. (2001) Amplitude, deformation and phase shift in amplitude modulation force microscopy: a numerical study for compliant materials. *Surf. Sci.*, **471**, 71.

66 San Paulo, A. and Garcia, R. (2001) Tip surface forces, amplitude, and energy dissipation in amplitude modulation (tapping mode) force microscopy. *Phys. Rev. B*, **64**, 193411.

67 Lozano, J.R. and Garcia, R. (2009) Theory of phase spectroscopy in bimodal atomic force microscopy. *Phys. Rev. B*, **79**, 014110.

68 Noy, A., Sanders, C.H., Vezenov, D.V., Wong, S.S., and Lieber, C.M. (1998) Chemically sensitive imaging in tapping mode by chemical force microscopy: relationship between phase lag and adhesion. *Langmuir*, **14**, 1508.

69 Behrend, O.P., Odoni, L., Loubet, J.L., and Burnham, N.A. (1999) Phase imaging: deep or superficial? *Appl. Phys. Lett.*, **75**, 2551.

70 Tamayo, J. (1999) Energy dissipation in tapping mode scanning force microscopy with low quality factors. *Appl. Phys. Lett.*, **75**, 3569.

71 Chen, X., Davies, M.C., Roberts, C.J., Tendler, S.J.B., Williams, P.M., and Burnham, N.A. (2000) Optimizing phase imaging via dynamic force curves. *Surf. Sci.*, **460**, 292.

72 Chen, X., Roberts, C.J., Zhang, J., Davies, M.C., and Tendler, S.J.B. (2002) Phase contrast and attraction repulsion transition in tapping mode atomic force microscopy. *Surf. Sci.*, **519**, L593.

73 Salapaka, M.V., Chen, D.J., and Cleveland, J.P. (2000) Linearity of amplitude and phase in tapping mode atomic force microscopy. *Phys. Rev. B*, **61**, 1106.

74 Sebastian, A., Salapaka, M.V., Chen, D.J., and Cleveland, J.P. (2001) Harmonic and power balance tools for tapping mode atomic force microscope. *J. Appl. Phys.*, **89**, 6473.

75 James, P.J., Atognozzi, M., Tamayo, J., McMaster, T.J., Newton, J.M., and Miles, M.J. (2001) *Langmuir*, **17**, 349.

76 Leclere, P., Dubourg, F., Kopp Marsaudon, S., Bredas, J.L., Lazzaroni, R., and Aimé, J.P. (2002) Dynamic force microscopy analysis of block copolymers: beyond imaging the morphology. *Appl. Surf. Sci.*, **188**, 524.

77 Martin, P., Marsaudon, S., Aimé, J.P., and Bennetau, B. (2005) Experimental determination of conservative and dissipative parts in the tapping mode on a grafted layer: comparison with frequency modulation data. *Nanotechnology*, **16**, 901.

78 Balantekin, M. and Atalar, A. (2003) Power dissipation analysis in tapping mode atomic force microscopy. *Phys. Rev. B*, **67**, 193404.

79 Sahin, O., Quate, C.F., Sogaard, O., and Atalar, A. (2004) Resonant harmonic response in tapping mode atomic force microscopy. *Phys. Rev. B*, **69**, 165416.

80 Mechler, A., Kokavecz, J., Heszler, P., and Lal, R. (2003) Surface energy maps of nanostructures: atomic force microscopy and numerical simulation study. *Appl. Phys. Lett.*, **82**, 3740.

81 D'Amato, M.J., Markus, M.S., Eriksson, M.A., and Carpick, R.W. (2004) Phase imaging and the lever sample tilt in dynamic atomic force microscopy imaging. *Appl. Phys. Lett.*, **85**, 4738.

82 Bodiguel, H., Montes, H., and Fretigny, C. (2004) Depth sensing and dissipation in tapping mode atomic force microscopy. *Rev. Sci. Instrum.*, **75**, 2529.

83 Wang, H., Djurisic, A.B., Chan, W.K., and Xie, M.H. (2005) Factors affecting phase and height contrast of diblock copolymer PS *b* PEO thin films in dynamic force mode atomic force microscopy. *Appl. Surf. Sci.*, **252**, 1092.

84 Holscher, H. and Schwarz, U.D. (2007) Theory of amplitude modulation atomic

force microscopy with and without Q control. *Int. J. Nonlinear Mech.*, **42**, 608.
85 Sahagun, E., Garcia Mochales, P., Sacha, G.M., and Saenz, J.J. (2007) Energy dissipation due to capillary interactions: hydrophobicity maps in force microscopy. *Phys. Rev. Lett.*, **98**, 176106.
86 Lin, S.M. (2007) Energy dissipation and dynamic response of an amplitude modulation atomic force microscopy subjected to a tip sample viscous force. *Ultramicroscopy*, **107**, 245.
87 Sheglov, D.V. and Latyshev, A.V. (2008) Kinetic contrast in atomic force microscopy. *J. Exp. Theor. Phys.*, **106**, 228.
88 Melcher, J., Xu, X., Raman, A., Carrasco Pulido, C., Gomez Herrero, J., de Pablo, P.J., and Carrascosa, J.L. (2009) Origins of phase contrast in the atomic force microscope in liquids. *Proc. Natl. Acad. Sci. USA*, **106**, 13655.
89 Urbakh, M., Klafter, J., Gourdon, D., and Israelachvili, J. (2004) The nonlinear nature of friction. *Nature*, **430**, 525.
90 Meyer, E., Hug, H.J., and Bennewitz, R. (2004) *Scanning Probe Microscopy, Lab on a Tip*, Springer, Berlin.
91 Sills, S., Gray, T., and Overney, R.M. (2005) Molecular dissipation phenomena of nanoscopic friction in the heterogeneous relaxation regime of a glass former. *J. Chem. Phys.*, **123**, 134902.
92 Martinez, N.F., Kaminski, W., Gomez, C.J., Albonetti, C., Biscarini, F., Perez, R., and Garcia, R. (2009) Molecular scale energy dissipation in oligothiophene monolayers measured by dynamic force microscopy. *Nanotechnology*, **20**, 434021.
93 Kantorovich, L.N. and Trevethan, T. (2004) General theory of microscopy dynamical response in surface probe microscopy: from imaging to dissipation. *Phys. Rev. Lett.*, **93**, 236102.
94 Oyabu, N., Pou, P., Sugimoto, Y., Jelinek, P., Abe, M., Morita, S., Perez, R., and Custance, O. (2006) Single atomic contact adhesion and dissipation in dynamic force microscopy. *Phys. Rev. Lett.*, **96**, 106101.
95 Socoliuc, A., Gnecco, E., Maier, S., Pfeiffer, O., Baratoff, A., Bennewitz, R., and Meyer, E. (2006) Atomic scale control of friction by actuation of nanometer sized contacts. *Science*, **313**, 207.
96 Schirmeisen, A. and Holscher, H. (2005) Velocity dependence of energy dissipation in dynamic force microscopy: hysteresis versus viscous damping. *Phys. Rev. B*, **72**, 045431.

Chapter 8

1 Garcia, R. and San Paulo, A. (1999) Attractive and repulsive interaction regimes in tapping mode atomic force microscopy. *Phys. Rev. B*, **60**, 4961.
2 Kokavecz, J., Horvath, Z.L., and Melcher, A. (2004) Dynamic properties of the Q controlled atomic force microscope. *Appl. Phys. Lett.*, **85**, 3232.
3 San Paulo, A. and Garcia, R. (2001) Amplitude, deformation and phase shift in amplitude modulation force microscopy: a numerical study for compliant materials. *Surf. Sci.*, **471**, 71.
4 Giessibl, F.J. (2003) Advances in atomic force microscopy. *Rev. Mod. Phys.*, **75**, 949.
5 Fukuma, T., Kimura, M., Kobayashi, K., Matsushige, K., and Yamada, H. (2005) Development of low noise cantilever deflection sensor for multienvironment frequency modulation atomic force microscopy. *Rev. Sci. Instrum.*, **76**, 053704.
6 Fukuma, T., Ichii, T., Kobayashi, K., Yamada, H., and Matsushige, K. (2005) True molecular resolution imaging by frequency modulation atomic force microscopy in various environments. *Appl. Phys. Lett.*, **86**, 034103.
7 Fukuma, T. and Jarvis, S.P. (2006) Development of liquid environment frequency modulation atomic force microscope with low noise deflection sensor for cantilevers of various dimensions. *Rev. Sci. Instrum.*, **77**, 043701.
8 Ando, T., Uchihashi, T., and Fukuma, T. (2008) High speed atomic force microscopy for nano visualization of dynamic biomolecular processes. *Prog. Surf. Sci.*, **83**, 337.
9 Fukuma, T. (2009) Wideband low noise optical beam deflection sensor with photothermal excitation for liquid environment atomic force microscopy. *Rev. Sci. Instrum.*, **80**, 023707.

10 Albrecht, T.R., Grutter, P., Horne, D., and Rugar, D. (1991) Frequency modulation detection using high *Q* cantilevers for enhanced force microscope sensitivity. *J. Appl. Phys.*, **69**, 668.

11 Bustamante, C. and Keller, D. (1995) Scanning force microscopy in biology. *Phys. Today*, **12**, 32.

12 Keller, D.J. and Chou, C.C. (1992) Imaging steep, high structures by scanning force microscopy with electron beam deposited tips. *Surf. Sci.*, **268**, 333.

13 Keller, D. (1991) Reconstruction of STM and AFM imaged distorted by finite size tips. *Surf. Sci.*, **253**, 353.

14 Keller, D.J. and Franke, F.S. (1993) Envelope reconstruction of probe microscope images. *Surf. Sci.*, **294**, 409.

15 Vesenka, J., Miller, R.R., and Henderson, E. (1994) 3 diemsional probe reconstruction for atomic force microscopy. *Rev. Sci. Instrum.*, **65**, 2249.

16 Villarrubia, J.S. (1994) Morphological estimation of tip geometry for scanned probe microscopy. *Surf. Sci.*, **321**, 287.

17 Villarrubia, J.S. (1997) Algorithms for scanned probe microscope, image simulation, surface reconstruction and tip estimation. *J. Res. Natl. Inst. Stand. Technol.*, **107**, 425.

18 Qian, X. and Villarrubia, J.S. (2007) General three dimensional image simulation and surface reconstruction in scanning probe microscopy using a dexel representation. *Ultramicroscopy*, **108**, 29.

19 Mazeran, P.E., Odoni, L., and Loubet, J.L. (2005) Curvature radius analysis for scanning probe microscopy. *Surf. Sci.*, **585**, 25.

20 Dahlen, G., Osborn, M., Okulan, N., Foreman, W., Chand, A., and Foucher, J. (2005) Tip characterization and surface reconstruction of complex structures with critical dimension atomic force microscopy. *J. Vac. Sci. Technol. B*, **23**, 2297.

21 Yacoot, A. and Koenders, L. (2008) Aspects of scanning force microscope probes and their effects on dimensional measurement. *J. Phys. D*, **41**, 103001.

22 Zia, Q. and Androsch, R. (2009) Effect of atomic force microscope tip geometry on the evaluation of the crystal size of semicrystalline polymers. *Meas. Sci. Technol.*, **20**, 097003.

23 Martinez, N.F., Kaminski, W., Gomez, C.J., Albonetti, C., Biscarini, F., Perez, R., and Garcia, R. (2009) Molecular scale energy dissipation in oligothiophene monolayers measured by dynamic force microscopy. *Nanotechnology*, **20**, 434021.

24 Heuberger, M., Dietler, G., and Schlapbach, L. (1996) Elastic deformations of tip and sample during atomic force microscope measurements. *J. Vac. Sci. Technol. B*, **14**, 1250.

25 Weihs, T.P., Nawaz, Z., Jarvis, S.P., and Pethica, J.B. (1991) Limits of imaging resolution for atomic force microscopy of molecules. *Appl. Phys. Lett.*, **50**, 3536.

26 Gan, Y. (2009) Atomic and subnanometer resolution in ambient conditions by atomic force microscopy. *Surf. Sci. Rep.*, **64**, 99.

27 Ohnersorge, F.M. (1999) Towards atomic resolution non contact dynamic force microscopy in a liquid. *Surf. Interface Anal.*, **27**, 379.

28 Moller, C., Allen, M., Elings, V., Engel, A., and Muller, D.J. (1999) Tapping mode atomic force microscopy produces faithful high resolution images of protein surfaces. *Biophys. J.*, **77**, 1150.

29 Stark, M., Moller, C., Muller, D.J., and Guckenberger, R. (2001) From images to interactions: high resolution phase imaging in tapping mode atomic force microscopy. *Biophys. J.*, **80**, 3009.

30 Kienberger, F. *et al.* (2003) Dynamic force microscopy imaging of native membranes. *Ultramicroscopy*, **97**, 229.

31 Kienberger, F., Mueller, H., Pastushenko, V., and Hinterdorfer, P. (2004) Following single antibody binding to purple membranes in real time. *EMBO Rep.*, **5**, 579.

32 Dong, M., Husale, S., and Sahin, O. (2009) Determination of protein structural flexibility by microsecond force spectroscopy. *Nat. Nanotechnol.*, **4**, 514.

33 Melcher, J., Xu, X., Raman, A., Carrasco Pulido, C., Gomez Herrero, J., de Pablo, P.J., and Carrascosa, J.L. (2009) Origins of phase contrast in the atomic force microscope in liquids. *Proc. Natl. Acad. Sci. USA*, **106**, 13655.

34 Viani, M.B., Pietrasanta, L.I., Thompson, J.B., Chad, A., Gebeshuber, I.C., Kindt, J.H., Richter, M., Hansma, H.G., and Hansma, P.K. (2000) Probing protein protein interactions in real time. *Nat. Struct. Biol.*, **7**, 644.

35 Yokokawa, M., Wada, C., Ando, T., Sakai, N., Yagi, A., Yoshimura, S.H., and Takeyasu, K. (2006) Fast scanning atomic force microscopy reveals the ATP/ADP dependent conformational changes of GroEL. *EMBO J.*, **25**, 4567.

36 Preiner, J., Tang, J., Pastushenko, V., and Hinterdorfer, P. (2007) Higher harmonic atomic force microscopy: imaging of biological membranes in liquid. *Phys. Rev. Lett.*, **99**, 046102.

37 Klinov, D. and Magonov, S. (2004) True molecular resolution in tapping mode atomic force microscopy with high resolution probes. *Appl. Phys. Lett.*, **84**, 2697.

38 Belikov, S. and Magonov, S. (2006) True molecular scale imaging in atomic force microscopy: experiment and modelling. *Jpn. J. Appl. Phys.*, **71**, 2158.

39 Kuna, J.J., Voıtchovsky, K., Singh, C., Jiang, H., Mwenifumbo, S., Ghorai, P.K., Stevens, M.M., Glotzer, S.C., and Stellacci, F. (2009) The effect of nanometer scale structure on interfacial energy. *Nat. Mater.*, **8**, 837.

40 Ohnesorge, F. and Binnig, G. (1993) True atomic resolution by atomic force microscopy through repulsive and attractive forces. *Science*, **260**, 1451.

41 San Paulo, A. and Garcia, R. (2000) High resolution imaging of antibodies by tapping mode atomic force microscopy: attractive and repulsive tip sample interaction regimes. *Biophys. J.*, **78**, 1599.

42 Patil, S., Martinez, N.F., Lozano, J.R., and Garcia, R. (2007) Force microscopy imaging of individual protein molecules with sub pico Newton force sensitivity. *J. Mol. Recogn.*, **20**, 516.

43 Thomson, N.H. (2005) The substructure of immunoglobulin G resolved to 25 kDa using amplitude modulation AFM in air. *Ultramicroscopy*, **105**, 103.

44 Martinez, N.F., Lozano, J.R., Herruzo, E.T., Garcia, F., Ritchter, C., Sulzbach, T., and Garcia, R. (2008) Bimodal atomic force microscopy imaging of isolated antibodies in air and liquids. *Nanotechnology*, **19**, 384011.

45 Dunlap, D.D., Maggi, A., Soria, M.R., and Monaco, L. (1997) Nanoscopic structure of DNA condensed for gene delivery. *Nucleic Acids Res.*, **25**, 3095.

46 Hansma, H.G., Laney, D.E., Benazilla, M., Sinsheimer, R.L., and Hansma, P.K. (1995) Applications for atomic force microscopy of DNA. *Biophys. J.*, **68**, 1672.

47 Rivetti, C., Guthold, M., and Bustamante, C. (1996) Scanning force microscopy of DNA deposited onto mica: equilibration versus kinetic trapping studied by statistical polymer chain analysis. *J. Mol. Biol.*, **264**, 919.

48 Pignataro, B., Chi, L., Gao, S., Anczykowski, B., Niemeyer, C., Adler, M., and Fuchs, H..

49 Pignataro, B., Chi, L., Gao, S., Anczykowski, B., Niemeyer, C., Adler, M., and Fuchs, H. (2002) Dynamic scanning force microscopy study of self assembled DNA protein nanostructures. *Appl. Phys. A*, **74**, 447.

50 Martinez, J., Yuzvinsky, T.D., Fennimore, A.M., Zettl, A., Garcia, R., and Bustamante, C. (2005) Length control and sharpening of atomic force microscope carbon nanotube tips assisted by an electron beam. *Nanotechnology*, **16**, 2493.

51 Yang, C. W., Hwang, I. S., Chen, Y.F., Chang, C.S., and Tsai, D.P. (2007) Imaging of soft matter with tapping mode atomic force microscopy and non contact mode atomic force microscopy. *Nanotechnology*, **18**, 084009.

52 Ercolini, E., Valle, F., Adamik, J., Witz, G., Metzler, R., De Los Rios, P., Roca, J., and Dietler, G. (2007) Fractal dimension and localization of DNA knots. *Phys. Rev. Lett.*, **98**, 058102.

53 Lyubchenko, Y.L. and Shlyaktenko, L.S. (2009) AFM analysis of structure and dynamics of protein DNA complexes. *Methods*, **47**, 206.

54 Schwarz, U.D., Holscher, H., and Wiesendanger, R. (2000) *Phys. Rev. B*, **62**, 13082.

55 Hoogenboom, B.W., Hug, H. J., Pellmont, Y., Martin, S., Frederix, P.L.T.M., Fotiadis, D., and Engel, A. (2006) Quantitative

dynamic mode scanning force microscopy in liquid. *Appl. Phys. Lett.*, **88**, 193109.
56 Muller, D.J., Fotiadis, D., Scheuring, S., Muller, S.A., and Engel, A. (1999) Electrostatically balanced subnanometer imaging of biological specimens by atomic force microscope. *Biophys. J.*, **76**, 1101.
57 Zhong, S., Li, H., Chen, X.Y., Cao, E.H., Jin, G., and Hu, K.S. (2007) Different interactions between the two sides of purple membrane with atomic force microscope tip. *Langmuir*, **23**, 4486.

Chapter 9

1 Durig, U. (1999) Relations between interaction force and frequency shift in large amplitude dynamic force microscopy. *Appl. Phys. Lett.*, **75**, 433.
2 Stark, R.W. and Heckel, W.M. (2000) Fourier transformed atomic force microscopy: tapping mode atomic force microscopy beyond the Hookian approximation. *Surf. Sci.*, **457**, 219.
3 Stark, M., Stark, R.W., Heckl, W.H., and Guckenberger, R. (2002) Inverting dynamic force microscopy: from signals to time resolved interaction forces. *Proc. Natl. Acad. Sci. USA*, **99**, 8473.
4 Rodriguez, T.R. and Garcia, R. (2002) Tip motion in amplitude modulation (tapping mode) atomic force microscopy: comparison between continuous and point mass models. *Appl. Phys. Lett.*, **80**, 1646.
5 Schroter, K., Petzold, A., Henze, T., and Thurn Albrecht, T. (2009) Quantitative analysis of scanning force microscopy data using harmonic models. *Macromolecules*, **42**, 1114.
6 Rabe, U., Turner, I., and Arnold, W. (1998) Analysis of the high frequency response of atomic force microscope levers. *Appl. Phys. A*, **66**, S277.
7 Stark, R.W. (2004) Spectroscopy of higher harmonics in dynamic atomic force microscopy. *Nanotechnology*, **15**, 347.
8 Stark, R.W., Schitter, G., Stark, M., Guckenberger, R., and Stemmer, A. (2004) State space model of freely vibrating and surface coupled cantilever dynamics in atomic force microscopy. *Phys. Rev. B*, **69**, 085412.
9 Crittenden, S., Raman, A., and Reifenberger, R. (2005) Probing attractive forces at the nanoscale using higher harmonic dynamic force microscopy. *Phys. Rev. B*, **72**, 235422.
10 Sahin, O., Quate, C.F., Sogaard, O., and Atalar, A. (2004) Resonant harmonic response in tapping mode atomic force microscopy. *Phys. Rev. B*, **69**, 165416.
11 Balantekin, M. and Atalar, A. (2005) Enhancing higher harmonics of a tapping cantilever by excitation at a submultiple of its resonance frequency. *Phys. Rev. B*, **71**, 125416.
12 Li, H., Chen, Y. and Dai, L. (2008) Concentrated mass cantilever enhances multiple harmonics in tapping mode atomic force microscopy. *Appl. Phys. Lett.*, **92**, 151903.
13 Yuan, L. and Jian Qiang, Q. (2009) Higher harmonics in tapping mode atomic force microscope. *Chin. Phys. Lett.*, **26**, 100703.
14 Hillebrand, R., Stark, M., and Guckenberger, R. (2000) Higher harmonics generation in tapping mode atomic force microscopy: insights into the tip sample interactions. *Appl. Phys. Lett.*, **76**, 3478.
15 Stark, M., Stark, R.W., Heckl, W.M., and Guckenberger, R. (2000) Spectroscopy of the anharmonic cantilever oscillations in tapping mode atomic force microscopy. *Appl. Phys. Lett.*, **77**, 3293.
16 Sahin, O., Yaralioglu, G., Grow, R., Zappe, S.F., Atalar, A., Quate, C., and Solgaard, O. (2004) High resolution imaging of elastic properties using harmonic cantilevers. *Sens. Actuators A*, **114**, 183.
17 Balantekin, M. and Atalar, A. (2005) Enhanced higher harmonic imaging in tapping mode atomic force microscopy. *Appl. Phys. Lett.*, **87**, 243513.
18 Wang, W.L. and Hu, S.J. (2005) Modal response and frequency shift of the cantilever in a noncontact atomic force microscope. *Appl. Phys. Lett.*, **87**, 183506.
19 Gabai, R., Segev, L., and Joselevich, E. (2005) Single polymer chains as specific transducers of molecular recognition in scanning probe microscopy. *J. Am. Chem. Soc.*, **127**, 11390.

20 Hu, S. and Raman, A. (2006) Chaos in atomic force microscopy. *Phys. Rev. Lett.*, **96**, 036107.

21 Preiner, J., Tang, J., Pastushenko, V., and Hinterdorfer, P. (2007) Higher harmonic atomic force microscopy: imaging of biological membranes in liquid. *Phys. Rev. Lett.*, **99**, 046102.

22 Turner, R.D., Kirkham, J., Devine, D., and Thomson, N.H. (2009) Second harmonic atomic force microscopy of living *Staphylococcus aureus* bacteria. *Appl. Phys. Lett.*, **94**, 043901.

23 Legleiter, J. and Kowalewski, T. (2005) Insights into fluid tapping mode atomic force microscopy provided by numerical simulations. *Appl. Phys. Lett.*, **87**, 163120.

24 Minne, S.C., Manalis, S.R., Atalar, A., and Quate, C.F. (1996) Contact imaging in the atomic force microscope using higher order flexural mode combined with a new sensor. *Appl. Phys. Lett.*, **68**, 1427.

25 Stark, R.W., Drobek, T., and Heckl, W. (1999) Tapping mode atomic force microscopy and phase imaging in higher eigenmodes. *Appl. Phys. Lett.*, **74**, 3296.

26 Girard, P., Ramonda, M., and Arinero, R. (2006) Dynamic atomic force microscopy operation based on high flexure modes of the cantilever. *Rev. Sci. Instrum.*, **77**, 096105.

27 Hoummady, M. and Farnault, E. (1998) Enhanced sensitivity to force gradients by using higher flexural modes of the atomic force microscope cantilever. *Appl. Phys. A*, **66**, S361.

28 Pfeiffer, O., Loppacher, C., Wattinger, C., Bammerlin, M., Gysin, U., Guggisber, M., Rast, S., Bennewitz, R., Meyer, E., and Guntherodt, H. J. (2000) Using higher flexural modes in non contact force microscopy. *Appl. Surf. Sci.*, **157**, 337.

29 Fukuma, T., Kimura, K., Kobayashi, K., Matsushige, K., and Yamada, H. (2004) Dynamic force microscopy at high cantilever resonance frequencies using heterodyne optical beam deflection method. *Appl. Phys. Lett.*, **85**, 6287.

30 Kawai, S., Kitamura, S., Kobayashi, D., Meguro, S., and Kawakatsu, H. (2005) An untrasmall amplitude operation of dynamic force microscopy with second flexural mode. *Appl. Phys. Lett.*, **86**, 193107.

31 Sugimoto, Y., Innami, S., Abe, M., Custance, O., and Morita, S. (2007) Dynamic force spectroscopy using cantilever higher flexural modes. *Appl. Phys. Lett.*, **91**, 093120.

32 Garcia, R. and Rodriguez, T.R.,Método de utilización de un microscopio de fuerzas y microscopio, PCT ES200501555.

33 Proksch, R. (2006) Multifrequency, repulsive mode amplitude modulated atomic force microscopy. *Appl. Phys. Lett.*, **89**, 113121.

34 Martinez, N.F., Patil, S., Lozano, J.R., and Garcia, R. (2006) Enhanced compositional sensitivity in atomic force microscopy by the excitation of the first two flexural modes. *Appl. Phys. Lett.*, **89**, 153115.

35 Patil, S., Martinez, N.F., Lozano, J.R., and Garcia, R. (2007) Force microscopy imaging of individual protein molecules with sub pico Newton force sensitivity. *J. Mol. Recogn.*, **20**, 516.

36 Martinez, N.F., Lozano, J.R., Herruzo, E.T., Garcia, F., Ritchter, C., Sulzbach, T., and Garcia, R. (2008) Bimodal atomic force microscopy imaging of isolated antibodies in air and liquids. *Nanotechnology*, **19**, 384011.

37 Lozano, J.R. and Garcia, R. (2008) Theory of multifrequency AFM. *Phys. Rev. Lett.*, **100**, 076102.

38 Lozano, J.R. and Garcia, R. (2009) Theory of phase spectroscopy in bimodal atomic force microscopy. *Phys. Rev. B*, **79**, 014110.

39 Dietz, C., Zerson, M., Riesch, C., Gigler, A.M., Stark, R.W., Rehse, N., and Magerle, R. (2008) Nanotomography with enhanced resolution using bimodal atomic force microscopy. *Appl. Phys. Lett.*, **92**, 143107.

40 Stark, R.W. (2009) Dynamics of repulsive dual frequency atomic force microscopy. *Appl. Phys. Lett.*, **94**, 063109.

41 Thota, P., MacLaren, S., and Dankowicz, H. (2007) Controlling bistability in tapping mode atomic force microscopy using dual frequency excitation. *Appl. Phys. Lett.*, **91**, 093108.

42 Stark, R.W., Naujoks, N., and Stemmer, A. (2007) *Nanotechnology*, **18**, 065502.

43 Bostanci, U., Abak, M.K., Aktas, O., and Dâna, A. (2008) Nanoscale charging hysteresis measurements by

multifrequency electrostatic force spectroscopy. *Appl. Phys. Lett.*, **92**, 093108.
44 Ding, X.D., An, J., Xu, J.B., Li, C., and Zeng, R.Y. (2009) Improving lateral resolution of electrostatic force microscopy by multifrequency method under ambient conditions. *Appl. Phys. Lett.*, **94**, 223109.
45 Li, J.W., Cleveland, J.P., and Proksch, R. (2009) Bimodal magnetic force microscopy: separation of short and long range forces. *Appl. Phys. Lett.*, **94**, 163118.
46 Kawai, S., Glatzel, T., Koch, S., Such, B., Baratoff, A., and Meyer, E. (2009) Systematic achievement of improved atomic scale contrast via bimodal dynamic force microscopy. *Phys. Rev. Lett.*, **103**, 220801.
47 Sadewasser, S., Villanueva, G., and Plaza, J.A. (2006) Special cantilever geometry for the access of higher oscillation modes in atomic force microscopy. *Appl. Phys. Lett.*, **89**, 033106.
48 Garcia Sanchez, D., Paulo, A.S., Esplandiu, M.J., Perez Murano, F., and Bachtold, A. (2007) Mechanical detection of carbon nanotube resonator vibrations. *Phys. Rev. Lett.*, **99**, 085501.
49 Garcia Sanchez, D., van der Zande, A.M., Paulo, A.S., Lassagne, B., McEuen, P.L., and Bachtold, A. (2008) Imaging mechanical vibrations in suspended graphene sheets. *Nano Lett.*, **8**, 1399.
50 Agarwal, P. and Salapaka, M.V. (2009) Real time estimation of equivalent cantilever parameters in tapping mode atomic force microscopy. *Appl. Phys. Lett.*, **95**, 083113.
51 Platz, D., Tholén, E.A., and Haviland, D.B. (2008) Intermodulation atomic force microscopy. *Appl. Phys. Lett.*, **92**, 153106.
52 Hutter, C., Platz, D., Tholen, E.A., Hansson, T.H., and Haviland, D.B. (2010) Reconstructing nonlinearities with intermodulation spectroscopy. *Phys. Rev. Lett.*, **104**, 05801.
53 Kolosov, O. and Yamanaka, K. (1993) Nonlinear detection of ultrasonic vibrations in an atomic force microscope. *Jpn. J. Appl. Phys.*, **32**, L1095.
54 Rabe, U. and Arnold, W. (1994) Acoustic microscopy by atomic force microscopy. *Appl. Phys. Lett.*, **64**, 1493.
55 Cuberes, M.T., Assender, H.E., Briggs, G.A.D., and Kolosov, O.V. (2000) Heterodyne force microscopy of PMMA/rubber nanocomposites: nanomapping of viscoelastic response at ultrasonic frequencies. *J. Phys. D*, **33**, 2347.
56 Shekhawat, G.S. and Dravid, V.P. (2005) Nanoscale imaging of buried structures via scanning near filed ultrasound holography. *Science*, **310**, 89.
57 Shekhawat, G., Srivastava, A., Avasthy, S., and Dravid, V. (2009) Ultrasound holography for noninvasive imaging of buried defects and interfaces for advanced interconnect architectures. *Appl. Phys. Lett.*, **95**, 263101.
58 Tetard, L., Passian, A., Venmar, K.T., Lynch, R.M., Voy, B.H., Shekhawat, G.S., Dravid, V.P., and Thundat, T. (2008) Imaging nanoparticles in cells by nanomechanical holography. *Nat. Nanotechnol.*, **3**, 501.
59 Cuberes, M.T. (2009) Intermittent contact heterodyne force microscopy. *J. Nanomater.*, 762016.
60 Tetard, L., Passian, A., Lynch, R.M., Voy, B.H., Shekhawat, G.S., Dravid, V.P., and Thundat, T. (2008) Elastic phase response of silica nanoparticles buried in soft matter. *Appl. Phys. Lett.*, **93**, 133113.
61 Garcia, R., Magerle, R., and Perez, R. (2007) Nanoscale compositional mapping with gentle forces. *Nat. Mater.*, **6**, 405.
62 Garcia, R. (2009) Images from below the surface. *Nat. Nanotechnol.*, **5**, 101.
63 Tetard, L., Passian, A., and Thundat, T. (2009) New modes for subsurface atomic force microscopy through nanomechanical coupling. *Nat. Nanotechnol.*, **5**, 105.
64 Sahin, O., Quate, C.F., Solgaard, O., and Atalar, A. (2007) An atomic force microscope tip designed to measure time varying nanomechanical forces. *Nat. Nanotechnol.*, **2**, 507.
65 Sahin, O. (2008) Time varying tip sample force measurements and steady state dynamics in tapping mode atomic force microscopy. *Phys. Rev. B*, **77**, 11505.
66 Sahin, O. and Erina, N. (2008) High resolution and large dynamic range nanomechanical mapping in tapping

mode atomic force microscopy. *Nanotechnology*, **19**, 445717.
67 Dong, M., Husale, S., and Sahin, O. (2009) Determination of protein structural flexibility by microsecond force spectroscopy. *Nat. Nanotechnol.*, **4**, 514.
68 Husale, S., Persson, H.H.J., and Sahin, O. (2009) DNA nanomechanics allows direct digital detection of complementary DNA and microRNA targets. *Nature*, **462**, 1075.
69 Huang, L. and Su, C.M. (2004) A torsional resonance mode AFM for in plane tip surface interactions. *Ultramicroscopy*, **100**, 277.
70 Kasai, T., Bhushan, B., Huang, L., and Su, C.M. (2004) Topography and phase imaging using torsional resonance mode. *Nanotechnology*, **15**, 9731.
71 Reinstadtler, M., Kasai, T., Rabe, U., Bhushan, B., and Arnold, W. (2005) Imaging and measurement of elasticity and friction using TR mode. *J. Phys. D*, **38**, R269.
72 Yurtsever, A., Gigler, A.M., Macias, E., and Stark, R.W. (2007) Response of a laterally vibrating nanotip to surface forces. *Appl. Phys. Lett.*, **91**, 253120.
73 Mullin, N. and Hobbs, J. (2008) Torsional resonance AFM in water. *Appl. Phys. Lett.*, **92**, 053103.
74 Mullin, N., Vasiliev, C., Tucker, J.D., Hunter, C.N., Weber, C.H.M., and Hobbs, J.K. (2009) Torsional tapping atomic force microscopy using T shaped cantilevers. *Appl. Phys. Lett.*, **94**, 173109.
75 Lee, H. L. and Chang, W. J. (2008) Coupled lateral bending torsional vibration sensitivity of atomic force microscope cantilever. *Ultramicroscopy*, **108**, 707.
76 Jesse, S., Kalinin, S.V., Proksch, R., Baddorf, A.P., and Rodriguez, B.J. (2007) Energy dissipation measurements on the nanoscale: band excitation method in scanning probe microscopy. *Nanotechnology*, **18**, 435503.
77 Mirman, B. and Kalinin, S.V. (2008) Resonance frequency analysis for surface coupled AFM cantilever in ambient and liquid environments. *Appl. Phys. Lett.*, **92**, 083102.
78 Jesse, S. and Kalinin, S.V. (2009) Principal component and spatial correlation analysis of spectroscopic imaging data in scanning probe microscopy. *Nanotechnology*, **20**, 085714.
79 Kalinin, S.V., Jesse, S., and Proksch, R. (2010) Sinc or sine? New methods for information acquisition and processing in scanning probe microscopy. *R&D Magazine*.
80 Nikiforov, M.P., Vertegel, A.A., Reukov, V.V., Thompson, G.L., Kalinin, S.V., and Jesse, S. (2009) Functional recognition imaging using artificial neural networks: applications to rapid cellular identification by broadband// electromechanical response. *Nanotechnology*, **20**, 405708.
81 Nikiforov, M.P., Thompson, G.L., Reukov, V.V., Jesse, S., Guo, S., Rodriguez, B.J., Seal, K., Vertegel, A.A., and Kalinin, S.V. (2010) Double layer mediated electromechanical response of amyloid fibrils in liquid environment. *ACS Nano*, **4**, 689.

Chapter 10

1 Lewis, A., Isaacson, M., Harootunian, A., and Murray, A. (1984) Development of a 500 Å spatial resolution light microscope. *Ultramicroscopy*, **13**, 227.
2 Pohl, D.W., Denk, S., and Lantz, M. (1984) Optical stethoscopy: image recording with resolution λ/20. *Appl. Phys. Lett.*, **44**, 651.
3 Novotny, L. and Hecht, B. (2006) *Principles of Nano Optics*, Cambridge University Press, New York.
4 Fischer, U.C. and Pohl, D.W. (1989) Observation of single particle plasmons by near field optical microscopy. *Phys. Rev. Lett.*, **62**, 458.
5 Betzig, E., Trautmann, J.K., Harris, T.D., Weiner, J.S., and Kostelak, R.L. (1991) Breaking the diffraction barrier: optical microscopy on a nanometric scale. *Science*, **251**, 1468.
6 Inouye, Y. and Kawata, S. (1994) Near field scanning optical microscope with a metallic probe tip. *Opt. Lett.*, **19**, 159.
7 Zenhausern, F., Martin, Y., and Wickramasinghe, H.K. (1995) Scanning interferometric apertureless microscopy: optical imaging at 10 angstrom resolution. *Science*, **269**, 1083.

8 Knoll, B. and Keilmann, F. (1999) Near field probing of vibrational absorption for chemical microscopy. *Nature*, **399**, 134.

9 Hillebrand, R., Knoll, B., and Keilmann, F. (2000) Pure optical contrast in scattering type scanning near field microscopy. *J. Microsc.*, **202**, 77.

10 Keilmann, F. and Hillenbrand, R. (2004) Near field microscopy by elastic light scattering from a tip. *Philos. Trans. R. Soc. Lond. A*, **362**, 787.

11 Huber, A.J., Kazantsey, D., Keilmann, F., Wittborn, J., and Hillebrand, R. (2007) Simultaneous IR material recognition and conductivity mapping by nanoscale near field microscopy. *Adv. Mater.*, **19**, 2209.

12 Keilmann, F. and Hillenbrand, R. (2008) Near field nanoscopy by elastic light scattering from a tip, in *Nano Optics and Near Field Optical Microscopy* (eds A. Zayats and D. Richard), Artech House, London, pp. 235 265.

13 Florin, E.L., Moy, V.T., and Gaub, H.E. (1994) Adhesion forces between individual ligand receptor pairs. *Science*, **264**, 415.

14 Lee, G.U., Kidwell, D.A., and Colton, R.J. (1994) Sensing discrete streptavidin biotin interaction with the atomic force microscope. *Langmuir*, **10**, 354.

15 Hinterdorfer, P., Baumgartner, W., Gruber, H.J., Schilcher, K., and Schindler, H. (1996) Detection and localization of individual antibody antigen recognition events by atomic force microscopy. *Proc. Natl. Acad. Sci. USA*, **93**, 3477.

16 Rief, M., Gautel, M., Oesterhelt, F., Fernandez, J.M., and Gaub, H.E. (1997) Reversible unfolding of individual titin immunoglobulin domains by AFM. *Science*, **276**, 1109.

17 Fritz, J., Katopodis, A.G., Kolbinger, F., and Anselmetti, D. (1998) Force mediated kinetics of single P selectin ligand complexes observed by atomic force microscopy. *Proc. Natl. Acad. Sci. USA*, **95**, 12283.

18 Tromas, C., Rojo, J., de la Fuente, J.M., Garcia, R., and Penades, S. (2001) Adhesion forces between Lewis(x) determinant antigens as measured by atomic force microscopy. *Angew. Chem., Int. Ed.*, **40**, 3052.

19 Butt, H.J., Capella, B., and Kappl, M. (2005) Force measurements with the atomic force microscope: technique, interpretation and applications. *Surf. Sci. Rep.*, **59**, 1.

20 Gianotti, M.I. and Vancso, G.J. (2007) Interrogation of single synthetic polymer chains and polysaccharides by AFM based force spectroscopy. *Chem. Phys. Chem.*, **8**, 2290.

21 Bizzarri, A.R. and Cannistraro, S. (2009) Atomic force spectroscopy in biological complex formation: strategies and perspectives. *J. Phys. Chem. B*, **113**, 52.

22 Stroh, C., Wang, H., Bash, R., Ashcroft, B., Nelson, J., Gruber, H., Lohr, D., Lindsay, S.M., and Hinterdorfer, P. (2004) Single molecule recognition imaging microscopy. *Proc. Natl. Acad. Sci. USA*, **101**, 12503.

23 Stroh, C.M., Ebner, A., Geretschlager, M., Freudenthaler, G., Kiebenger, F., Kamruzzahan, A.S.M., Smith Gill, S.J., Gruber, H.J., and Hinterdorfer, P. (2004) Simultaneous topography and recognition imaging using force microscopy. *Biophys. J.*, **87**, 1981.

24 Ebner, A., Kienberger, F., Kada, G., Stroh, C.M., Geretschlager, M., Kamruzzahan, A.S.M., Wildling, L., Johnson, W.T., Ashcroft, B., Nelson, J., Lindsay, S.M., Gruber, H.J., and Hinterdorfer, P. (2005) Localization of single avidin biotin interaction using simultaneous topography and molecular recognition imaging. *Chem. Phys. Chem.*, **6**, 897.

25 Preiner, J., Ebner, A., Chtcheglova, L., Zhu, R., and Hinterdorfer, P. (2009) Simultaneous topography and recognition imaging: physical aspects and optimal imaging conditions. *Nanotechnology*, **20**, 215103.

26 Preiner, J., Losilla, N.S., Ebner, A., Annibale, P., Biscarini, F., Garcia, R., and Hinterdorfer, P. (2009) Imaging and detection of single molecule recognition events on organic semiconductor surfaces. *Nano Lett.*, **9**, 571.

27 Ebner, A., Wildling, L., Zhu, R., Rankl, C., Haselgrubbler, T., Hinterdorfer, P., and Gruber, H.J. (2008) Functionalization of

probe tips and supports for single molecule recognition force microscopy. *Top. Curr. Chem.*, **285**, 29.

28 Day, H.C. and Allee, D.R. (1993) Selective area oxidation of silicon with a scanning force microscope. *Appl. Phys. Lett.*, **62**, 2691.

29 Perez Murano, F., Abadal, G., Barniol, N., Aymerich, X., Servat, J., Gorostiza, P., and Sanz, F. (1995) Nanometer scale oxidation of Si(100) surfaces by tapping mode AFM. *J. Appl. Phys.*, **78**, 6797.

30 Sugimura, H. and Nakagiri, N. (1997) Nanoscopic surface architecture based on scanning probe electrochemistry and molecular self assembly. *J. Am. Chem. Soc.*, **119**, 9226.

31 Xu, S. and Liu, G.Y. (1997) Nanometer scale fabrication by simultaneous nanoshaving and molecular self assembly. *Langmuir*, **12**, 127.

32 Binnig, G., Despont, M., Drechsler, U., Haberle, W., Luywyche, M., Vettiger, P., Mamin, H.J., Chui, B.W., and Kenny, T.W. (1999) Ultrahigh density atomic force microscopy data storage with erase capability. *Appl. Phys. Lett.*, **74**, 1329.

33 Piner, R.D., Zhu, J., Xu, F., Hong, S.H., and Mirkin, C.A. (1999) Dip pen nanolithography. *Science*, **283**, 661.

34 Maoz, R., Frydman, E., Cohen, S.R., and Sagiv, J. (2000) *Adv. Mater.*, **12**, 725.

35 Hoeppener, S., Maoz, R., Cohen, S.R., Chi, L., Fuchs, H., and Sagiv, J. (2002) Metal nanoparticles, nanowires, and contact electrodes self assembled on patterned monolayer templates: a bottom up chemical approach. *Adv. Mater.*, **14**, 1036.

36 Li, Y., Maynor, W., and Liu, J. (2001) Electrochemical AFM 'dip pen' nanolithography. *J. Am. Chem. Soc.*, **123**, 2105.

37 Cavallini, M., Biscarini, F., Leon, S., Zerbetto, F., Bottari, G., and Leigh, D.A. (2003) Information storage using supramolecular patterns. *Science*, **299**, 531.

38 Lyuksyutov, S.F., Vaia, R.A., Paramove, P.B., Juhl, S., Waterhouse, L., Ralich, R.M., Sigalov, G., and Sancaktar, E. (2003) Electrostatic nanolithography in polymers using atomic force microscopy. *Nat. Mater.*, **2**, 468.

39 Liu, J.F. and Miller, G.P. (2007) Field assisted nanopatterning. *J. Phys. Chem. C*, **111**, 10758.

40 Dagata, J.A. (1995) Device fabrication by scanned probe oxidation. *Science*, **270**, 1625.

41 Tseng, A.A., Notargiocomo, A., and Chen, T.P. (2005) Nanofabrication by scanning probe microscope lithography: a review. *J. Vac. Sci. Technol. B*, **23**, 877.

42 Samorí, P. (2005) Exploring supramolecular interactions and architectures by scanning force microscopies. *Chem. Soc. Rev.*, **34**, 551.

43 Garcia, R., Martinez, R.V., and Martinez, J. (2006) Nano chemistry and scanning probe nanolithographies. *Chem. Soc. Rev.*, **35**, 29.

44 Snow, E.S. and Campbell, P.M. (1995) AFM fabrication of sub 10 nanometer metal oxide devices with *in situ* control of electrical properties. *Science*, **270**, 1639.

45 Matsumoto, K., Gotoh, Y., Maeda, T., Dagata, J.A., and Harris, J.S. (2000) Room temperature single electron memory made by pulse mode atomic force nano oxidation process on atomically flat α substrate. *Appl. Phys. Lett.*, **76**, 239.

46 Fuhrer, A., Luscher, S., Ihn, T., Heinzel, T., Ensslin, K., Wegscheider, W., and Bichler, M. (2001) Energy spectra of quantum rings. *Nature*, **413**, 822.

47 Bouchiat, V., Faucher, M., Thirion, C., Wernsdorfer, W., Fournier, T., and Pannetier, B. (2001) Josephson junctions and superconducting quantum interference devices mada by local oxidation of niobium ultrathin films. *Appl. Phys. Lett.*, **79**, 123.

48 Calleja, M., Tello, M., Anguita, J., Garcia, F., and Garcia, R. (2001) Fabrication of gold nanowires on insulating substrates by field induced mass transport. *Appl. Phys. Lett.*, **79**, 2471.

49 Chen, C.F., Tzeng, S.D., Chen, H.Y., and Gwo, S. (2005) Silicon microlens structures fabricated by scanning probe gray scale oxidation. *Optics Letters*, **30**, 652.

50 Pellegrino, L., Yanagisawa, Y., Ishikawa, M., Matsumoto, T., Tanaka, H., and Kawai, T. (2006) $(Fe, Mn)_3O_4$ nanochannels

fabricated by AFM local oxidation nanolithography using Mo/poly(methyl methacrylate) nanomasks. *Adv. Mater.*, **18**, 3099.

51 Rochdi, N., Tonneau, D., Jandard, F., Dallaporta, H., Safarov, V., and Gautier, J. (2008) Electrical conductivity of ultra thin silicon nanowires. *J. Vac. Sci. Technol., B*, **26**, 159.

52 Martinez, J., Martinez, R.V., and Garcia, R. (2008) Silicon nanowire transistors with a channel width of 4 nm fabricated by atomic force microscope nanolithography. *Nano Lett.*, **8**, 3636.

53 Garcia, R., Calleja, M., and Rohrer, H. (1999) Patterning of silicon surfaces with non contact atomic force microscopy: field induced formation of nanometer size water bridges. *J. Appl. Phys.*, **86**, 1898.

54 Tello, M. and Garcia, R. (2001) Nano oxidation of silicon surfaces: comparison of noncontact and contact atomic force microscopy methods. *Appl. Phys. Lett.*, **79**, 424.

55 Calleja, M., Tello, M., and Garcia, R. (2002) Size determination of field induced water menisci in noncontact atomic force microscopy. *J. Appl. Phys.*, **92**, 5539.

56 Dagata, J.A., Perez Murano, F., Martin, C., Kuramochi, H., and Yokoyama, H. (2004) Current, charge, and capacitance during scanning probe oxidation. *J. Appl. Phys.*, **96**, 2386.

57 Kinser, C.R., Schmitz, M.J., and Hersam, M.C. (2005) Kinetics and mechanism of atomic force microscope local oxidation on hydrogen passivated silicon in inert organic solvents. *Nano Lett.*, **5**, 91.

58 Martinez, R.V., Martinez, J., Chiesa, M., Garcia, R., Coronado, E., Pinilla Cienfuegos, E., and Tatay, S. (2010) Large scale nanopatterning of single proteins used as carriers of magnetic nanoparticles. *Adv. Mater.*, **22**, 588.

Index

Amplitude Modulation Atomic Force Microscopy. Ricardo García

ISBN: 978-3-527-40834-4